The Flotation Characteristics of Magnetic/4C (Fe_7S_8) and Non–magnetic/5C (Fe_9S_{10}) Pyrrhotite Superstructures

Ravinder S. Multani

Department of Mining and Materials Engineering
McGill University
Montreal, Quebec, Canada
April 2018

A thesis submitted to McGill University in partial fulfillment of the requirements of the degree of Doctor of Philosophy

The inexplicable figure that initiated this thesis…

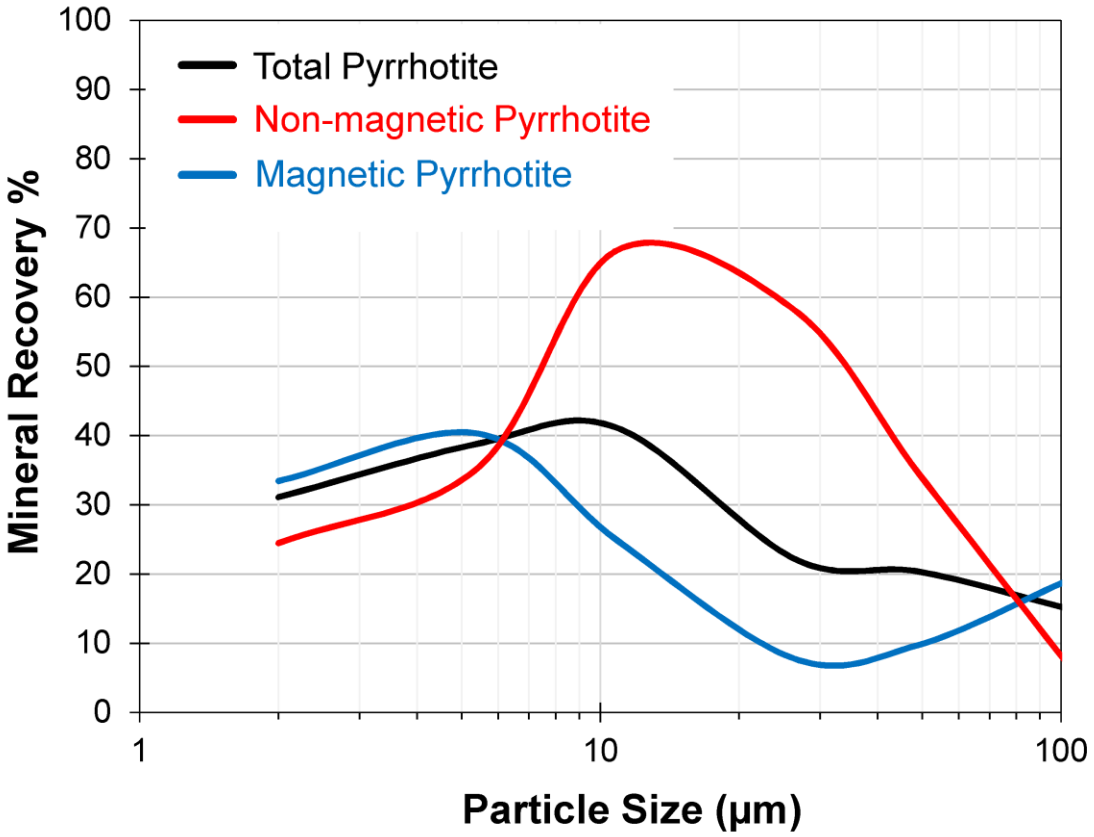

Flotation recovery-by-size relationship of pyrrhotite and its superstructures (magnetic/4C – Fe_7S_8 and non-magnetic/5C – Fe_9S_{10}); courtesy Lori Kormos – XPS (Sudbury, Ontario).

Abstract

Pyrrhotite ($Fe_{(1-x)}S$; $0 < x \leq 0.125$) is a common sulfide gangue mineral (waste) in base metal mining operations, and presents many challenges in the separation/concentration of valuable base metal sulfides during froth flotation, especially pentlandite ($(Ni,Fe)_9S_8$). It has several superstructures which are a result of its variable iron content, with these being separated into two main categories: *magnetic/monoclinic pyrrhotite* (Fe_7S_8 {4C}) and *non–magnetic/hexagonal pyrrhotite* (Fe_9S_{10} {5C}, $Fe_{10}S_{11}$ {11C}, $Fe_{11}S_{12}$ {6C}). The magnetic (Fe_7S_8) and non-magnetic (Fe_9S_{10}) superstructures are the most common and typically found as intergrown mixtures, thus they were the focus of this thesis. Historically, it was thought that the superstructures behaved similarly during flotation; however, it is now known that they exhibit very different flotation responses (as a result of their crystallography), especially with respect to particle size. Overall, the non-magnetic superstructure (Fe_9S_{10}) is stated to be more floatable. This has raised concerns from the mineral processing industry as the superstructure flotation difference means that pyrrhotite depression strategies currently employed may not be adequate, which would yield lower than expected concentrate grades and reduce its overall value. In the past 3 decades, a limited number of research articles have been published on this subject, and unfortunately much of the superstructure flotation data is contradictory with only two in-depth studies providing much of the reliable and consistent information. As there is still a great deal of confusion surrounding the superstructures and their flotation behaviour, this Ph.D. study was initiated to address the current knowledge gaps with a two-step approach; (1) single mineral studies; and (2) batch ore flotation studies.

Initial test work focused on small-scale single mineral studies (0.25 – 1 g) that represented *ideal systems* (low oxygen environments where surface oxidation was minimized) where purified superstructures with fresh surfaces could be compared. The studies were comprised of (i) mineral surface potential analysis with/without reagents for pH 2 – 11; (ii) PAX collector adsorption tests at pH 7, 8.5, and 10; and (iii) microflotation tests with/without sonication pre-treatment for pH 7 – 11.

The second part of the test work examined superstructure behaviour in reactive environments (in the presence of oxygen, grinding media, pulp ions, and other sulfide minerals). This was accomplished by batch flotation studies (pH 9.2 – 9.5) on well characterized ore samples (1 – 2 kg) representing *real systems* during which the superstructures were in intimate contact with grinding media/slurry and oxygen. The studies were conducted with and without DETA/SMBS depressant combinations, with focus on superstructure recovery-by-size relationships. DETA/SMBS depressant was used as it imparts a surface cleaning effect by removing adsorbed Cu^{2+} and Ni^{2+} activating ions, degrades polysulfides, and xanthate collector on pyrrhotite and therefore aided in determining why the superstructures behave differently in oxidative environments.

Based on these studies, it is clear that pyrrhotite superstructure flotation behaviour is governed by their different surface reactivities which becomes apparent in *real systems*. This reactivity difference stems from their crystallography; magnetic/monoclinic pyrrhotite (Fe_7S_8) contains more structural vacancies and Fe^{3+} compared to non-magnetic/hexagonal pyrrhotite (Fe_9S_{10}). This difference is sufficient in causing magnetic pyrrhotite to be more reactive, especially towards oxygen, resulting in severe surface passivation by iron (oxy)hydroxides which renders it more hydrophilic over non-magnetic pyrrhotite. In *ideal systems*, both superstructures have virtually the same flotation response, in *real systems* where their surfaces are allowed to interact with oxygen and equipment/slurry, their flotation behaviour changes significantly. The major contributing factors that cause measurable differences in superstructure flotation responses are: presence of oxygen (oxidative conditions), alkaline conditions (pH > 9), and presence of activating ions (*e.g.* Cu^{2+} and Ni^{2+}). Fortunately, both superstructures can be treated to behave similarly and be depressed to the same degree in real systems with the use of surface acting agents such as DETA/SMBS depressants (non-magnetic pyrrhotite requires higher dosages as it contains more adsorbed ions/polysulfides).

This thesis has dispelled many myths/contradictions surrounding the pyrrhotite superstructures and has enhanced their knowledge base (contributing 4 articles to the

literature). The findings will certainly be valuable to the mineral processing industry where pyrrhotite rejection is targeted.

Résumé

La pyrrhotite ($Fe_{(1-x)}S$; $0 < x \leq 0,125$) est un minéral de gangue sulfuré très répandu dans les opérations minières de métaux communs et présente de nombreux défis dans la séparation/concentration des sulfures de métaux précieux lors de la flotation, en particulier la pentlandite ($(Ni, Fe)_9S_8$). Il a plusieurs superstructures en raison de sa teneur en fer variable, ils sont séparés en deux catégories principales: pyrrhotite magnétique/monoclinique (Fe_7S_8 {4C}) et pyrrhotite non-magnétique/hexagonale (Fe_9S_{10} {5C}, $Fe_{10}S_{11}$ {11C}, $Fe_{11}S_{12}$ {6C}). Les superstructures magnétique (Fe_7S_8) et non-magnétique (Fe_9S_{10}) sont les plus communes et se retrouvent généralement sous la forme de mélanges intergrands. Elles ont donc fait l'objet de cette thèse. Historiquement, on pensait que les superstructures se comportaient de la même manière pendant la flotation, mais on sait maintenant qu'elles présentent des réponses de flotation très différentes (résultat de leur cristallographie), en particulier en ce qui concerne la taille des particules. Dans l'ensemble, la superstructure non-magnétique (Fe_9S_{10}) est plus flotante. Cela a soulevé des inquiétudes de la part de l'industrie minière, car la différence de flotation de la superstructure signifie que les stratégies de dépression de la pyrrhotite actuellement utilisées peuvent ne pas être adéquates, ce qui donnerait des teneurs en concentrés plus faibles que prévu et réduirait sa valeur globale. Au cours des trois dernières décennies, seuls quelques articles ont été publiés sur ce sujet, malheureusement, une grande partie des données de flottation de la superstructure est contradictoire avec seulement deux études approfondies fournissant une grande partie de l'information fiable et cohérente. Comme il existe encore beaucoup de confusion autour des superstructures et de leur comportement en flotation, ce doctorat une étude a été lancée et a comblé les lacunes actuelles en matière de connaissances en adoptant une approche en deux étapes; (1) études minérales singulier; et (2) des études de flotation par batch.

Les premiers essais se sont concentrés sur des études minérales singulier à petite échelle (0,25 à 1 g) qui représentaient des systèmes idéaux (environnements à faible teneur en oxygène où l'oxydation superficielle était minimisée) où des superstructures purifiées avec des surfaces fraîches pouvaient être comparées. Les études comprenaient (i) une analyse du

potentiel de surface minéral avec et sans réactif pour pH 2 – 11; (ii) des tests d'adsorption du collecteur PAX à pH 7, 8,5 et 10; et (iii) des tests de microflotation avec et sans prétraitement par ultrasons pour pH 7 – 11.

La deuxième partie du travail d'essai a examiné le comportement de la superstructure dans des environnements réactifs (en présence d'oxygène, de milieux de broyage, d'ions de pâte et d'autres minéraux sulfurés). Ceci a été réalisé par des études de flotation par batch (pH 9,2 - 9,5) sur des échantillons de minéral bien caractérisés (1 – 2 kg) représentant des systèmes réels au cours desquels les superstructures étaient en contact intime avec des milieux de broyage et de l'oxygène. Les études ont été complétées avec et sans combinaison dépresseur DETA/SMBS en mettant l'accent sur les relations de récupération par taille de superstructure. Un dépresseur DETA/SMBS a été utilisé pour éliminer les ions activateurs de Cu^{2+} et Ni^{2+} adsorbés, dégrader les polysulfures et le collecteur de xanthate sur la pyrrhotite, ce qui a permis de déterminer pourquoi les superstructures se comportent différemment dans les environnements oxydants.

Sur la base de ces études, il est clair que le comportement de flotation de la superstructure de pyrrhotite est régi par leurs différentes réactivités de surface qui deviennent apparentes dans les systèmes réels. Cette différence de réactivité provient de leur cristallographie; la pyrrhotite magnétique/monoclinique (Fe_7S_8) contient plus de lacunes structurelles et Fe^{3+} comparé à la pyrrhotite non-magnétique/hexagonale (Fe_9S_{10}). Cette différence est suffisante pour que la pyrrhotine magnétique soit plus réactive, surtout vis-à-vis de l'oxygène, entraînant une passivation sévère de la surface par les hydroxydes de fer qui la rendent plus hydrophile par rapport à la pyrrhotine non-magnétique. Dans les systèmes idéaux, les deux superstructures ont pratiquement la même réponse de flotation, dans les systèmes réels où leurs surfaces peuvent interagir avec l'oxygène et l'équipement/le lisier, leur comportement de flotation change de manière significative. Les principaux facteurs qui provoquent des différences mesurables dans les réactions de flotation de la superstructure sont: présence d'oxygène (conditions oxydatives), conditions alcalines (pH > 9) et présence d'ions activateurs (par exemple Cu^{2+} et Ni^{2+}). Heureusement, les deux superstructures peuvent être traitées de manière similaire et être déprimées au même degré dans les systèmes

réels avec des agents tensioactifs tels que les dépresseurs DETA/SMBS (la pyrrhotite non-magnétique nécessite des dosages plus élevés car elle contient plus d'ions adsorbés/polysulfures).

Cette thèse a dissipé de nombreux mythes/contradictions entourant les superstructures de pyrrhotite et a amélioré leur base de connaissances (contribuant 4 articles à la littérature). Les découvertes seront certainement utiles à l'industrie de traitement des minerais où le rejet de pyrrhotite est visé.

Acknowledgements

I've been very fortunate to complete my Ph.D. study at McGill University and throughout the course of this project I've also had the great pleasure of meeting numerous academics and industry experts in the metallurgical field. It has been a great journey and a point in my life that I will value forever.

First and foremost, I am extremely grateful for the supervision of Professor Kristian E. Waters, who always maintained interest in this project and provided constructive feedback. He trusted my judgement and gave me virtually full reign over this project, allowing me to truly learn from project failures/setbacks and my own shortcomings. He also promoted personal development through conference travel (both domestic and abroad) from which I certainly benefitted, both academically and socially :). Overall, I couldn't have asked for a better mentor.

This project was suggested as a Ph.D. study by Virginia Lawson (currently Jameson Cell Technology Manager at Glencore Technology) and I'm thankful for her recommendation as the project was quite demanding and forced a review of much of the pyrrhotite literature, resulting in a review article (along with 3 other articles) that should benefit the mineral processing industry. Vale Base Metals and Glencore (Sudbury Integrated Nickel Operations) are acknowledged for generously providing ore samples and in-kind support for the batch flotation test work, as well, XPS center for use of their laboratory facilities and technical staff to conduct some of the flotation test work and mineralogical analysis. Duly noted is the assistance from Scott Wojtowicz, Yvon Boudreau, and Alex Lamarche (XPS technical staff).

I am very grateful to the Faculty of Engineering at McGill University for granting me a McGill Engineering Doctoral Award (MEDA). Sincere appreciation is expressed for the financial support provided for this project by Natural Sciences and Research Council of Canada (NSERC) and industrial sponsors: Vale Base Metals, SGS Canada Inc., Shell Canada Ltd., XPS – Expert Process Solutions, COREM, Barrick Gold Corporation, Teck Resources Limited and ChemIQA. These funds permitted myself, along with other graduate students, to conduct meticulous research and test many abstract ideas along the way.

There are simply too many individuals to name from the Mining and Materials Engineering Department that made my graduate studies very enjoyable, so I will simply acknowledge the *entire* Department here :). I certainly enjoyed the Greek philosophy lessons from Professor George P. Demopoulos and playful banter concerning time management, also, the never-ending uneventful competitions with Professor Mathieu Brochu will never be forgotten (but certainly missed). For the record, I never lost. The Mineral Processing Group and Ray Langlois are sincerely acknowledged for fruitful discussions and their constructive criticism during dry-run presentations, I truly enjoyed working with everyone…even Ray – I will ensure that the monthly prank calls will continue after my leave. Hats off to Ray for keeping the mineral processing labs extremely organized and safe working environments – a clean and organized space is a productive space. Technical staff Monique Riendeau, and Ranjan Roy and Andrew Golsztajn of the Department of Chemical Engineering are thanked for their continuous assistance with analytical instruments and surface chemistry discussions. Administrative staff must be acknowledged for keeping the Department in excellent working order, without whom, us researchers would not be as efficient. I must especially stress the great assistance Barbara Hanley (*she who must be obeyed*) provides all graduate students. I'm very fortunate to have had our long therapeutic conversations concerning a range of topics; anywhere from departmental policies to Dilbert comics to world travel, you will be sincerely missed.

A deep appreciation is expressed towards my parents (Surinder and Harjit Multani) for their unconditional love, continuous support, and instilling in me the work ethic I have today. I should also thank them for never failing to ask "how much longer till you to get your Ph.D.?" as this always made me write faster. As well, my sisters (Suman and Pawan) are acknowledged for their encouragement, positivity, and providing a necessary social break between experiments. Mr. and Mrs. Rowland are sincerely thanked for providing the perfect place to finalize this thesis – thank you very much.

Last, but never least, Lindsay, my best friend, fiancée and timekeeper, without whom this thesis would have taken twice as long to write. I sincerely appreciate your unwavering support and *allowing* me to be 8 hrs away for half our relationship. I love you.

Preface and Contribution of Authors

This doctoral thesis is presented in the traditional monograph style and summarizes information from four manuscripts; one of which is published and three have been submitted to peer-reviewed journals and are currently under review. The thesis comprises of 7 Chapters and 2 Appendices, a detailed description of each Chapter/Appendix is provided in the Thesis Organization Section of Chapter 1 (Introduction). All information presented in this thesis was written by the candidate with supervision from Dr. Kristian E. Waters who co-authored all publications. All the experimental test work was designed by the candidate and conducted either alone or with assistance from certain individuals (see Acknowledgements Section). A general description of each peer-reviewed journal publication and its incorporation into the thesis is presented as follows:

Publication #1 is a review article on pyrrhotite superstructures and their properties that impact their mineral processing. The article accounts for majority of Chapter 2, which is a literature review.

Publication #2 summarizes the results of single mineral studies on pyrrhotite superstructures in an *ideal system* (fresh mineral surfaces in low oxygen environments). Co-authors Hillary Williams, Bailee Johnson and Ronghao Li contributed to the experimental test work and data analysis. This article forms majority of Chapter 4.

Publications #3 and #4 summarize the findings of batch flotation studies on a challenging/reactive ore used a case study, the test conditions represented *real systems* (oxidative environments) where mineral surfaces were permitted to interact with equipment/slurry and oxygen. These articles form majority of Chapter 6.

Publication #1:

Multani, R.S. & Waters, K.E. (2017). A Review of the Physicochemical Properties and Flotation of Pyrrhotite Superstructures (4C – Fe_7S_8/ 5C – Fe_9S_{10}) in Ni–Cu Sulphide Mineral Processing. *The Canadian Journal of Chemical Engineering, 95*(12). DOI: 10.1002/cjce.23099.

Publication #2 (under review):

Multani, R.S., Williams, H., Johnson, B., Li, R. & Waters, K.E. (2018). The Effect of Superstructure on the Zeta Potential, Xanthate Adsorption, and Flotation Response of Pyrrhotite.

Publication #3 (under review):

Multani, R.S. & Waters, K.E. (2018). Pyrrhotite Depression Studies with DETA & SMBS on a Ni–Cu Sulfide Ore.

Publication #4 (under review):

Multani, R.S. & Waters, K.E. (2018). Flotation Recovery–by–Size Comparison of Pyrrhotite Superstructures with and without Depressants.

Contents

List of Figures

List of Tables

Chapter 1
Introduction

Metals in the earth's crust are generally found as sulfide, oxide, and silicate minerals (inorganic compounds) and rarely in their native metallic form. Thus, they normally require industrial processing (mineral processing and extractive metallurgy: pyrometallurgy and hydrometallurgy) for their concentration, extraction, and purification.

The subject matter of this thesis pertains to mineral processing, more specifically, the behaviour of an iron sulfide mineral (pyrrhotite) and its *superstructures* during the concentration of copper and nickel sulfide minerals from Cu-Ni sulfide ore deposits in Canada. These pyrrhotite superstructures pose many operational challenges in achieving saleable high-grade copper/nickel concentrates. This research study was proposed by industrial sponsors with the objective of increasing the knowledge base of pyrrhotite superstructures, especially their behaviour during froth flotation.

1.1 Froth Flotation

In mineral processing, ore deposits comprised of valuable minerals are mined and subsequently crushed/ground to sizes which allow for the liberation of minerals, after which separation and concentration of valuable from gangue minerals (waste) is accomplished by exploiting their physical and chemical properties. Several separation techniques (optical sorting, density, magnetic susceptibility, electrical conductivity, and froth flotation) are available and their use depends on the particular ore deposit being processed; generally a

combination of techniques is used [1]. Comparison of the separation techniques based on their effective size range of application is presented in **Figure 1.1**. As can be observed, froth flotation exhibits a very large size range of application when compared to other techniques, and is commonly used in many, if not most, mineral concentration processes. Copper and nickel sulfide ores are generally concentrated using froth flotation for its ease of use and cost effectiveness compared to other techniques. Magnetic separation is sometimes incorporated in the plant flow sheet ahead of froth flotation to remove magnetic gangue minerals (*e.g.* magnetite and magnetic pyrrhotite).

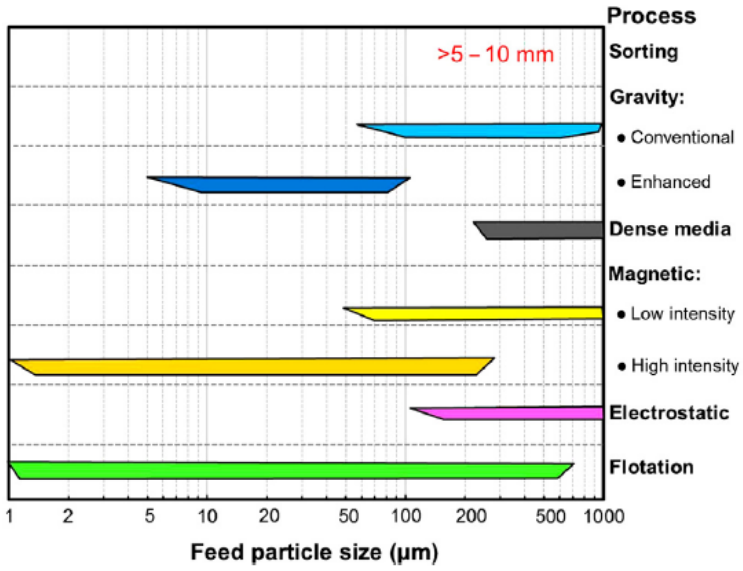

Figure 1.1 *– Mineral separation techniques and their effective range of application, reproduced from Wills and Finch (2016)* [1].

Froth flotation makes use of the minerals' surface wettability to selectively separate and concentrate valuable minerals from gangue minerals. A slurry is introduced into a froth flotation cell, an example is provided in **Figure 1.2**, where rising bubbles collide with particles; hydrophobic particles attach to these bubbles and report to the froth phase that is continuously skimmed and collected (the concentrate typically requires subsequent cleaning stages). For the purposes of this thesis, the cell overflow will be referred to as the concentrate (valuable product). It must be noted that for some ores "reverse flotation" is used to preferentially float gangue minerals that are collected as the overflow, the tailings would

retain the valuable minerals. For certain minerals such as sulfides, they exhibit some degree of natural hydrophobicity, however, this property is not typically exploited as it does not guarantee consistent mineral recovery and cannot be sustained due to variations in the feed ore during industrial plant operations. Thus, many reagents are added, *collectors* being the workhorse of mineral flotation. Collectors enhance the mineral's hydrophobicity by selectively attaching to valuable minerals while others, *depressants*, act to depress mineral flotation by selectively interacting with floatable gangue minerals. Other reagents also play a role (*e.g.* frothers, activators, pH modifiers, and pulp potential modifiers) and can further enhance the separation efficiency of the flotation cell.

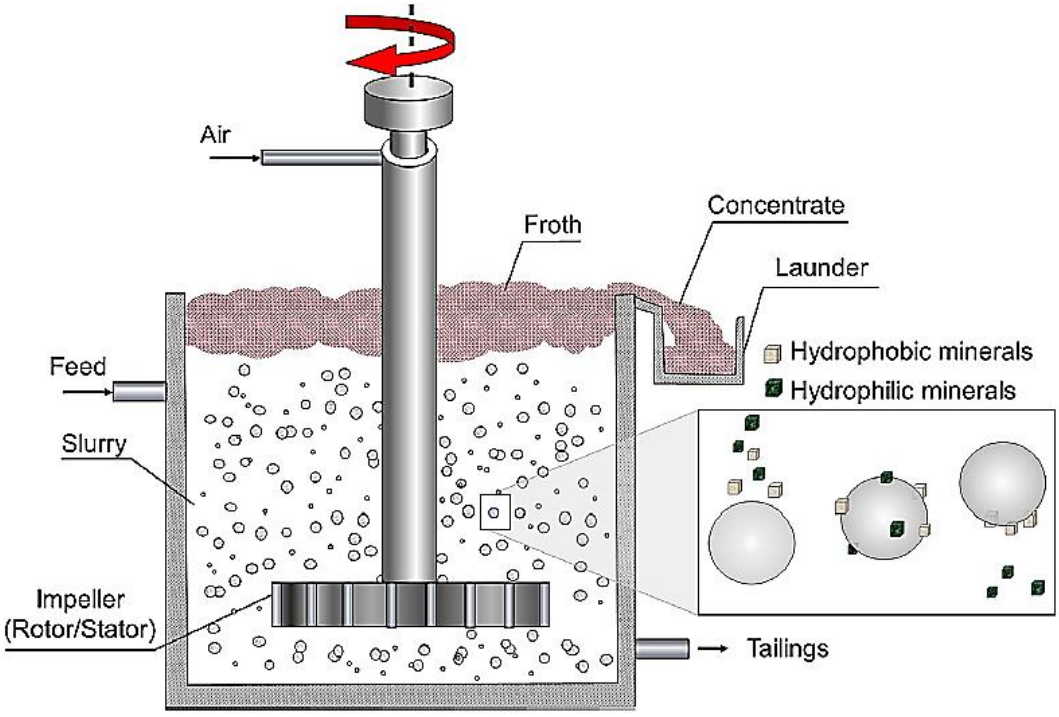

Figure 1.2 *– Froth flotation in a mechanical cell, reproduced from Wills and Finch (2016)* [1].

In base metal mining (Cu, Ni, Zn, Pb, and Mo), the metals are typically found as sulfide minerals (sometimes as oxides closer to the Earth's surface) and xanthate collectors are commonly used since they are very selective for such metals. Depending on the type of ore body, various operating parameters are used to ensure maximum separation from gangue minerals to yield maximum profit. In the selective separation of valuable sulfides, a key

consideration is floatable sulfide gangue that has the ability to kinetically compete with valuable sulfides and report to the concentrate, typically these are pyrite (FeS_2) and pyrrhotite ($Fe_{(1-x)}S$; $0 < x \leq 0.125$).

1.2 Pyrrhotite ($Fe_{(1-x)}S$; $0 < x \leq 0.125$) and its Complexity

Pyrrhotite is a very common iron sulfide mineral (second in mass after pyrite), having a non–stoichiometric formula $\mathbf{Fe_{(1-x)}S}$, where $0 < x \leq 0.125$, permitting many "superstructures" that are all based on the hexagonal NiAs crystal subcell [2, 3]. Most base metal sulfide ores contain pyrrhotite, with common examples being Cu–Ni, Pb–Zn and those containing platinum–group elements (PGE) [4]. The Fe–S system, presented in Section 2.2.1, is quite complex and gives rise to several pyrrhotite superstructures. Of these, only four are known to exist naturally (room temperature phases) and are separated into two main categories: "magnetic/monoclinic" (Fe_7S_8 {4C}) and "non–magnetic/hexagonal" (Fe_9S_{10} {5C}, $Fe_{10}S_{11}$ {11C}, $Fe_{11}S_{12}$ {6C}) pyrrhotite, Note: "4C" denotes a unit cell dimension 4 times that of the NiAs lattice in the *c*-direction. At times, the stoichiometric end member troilite (FeS) is also grouped with pyrrhotite, however, it should be clarified here that in the context of mineral processing troilite is a distinct mineral with different flotation properties than pyrrhotite [3, 5]. Since magnetic (Fe_7S_8) and non-magnetic (Fe_9S_{10}) pyrrhotite are the more common superstructures, generally found as intergrown mixtures, they were the primary focus of this research study [6].

1.3 Mineral Processing of Pyrrhotite

Due to pyrrhotite's abundance, as well as its association with most base metal sulfide ores, it is processed alongside these valuable minerals; in most cases considered to be sulfide gangue with little economic value. Pyrrhotite containing PGEs in solid solution, discrete fine–grained platinum–group minerals (PGM), Ni in solid solution, or very fine–grained disseminated pentlandite ($(Ni,Fe)_9S_8$) are among the few exceptions where its recovery is sought [7, 8]. Historically in Canada, pyrrhotite was recovered to the base metal concentrate (*e.g.* nickel–copper sulfide) from mineral processing plants that fed smelting

operations, resulting in significant SO_2 emissions and large slag volumes that limited nickel throughput thereby increasing smelting costs [9]. Environmental legislations were introduced in the 1970s (Sudbury, Ontario) to reduce SO_2 emissions *via* capture and treatment in acid plants, after which pyrrhotite rejection at the concentrator was sought as it typically contained > 75 wt% of the feed sulfur [10]. In addition, aside from trace nickel, most pyrrhotites contain very little valuable elements and consequently dilute the concentrate grade, where specific recovery of iron is much more economical from clean iron ore imported from Brazil or Australia [9].

Since the 1980s (and possibly earlier), pyrrhotite rejection has become common practice with recent rejection numbers as high as 85% of feed pyrrhotite at Glencore's Strathcona Mill (previously Xstrata Nickel) [9]. Several pyrrhotite rejection flow sheets exist, some incorporate magnetic separation where the magnetic (Fe_7S_8) and non-magnetic (Fe_9S_{10}) superstructures are independently rejected in the magnetic and non–magnetic circuits, respectively, with different depression strategies employed. Others reject both varieties in the same flotation circuit for several reasons: maintenance/capital costs of magnetic separators as well as inadequate separation efficiencies, variable ore composition (changing non–magnetic/magnetic pyrrhotite feed ratios), and improved metallurgy with simultaneous depression of both pyrrhotites. For these reasons, many Cu–Ni operations are transitioning away from magnetic separators and have opted to float them in the same circuit. Interestingly, the data shows differences in superstructure flotation behaviour and as such industrial concentrators are now actively monitoring the superstructure ratios both in the feed and final concentrate.

1.4 Differences in Magnetic (Fe_7S_8) and Non-magnetic (Fe_9S_{10}) Pyrrhotite Flotation

Historically, countless pyrrhotite flotation studies were conducted to understand its physicochemical properties (especially in association with pentlandite – $(Ni,Fe)_9S_8$ and chalcopyrite – $CuFeS_2$), however, these rarely distinguished the type of pyrrhotite used as the belief was that both superstructures behaved similarly. Generally, the differences, if

reported, were perceived to be minor and comprehensive studies did not receive attention. On the contrary, there is now ample evidence from recent studies suggesting the two superstructures exhibit different flotation responses, sometimes significant enough to have an impact on its rejection [11-17]. The literature is in agreement with this statement, however it is also complemented with contradictions as to which superstructure is "more" floatable in the pH range of interest (typically alkaline) as well as more prone to oxidation (sensitive to pulp potential), which is detrimental to pyrrhotite's floatability. Such contradictions have led to a few in–depth studies, namely the Ph.D. theses of Kolahdoozan (1996) and Becker (2009); relating ore mineralogy, pyrrhotite crystallography, collector adsorption, activation/depression by surface modifiers, pH, and oxidation to flotation of the two superstructures with very promising results [11, 13].

It is now generally agreed that in real systems (industrial) non–magnetic pyrrhotite is much more floatable than magnetic pyrrhotite as will be discussed later in this study. Furthermore, the effect of particle size is peculiar especially in the context of pyrrhotite flotation, since flotation by size is generally well understood as it has been extensively reviewed [16, 18-20]. Recently, industrial data presented by Lawson *et al.* (2014) showed that non–magnetic pyrrhotite appears to follow conventional flotation recovery based on particle size (largest in intermediate fractions; 10 – 100 μm), while magnetic pyrrhotite is largely recovered in the finest fractions (< 10 μm) where entrainment effects have been minimized by froth washing [16]. This suggests a surface chemical phenomenon since finer particles exhibit larger areas where surface effects are amplified.

These superstructure flotation differences highlight the fact that there are still gaps in the understanding of their flotation behaviour and depression, which is largely the result of their crystallography that alters their surface reactivity and therefore surface chemistry.

1.5 Current Gaps in the Understanding of Pyrrhotite Superstructures

Recent pyrrhotite superstructure studies have provided great insight and shed light on areas that confounded many researchers in the past. The studies have certainly validated

the need to investigate the superstructures more closely since there are still gaps in the understanding of their relative floatabilities and surface chemistries; namely collector–mineral adsorption mechanisms, surface charges, surface ion speciation, pulp ion effects, particle size effects, superstructure ratios (presence of one impacting the other by galvanic interaction), and mineral associations with other base metal sulfides.

A large portion of the superstructure studies in the literature have been on single mineral systems (synthetic and purified superstructures from ores) and relatively small–scale (0.25 – 5 g samples). This, in part, is due to the fact that sourcing several kilograms of well characterized ore feed (containing known superstructure ratios) is very challenging and most likely restricted previous researchers to small-scale fundamental studies. Although much of the single mineral experimental work has been fruitful towards the understanding of the mechanisms at work, other industrial observations could not be tested or reproduced at the lab-scale. Furthermore, common flotation test conditions such as adequate pulp density, froth phase, and presence of copper and nickel sulfide minerals (*i.e.* mixed mineral systems) that are common to industrial operations and to some degree in batch flotation tests (≥ 500 g), were also not incorporated and may have some influence on the results. Larger batch flotation tests are preferred as they would be more representative of plant practices (*e.g.* freshly ground ore followed by immediate flotation) and can provide valuable information on superstructure floatability in mixed mineral systems (real systems).

1.6 Research Objectives

With depleting head grades of many sulfidic ore bodies coupled with stagnant prices of many base metals, increased mining activities will inevitably result in increased waste rock rejection where pyrrhotite is the major sulfide gangue. In such times, in-depth knowledge of superstructure surface chemistry and flotation behaviour becomes a matter of greater importance. Thus, this study was undertaken to address the major knowledge gaps in the literature with the main goal of determining the primary mechanisms responsible for the different superstructure flotation behaviour observed in both lab-scale and industrial settings.

To supplement the fundamental studies currently in the literature, the approach of this thesis was to first conduct small-scale single mineral studies (0.25 – 1 g) on purified superstructures representing ideal systems (low oxygen environments) where the mineral surfaces were fresh (unoxidized). Subsequently, large batch flotation studies (≥ 1 kg) became the focus to reproduce industrial results and gain a better understanding of the mechanisms at work in real systems (reactive/oxidative environments). The latter would certainly be relevant to industrial operations seeking to reject both pyrrhotite superstructures.

Major objectives of this thesis:

(1) To investigate and compare the surface chemical properties of non-magnetic (Fe_9S_{10}) and magnetic (Fe_7S_8) pyrrhotite superstructures by means of: **(i)** mineral surface potentials (zeta potential) with and without reagents ($NiSO_4$, $CuSO_4$, and potassium *n*-amyl xanthate (PAX) collector); and **(ii)** PAX collector adsorption in neutral-alkaline pH range (7, 8.5, and 10) to understand the collector attachment mechanisms;

(2) To investigate and compare the flotation properties of the superstructures in both idealized ("fresh surfaces") and real ("reacted surfaces") systems by means of: **(i)** microflotation with and without sonication pre-treatment; and **(ii)** batch flotation tests under various conditions (collector only, DETA/SMBS depressants, and acidification/aeration) to manipulate surfaces; recovery-by-size analysis being a primary focus; and

(3) Summarize the major contributing factors responsible for the different superstructure flotation behaviour

1.7 Thesis Organization

This thesis is presented in the traditional monograph style and organized into 7 Chapters and 2 Appendices. The Chapters summarize the relevant superstructure literature; the methods employed in the experimental test work; findings of single mineral and batch

flotation studies; and global conclusions with suggestions for future studies. More specifically, the Chapter and Appendix details are as follows:

Chapter 1 provided the pyrrhotite superstructure context, highlighted current knowledge gaps, and presented the research objectives of this study;

Chapter 2 is a thorough review of the literature on pyrrhotite superstructures (focus on non-magnetic {Fe_9S_{10}} and magnetic {Fe_7S_8} pyrrhotite) and their mineral processing in relation to Cu-Ni sulfide deposits. Topics covered were the complicated superstructure nomenclature, characterization methods, aqueous stability, surface charges, superstructure–reagent interactions, and flotation;

Chapter 3 details the methodology (procedures and analytical instruments) used over the course of this thesis;

Chapter 4 summarizes the results and major findings of the single mineral studies (superstructure zeta potentials, PAX adsorption, and microflotation);

Chapter 5 summarizes the results and major findings of the first batch flotation study with and without DETA/SMBS depressants, comparing 4 Cu-Ni sulfide ores having different non-magnetic/magnetic pyrrhotite ratios {5/95, 30/70, 50/50, 95/5%}. The study also assessed superstructure flotation recovery-by-size relationships (split into two fractions: fines {–38 μm} and coarse {+38 μm});

Chapter 6 details the results and major findings of the second batch flotation study with and without DETA/SMBS depressants. A challenging/reactive Cu-Ni sulfide ore (non-magnetic/magnetic pyrrhotite ratio = 42/58%) was used as a case study to assess superstructure flotation. Superstructure flotation recovery-by-size (cyclosized fractions) was also investigated to reproduce industrial results and evaluate the effects of DETA/SMBS depressant combination on both superstructures; and

Chapter 7 presents the conclusions derived from this research, claims to originality of this work, and suggestions for future studies that will address areas still requiring attention; and

Appendix A provides extra information for Chapter 3 and **Appendix B** provides supplementary information for Chapter 5

Chapter 2
Literature Review

2.1 Introduction

Presently, there is a great deal of confusion surrounding pyrrhotite since it has numerous superstructures with different crystal symmetries (to compound the confusion, these are continuously revised in the literature), magnetic susceptibilities, characterization difficulties, stability and reactivity towards oxygen and flotation reagents/pulp ion interactions which lead to considerably different results, especially in flotation studies. Moreover, the literature is plagued with inconsistencies which tend to stem from inadequate mineral characterization and preparation prior to study, yielding contradictory results on similar materials. Therefore, this literature review was approached with great caution. Much of the focus was placed on the physicochemical properties of the two primary superstructures: non–magnetic (Fe_9S_{10} {5C} – "hexagonal") and magnetic (Fe_7S_8 {4C} – "monoclinic") pyrrhotite as these are the most common types and generally found as intergrown mixtures.

The review is organized to cover various aspects of pyrrhotite and its superstructures; nomenclature and structural information (vacancies, Fe^{2+}/Fe^{3+} content and magnetism), characterization methods (ICP/AAS, XRD, and microscopy), stability (E_h/pH, reactivity towards oxygen and mechanisms), surface chemistry (surface charge, reagent/pulp ion interactions), and flotation.

2.2 Pyrrhotite Structures

2.2.1 Brief History, Fe–S Phase Diagram, Superstructure Nomenclature

The study of pyrrhotite dates back more than a century with countless researchers having contributed to the understanding of its complex superstructures and phase relations in the Fe–S system. Alsen (1925)[21] first described pyrrhotite as having the hexagonal nickel arsenide (NiAs) subcell (a = 3.45 Å, c = 5.74 Å), where the Fe atoms occupy octahedral sites between the hexagonal close–packed S layers [3]. From studying synthetic pyrrhotites, Hagg and Sucksdorff (1933)[22] determined the non–stoichiometric composition of pyrrhotite was due to iron vacancy, furthermore, Bertaut (1953)[23] correctly deduced that magnetic pyrrhotite (Fe_7S_8 {4C}) contained ordered Fe vacancies in alternate layers along the c–axis and in addition proposed that it may be written as $Fe_2^{3+}Fe_5^{2+}S_8$ to account for charge imbalance within the structure. This ordered vacancy and ferrous/ferric interpretation was further translated to other pyrrhotites with different vacancy distributions. Interest in pyrrhotite and its superstructures increased after it was deemed a potential "geothermometer" and sparked a concerted effort on pyrrhotite phase relations in the Fe–S system (ambient to high temperature; 25 – 1200ºC) [24, 25]. In the same period several researchers worked on methods of superstructure quantification in given mixtures using both natural ore and synthetic samples as standards with success (summarized in *XRD* Section (2.2.4.2)), however, this also shed light on two leading issues among researchers. Firstly, most synthetic samples contained metastable pyrrhotite phases as well as inclusions of other iron–sulfides (*e.g.* pyrite) as a result of "dry sulfide" synthesis procedures which lead to considerable disagreement over pyrrhotite phase relations and crystallography below 350ºC [26-30]. Note: for "dry sulfide" synthesis, a typical method involved solid state reaction of pure Fe and S in evacuated silica tubes under varying equilibration times at high temperatures (*e.g.* 24 hrs to 16 weeks, > 500ºC) followed by immediate quenching that resulted in many metastable phases [9, 25, 27, 28]. Secondly, aside from the four naturally occurring pyrrhotites (Fe_7S_8, Fe_9S_{10}, $Fe_{10}S_{11}$, $Fe_{11}S_{12}$), high temperature studies/synthesis methods gave rise to numerous

superstructures for which the literature lacked standard nomenclature and brought about great confusion when referring to specific superstructures – this issue still persists. Nakazawa and Morimoto (1970, 1971)[31, 32] investigated synthetic superstructure single crystals between room temperature and 320ºC, however, they followed a separate approach to those by previous researchers; studying the crystals at elevated temperatures using a precession camera and presented modifications to high temperature superstructures thereby developing the nomenclature (NA, MC, NC types – discussed in the next Section), essentially basing *all* pyrrhotites on the NiAs subcell. This was a significant advancement in understanding the Fe–S system; in spite of this, the authors were still limited as they could not study the phase relations in detail and also encountered metastability with respect to magnetic pyrrhotite (Fe_7S_8 {4C}) [27, 30]. The root cause of the inconsistencies in the system (below 350ºC) was largely attributed to reduced reaction rates at low temperatures in dry sulfide synthesis methods, leading to metastability. Most researchers came to the understanding that the pyrrhotite phases were unquenchable and even prolonged annealing after synthesis could not mitigate the problem, many researchers eventually reverted to natural specimens to fill in the data points for low and room temperature phases, though, this was not ideal since ore specimens always contain contaminant elements/minerals [24, 30]. Alas, hydrothermal synthesis techniques provided the necessary reaction rates to produce large "pristine" single crystals (1 – 2 mm) that were thermodynamically stable and free of contaminants [33]. Kissin (1974)[27] and Kissin and Scott (1982)[24] used this particular technique for pyrrhotite after it showed success for cinnabar (HgS) and sphalerite ((Zn,Fe)S) systems [34, 35]. The generally accepted portion of the Fe–S system (low temperature) where pyrrhotites reside is that proposed by Kissin and Scott (1982)[24], most contemporary modifications are based on this dataset. Wang and Salveson (2005)[25] combined this dataset with the best available high temperature phase diagrams to show the complete FeS–FeS_2 phase relations from 25 – 1200ºC, presented in **Figure 2.1**(a). As the diagram is quite complex, to summarize the relevant superstructure phase relations in the low temperature region, a simplified version of the diagram presented by Kissin and Scott (1982)[24] is also shown in **Figure 2.1**(c), reproduced from Gordon and McDonald (2016)[36].

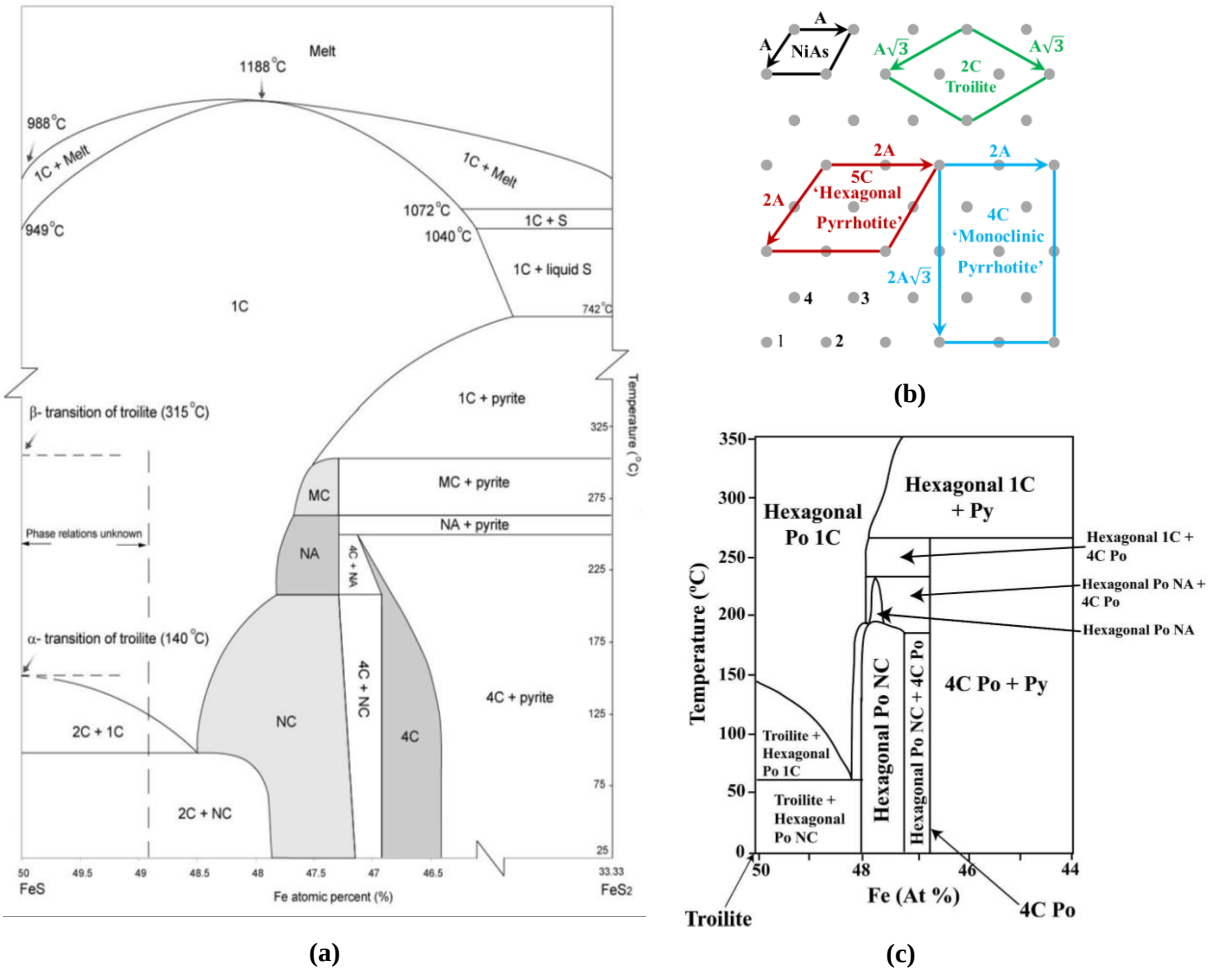

Figure 2.1 *– (a) Phase diagram for the Fe–S system (FeS to FeS_2 segment) depicting the stability fields of the pyrrhotite superstructures terminology from Nakazawa and Morimoto (1970, 1971)[31, 32] and Morimoto et al. (1975)[30], reproduced from Wang and Savleson (2005)[25]; (b) Unit cells of naturally occurring pyrrhotites projected onto the (001) plane and compared to NiAs cell, modified from Posfai et al. (2000)[3]; (c) Simplified phase diagram of pyrrhotite superstructures, reproduced from Gordon and McDonald (2016)[36].*

Figure 2.1(a) shows the range of interest – displaying all pyrrhotite superstructures ($\mathbf{Fe_{(1-x)}S}$, $0 < x \leq 0.125$); at high temperatures (> 350ºC) pyrrhotite is mainly present as the hexagonal 1C variety (*i.e*. NiAs structure), upon cooling to 25ºC, the disordered iron deficient forms (NA, MC, NC, and 4C) become stable yielding several *superstructures*. An interesting property of the NiAs structure is that it allows the omission of metal atoms along certain orientations, for the case of pyrrhotite it is along the *c*–axis. Based on the degree of Fe deficiency ($0 < x \leq 0.125$), many pyrrhotite compositions are possible (Fe_7S_8 to $Fe_{11}S_{12}$, with troilite – FeS being the end member and the extreme case), all being derivatives of the NiAs

subcell, thus referred to as *superstructures*. In the literature, the different pyrrhotites have been given many names; referred to as "magnetic" and "non–magnetic" pyrrhotite, sometimes "NA", "MC", "NC" and/or "4C", at times only referenced by its crystal symmetry (monoclinic, hexagonal, orthorhombic, *etc.*). The generally accepted convention is to denote pyrrhotite as a derivative of the NiAs subcell, where the "N" and "M" are integer and non–integer multiples of the NiAs lattice, respectively, "A" and "C" referring to its unit cell dimension along the *a*–axis and *c*–axis, respectively. For simplicity, mineral processing convention is to refer to pyrrhotite superstructures based on their magnetic property, separating the superstructures into two main categories; *magnetic* (Fe_7S_8 {4C}) and *non–magnetic* (Fe_9S_{10} {5C}, $Fe_{10}S_{11}$ {11C}, $Fe_{11}S_{12}$ {6C}) pyrrhotite. **Figure 2.1**(b) displays the unit cells of naturally occurring pyrrhotites as well as the NiAs structure for comparison. Room temperature (natural) pyrrhotites virtually have stoichiometric compositions and thus have the generic formula: $\mathbf{Fe_{(n-1)}S_n}$ for ($n \geq 8$), (n/2)C–type (for n even) and nC–type (for n odd), troilite (FeS) being a special case with very large n [32]. Pyrrhotites, however, do show a range in metal/S ratios; a review of those present in selected nickel and PGE ore deposits (Merensky and Nkomati – South Africa; Phoenix – Botswana; and Sudbury – Canada) was given by Becker *et al.* (2010)[4]. In the same study an interesting observation was made with regards to nickel deportment into pyrrhotite as solid solution, which may partly explain the better flotation of non-magnetic over magnetic pyrrhotite. In deposits containing intergrown pyrrhotite mixtures (non-magnetic (Fe_9S_{10}) and magnetic (Fe_7S_8)), non-magnetic pyrrhotite was found to preferentially accommodate more nickel (0.75 ± 0.10 wt% Ni) than its magnetic counterpart (0.43 ± 0.18 wt% Ni). For ores containing single phase pyrrhotite, non-magnetic pyrrhotite was found to contain about the same (0.75 ± 0.19 wt% Ni) whereas magnetic pyrrhotite was more nickel–rich (up to 2 wt% Ni) [4, 37].

Table 2.1 summarizes all pyrrhotite superstructures along with their known properties, **Table 2.2** provides more details about the natural (room temperature) pyrrhotites. The natural pyrrhotites are generally found with other iron sulfides. When a significant amount of iron–rich pyrrhotite is present (*i.e.* $Fe_{11}S_{12}$ {6C}) it is typically associated with troilite (FeS); on the other hand, the most iron deficient pyrrhotite (*i.e.* magnetic Fe_7S_8 {4C})

is often found with pyrite (FeS_2), mixtures of Fe_9S_{10} {5C} and Fe_7S_8 {4C} can also have pyrite. All these associations are in agreement with those found in **Figure 2.1**(a,c) [24, 37].

Table 2.1 *– Summary of the different pyrrhotite structures and their properties, adapted from Posfai et al. (2000)[3], Fleet (2006)[38], Becker (2009)[13] and references therein. Note: pm – paramagnetic; afm – antiferromagnetic; fm – ferrimagnetic.*

Type	Ideal Composition	Structure	Magnetic Properties	Other names	Stability	Occurrence
1C	FeS	Hex	pm	–	High temp. phase	Synthetic
2C	FeS	Hex	afm	Troilite	< 147ºC	**Natural** & lunar
NC	Fe_9S_{10}, $Fe_{10}S_{11}$, $Fe_{11}S_{12}$	Hex, Ortho, Mon	afm	Non–magnetic, 5C, 11C, 6C, intermediate pyrrhotite	< 209ºC	**Natural**
NA	Fe_7S_8	Trig	afm	2A, 3C	< 262ºC	Synthetic
MC	–	Hex?	afm	–	< 315ºC	Synthetic
4C	Fe_7S_8	Mon	fm	Magnetic pyrrhotite	< 254ºC	**Natural**
–	$Fe_{7+x}S_8$	Mon	afm	Anomalous pyrrhotite	?	**Natural**

Table 2.2 *– Structural information for room temperature (natural) pyrrhotite superstructures.*

Type	Ideal Composition	Vacancy (%)	Proposed Formula for Charge Neutrality	$\left[\frac{Fe^{3+}}{Total\ Fe}\right]$ %	Ideal Atomic %		Ideal Weight %	
					Fe	S	Fe	S
2C	FeS	0.0	$Fe^{2+}S^{2-}$	0.0	50.00	50.00	63.53	36.47
6C	$Fe_{11}S_{12}$	8.3	$Fe_2^{3+}Fe_9^{2+}S_{12}^{2-}$	18.2	47.83	52.17	61.49	38.51
11C	$Fe_{10}S_{11}$	9.1	$Fe_2^{3+}Fe_8^{2+}S_{11}^{2-}$	20.0	47.62	52.38	61.29	38.71
5C	Fe_9S_{10}	10.0	$Fe_2^{3+}Fe_7^{2+}S_{10}^{2-}$	22.2	47.37	52.63	61.05	38.95
4C	Fe_7S_8	12.5	$Fe_2^{3+}Fe_5^{2+}S_8^{2-}$	28.6	46.67	53.33	60.38	39.62

For superstructure (2C, 4C, 5C, 6C, 11C) unit cell dimensions, Becker *et al.* (2010)[4] presented a brief summary, several researchers have provided their refinements as well and due to the breadth of information for each structure they are only referenced here [39-44].

2.2.2 Vacancies and Fe^{2+}/Fe^{3+} ratios

The frequently referenced vacancy distribution diagrams of the two most common pyrrhotite superstructures (magnetic {Fe_7S_8} and non-magnetic {Fe_9S_{10}}) are displayed in **Figure 2.2** (modified from Vaughan *et al.* (1971)[45]); other researchers have also suggested similar vacancy distributions by further refining the structures, although they proposed partially vacant iron sites rather than fully vacant [41-44]. The magnetic and non-magnetic superstructures have alternating layers of full site occupancy and vacancy containing layers. In the vacancy layers (iron deficient), iron speciation is predominantly ferric (Fe^{3+}) as the removal of ferrous (Fe^{2+}) ions from the lattice results in an internal charge imbalance, thus the surrounding ferrous atoms take the form of ferric iron for charge neutrality [23, 46]. **Table 2.2** presents structural information on room temperature pyrrhotites with their proposed formulae for charge neutrality. The magnetic structure, Fe_7S_8, is considered charge neutral when described as $Fe_2^{3+}Fe_5^{2+}S_8$, of which ~ 29% of the iron is ferric. The non-magnetic structure, Fe_9S_{10}, can be described as $Fe_2^{3+}Fe_7^{2+}S_{10}$, of which ~ 22% of the iron is ferric. The presence and proportionality of ferric iron is an important factor when correlating structural differences between pyrrhotites and their reactivity towards oxygen (oxidation), where ferric

iron is postulated as being an internal oxidizing agent in the structure and may be one reason why magnetic pyrrhotite oxidizes more readily in comparison to non-magnetic pyrrhotite [14]. Moreover, Fe(III)–S bonds are stated to be most reactive in pyrrhotite towards oxygen and facilitate electron transfer from Fe^{2+} and S^{2-} to oxygen at the surface, supporting the hypothesis that increased ferric iron concentrations correlate to increased oxidation rates [46]. This concept is further discussed in the *Mechanisms* Section (2.3.1.2).

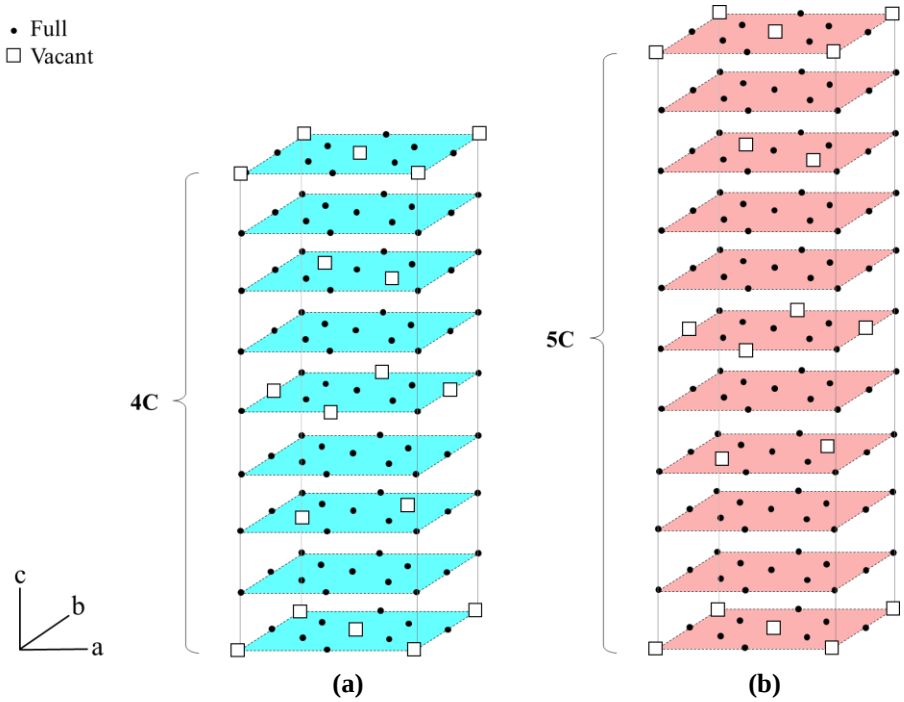

Figure 2.2 *– Illustration of the iron atoms and vacancy distribution – sulfur atoms omitted for clarity; (a) magnetic Fe_7S_8 {4C} pyrrhotite; (b) non–magnetic Fe_9S_{10} {5C} pyrrhotite, modified from Vaughan et. al (1971)[45].*

2.2.3 Magnetism

Pyrrhotite has received considerable attention for its many different properties; one of which is response to a magnetic field which is quite different amongst its superstructures. As mentioned previously, natural pyrrhotites can be categorized many ways (magnetism, iron deficiency – NC/4C, and crystal symmetry – hexagonal/monoclinic), in mineral processing common reference is based on magnetism and sometimes crystal symmetry. After magnetite, *monoclinic* pyrrhotite (Fe_7S_8 {4C}) has the highest magnetic susceptibility, large enough that it can easily be separated by low–intensity magnetic separators [7, 8]. Generally, *monoclinic*

pyrrhotite is the sole *magnetic* pyrrhotite whereas the *hexagonal* superstructures (Fe_9S_{10} {5C}, $Fe_{10}S_{11}$ {11C}, and $Fe_{11}S_{12}$ {6C}) are grouped together as *non–magnetic* pyrrhotite. Numerous magnetic studies have been conducted on natural and synthetic pyrrhotites, most often on the two common superstructures (4C and 5C) [25, 39, 47-54]. The magnetisation is the result of ordered iron vacancy within the structural layers that yields a net magnetic moment for the 4C and a net "0" moment for 5C, 11C, and 6C superstructures; 4C and 5C are depicted in **Figure 2.3** [25]. Furthermore, based on the work of Li and Franzen (1996)[50], Wang and Salveson (2005)[25] suggest that a periodic damping magnetization relationship exists when proceeding from 4C to 2C pyrrhotite (iron–deficient to iron–rich pyrrhotites, ending at troilite); a result of the unique vacancy distribution in each superstructure (the relationship is illustrated in **Figure 2.4**). The most iron–deficient structure, 4C, exhibits the largest net magnetic moment whereas all subsequent stoichiometric NC pyrrhotites (Fe_9S_{10}, $Fe_{10}S_{11}$, $Fe_{11}S_{12}$) and troilite (FeS) have no net moments. The non–stoichiometric pyrrhotites (non–integral or 'MC') also exhibit net magnetic moments (all lower than 4C), however, as discussed earlier (**Table 2.1** and **Figure 2.1**(a)) these structures do not occur naturally and thus have received little attention.

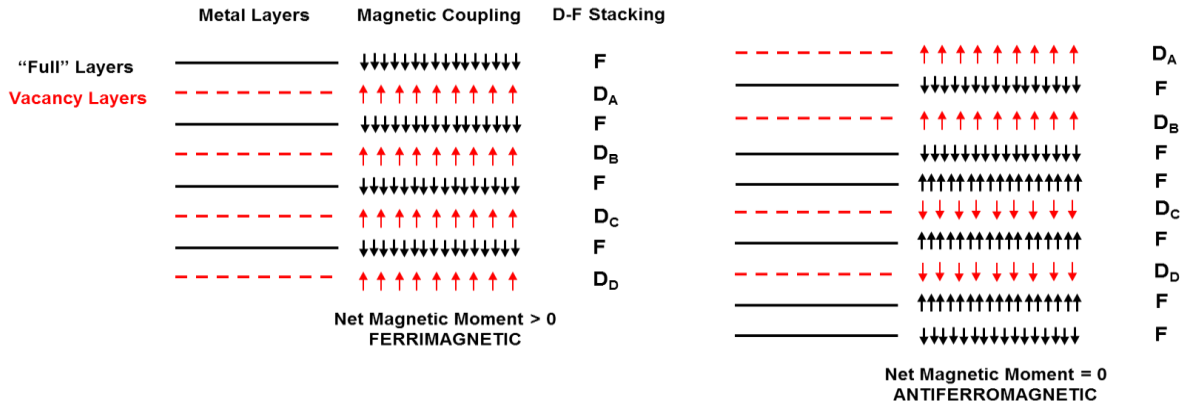

Figure 2.3 *– Stacking sequence of the metal vacancy layers (D_A – D_D) and vacancy free layers (F); (left) magnetic Fe_7S_8 {4C} pyrrhotite; (right) non–magnetic Fe_9S_{10} {5C} pyrrhotite, reproduced from Wang and Salveson (2005)[25].*

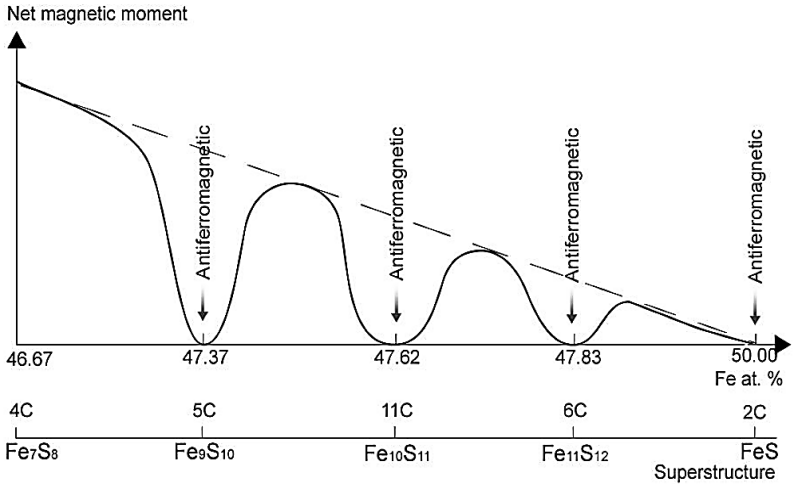

Figure 2.4 *– Periodical pattern of net magnetic moment and pyrrhotite composition, reproduced from Wang and Salveson (2005)[25].*

2.2.4 Mineral Characterization

2.2.4.1 Total Pyrrhotite Content

For base metal sulfide ores, feed mineral quantification is based on feed assays which account for base metals (Cu, Ni, Fe, Co, Pb, Zn, and Mo), sulfur, and common oxides (SiO_2, Al_2O_3, and MgO). The feed typically contains 2 – 3 valuable minerals and the remaining oxides/silicates are grouped together as non–sulfide gangue (NSG) and generally pyrrhotite/pyrite as sulfide gangue. From the metal and sulfur assays, equations are derived from ideal atomic formulae of the minerals to convert elements to minerals. In certain cases (*e.g.* the Sudbury Basin (Canada)), valuable metals replace other metals in non–valuable minerals (*i.e.* Ni present as solid solution in pyrrhotite) and through microprobe analysis this information can be retrieved to account for the metal deportment. An example was given for Cu–Ni sulfide ores (chalcopyrite (Cp)–pentlandite (Pn), respectively, pyrrhotite (Po) being the major sulfide gangue) from the Sudbury Basin by Lawson *et al.* (2005)[12]. It was assumed that 0.8 wt% Ni was present in pyrrhotite as solid solution (Note: the calculation also assumes there is no pyrite, if present, it is grouped with pyrrhotite):

From Cu, Ni and S assays:

$$\mathbf{\%Cp} = 2.886*(\mathbf{\%Cu}) \quad (2.1)$$

$$\mathbf{\%Pn} = 0.0588*(\mathbf{\%Cu}) + 2.8633*(\mathbf{\%Ni}) - 0.0583*(\mathbf{\%S}) \quad (2.2)$$

$$\mathbf{\%Po} = -2.617*(\mathbf{\%Cu}) - 2.4189*(\mathbf{\%Ni}) + 2.5938*(\mathbf{\%S}) \quad (2.3)$$

$$\mathbf{\%Gangue} = 100 - \mathbf{\%Cp} - \mathbf{\%Pn} - \mathbf{\%Po} \quad (2.4)$$

The above equations are required for calculating *total pyrrhotite* content in the ores. For individual superstructure content (non–magnetic {Fe_9S_{10}, 5C} and magnetic {Fe_7S_8, 4C}) other techniques are needed to determine their ratios as the metal atomic and weight % in 5C and 4C are too close to differentiate (**Table 2.2**). A variety of analytical methods can be used to distinguish and quantify the superstructures; X–ray diffraction (XRD) being primary and microscopy (optical and electron) being secondary (generally qualitative). The following Sections provide a general summary of the relevant techniques.

2.2.4.2 XRD

The XRD patterns of all pyrrhotite superstructures are very similar; 4C, 5C, and 6C reference patterns are presented in **Figure 2.5**(a) (Co Kα radiation) to demonstrate the difficulty in differentiating the superstructures (2C troilite shown for comparison). Superstructure quantification is a cumbersome task and normally requires a significant effort in developing calibration curves (primary issues are sourcing high purity single phase natural pyrrhotite specimens {normally upgraded} and the type of calibration/quantification method to use). Several quantitative XRD methods exist in the literature, the basis of most if not all dates to the early 1960s where the characteristic peaks of non-magnetic and magnetic superstructures were used to determine their relative proportions, **Figure 2.5**(b)[55, 56].

There is minor disagreement in the literature as to the *d*–spacing of these peaks (analytical differences arising from compositional/structural variation in pyrrhotites from natural specimens), though the values are generally similar. Non–magnetic (Fe_9S_{10} {5C}) pyrrhotite contains a singlet ($d \approx 2.066$ Å) and magnetic pyrrhotite (Fe_7S_8 {4C}) contains doublets ($d \approx 2.066/2.056$ Å), the low angle peak is virtually identical for both structures and the high angle peak of near equal intensity for 4C is separated by about $0.30 - 0.35^{o}2\theta$[6, 27, 28, 57]. As such, quantitative methods make use of this special feature; two separate approaches are *peak intensity ratio* and *homogenization*, the former is used extensively in the mineral processing industry for its ease of use.

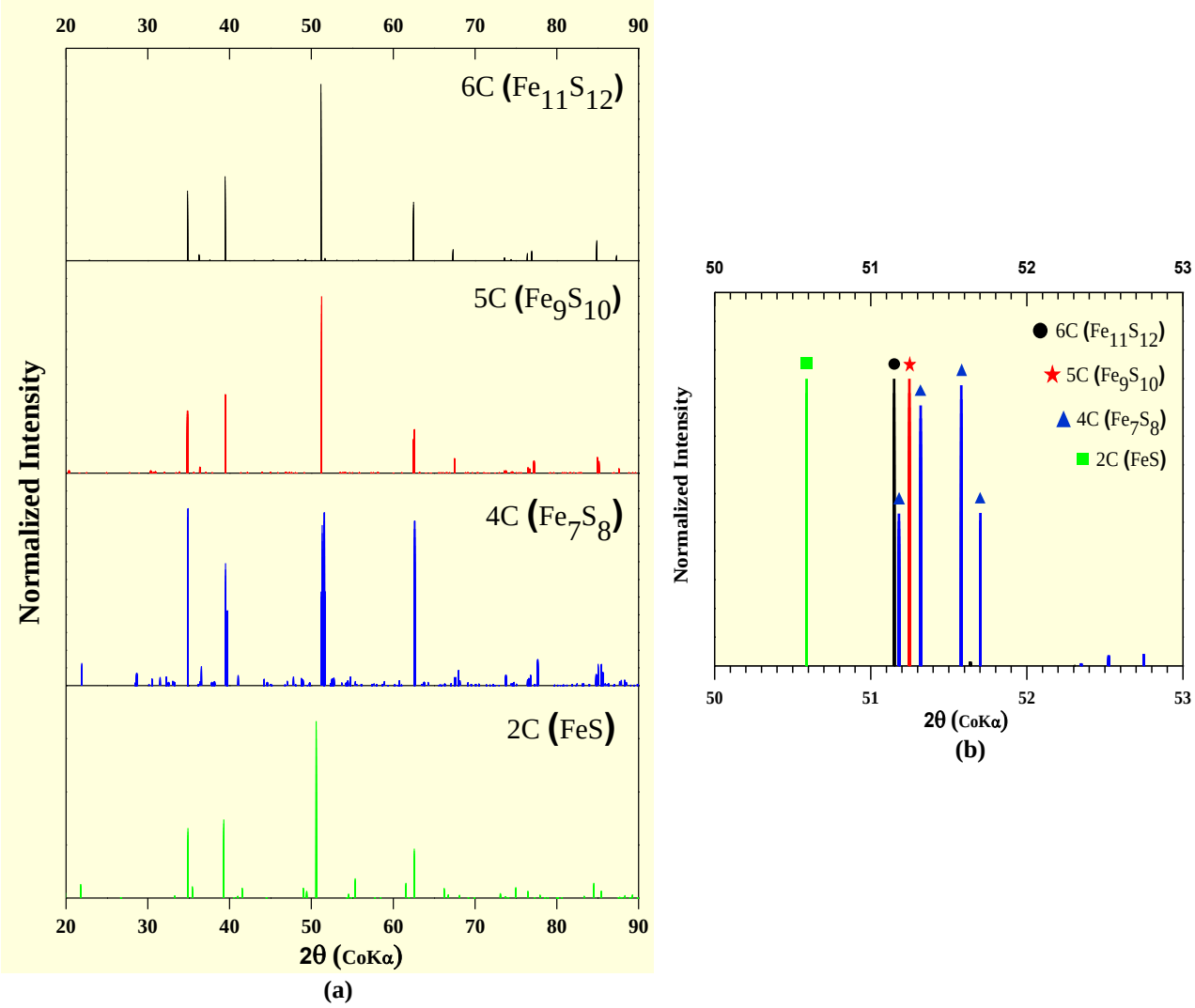

Figure 2.5 *– (a) XRD (CoKα radiation) reference patterns of troilite: 2C – FeS (Skala et al., 2006[58]) and pyrrhotite superstructures: 4C – Fe_7S_8 (Powell et al., 2004[39]); 5C – Fe_9S_{10} (Elliot, 2010[43]); and 6C – $Fe_{11}S_{12}$ (DeVilliers and Liles, 2010[42]); (b) Displays 50°2θ to 53°2θ range.*

The *peak–ratio* method (sometimes referred to as "*d*(102)") is essentially a ratio of the low and high angle peaks that is cross–referenced against a calibration curve (made from mechanical mixtures of purified non-magnetic {5C} and magnetic {4C} and pyrrhotite) yielding % non-magnetic pyrrhotite, magnetic pyrrhotite determined by difference [57, 59]. The type of ratio to calculate is also a matter of debate, however, the common ones can be found in Arnold (1966)[59] and Graham (1969)[57] which are typically used in industry; their calibration curves are depicted in **Figure 2.6** and **Figure 2.7**. For a given base–metal sulfide

ore, total pyrrhotite content is determined *via* metal/sulfur assays and the non-magnetic (Fe_9S_{10} {5C}) proportion calculated from the calibration curves.

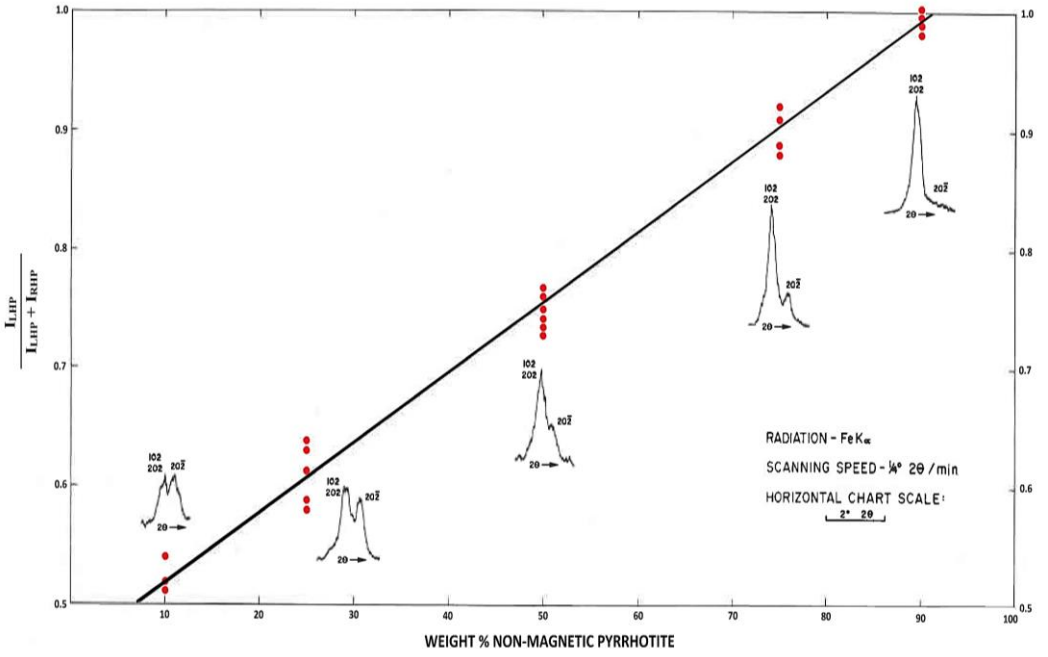

Figure 2.6 *– Intensity ratios of various weighted mixtures of non-magnetic (Fe_9S_{10} {5C}) and magnetic (Fe_7S_8 {4C}) pyrrhotite, I_{LHP} and I_{RHP} represent the intensity of the left-hand (102, 202) and right-hand ($20\bar{2}$) peaks, respectively. Modified from Arnold (1966)[59].*

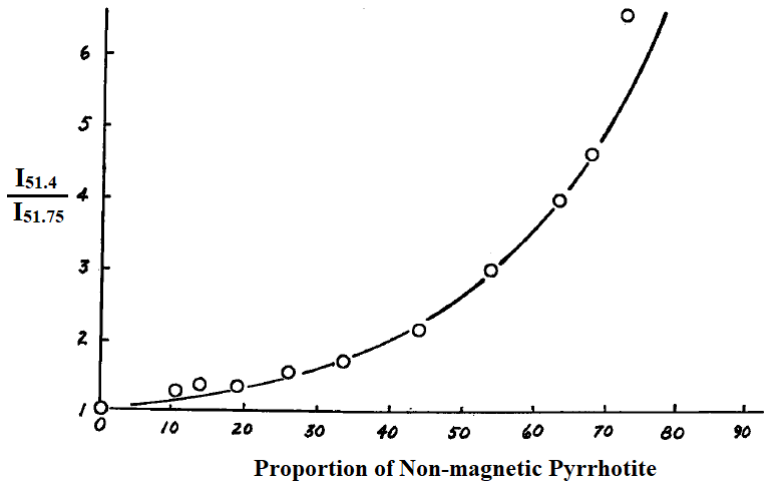

Figure 2.7 *– Intensity ratios ($I_{51.4}/I_{51.75}$) of various mixtures of non-magnetic (Fe_9S_{10} {5C}) and magnetic (Fe_7S_8 {4C}) pyrrhotite, reproduced from Graham (1969)[57].*

Researchers seeking a higher degree of accuracy (*e.g.* for pyrrhotite phase relations in the Fe–S system) prefer to use the *homogenization* method as the fundamental assumption in

the *peak–ratio* method is that the magnetic pyrrhotite (4C) doublet is of equal intensity. This may not be true for all magnetic pyrrhotites as discussed by Kissin (1974)[27] and may result in lower accuracy. The main objective of the *homogenization* method is to invert 4C in single phase and 4C/5C pyrrhotite intergrowth samples into a metastable non-magnetic (single phase 5C) pyrrhotite to give a single low angle peak, ensuring that the error associated with the 4C doublet is minimized [6, 24, 27]. The procedure involves heat treating the samples at 350 ^{o}C in evacuated/sealed silica tubes for a period of time after which the samples are immediately quenched. The proposed treatment time varies but is generally between 3 and 20 mins (lower times are preferred to avoid the exsolution of pyrite), Yund and Hall (1969)[29] and Kissin and Scott (1982)[24] are useful references [6, 27, 60].

Lastly, phase quantification can also be accomplished by XRD software (*e.g.* AutoQuan, TOPAS, and HighScore) using the entire spectra as opposed to just the characteristic peaks, Rietveld refinement is employed (optimized parameters) using appropriate crystal structure files available in the literature (4C and 5C). The technique largely depends on the expertise of the user and the quality of the crystal structure files, which are refined every few years and care must be taken on their use. The detection limit of XRD is about 3 – 5 wt% at best, below which other more sensitive techniques are required (*e.g.* microscopy), which may prove useful for samples with a low pyrrhotite content (*e.g.* flotation tails) or low grade ore deposits [13, 61].

2.2.4.3 Microscopic Methods

Examination of polished surfaces by reflected–light microscopy was one of the early methods used to qualitatively distinguish between pyrrhotites in two–phase mixtures. Simply polishing the surfaces was normally not sufficient, the surface often required alteration in order to enhance the contrast between the superstructures as their natural reflectivities are very similar [59]. Two commonly used techniques are surface etching (either by hydroiodic or chromic acid) and the application of a magnetic colloid (a ‘soapy’ suspension containing fine magnetite particles) that highlight ferrimagnetic regions (*i.e.* magnetic {4C} pyrrhotite) called Bitter patterns [6, 24, 25, 45]. These methods work particularly well at highlighting the grain boundaries between 4C/5C superstructures, especially in large–grained pyrrhotite

mixtures. Their use as quantitative methods, however has limitations, in that they are tedious, can be unreliable at times (differentiating fine 4C/5C intergrowths), and to some degree rely on the expertise of the technician [57].

Scanning Electron Microscopy (SEM) is routinely used (automated systems such as Quantitative Evaluation of Minerals by Scanning Electron Microscopy (QEMSCAN) and Mineral Liberation Analyser (MLA)) to identify pyrrhotite by Energy Dispersive X–ray Spectroscopy (EDS) using Fe/S ratios unique to pyrrhotite, however, currently it cannot accurately quantify the superstructures since their ratios are too similar (**Table 2.2**). Since the silicon drift detector (SDD) technology is advancing well with increasing capabilities, future EDS detectors may be able to resolve this issue. Becker (2009)[13] was successful in using the BSE signal to discriminate between the superstructures and this development is certainly a step forward. However, as it currently stands, it is specialized and technician dependent since tuning of the settings is an iterative process. Furthermore, the method may be influenced by crystal orientations and the results could vary somewhat from one ore to another. Lastly, it may be difficult to obtain appreciable contrast between intergrowths within fine grain sizes. Some progress has been made in this area by other methods but these are still under development, such as Electron Back–Scatter Diffraction (EBSD) as the basis of comparison (analogous to XRD).

Presently, mineralogical programs use quantitative XRD coupled with chemical and QEMSCAN/MLA assays to account for the non-magnetic (5C)/magnetic (4C) superstructure ratio and total pyrrhotite, respectively. For many programs this is adequate though in some cases it is desirable to quantify the superstructures in the SEM, two examples are mineral associations (liberation) of individual superstructures and samples containing < 5 wt% pyrrhotite.

2.3 Aqueous Stability and Oxidation

2.3.1 Aqueous Stability (E_h–pH)

For minerals in aqueous suspensions (under flotation–relevant conditions), their thermodynamic stabilities can be summarized by Pourbaix diagrams (phase diagram

correlating solution oxidation–reduction potential {ORP} to its pH), occasionally called "E_h–pH" diagrams. Note: E_h (SHE, Volts) = $E_{\{measured\}}$ + $E_{h\{reference\}}$; SHE = Standard Hydrogen Electrode; and $E_{\{measured\}}$ = $E_{\{saturated\ calomel\ electrode\}}$ or $E_{\{Ag/AgCl\}}$. **Figure 2.8**(a) displays the 3 main Zones (strongly oxidizing, moderate/mildly oxidizing, and reducing) and the upper and lower dashed lines represent water stability limits. Most flotation processes operate in Zones 1 and 2 (base–metal sulfides primarily in Zone 2), the E_h is largely controlled by dissolved oxygen (DO) content where increase in aeration/DO directly increases E_h, likewise, removal of oxygen reduces E_h (by nitrogen purging, addition of reductants, and/or use of mild steel grinding media). For the Fe–S–H_2O system, dominant species are presented in **Figure 2.8**(b) at ambient conditions (25ºC, 1 atm, 10^{-6} mol/L Fe and S). As the diagram is based on thermodynamic "long–term" stability (species having the lowest Gibbs free energy), metastable "kinetic" species are usually not presented, however, to allow the diagram to be applicable to flotation systems some of these kinetically dominant species are shown in *red* (*e.g.* S^o and $Fe(OH)_3$).

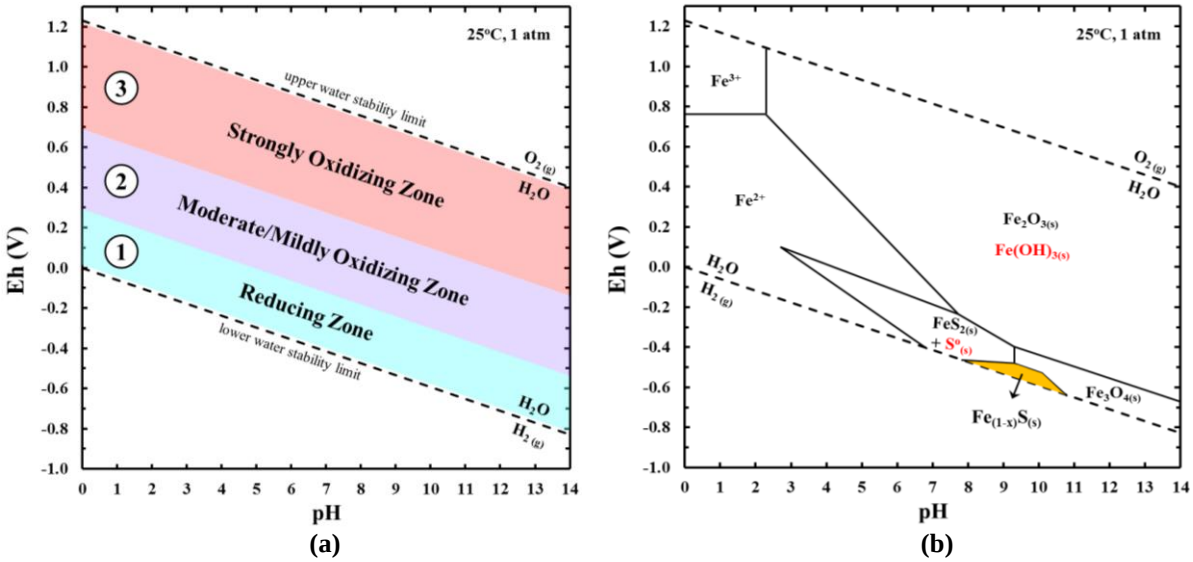

Figure 2.8 *– (a) General Pourbaix diagram highlighting 3 main zones; (b)Pourbaix diagram for the Fe–S–H_2O system highlighting pyrrhotite in yellow, calculated at 25ºC, 1 atm, 10^{-6} mol/L Fe and S using HYDRA and MEDUSA (Puigdomenech, 2009, 2010)*[62, 63].

At low pulp potentials (–450 to –650 mV E_h) and alkaline pH (8 to 11), pyrrhotite is expected to be stable. Any deviation from these conditions leads to mineral dissolution and/or oxidation, resulting in either leaching of iron (Fe^{2+} or Fe^{3+}) below pH 8 (certain E_h) and/or

reprecipitation/oxidation as iron hydroxide, $Fe(OH)_3$, in the pH range 2 to 14 (most E_h). It must be noted that hematite (Fe_2O_3) and magnetite (Fe_3O_4) are end oxidation products of pyrrhotite, where iron oxyhydroxides and hydroxides (as well as sulfur and polysulfides) are intermediate phases that are kinetically relevant to flotation processes. Pyrrhotite surface oxidation is discussed in *Mechanisms* Section (2.3.1.2) and direct links are made to its Pourbaix diagram (surface and sub-surface speciation).

2.3.1.1 Reactivity and Oxygen Demand

Pyrrhotite is known to be a very reactive mineral especially with oxygen, exposure of a freshly fractured pyrrhotite surface to air even for a few seconds was found to oxidize half the iron in the first few surface layers [64, 65]. During flotation it is a major oxygen sink in the pulp, similarly, in tailings environments it continues to be reactive and is the primary cause of acid mine drainage and self–heating issues in nickel sulfide operations [65, 66]. Numerous reactivity/oxidation studies have been conducted on pyrrhotite to understand its complex surface reactions, though many do not state the type of superstructure(s) being investigated. A handful do mention the superstructure–type and shed some light as to the reactivity of 4C and 5C pyrrhotite, these are summarized in Janzen (1996)[67], Gauvreau (2002)[68], Becker (2009)[13], Ekmekci *et al.* (2010a,b)[69, 70] and referenced here [61, 71-76]. Although there are disagreements as to which superstructure is more reactive (with supporting evidence on both sides), the overall trend is that 4C magnetic pyrrhotite is more reactive than its 5C non–magnetic counterpart, and therefore is said to be more susceptible to surface oxidation.

Oxidation of pyrrhotite superstructures is expected to be different for several reasons: structural %vacancy, Fe^{3+} content, mineral locking – galvanic interactions, and trace metal content. Becker (2009)[13] and Becker *et al.* (2010)[14] presented oxygen uptake factor results of different ore samples containing > 75% pyrrhotite, each containing different amounts of superstructures, conducted at pH 7 and 10. As described by the authors, the oxygen uptake factor was calculated by fitting an exponential curve to the data for dissolved oxygen concentration versus time, after which the first order rate constant was taken from this curve [14]. The results show a significant difference between oxygen uptake for the

different superstructures when comparing pH 7 and 10, with higher pH leading to much higher uptake, suggesting severe oxidation in alkaline conditions as expected. Interestingly, the trends are not all the same: 4C magnetic pyrrhotite ores exhibited higher uptake under each condition, implying greater oxidation rates for this superstructure as previously suspected.

Pyrrhotite found in ores with other sulfides (semiconductors) will naturally have galvanic interactions through mineral locking as well as with the grinding media *via* pulp, the flow of electrons is dependent on the electrochemical series of the minerals (rest potentials) and pulp DO [66, 77, 78]. In the case of pyrrhotite that is locked (binary particles) with pentlandite, chalcopyrite, or even pyrite (which are more noble, *i.e.* higher rest potentials) will accelerate the oxidation of pyrrhotite. It must be noted that magnetic pyrrhotite is expected to oxidize faster than non-magnetic pyrrhotite not only because it contains higher %vacancies and proportion of Fe^{3+} but also because it is commonly found with pyrite (**Figure 2.1**(a)) [37].

Trace metal content, typically nickel and cobalt substitution for iron in pyrrhotite, will result in a positive effective charge near the nickel or cobalt sites in the structure, which, according to Janzen (1996)[67], would restrict the movement of lattice electrons and therefore hinder mineral oxidation [13]. Kwong (1993)[75] studied monoclinic pyrrhotite and the effect of nickel and cobalt content on its oxidation rate; the results suggest that higher trace metal content correlates with slight lowering of the oxidation rate.

Depending on the purity of the samples studied (and whether or not the researchers quantified both superstructure types, which is sometimes overlooked), galvanic effects and trace metal content, several studies in the literature may have biased their oxidation results which could have led to different findings. Based on the current literature, there are more references advocating that 4C magnetic pyrrhotite is the more reactive superstructure towards oxygen, which, as will be discussed in the following Section is one of the reasons for its poor flotation when compared to 5C non-magnetic pyrrhotite.

2.3.1.2 Mechanisms (Reactions and Metal Deficient Sulfides)

In the context of mineral flotation, aside from feed handling (prolonged stockpiling), surface oxidation is largely influenced by pulp potential. In flotation, oxygen is normally the final electron acceptor and its presence increases the pulp potential. Other reagents such as sodium sulfite are sometimes added to ensure a reducing environment and allow certain reactions to be more effective (*e.g.* diethylenetriamine [DETA] chelation). For sulfide minerals, **Figure 2.9** presents possible reactions that can occur on the surface, with most of these oxidation products being hydrophilic and therefore detrimental to pyrrhotite flotation [1].

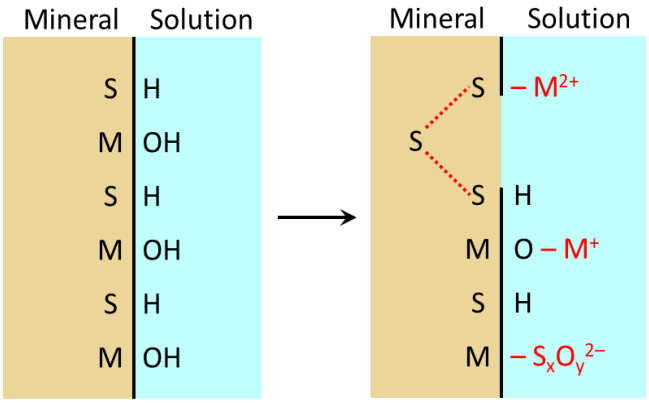

Figure 2.9 *– Sulfide mineral; (left) hydrated surface; (right) oxidized surface. Modified from Wills and Finch (2016)[1].*

Complete oxidation of the pyrrhotite surface can be described by reactions (5) and (6):

$$Fe_{(1-x)}S + (2 - ½x)O_2 + xH_2O \rightarrow (1 - x)Fe^{2+} + SO_4^{2-} + (2x)H^+ \quad where\ 0 < x \leq 0.125 \quad (2.5)$$

Where Fe^{2+} is further oxidized to Fe^{3+}:

$$Fe^{2+} + ¼\ O_2 + ½\ H_2O \rightarrow Fe^{3+} + OH^- \quad (2.6)$$

If pH > ~ 4, Fe^{3+} hydrolyzes and precipitates as iron oxyhydroxide or hydroxide (goethite – FeOOH or ferrihydrite – $Fe(OH)_3$):

$$Fe^{3+} + 3H_2O \rightarrow Fe(OH)_3(s) + 3H^+ \quad (2.7)$$

Thus, if pyrrhotite is completely oxidized, SO_4^{2-} and $Fe(OH)_3$ products render the surface hydrophilic due to strong interaction with water (hydrogen bonding) and little attraction

towards anionic collectors (both products having the same charge as anionic collectors such as xanthates). For incomplete surface oxidation (common in mildly oxidative conditions), the sulfur species on the pyrrhotite surface is partially oxidized (modified reaction for alkaline conditions from (5)):

$$Fe_{(1-x)}S + ½ (1 - x)O_2 + (1 - x)H_2O \rightarrow (1 - x)Fe^{2+} + S^o + 2(1 - x)OH^- \quad (2.8)$$

The iron would oxidize to Fe^{3+} and hydrolyze, precipitating as iron hydroxide. The implications of surface sulfur species will be discussed for collectorless pyrrhotite flotation: essentially sulfide and polysulfide species are hydrophobic and therefore mildly oxidative conditions normally promote pyrrhotite flotation (even without collectors). With continued oxidation, surface sulfur continues to transition through several sulfur complexes (disulfide, polysulfides, elemental sulfur, sulfite, and eventually sulfate), where the last set of species is hydrophilic (not conducive towards flotation).

Many studies have suggested progressive oxidation of pyrrhotite results in a predominantly iron(III) oxide (or hydroxide/oxyhydroxide) surface, where the sublayers are enriched with sulfur. Initially, iron (oxy)hydroxides are formed during first stage of oxidation (in the presence of water) selectively removing iron from the pyrrhotite lattice. Immediately below this iron–rich layer sulfur is reorganized into disulfides and forms a marcasite–type structure (orthorhombic FeS_2), with continued oxidation monosulfides are eventually oxidized to disulfides and polysulfides (promoting S–S covalent bonding)[2, 46, 65, 79, 80]. This oxidation was found to result in the zonation of at least 35 Å (3.5 nm) section of the surface (**Figure 2.10**, 4C magnetic pyrrhotite given as an example), where layers immediately below the first surface layer were determined to be sulfur–rich with respect to iron (referred to as "metal deficient sulfides"). As expected, this oxidation process is complimented by the Fe–S–H_2O Pourbaix diagram (**Figure 2.8**(b)), where similar pyrrhotite surface oxidation products can be found when transitioning from low to high E_h environments.

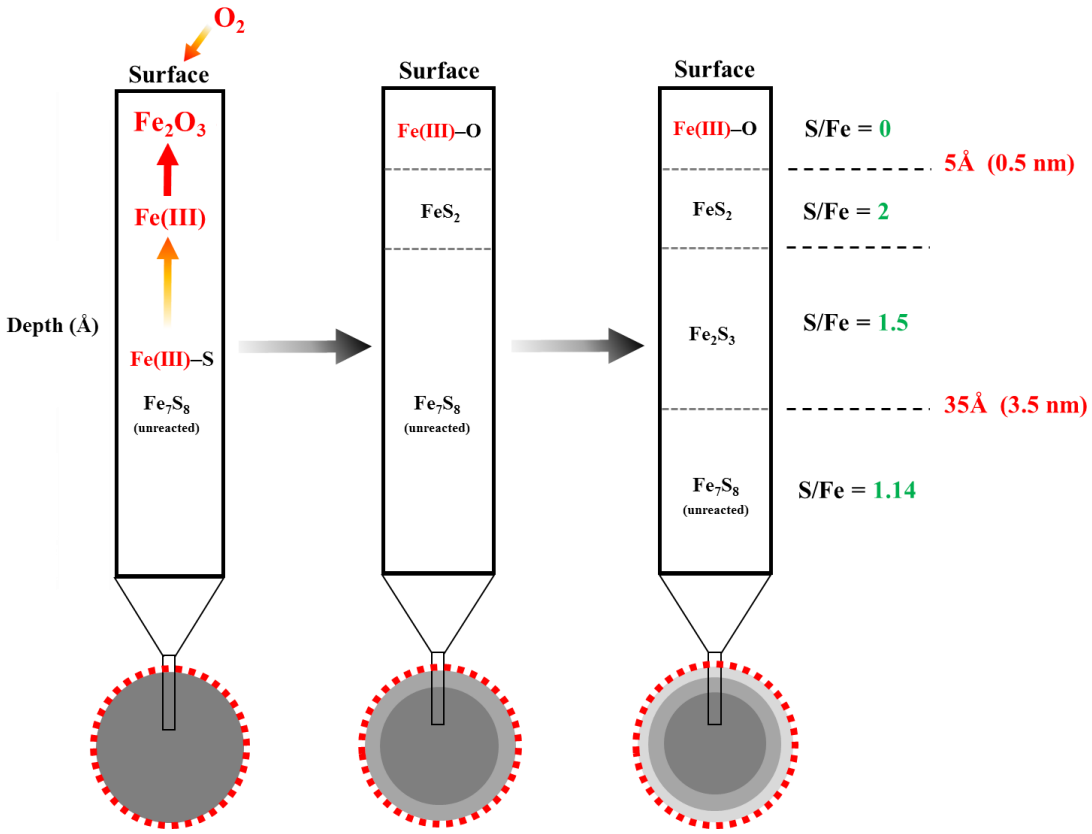

Figure 2.10 *– Depiction of magnetic (Fe_7S_8 {4C}) pyrrhotite progressive surface oxidation leading to alteration zones, referred to as "metal–deficient sulfides". Non-magnetic (Fe_9S_{10} {5C}) is expected to oxidize similarly, however, kinetically it is much slower. Adapted from Belzile et al. (2004)[2].*

Although most studies agree in this surface zonation/sulfur enrichment, there is disagreement as to the mechanism by which it occurs. The most prevalent mechanism is one in which surface adsorbed oxygen is reduced to O^{2-} by electron transfer from the bulk structure (from Fe^{2+} and S^{2-}), facilitated by swift electron transfer between Fe^{2+} and Fe^{3+} in the lattice [2, 46]. In particular, the most reactive sites for oxygen reduction are perceived to be Fe(III)–S bonds. The presence of structural vacancies is presumed to promote the diffusion iron from the bulk to the surface, transporting iron to form an iron oxyhydroxide or oxide and leaving iron deficient thus sulfur rich layers below [46, 65, 80].

Based on this proposition (vacancies facilitating surface oxidation), many researchers have hypothesized that 4C magnetic pyrrhotite (Fe_7S_8) having larger vacancy concentration (12.5%) as well as more proportional Fe^{3+} (~ 29% of total iron) would likely oxidize at a faster rate than the other superstructures, namely 5C non–magnetic pyrrhotite

(Fe_9S_{10}), which is less vacant (10%) and has less proportional Fe^{3+} (~ 22% of total iron) [14]. Many authors have demonstrated similar findings[13, 72, 73, 76], some have suggested the opposite view[2, 71] whereas some have stated that there is no perceivable difference in oxidation rate for either structure [61, 67]. The differences in the findings from these studies may be explained by the association of the pyrrhotite samples with other minerals (locking to chalcopyrite, pentlandite, pyrite, *etc.*) or its trace metal content (*e.g.* nickel and cobalt), both of which can impact its oxidation rate and may have led to dissimilar results.

2.3.2 Zeta Potential and Interaction with Pulp Ions/Reagents

2.3.2.1 Zeta Potential

A mineral placed in an aqueous solution exhibits a natural surface charge causing an imbalance at the mineral–water interface. At this boundary, changes to the molecular environment result in a structural reorganization of the mineral surface species to satisfy the conditions in the bulk solution. Such changes to the surface generally lead to a separation of electrical charge and the formation of an electrical potential in reference to the bulk solution [81]. The surface charge can be organized into three categories: (1) *permanent* structural charge; (2) *co–ordinative* surface charge; and (3) *dissociated* surface charge. The *permanent* structural charge (σ_o) occurs due to isomorphic substitution in minerals. For example, Al^{3+} substitutes for Si^{4+} in phyllosilicates, which leads to a charge imbalance in the crystal and results in a net negative structural charge on the Si basal plane. The *co–ordinative* surface charge (σ_β) is the result of surface functional groups (such as H^+ and OH^-). The difference between these two charges is normally not zero and therefore requires counterions from the bulk solution for electroneutrality to be reached, thus the requirement for the *dissociated* surface charge (σ_d). This results in an electrical double layer for which electroneutrality is maintained, $\sigma_o + \sigma_\beta + \sigma_d = 0$. Several electrical double layer models have been proposed, with the Stern–Grahame rendition being commonly applied.

The electrical potential difference across a section of the mineral–water interface can be determined by zeta potential measurements (electroacoustic, electrophoresis, or streaming potential), which corresponds to the electrical potential at the shear plane (slipping

plane) between the moving and stationary phases (presumed to be close to the outer Helmholtz plane – OHP) [82]. The absolute value of the zeta potential is not known (only approximated), nonetheless, the most useful information is the isoelectric point (IEP) where the plane of shear shows a net zero potential. This value has clear implications in flotation since one can infer pH ranges where collector/depressants can adsorb (electrostatically) on the mineral surface and also the interactions of this surface with pulp ions. The electrical double layer model and the location of zeta potential are illustrated in **Figure 2.11**.

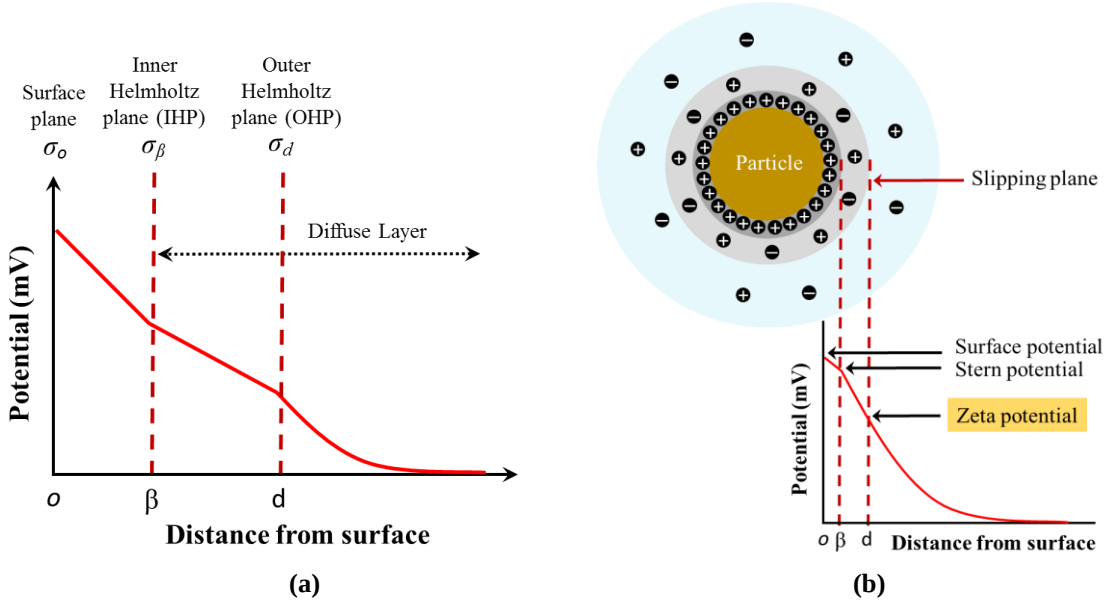

Figure 2.11 *– (a) Electrical double layer model; (b) location of zeta potential, adapted from Rao (2004)[82].*

In aqueous solutions, sulfide mineral surfaces are hydrated. Alternating anionic (*i.e.* S^{2-}) and cationic (*i.e.* Fe^{2+}/Fe^{3+}, Ni^{2+}, Cu^{2+}, *etc.*) surface sites are present which exhibit partial charges (dipoles) due to different electron densities surrounding the ions in the crystal. As a result, water molecules are attracted to these sites through electrostatic interactions and dissociate to hydroxyls and protons. The hydroxyl groups coordinate with metal ions and the protons associate with surface sulfides, forming the stern layer. At low pH conditions, sulfide and oxide minerals will have a net positive surface charge (due to H^+ ions surface saturation), with increasing pH, H^+ ions migrate from the surface to the bulk leaving it dually charged where at a specific pH it has a net neutral potential (IEP). With a subsequent increase in the

pH, more H^+ ions leave the surface exposing negative surface sites, rendering the surface net negative.

Freshly ground sulfide minerals (unoxidized) generally have a pH_{IEP} between 2 and 3.5, which is very similar to that of sulfur [1, 83]. With oxidation (exposure to oxygen), metal oxyhydroxide/hydroxide species form on the surface which shift the pH_{IEP} to higher values (*i.e.* pyrrhotite surfaces eventually resemble those of $Fe(OH)_3$ and/or Fe_2O_3 where pH_{IEP} > 6). **Table 2.3** summarizes pyrrhotite pH_{IEP} values reported in the literature, displaying a wide pH range (2 – 9.6) resulting from different degrees of surface oxidation, highlighting the necessity of mineral pretreatment before analysis. Freshly ground pyrrhotite non-magnetic and magnetic superstructures would be expected to have similar pH_{IEP}, close to pH 3 – 3.5 [83]. The discrepancies can be attributed to inadequate or complete lack of mineral pretreatments.

Table 2.3 *– Summary of pH_{IEP} of pyrrhotite reported in the literature.*

pH_{IEP}	Pyrrhotite type	Condition	Natural/Synthetic	Reference
< 2	–	Uncontrolled atm.	natural	[84]
2	–	–	natural	[85]
2	–	N_2 atm., 245ºC	synthetic	[84]
2 – 2.5	–	–	synthetic	[86]
2.7	–	N_2 atm., 230ºC	synthetic	[84]
3 – 3.4	FeS	–	–	[83]
5.5	–	–	natural	[87]
5.8	–	Uncontrolled atm.	natural	[84]
8.42	Fe_7S_8 (mag/4C)	–	synthetic	[11]
8.73	Fe_9S_{10} (non-mag/5C)	–	synthetic	[11]
9.6	Fe_7S_8 (mag/4C)	–	natural	[11]

2.3.2.2 Zeta Potential Studies (Ion/Reagent Effects)

Ions present in the flotation pulp from the dissolution of minerals and/or by addition of reagents can adsorb onto mineral surfaces by electrostatic attraction thereby altering the surface charge of the minerals, affecting reagent/mineral interactions. For pyrrhotite, Cu^{2+}, Ni^{2+}, Fe^{2+}, Fe^{3+}, and Ca^{2+} (*via* lime addition) are common ions in flotation as the mineral is closely associated with copper and nickel sulfide minerals. **Figure 2.12** displays the effects of such ions, generally the higher the concentration of the ion the larger the shift in pH_{IEP} [88]. At the moment, the literature is lacking zeta potential data on non-magnetic (5C)/magnetic (4C) superstructures, available studies are based on "pyrrhotite" only (they do not discriminate between the superstructures) and the effects of pulp ions/reagents on individual superstructures are inferred from flotation studies.

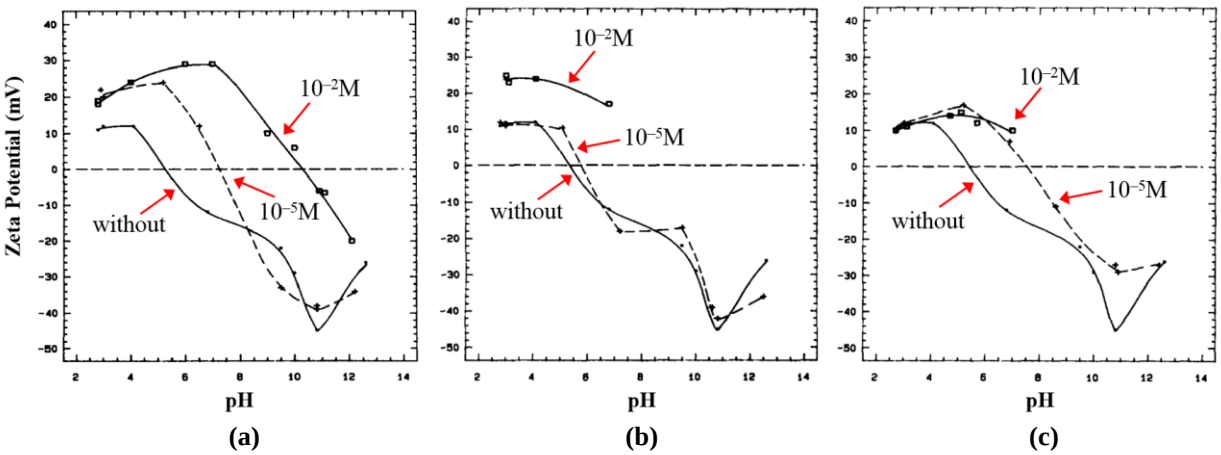

Figure 2.12 *– Zeta potential of pyrrhotite with and without 10^{-2} and 10^{-5} mol/L: (a) $CuCl_2{\cdot}2H_2O$; (b) $NiCl_2{\cdot}6H_2O$; and (c) $FeCl_2{\cdot}2H_2O$; modified from Acar and Somasundaran (1992)[88].*

In the presence of collector (*i.e.* xanthates, which are negatively charged at pH > 5), adsorption onto pyrrhotite takes place in two stages: firstly, by *physisorption* (electrostatic) followed by *chemisorption* (bond formation) which is electrochemical and requires oxygen, resulting in dixanthogen formation on pyrrhotite surfaces (discussed in the next Section). Thus, pyrrhotite surface potential (*i.e.* surface charge) is lowered after xanthate adsorption. For pyrrhotite, as is the case for many sulfides, pulp potential (ORP) plays a critical role in the adsorption of xanthate, in a low oxygen environment xanthate adsorption is significantly hindered and pyrrhotite surface potentials are not lowered. However, in the presence of pulp

ions, in other words metal cations that accidentally activate pyrrhotite, xanthate adsorption is significantly improved. The pyrrhotite surface becomes positively charged over a wide pH range (as shown in **Figure 2.12**), even at pH 10, which provides the necessary positive surface sites for xanthate to adsorb electrostatically. To deactivate pyrrhotite surfaces, several surface modifiers/depressants are available, one commonly used is diethylenetriamine (DETA), a chelant compound that removes adsorbed Cu^{2+} and Ni^{2+} (usually dosed in conjunction with sodium sulfite). The chelants act to preferentially bind to these metal cations thereby limiting their activity and interaction with other species such as collectors. The mechanism of deactivation is generally understood, DETA solubilizes the surface adsorbed cations, though a portion of the DETA (free or DETA–metal complexes) is said to reside on pyrrhotite surfaces as well (electrostatically bound). Data from Xu *et al.* (1997)[87] supports this proposition where the researchers found that in the pH range 6 – 9, DETA made the pyrrhotite surface more positive compared to the mineral alone; however, at pH > 10 the effect was largely minimized where DETA is expected to be neutrally charged.

2.3.2.3 Reagent–Mineral Surface Interactions (Chemistry and Adsorption)

The dissolution of xanthate collectors in aqueous solutions results in different xanthate speciation and is a function of pH and E_h. As stated by Somasundaran and Wang (2006)[89], the pKa value for xanthic acid is difficult to measure but a conservative value of approximately 5 is accepted (not explicitly stated for the different carbon chain lengths, however, similar nonetheless). Below pH 5 the collector primarily exists as the undissociated xanthic acid (HX), at pH 5 it is a 50/50% mixture (HX and X^-), above pH 5, it exists mainly as the negatively charged xanthate molecule (X^-). Most base metal sulfide flotation processes operate in the neutral to alkaline pH range, where incidentally both collector and mineral surfaces are negatively charged, which suggests minimal interaction due to repulsive electrostatic forces. However, it is well known that xanthate adsorption occurs in the neutral to alkaline pH range for many sulfide minerals and is the result of chemical bonding on the mineral surface (*chemisorption*) which overcomes the repulsive forces. Furthermore, this adsorption mechanism is also known to be electrochemical in nature, which upon adsorption xanthate is oxidized[1], with the general anodic adsorption reaction given by:

$$MS + X^- \leftrightarrow MS(X) + e^- \quad (2.9)$$

In flotation pulps, the final electron acceptor is dissolved oxygen, and the cathodic reaction is given by:

$$½\ H_2O + ¼\ O_2 + e^- \leftrightarrow OH^- \quad (2.10)$$

If the pulp potential (*open circuit potential* or *mixed potential*) is relatively high (common for flotation since the pulp is continuously aerated), the adsorbed xanthate is further oxidized to dixanthogen which precipitates on the mineral surface (oxygen as the final electron acceptor):

$$2X^- \leftrightarrow X_2 + 2e^- \quad (2.11)$$

For the X^-/X_2 half reaction, **Table 2.4** summarizes the standard redox potentials for different xanthates. Using this reference, the Nernst equation ($E_h = E_h^o - \frac{RT}{nF}\ln K$) can be applied to yield the potential at which xanthate will spontaneously oxidize. Where ***R*** ≡ gas constant [8.314 J/(mol·K)], ***T*** ≡ absolute temperature [K], ***n*** ≡ number of electrons exchanged, ***F*** ≡ Faraday's constant (96, 485 C/mol), and ***K*** ≡ reaction quotient at equilibrium [unit less]. At pH > 5 and standard conditions, the equation can be reduced to:

$$E_h = E_h^o - 0.0591 \log[X^-] \quad (2.12)$$

Table 2.4 *– Xanthate standard redox potentials, E_h^o, for X^-/X_2 couple, adapted from Winter and Woods (1973)[90].*

Alkyl group	E_h^o (Volts)
Methyl	– 0.004
Ethyl	– 0.057
n–Propyl	– 0.090
n–Butyl	– 0.128
n–Amyl	– 0.158
n–Hexyl	n.d.

For example, using potassium *n*–amyl xanthate (PAX) concentration of 10^{-4} mol/L, E_h^o = – 0.158V, and Equation (2.12), the calculated E_h value is 0.078V. Above this potential, xanthate will oxidize. This indicates the importance of pulp potential on collector adsorption,

since for certain sulfide minerals their hydrophobicity is linked to either the metal–xanthate (MX) or dixanthogen (X_2) surface complexes [91]. For pyrrhotite, having a rest potential higher than 0.078V for a large portion of the alkaline pH range (**Figure 2.13**), the expected surface species is dixanthogen.

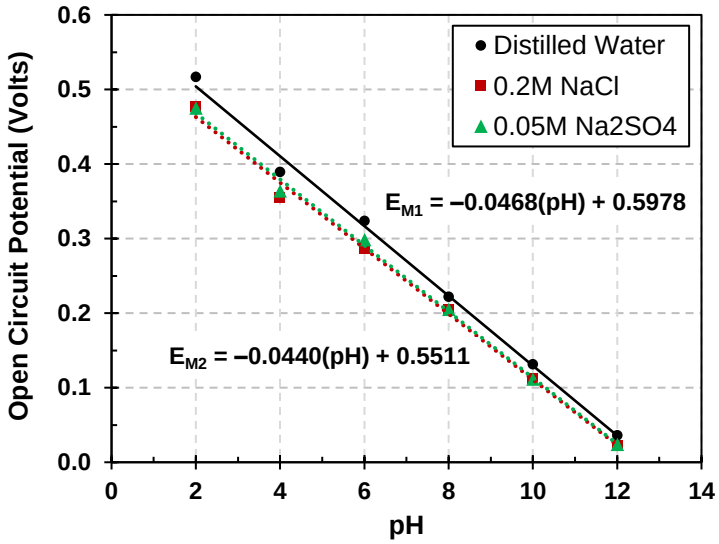

Figure 2.13 *– Pyrrhotite open circuit potential (E_M) as a function of pH in different electrolyte solutions: (i) distilled water (E_{M1}); (ii) 0.2M NaCl solution (E_{M2}); (iii) 0.05M Na_2SO_4 solution (E_{M2}), adapted from Moslemi et al. (2011)*[92].

There are a few mechanisms detailed in the literature as to how dixanthogen forms on the pyrrhotite surface. The most popular theory is that pyrrhotite is partially oxidized to expose a positively charged Fe(III) hydroxyl–polysulfide surface complex (Po‖(OH)$[S]^+$) which allows xanthate attachment through *coulombic* attraction, referred to as *physisorption* (different to Equation (9)), instead of *chemisorption* [93-96]. The adsorbed xanthate may then be oxidized to dixanthogen (chemical bond formation) by oxygen at higher pulp potentials, which is responsible for pyrrhotite's hydrophobicity:

$$Po‖ + H_2O \leftrightarrow Po‖(OH)[S]^+ + H^+ + 2e^- \quad (2.13)$$

$$Po‖(OH)[S]^+ + X^- \leftrightarrow Po‖(OH)[S][X] \quad (2.14)$$

$$Po‖(OH)[S][X] + X^- \leftrightarrow Po‖(OH)[S][X_2] + e^- \quad (2.15)$$

If this partially oxidized surface (containing Po‖(OH)$[S]^{+}$) is taken to be the initial active site for xanthate adsorption, fresh or partially oxidized magnetic pyrrhotite (Fe_7S_8 {4C}) is expected to contain more Fe(III) surface sites than 5C non–magnetic pyrrhotite (Fe_9S_{10} {5C}), **Table 2.2**, which would promote higher xanthate adsorption onto magnetic pyrrhotite.

A comprehensive study by Kolahdoozan (1996)[11] was conducted on three samples (synthetic non-magnetic {5C} and magnetic {4C}, and a natural ore containing magnetic {4C} pyrrhotite) over a large pH range (2 – 12). Potassium *n*–amyl xanthate (PAX) collector adsorption studies were conducted under various conditions (as is, oxidative, cyanide, and copper pre–conditioning) to infer differences in the superstructure–collector interactions at flotation–relevant pH (7, 8.5 and 10), displayed in **Figure 2.14** [11, 97]. Alkaline conditions were detrimental as anticipated (increased surface oxidation and ion exchange between adsorbed xanthate and OH^{-} groups at higher pH), however, it should be noted that all tested samples gave different results (Note: natural ore contained pentlandite and chalcopyrite contaminant minerals thereby increasing its PAX adsorption). The synthetic sample data suggests different collector adsorption mechanisms between the superstructures under differing conditions, therefore implying different mineral surface speciation. Furthermore, magnetic pyrrhotite consistently adsorbed more PAX than non-magnetic pyrrhotite (possibly the result of more Fe(III) surface sites on magnetic pyrrhotite), except in the presence of pulp ions (in this particular case it was Cu^{2+}). This further suggests different surface speciation. The copper cations appear to promote higher xanthate adsorption densities on the non-magnetic superstructure even at highly alkaline pH (10), which may explain the better floatability of non-magnetic over magnetic pyrrhotite in industrial flotation pulps as compared to lab–scale controlled tests with minimal dissolved ions (yielding conflicting results as to which superstructure is more floatable).

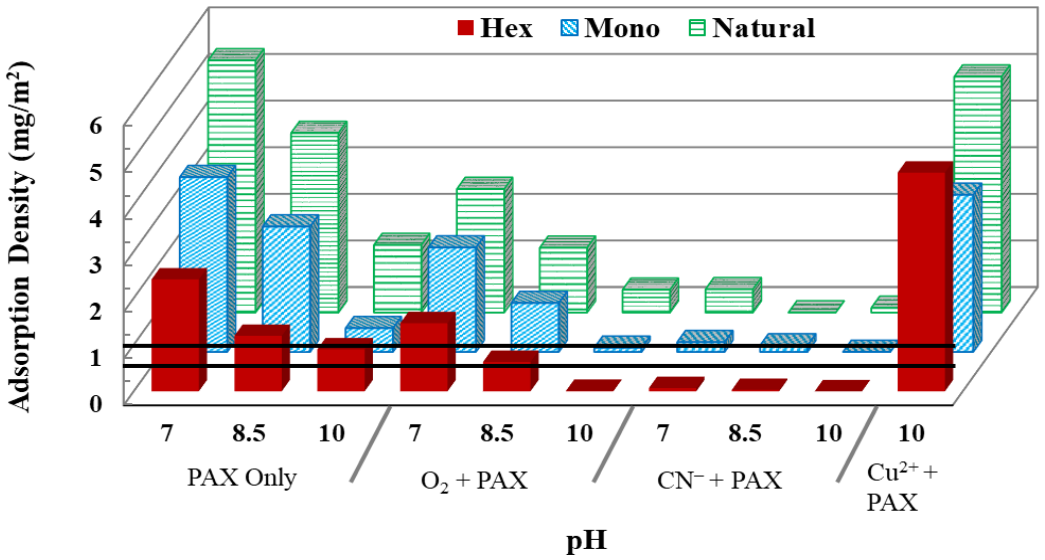

Figure 2.14 *– Potassium n–amyl xanthate (PAX) adsorption density (mg PAX/m^2) on synthetic Hex/Non-magnetic pyrrhotite (Fe_9S_{10} {5C}), synthetic Mono/Magnetic pyrrhotite (Fe_7S_8 {4C}), and Natural Magnetic (Fe_7S_8 {4C}) pyrrhotite at pH 7, 8.5, and 10 under several conditions; (i) as is; (ii) oxygen pre–conditioning; (iii) cyanide pre–conditioning; and (iv) copper pre–conditioning. Lower and upper black lines represent 70% and 100% monolayer surface coverage, respectively, modified from Kolahdoozan (1996)[11].*

2.4 Pyrrhotite Flotation

Pyrrhotite flotation has been extensively studied over the past half century under the premise that all pyrrhotite superstructures behave similarly if not identically during flotation. Recent research suggests there is a measurable difference in the flotation of the different superstructures and requires further study as the mineral is ubiquitously associated with several valuable sulfide minerals (*e.g.* pentlandite, chalcopyrite, galena, and sphalerite) and platinum–group elements (PGEs) [4]. It must be noted that recovery of pyrrhotite into the concentrate is normally undesirable as it has little economic value (iron ores are more convenient iron sources), dilutes the concentrate grade, is a significant contributor of SO_2 emissions at the smelting stage (mitigated *via* capture and treatment in acid plants), and contributes to larger slag volumes that limit valuable metal throughput thereby increasing smelting costs, thus its depression is targeted in most base metal operations [9, 10]. Ore bodies where the pyrrhotite is hosting finely disseminated base metals (typically nickel) or is associated with PGEs (*e.g.* Merensky Reef, South Africa) are special cases where its recovery

is sought [7, 8]. In the following Sections, pyrrhotite flotation is initially discussed under a general context with subsequent focus on superstructure flotation.

2.4.1 Collectorless Flotation

Pyrrhotite, similar to many other sulfide minerals (*e.g.* chalcopyrite), exhibits some degree of natural hydrophobicity, which is the result of mild surface oxidation (see *Mechanisms* Section)[77]. Many surface species have been proposed by several researchers, including elemental sulfur (*Mechanisms* Section, Equation (8)), polysulfides, metal deficient sulfides, and the intermediate surface sulfur oxidation complex $Fe(OH)(S_2)$, essentially all relaying that excess surface sulfur is the responsible species [14, 93]. The latter is commonly noted as one of the likely species responsible for pyrrhotite's collectorless floatability, with its formation given by Equation (16):

$$FeS_{1.13} + H_2O \leftrightarrow Fe(OH)S_2 + S_2^{2-} + H^+ + e^- \quad (2.16)$$

Although some pyrrhotite may be recovered in this fashion, the limited hydrophobicity is not sufficient for collectorless flotation in practice (it is also difficult to control partially oxidized surfaces in industrial operations as well), therefore collectors are used [1]. Pyrrhotite recovery is generally not desired and thus several strategies are employed to prevent collectorless flotation of pyrrhotite, or inadvertent activation.

2.4.2 Flotation with Xanthate Collectors

For copper, nickel, zinc, molybdenum, gold, precious group metals, and even oxidized sulfide minerals, alkyl xanthate collectors are the most important and widely used due to their affinity to base metals [1]. Xanthates (X^-), 'thiol collectors', are negatively charged for pH > 5 and form either metal–xanthate (MX) or dixanthogen (X_2) surface complexes with base metal sulfides *via* chemisorption mechanisms (pyrrhotite initially being physisorption and subsequently chemisorption for dixanthogen formation; *Reagent-Mineral Surface Interactions* Section (2.3.2.3)) [91, 93]. The general formula is given as $[ROCS_2^-]$, where 'R' is the alkyl carbon chain (between 2 and 8) [1]. In plant practice, Na^+ and K^+ salts of isobutyl xanthate (SIBX or PIBX) or *n*–amyl xanthate (SAX or PAX) are commonly used for base metal sulfide recovery. Alkaline pH (> 9.2) is generally employed during flotation

since Cu and Ni sulfides are still sufficiently floatable whereas pyrrhotite is sufficiently depressed in this region: $Fe(OH)_3$ surface formation on pyrrhotite and OH^- ion exchange with surface adsorbed xanthate are promoted. It must be noted, however, that significant pyrrhotite recovery can still occur at these same conditions when xanthate collector is overdosed.

2.4.3 Pyrrhotite Depression

Pyrrhotite normally competes with valuable minerals during flotation, notably pentlandite ($(Ni,Fe)_9S_8$), and reduces final concentrate grade in addition to reducing smelter capacity and having SO_2 emission implications, thus relatively high pyrrhotite rejection (> 80%) is targeted. Two examples of industrial concentrators practising pyrrhotite rejection are Vale's Clarabelle Mill and Glencore's Strathcona Mill, their flow sheets are presented in **Figure 2.15**. Clarabelle Mill 2005 flow sheet consisted of magnetic/non-magnetic circuits effectively isolating the pyrrhotite superstructures (now different) and Glencore's Strathcona Mill 2010 flow sheet treated both pyrrhotite superstructures in the same flotation circuit. Some of the commonly used industrial strategies to selectively depress pyrrhotite (typically at pH > 9.2) are as follows:

(1) **Collector starvation** (staged addition), copper and nickel sulfides are expected to preferentially take up more collector than pyrrhotite and therefore exhibit higher floatabilities at low collector dosages;

(2) **Aeration** (selectively inducing oxidation on pyrrhotite surfaces), high pulp potentials promote ferric hydroxide and/or ferric oxyhydroxides on pyrrhotite effectively rendering it hydrophilic (pyrrhotite tends to be the oxygen sink in the pulp), though care must be taken in order to prevent significant pentlandite oxidation especially in the fine fractions;

(3) **Flotation at low E_h**: this prevents dixanthogen formation on pyrrhotite surfaces and yet can still allow dixanthogen formation onto pentlandite;

(4) **High pH** (by lime) with sulfite (*e.g.* $Na_2S_2O_5$ or Na_2SO_3) have shown promise in effectively depressing pyrrhotite by desorbing collector and decomposing hydrophobic sulfide films (polysulfides); and

(5) **Choice of grinding media** (such as high chrome steel) has shown improvements in Po–Pn selectivity by altering the galvanic interactions in the grind, reducing pyrrhotite activation

Useful references for the stated mechanisms and operational rejection strategies are Rao and Finch (1991)[94], Bozkurt *et al.* (1998)[95], Kelebek (1993)[98], Senior *et al.* (1994)[20], Khan and Kelebek (2004)[99], Miller *et al.* (2005)[8], Lawson *et al.* (2005)[12], Manouchehri (2014)[7], Lawson *et al.* (2014)[16], and Wills and Finch (2016)[1].

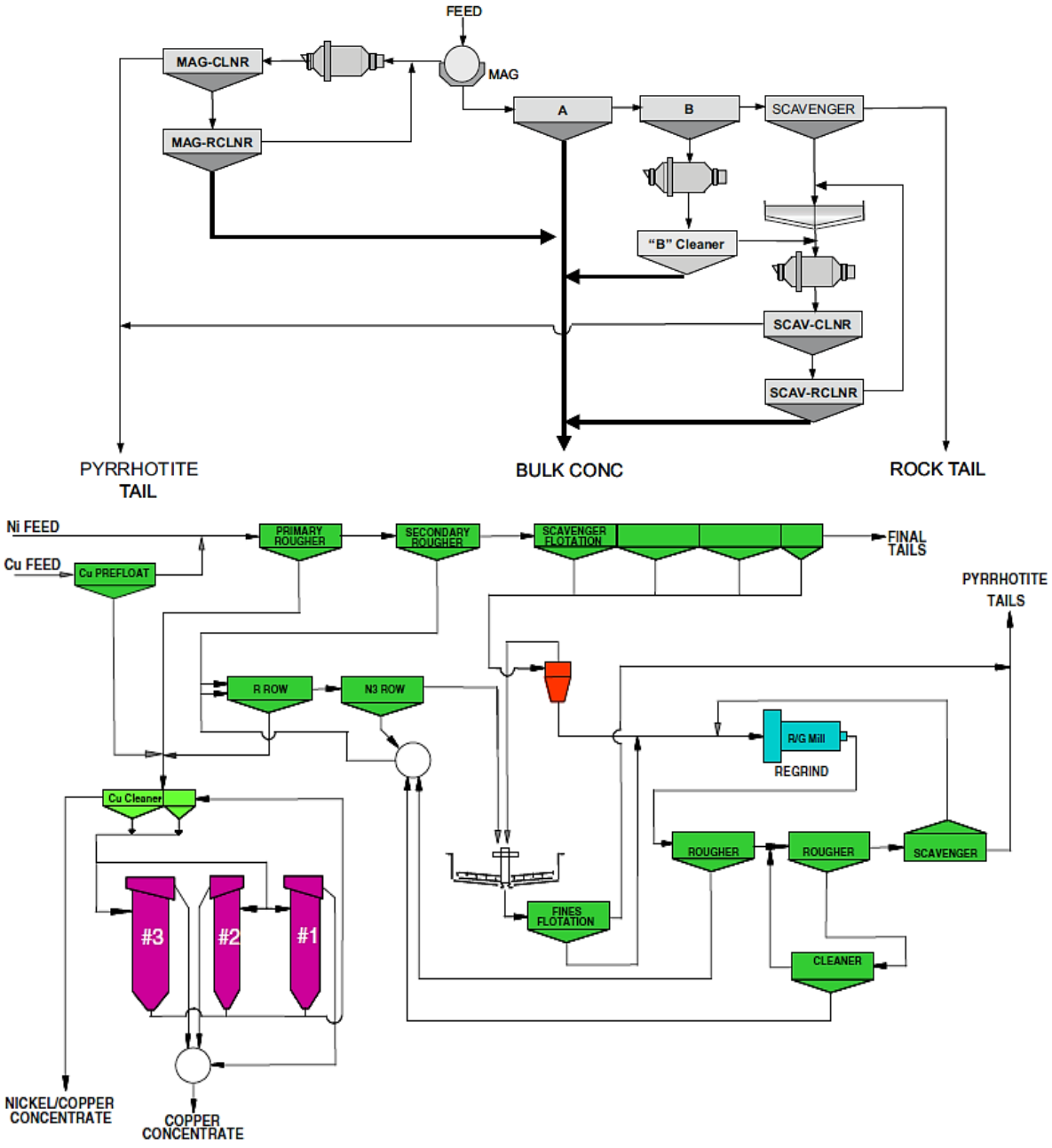

Figure 2.15 *– Pyrrhotite rejection flow sheets: (top) Vale's Clarabelle Mill 2005 flow sheet with magnetic/non-magnetic circuits, reproduced from Lawson et al. (2005)[12]; (bottom) Glencore's Strathcona Mill 2010 flow sheet, reproduced from Peek et al. (2011)[9].*

Aside from these strategies, depressants are added to further decrease pyrrhotite's flotation response, with three common depressants being diethylenetriamine (DETA), triethylenetetramine (TETA), and cyanide (CN^-). The first two are chelating agents that remove adsorbed base metal ions (Cu^{2+} and Ni^{2+} are primary examples) that accidentally activate pyrrhotite by providing favourable surface sites for xanthate adsorption. The copper and nickel xanthate complexes have $-\log(K_{sp})$ values several orders higher than those of iron–xanthates (they are significantly more stable) and thus enhance its floatability. These amine–based chelants preferentially complex with surface adsorbed (thereby solubilizing) Cu^{2+}, Ni^{2+}, Co^{2+}, and even Fe^{2+} ions; interestingly, they are non–selective towards Fe^{3+} ions (which remain as $Fe(OH)_3$ on pyrrhotite surface and promote its depression under oxidizing conditions) [100]. It has been postulated that these chelants are more effective at solubilizing surface adsorbed metals from oxidized ores, where the activation products are metal oxides (*e.g.* NiO and CuO) which have higher solubilities in the presence of DETA [100]. Alongside DETA and TETA, sulfur dioxide (SO_2) has been traditionally used which improves the chelation reactions for several reasons:

(1) Providing a reducing environment that decreases the rest potential of pyrrhotite below which dixanthogen (X_2) cannot form;

(2) Ensuring that dissolved Fe^{3+} is reduced to Fe^{2+} which remains solubilized by the chelants (Fe^{3+} ions are not complexed, under mildly oxidative conditions Fe^{3+} can adsorb onto pyrrhotite and provide sites, *i.e.* $Fe(OH)[S]^+$, for xanthate adsorption by physisorption mechanisms);

(3) Solubilizing surface polysulfides (hydrophobic species) from the pyrrhotite surface that enhance its floatability; and

(4) Aiding the decomposition of surface xanthate complexes into carbon disulfide [1, 64, 101, 102]. In practice, SO_2 (gas) is replaced with reagents providing equivalent sulfite content such as sodium metabisulfite ($Na_2S_2O_5$) and sodium sulfite (Na_2SO_3)

Cyanide apparently preferentially adsorbs onto iron sulfide minerals to form extremely stable iron–cyanide surface complexes which are hydrophilic and also prevent the

chemisorption of xanthate. In addition, they also reduce the mixed potential of the mineral surface, preventing dixanthogen formation on pyrrhotite.[103] Cyanide also forms soluble xanthate complexes reducing xanthate available for sulfide gangue minerals such as pyrrhotite and pyrite [1].

Other occasionally used depressants are polymeric reagents such as modified guar gum, carboxylmethylcellulose (CMC), and organic–based depressants by Huntsman Chemicals ("SD" series – starches/mono amines/lignosulfonates mixtures, and "HQS" series – modified dextrin) [7].

2.4.4 Pyrrhotite Superstructure Flotation Studies (Non–magnetic: Fe_9S_{10} {5C} and Magnetic: Fe_7S_8 {4C})

There is a large volume of data which exists for laboratory flotation studies of pyrrhotite in both single and mixed–mineral systems (both microflotation {1 – 5 g} and bench–scale {1 – 2 kg}); most commonly with nickel and copper sulfides (*e.g.* pentlandite and chalcopyrite, respectively). The majority of the pyrrhotite is found as an intergrown mixture of non-magnetic (5C) and magnetic (4C) superstructures though a significant portion of these studies fail to characterize or simply do not mention the crystallographic structure(s) of the pyrrhotite under investigation. Thus, the results are attributable to a mixed Po system and individual superstructure floatability is difficult to infer. Both academically and industrially this is now becoming a critical piece of information when dealing with pyrrhotite. Historically speaking, the accepted norm appears to be that all pyrrhotites behaved similarly if not the same in the flotation pulp as their Fe/S atomic and weight ratios are nearly identical and their flotation responses did not vary significantly to warrant intricate studies. Since 4C is ferrimagnetic and 5C is antiferromagnetic (sometimes regarded as *paramagnetic*), industrial processing typically incorporated magnetic and non–magnetic circuits where both superstructures were largely isolated, thus their simultaneous flotation received less attention. As some concentrators are seeing more non-magnetic pyrrhotite in their feeds (*e.g.* historically primarily 4C and presently 4C/5C equal mixtures) and the use of magnetic separators in copper and nickel sulfide processing is fading, simultaneous 4C/5C pyrrhotite

flotation is becoming common practice. The flotation responses of the superstructures in these circuits are generally not the same, non-magnetic being more floatable and difficult to depress, whereas magnetic is more easily rejected [16].

Over the past two decades a handful of researchers have focused on the pyrrhotite superstructures with a major emphasis on their floatability under neutral to alkaline pH conditions [11, 13-17]. From some of these studies, lab–scale microflotation conditions and results are summarized in **Table 2.5**. The findings are quite different due to sample–type tested (synthetic versus natural ore pyrrhotites) and the care taken to characterize the superstructures. Overall, the following statements can be derived from these studies:

(1) Synthetic "pure" pyrrhotite superstructures (*i.e.* no contamination of other base metal sulfides) have virtually the same floatability when unexposed to air and in the presence of collector only, flotation differences are seen in neutral/alkaline pH conditions but these are minor. This implies that the superstructures whose surfaces have been preserved have equivalent flotation response;

(2) Pyrrhotite superstructures purified from natural ore specimens exhibit different floatabilities, with non–magnetic pyrrhotite (5C) determined to be much more floatable over magnetic pyrrhotite (4C) especially in alkaline pH (10). This difference was interpreted as the result of the superstructure's reactivity towards oxygen (magnetic pyrrhotite being more reactive; also discussed in this review) and mineral associations with pentlandite and chalcopyrite that enhance pyrrhotite's floatability. Interestingly, magnetic pyrrhotite ores from different locations did not behave the same. It was concluded that pyrrhotite crystallography plays a major role, however other factors such as surface reactivity/oxidation, Fe^{3+} and trace metal content (*e.g.* Ni as solid solution), and mineral associations also influence pyrrhotite flotation and thus must be accounted for when comparing the superstructures.

Table 2.5 *– Summary of Non–mag Po (Fe_9S_{10} {5C}) and Mag Po (Fe_7S_8 {4C}) microflotation studies [11, 13-15].*

	Kolahdoozan (1996)[11]	**Becker (2009)[13]/ Becker *et al.* (2010)[14]**	**He *et al.* (2012)[15]**
Feed Samples	**1 natural Po** **Sudbury** (78% mag Po; upgraded to 92%) **2 synthetic Po** ~95% mag Po ~95% non–mag Po	**5 natural Po** **Sudbury CCN** (75.4% non–mag Po) **Phoenix** (81.8% mag Po) **Sudbury Gertrude** (63.0% mag Po) **Sudbury Gertrude West** (85.2% mag Po) **Nkomati** (83.8% mixed Po)	**2 natural Po** **Mengzi** (>94% mag Po **Mengzi** (>94% non–mag Po)
Superstructure Characterization	AAS/Leco sulfur analyser, XRD	AAS/Leco sulfur analyser, QXRD, Optical Microscopy, Automated SEM	<AAS/Leco> ?, XRD
Microfloat Test Conditions	pH 2 – 12 Uncontrolled ORP (E_h) Collector: PAX Depressants: O_2 (oxidation) & CN^- Activator: $CuSO_4$	pH 7 and 10 Uncontrolled ORP (E_h) Collectors: SNPX and SIBX Depressants: Sty 504 Activator: $CuSO_4$	pH 4 – 12.5 ORP tested 100 – 600mV E_h (controlled using $(NH_4)_2S_2O_8$ and $Na_2S_2O_4$) Collectors: SNBX, sodium diethyl dithiocarbamate and sodium butyl dithiophosphate Activator: $CuSO_4$
Results/ Conclusions	- Natural ore floated best (likely due to association with pentlandite and chalcopyrite) - Synthetic mag and non–mag Po flotation was similar for all pH conditions - Neutral to moderately alkaline pH (7 – 8.5), mag Po floated slightly better - Strongly alkaline pH (10), non–mag Po floated slightly better - $CuSO_4$ activation increased flotation of all samples, non–mag Po recovery was ~5% higher than mag Po	- Non–mag Po (Sudbury CCN) was least reactive towards oxidation and exhibited the highest floatability (higher flotation at pH 7 than pH 10) - Mag Po flotation was dependent on the sample (result of different reactivity towards oxidation), all mag Po sample flotation recovery was lower than non–mag Po (pH 7 higher than pH 10) - Flotation results cannot be entirely attributed to Po–type alone, rather it is a combination of crystallography, reactivity to oxygen, mineral chemistry (Fe^{3+} and Ni^{2+} content), and mineral associations (*e.g.* pentlandite–pyrrhotite binary particles)	- Mag and non–mag Po exhibited different flotation responses under all pH conditions - Mag Po had higher recovery under all conditions with all 3 collectors - Recoveries were highest for both mag and non–mag Po with sodium butyl dithiophosphate than SNBX and sodium diethyl dithiocarbamate - $CuSO_4$ activated both mag and non–mag Po (non–mag activation was variable based on collector used, best was dithiophosphate) - At pH 5, optimal ORP (E_h) for flotation was determined to be 125–580 mV for mag Po (max at 350 mV) and 200–550 mV for non–mag Po (max at 300 mV)

Two studies (Kolahdoozan (1996)[11] and Becker (2009)[13]) are discussed further due to their in–depth analysis of pyrrhotite superstructure flotation. Kolahdoozan (1996)[11], as

mentioned previously, studied two synthetic non-magnetic and magnetic superstructures (made by the "dry sulfide" synthesis method) and one magnetic pyrrhotite purified from a natural ore specimen. Some of the relevant data is reproduced in **Figure 2.16**. Both synthetic superstructures follow the traditional trend; floating extremely well below pH 7 and exhibiting a steep decline under alkaline conditions due to accelerated oxidation and collector–hydroxyl ion exchange at high pH. Synthetic superstructure flotation was virtually the same under most pH conditions (with some difference at pH 10 and higher), the effects of depressants and activator can be observed in **Figure 2.16**(b). Copper activation demonstrates the effect of pulp ions (others being Ni^{2+}, Co^{2+} and Fe^{2+}), whereby at pH 10 the superstructures are expected to be heavily depressed, but will float (results comparable to pH 7). From a kinetic standpoint, magnetic pyrrhotite is expected to oxidize faster as discussed previously and therefore non-magnetic pyrrhotite may exhibit higher floatability as its surfaces are less passivated but it may also be more amenable to surface activation for the same reason, this may aid in explaining the difference in their flotation responses in an industrial setting.

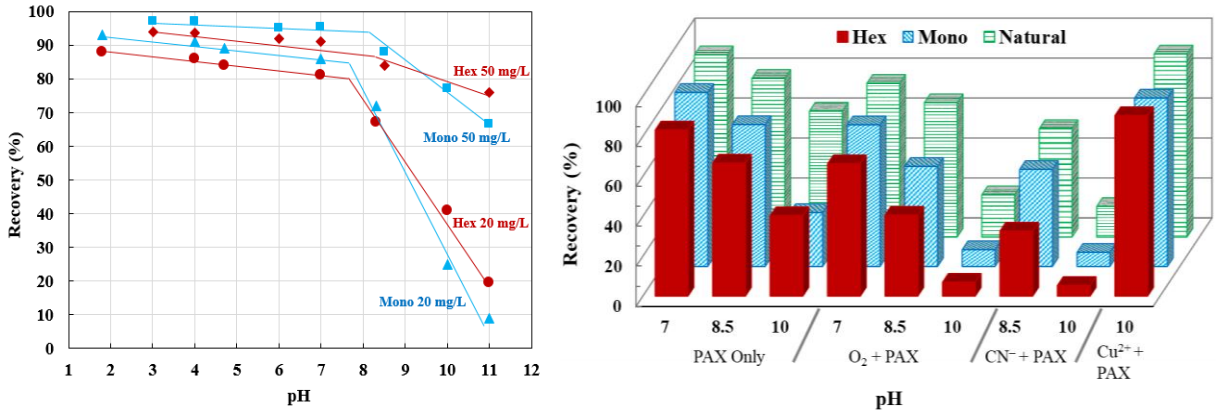

Figure 2.16 *– (a) Microflotation results of synthetic pyrrhotite superstructures: non–mag/hex Po (Fe_9S_{10} {5C}) and mag/mono Po (Fe_7S_8 {4C}) with PAX collector (mg/L) over 2 – 11 pH range; (b) microflotation results of synthetic (non–mag/hex and mag/mono Po) and natural (mag/mono) Po at pH 7, 8.5, and 10 under different conditions; (i) with PAX collector only; (ii) oxygen pre–conditioning; (iii) cyanide pre–conditioning; (iv) copper pre–conditioning, modified from Kolahdoozan (1996)*[11].

Becker (2009)[13] studied non-magnetic (5C) and magnetic (4C) superstructure samples purified from different ore specimens (five in total). Many tests were conducted of which

oxygen uptake (reactivity towards oxidation) and microflotation are discussed in this Section, microflotation results are reproduced in **Figure 2.17** [13]. Observing the flotation responses, it is immediately apparent that flotation at pH 7 is much higher than that in the alkaline pH 10 (with differing results for each superstructure); similar to the findings of Kolahdoozan (1996)[11]. The results indicate that non-magnetic pyrrhotite is more floatable at alkaline pH whereas the magnetic and mixed (non-magnetic/magnetic) samples were likely oxidized/passivated. The anomalous samples were Phoenix magnetic and Nkomati mixed pyrrhotite for which the strange flotation response can be explained by mineral locking. The former having 16.9 wt% pentlandite and 0.22 wt% chalcopyrite and the latter having 6.61 wt% pentlandite and 2.92 wt% chalcopyrite (as well as locking to the floatable non–magnetic pyrrhotite), both of which have significantly higher floatabilities than pyrrhotite. Although there are notable differences in the ores, the general trend appears to be that the non–magnetic variety is more floatable. The commonly cited explanation is that non–magnetic pyrrhotite is less reactive towards oxidation thereby preserving its surface and allowing collector attachment, although other factors can play a major role as well (see **Table 2.5**).

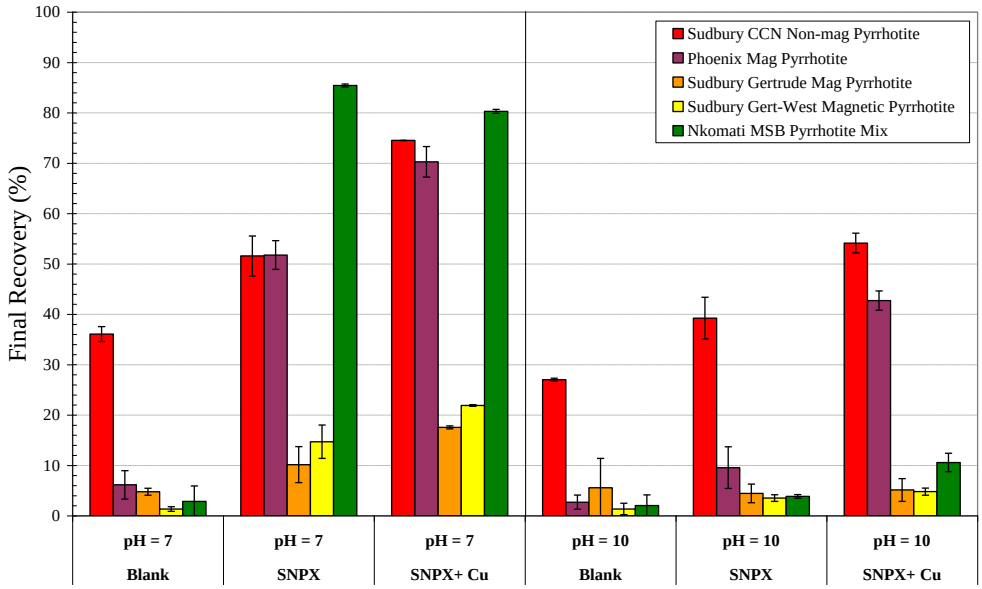

Figure 2.17 *– Microflotation results of different pyrrhotite ore samples, non–mag Po (Fe_9S_{10} {5C}) and mag Po (Fe_7S_8 {4C}), at various pH and reagent conditions, reproduced from Becker (2009)[13].*

Aside from microflotation, bench–scale batch (> 1 kg) and pilot plant studies where the researchers have characterized/balanced the superstructures are scarce in the literature. These tests are desired as they would be more representative of plant practices (*e.g.* freshly ground ore followed by immediate flotation) and provide valuable information on the floatability of the superstructures at higher pulp densities and with a froth phase (examples include grinding media effects, size–by–size floatability, mineral interactions (*e.g.* galvanic), mineral associations and their impact on the superstructures, *etc.*). One notable example is from the study of Wercholaz (2009)[104] on different pyrrhotite ores presented by Lawson *et al.* (2014)[16], as detailed in **Figure 2.18** where the data is shown as pentlandite selectivity against non-magnetic (*hex Po*), magnetic (*mono Po*), and mixed (non-magnetic/magnetic) pyrrhotite superstructures. Although many variables must be considered, the data complements Becker (2009)[13], supporting the pyrrhotite floatability trend generally observed for Cu–Ni ores: non-magnetic > non-magnetic/magnetic (mixed Po) > magnetic pyrrhotite. Other datasets where the non–magnetic and magnetic streams have been studied separately in which the two superstructures are largely isolated also provide information as to their independent flotation responses. The results indicate similar superstructure behaviour to the microflotation studies in that non–magnetic pyrrhotite is more floatable. The reader is referred to studies by Lawson *et al.* (2005)[12], He *et al.* (2008)[105] and Manouchehri (2014)[7].

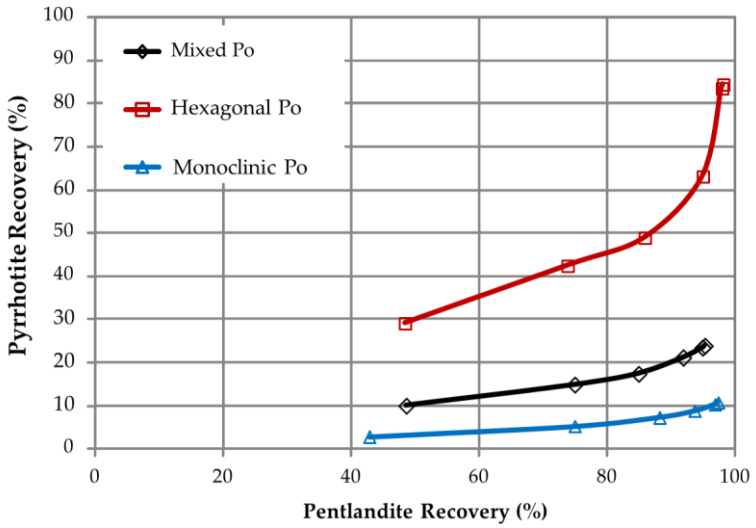

Figure 2.18 *– Pentlandite–pyrrhotite selectivity for different ores containing different superstructure types (non–mag/hexagonal Po (Fe_9S_{10} {5C}) and mag/monoclinic Po (Fe_7S_8 {4C}); reproduced from Wercholaz (2009)[104].*

As the flotation of both non-magnetic and magnetic superstructures in the same flotation pulp is becoming common practice over the use of magnetic separators in Cu–Ni sulfide mineral processing (which gave magnetic and non–magnetic circuits), concentrators are actively tracking the superstructure types in their feeds and final concentrates and such data is now making its way into the literature. Recently, Lawson *et al.* (2014)[16] presented size–by–size non-magnetic (*hexagonal*) and magnetic (*monoclinic*) pyrrhotite flotation recoveries both in conventional cells and columns in Cu–Ni concentrators (**Figure 2.19**(a)) where non-magnetic was primarily recovered in the intermediate size fractions and magnetic was mainly recovered in the finest fractions.

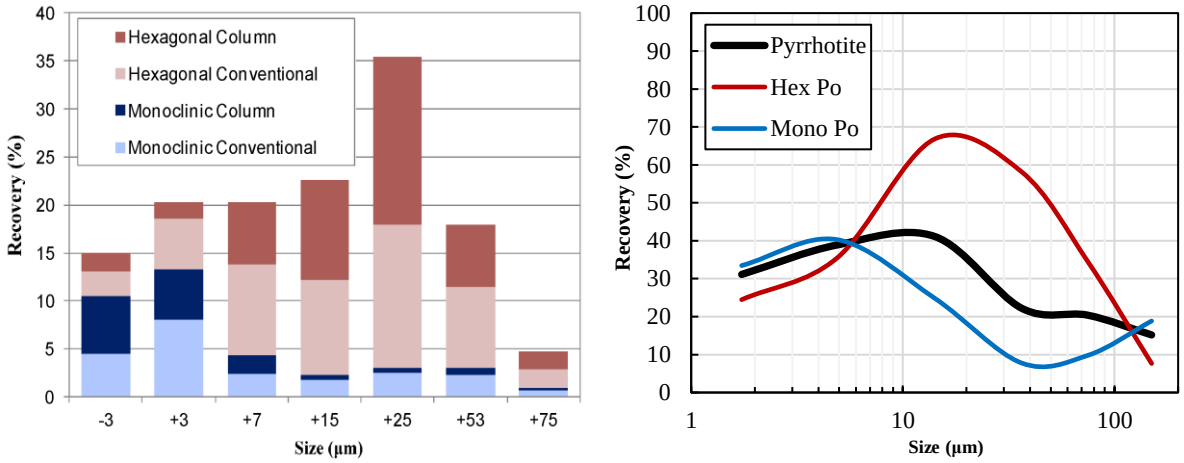

Figure 2.19 *– Size–by–size pyrrhotite superstructure: (a) recovery in conventional cells and columns (same trend for 2 Cu–Ni operations), reproduced from Lawson et al. (2014)[16]; (b) recovery to final concentrate, typical relationship observed across many worldwide concentrators ("pyrrhotite" is the combined weighted mono and hex Po recoveries), used with permission from Lori Kormos (Principal Geoscientist, XPS – Expert Process Solutions).*

The magnetic pyrrhotite recovery was largely attributed to flotation over entrainment as froth washing was implemented for entrainment control. Overall, in the simultaneous flotation of non-magnetic and magnetic pyrrhotite superstructures in Cu–Ni operations, magnetic pyrrhotite is easily rejected whereas non-magnetic is much more difficult. The preferential size–by–size superstructure flotation is also peculiar. Non-magnetic pyrrhotite is more floatable over magnetic pyrrhotite in the intermediate sizes likely due to a less passivated surface (which also allows it to become more activated by Cu^{2+} and Ni^{2+}ions) and has the

typical bell–shaped size–by–size recovery. However, the flotation of the fine magnetic pyrrhotite is not entirely understood at the moment, and a definitive explanation has yet to be presented. One theory is that fine pyrrhotite particles, having significantly larger surface areas in comparison to its intermediate sizes, requires more oxygen to reach the same degree of oxidation/passivation, presenting a kinetic window that allows it to attach to collectors and also become activated by pulp ions (*i.e.* Cu^{2+} and Ni^{2+}). Another theory is a surface chemical phenomenon arising from the unique surface chemistry of magnetic over non-magnetic pyrrhotite (a result of their different Fe^{2+}/Fe^{3+} ratios) that may permit different mineral surface/reagent interactions making fine magnetic pyrrhotite sufficiently floatable. Lastly, magnetic aggregation of fine magnetic pyrrhotite particles (< 10 μm) has also been postulated where these aggregates float as intermediate size classes (rather than fine particles) thereby becoming more floatable due to improved bubble–particle attachment. **Figure 2.19**(b), complementing **Figure 2.19**(a), displays the typical size–by–size non-magnetic (*hex*) and magnetic (*mono*) pyrrhotite recoveries to final concentrate seen in several Cu–Ni concentrators worldwide, Cu–Zn, and even in Cu concentrators where the superstructures are present. The interesting finding from this information is that the size–by–size superstructure recovery relationship is not an artefact of a specific plant's operating practice but can be attributed to the superstructures themselves (crystallography) as the relationship holds across several concentrators processing pyrrhotite.

In summary, the studies in the literature highlight the fact that there are measurable/quantifiable differences in the flotation of the two superstructures (non-magnetic and magnetic pyrrhotite). The synthetic mineral studies imply that the superstructures have similar floatabilities and that cations in the flotation pulp such as Cu^{2+} (Ni^{2+} is presumed to have a similar effect) enhance the flotation of both superstructures at alkaline pH, although non-magnetic pyrrhotite is likely more activated as it exhibited higher recoveries after activation (supported by PAX adsorption studies as well). Tests conducted on purified superstructures from ore samples suggest that the non-magnetic variety is much more floatable, this is generally credited to the reactivity of the superstructures towards oxidation. The magnetic variety is very reactive (result of crystallography) and is quickly passivated by

ferric hydroxides whereas non-magnetic pyrrhotite is kinetically less reactive and therefore permits more collector adsorption and at the same time able to become more surface activated by pulp ions. Analysis of superstructure recovery in worldwide plant operations indicates that non-magnetic pyrrhotite is much more difficult to depress whereas magnetic is easily rejected. In addition, a recovery–by–size relationship is seen where non-magnetic is largely recovered in the intermediate sizes (magnetic pyrrhotite significantly depressed likely due to oxidation) and that magnetic pyrrhotite is primarily recovered in the finest sizes, a few theories were discussed for this peculiar trend.

The reviewed studies shed light on the different behaviour of the superstructures in the flotation pulp and have certainly improved the understanding of the mechanisms at work. There are, however, areas that require further study such as the role of other minerals on superstructure reactivity and recovery in the pulp (*e.g.* pentlandite, chalcopyrite, and pyrite), preferential magnetic recovery in the fine size fractions (yet to be reproduced at the lab-scale) and the effects of non-magnetic pyrrhotite flotation on magnetic pyrrhotite (galvanic effects of the superstructures on one another). Thus far, a large portion of the superstructure studies have been on single mineral systems (synthetic and purified superstructures from ores) and relatively small–scale (0.25 – 5 g samples), thus other effects could not be tested, therefore bench–scale batch (≥ 1 kg) tests are proposed especially to study the recovery–by–size relationship in a controlled lab setting.

This literature review covered several important topics, these include the complicated superstructure nomenclature, characterization methods, aqueous stability, surface charges and superstructure–reagent interactions, and flotation. Due to the breadth of information presented, it was thought that a summary of the major points would be valuable to the reader. The key points are therefore presented in **Table 2.6**.

Table 2.6 *– Key points summarized from the various sections covered in the literature review.*

Pyrrhotite ($Fe_{(1-x)}S$, $0 < x \leq 0.125$) Superstructure Nomenclature and Characterization Methods					
Pyrrhotite (Po) Superstructure	**Type**	**Ideal Composition**	**% Vacancy**	**Charge Neutral Formula**	**Characterization Methods**
Non-magnetic (antiferromagnetic)	6C	$Fe_{11}S_{12}$	8.3	$Fe_2^{3+}Fe_9^{2+}S_{12}^{2-}$	Quantitative **Total Po**: Chemical and QEMSCAN/MLA assays **Superstructure Ratio**: XRD (peak intensity ratio or Rietveld)
	11C	$Fe_{10}S_{11}$	9.1	$Fe_2^{3+}Fe_8^{2+}S_{11}^{2-}$	
	5C	Fe_9S_{10}	10.0	$Fe_2^{3+}Fe_7^{2+}S_{10}^{2-}$	
Magnetic (ferrimagnetic)	4C	Fe_7S_8	12.5	$Fe_2^{3+}Fe_5^{2+}S_8^{2-}$	Qualitative **Microscopy**: Optical (acid etching + magnetic colloid) or SEM (EDS, BSE, EBSD)

Superstructure Aqueous Stability and Flotation			
Condition	**Surface Potential/Charge**	**Reagent Interactions**	**Flotation**
Fresh (minimal contact with oxygen; ideal system)	Same for non-magnetic and magnetic pyrrhotite (pH_{IEP} ~ 3.5)	Data suggests different superstructure–reagent interactions; 4C uptakes more xanthate under most conditions (possibly due to more $Fe(OH)[S]^+$ sites), 5C is better activated by Cu^{2+}. This suggests that the unique surface chemistries resulting from their different Fe^{2+}/Fe^{3+} ratios perhaps are causing the differences. Additionally, though higher surface densities of collector are observed on 4C, this does not translate to flotation very well as both fresh 5C and 4C have similar floatabilities. Both minerals uptake significant amounts of collector and the differences may not be significant for flotation (requires further research).	Freshly ground 5C and 4C superstructures (mildly oxidative conditions) are expected to have similar flotation responses as shown: 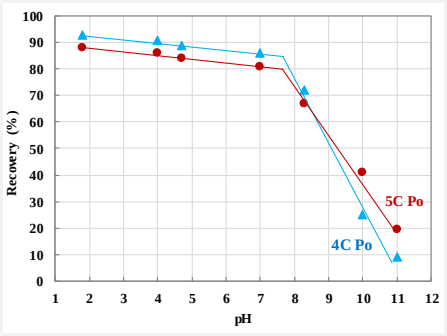
In the presence of oxygen (real systems)	Non-magnetic Pyrrhotite: $pH_{IEP} > 3.5$ Magnetic Pyrrhotite: $pH_{IEP} >> 3.5$	In a high redox environment (*i.e.* flotation pulp), 4C is expected to oxidize at a much faster rate than 5C. Initially, 4C may uptake more collector (due to an increase in $Fe(OH)[S]^+$ sites that are favourable for xanthate attachment). However, due to its reactive nature 4C surfaces will quickly passivate ($Fe(OH)_3$ surface precipitation) and render itself hydrophilic, having poor response towards collector and pulp ions. 5C will also reach a similar state, however much more slowly and therefore a kinetic window is created where 5C surfaces are kinetically stable and amenable to collector attachment and surface activation by Cu^{2+} and Ni^{2+} ions.	In "real systems" (mild to strongly oxidative conditions and in the presence pulp ions such as Cu^{2+} and Ni^{2+}), 5C and 4C have very different flotation responses; 5C is much more floatable (partially oxidized) over 4C (heavily oxidized). In plant operations 5C is difficult to depress whereas 4C is easily rejected (difference attributed to their degree of surface oxidation that results from their distinct crystal symmetries). A recovery-by-size relationship for the superstructures is also observed in many worldwide operations: 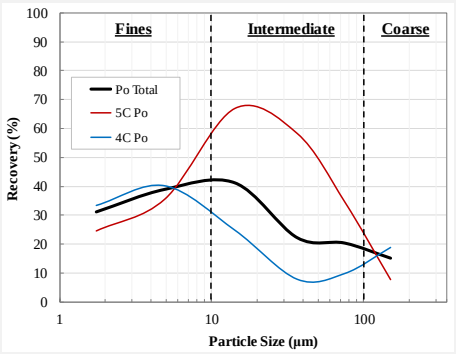

Chapter 3
Methodology

Seven ore samples were used during the course of this research, six were sourced from the Sudbury Basin (Ontario, Canada) and one from Voisey's Bay (Newfoundland and Labrador, Canada). Since certain ore samples were only used for particular studies, this Chapter is organized to cover the procedural information for each study after which a list of ore characterization techniques and description of instruments is provided. It must be noted that due to significant variability in the ores, it was deemed more appropriate to present the individual ore information (size-by-size mineralogy and superstructure ratios) in the relevant Chapters (4 – 6).

3.1 Experimental Procedures for Single Mineral and Batch Flotation Studies

3.1.1 Single Mineral Studies

The single mineral studies ((1) mineral surface potentials; (2) potassium *n*-amyl xanthate (PAX) adsorption; and (3) microflotation) were conducted on purified magnetic and non-magnetic superstructure powders. This section describes the mineral purification, zeta potential, PAX adsorption, and microflotation procedures employed.

3.1.1.1 Magnetic Pyrrhotite (Fe_7S_8) Purification Procedure

A pyrrhotite ore specimen was purchased from Excalibur Mineral Corp. containing an unknown mixture of non–magnetic and magnetic pyrrhotite; originally sourced from a Cu–Ni sulfide deposit (Sudbury Basin, Ontario, Canada). The specimen was crushed (jaw crusher), briefly pulverized, and wet sieved with 38 μm screen. The oversize (+38 μm) was air dried (12 hrs) and sieved into 4 fractions: +106 μm, –106/+75 μm, –75/+53 μm, and –53/+38 μm, while the undersize was kept as is. All size fractions were subjected to magnetic separation by a hand magnet (1000 Gauss) with 4 stages of purification (Note: –38 μm fraction was purified wet). The magnetic fractions were retained as "magnetic pyrrhotite" and non–magnetic fractions were discarded. All purified material was then vacuum filtered during which it was washed with reagent grade acetone 4 times to replace any moisture and subsequently dried in a vacuum oven (80^{o}C) for 12 hrs. A representative sample of each size fraction was taken for characterization (composition and superstructure quantification). The final material was then stored in a freezer until it was used for experimental testing.

Note: the +106 μm fraction was kept in reserve, –106/+38 μm range was retained for microflotation tests, and –38 μm fraction was used for zeta potential and PAX adsorption tests. The –38 μm fraction was also analyzed for its average surface area (g/m^2) by the BET method in order to calculate PAX adsorption density (mg PAX/m^2) on mineral surfaces (adsorption tests). The average magnetic pyrrhotite (–38 μm) BET surface area was 1.86 m^2/g.

3.1.1.2 Non–magnetic Pyrrhotite (Fe_9S_{10}) Purification Procedure

Non–magnetic pyrrhotite required much more processing as compared to magnetic pyrrhotite. The ore was sourced from Voisey's Bay (Newfoundland and Labrador, Canada) since it was known to contain pyrrhotite primarily in the non–magnetic form. The ore was crushed to 100% passing 4 Mesh (4.76 mm) and riffled to 1 kg representative samples. Grind calibration was performed for P80 ≈ 75 μm in a laboratory rod mill (100% mild steel rods). Flotation was conducted in a 2 L Denver Cell (pH 9.5 (using lime), 200 g/t potassium *n*–amyl xanthate (PAX) collector, and methyl isobutyl carbinol (MIBC) frother), requiring 15 minutes of aeration conditioning prior to collector and frother addition. The objective was to

remove virtually all pentlandite and chalcopyrite with some non–magnetic pyrrhotite by making use of the minerals' different flotation kinetics, thus the ore was floated until the froth resembled pyrrhotite. The final concentrate was discarded while the flotation tails were further processed. The tails were wet sieved (38 μm screen), the oversize (+38 μm) was air dried for 12 hrs and sieved into 4 fractions: +106 μm, –106/+75 μm, –75/+53 μm, and –53/+38 μm while the under size (–38 μm) was kept wet. All size fractions were subjected to magnetic separation by a hand magnet (1000 Gauss) with 4 stages of purification to remove any magnetite and magnetic pyrrhotite. The magnetic fraction was discarded while the non–magnetic fraction was retained for final treatment with Frantz Isodynamic Separator to isolate non–magnetic pyrrhotite from non–sulfide gangue minerals (*e.g.* quartz). This apparatus allows for the separation of "non-magnetic" pyrrhotite (which is *antiferromagnetic /paramagnetic*) from "non-magnetic" quartz (which is *diamagnetic*) under a high applied magnetic field strength. The purified non–magnetic pyrrhotite was then conditioned with acetone and vacuum filtered (4 cycles) to dissolve adsorbed PAX and replace any moisture, after which it was dried in a vacuum oven (80^{o}C) for 12 hrs. A representative sample of each size fraction was taken for characterization (composition and superstructure quantification). The final material was then stored in a freezer until it was used for experimental testing.

Note: the +106 μm fraction was kept in reserve, –106/+38 μm range was retained for microflotation tests, and –38 μm fraction was used for zeta potential and PAX adsorption tests. The –38 μm fraction was also analyzed for its average surface area (g/m^2) by the BET method in order to calculate PAX adsorption density (mg PAX/m^2) on mineral surfaces (adsorption tests). The average non-magnetic pyrrhotite (–38 μm) BET surface area was 6.63 m^2/g.

3.1.1.3 Zeta Potential Procedure

Superstructure zeta potentials were determined using the electrophoretic method at room temperature. As pyrrhotite is very prone to oxidation especially in the presence of air, it was decided that the use of freshly ground powders (by mortar and pestle) for every analysis would be appropriate to mitigate oxidation effects. Additionally, the background electrolyte solution (0.001 mol/L KCl) was purged with nitrogen gas for 30 minutes before use and

continuously purged during pH adjustment (2 – 11; adjusted with either reagent grade KOH or HNO_3) to ensure low dissolved oxygen content (which could also partially oxidize the pyrrhotite powders before analysis).

Approximately 0.1 g of –38 μm powder (either non–magnetic or magnetic pyrrhotite) was placed in a mortar with 5 mL of nitrogenated electrolyte solution (pH–adjusted) and ground for 10 seconds. A few drops of the ground slurry were then transferred to a glass vial containing pH–adjusted electrolyte solution and subsequently placed in a sonication bath for 10 seconds. Finally, an aliquot of the sonicated solution was transferred to a glass cuvette and analyzed for zeta potential. A minimum of 3 replicates were taken at each pH.

After baseline testing (mineral alone), a series of tests were also conducted with reagents (0.0001 mol/L); $NiSO_4$, $CuSO_4$, and PAX to assess their impact on superstructure zeta potential. The original procedure was changed slightly to accommodate a reagent conditioning step (2 minutes) just before analysis.

3.1.1.4 PAX Adsorption Procedure

PAX Purification

Purification of commercial grade PAX (80 – 90% purity) was necessary as it commonly contains oxidation products (dixanthogen, polysulfides, *etc.*) that are formed from side reactions. For fundamental lab-scale studies it was necessary to have higher purity PAX (> 99%), thus the commercial grade PAX was further purified using a slightly modified procedure proposed by Rao (1971)[106]. Commercial grade PAX powder (100 g) was dissolved in a 1 L stirred acetone solution (40 ^oC), the temperature was maintained during dissolution (10 mins). An undissolved mass remained in the solution after 10 mins which would slowly settle to the bottom of the reactor when solution agitation was stopped. This impurity was removed using a filter funnel. The filtrate (containing dissolved PAX) was allowed to cool to room temperature after which ~ 2 L petroleum ether solution was added, effectively precipitating PAX which was then filtered. The PAX solid was then subjected to above purification procedure 3 more times. After purification, the PAX powder was stored

in petroleum ether to prevent oxidation to dixanthogen. The purity was verified with UV/Vis Spectroscopy at the characteristic PAX peak of 301 nm using calibration standards. During the initial scan, other xanthate species or degradation products were not observed.

Adsorption Tests

Adsorption tests were conducted for the purpose of developing PAX adsorption isotherms for the superstructures at pH 7, 8.5, and 10. This was accomplished in two stages. The first stage was where a set of tests ("time series") were completed to determine the minimum time required to reach adsorption equilibrium at the different pH conditions. Prior to each test, 0.25 g of mineral powder (–38 μm) was treated with an ultrasonicator probe for 20 seconds in 60 mL of deionized water. This treatment removed any surface oxidation products (*i.e.* metal hydroxides and oxides) resulting from the mineral purification step, following the treatment the solution was slowly decanted. The remaining powder was then placed into a 125 mL conical beaker containing 100 mL of 100 mg/L PAX solution at room temperature that was pre–adjusted to a specific pH (7, 8.5, and 10) by reagent grade potassium hydroxide (KOH).

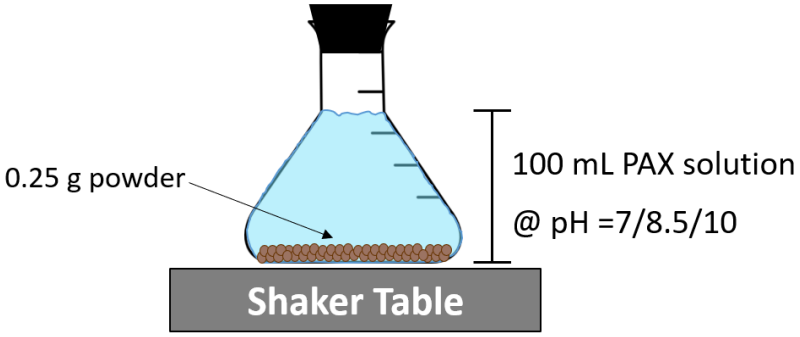

Figure 3.1 *- Adsorption test set-up.*

Immediately after the powder was placed in the PAX solution, a rubber stopper capped the beaker which was then placed on a shaking table (**Figure 3.1**), the table was turned on (300 revolutions/min) and the timer started. During the test, the pH was maintained with KOH or nitric acid (HNO_3) and approximately 5 mL aliquots were taken over time. These aliquots were centrifuged after which the supernatant was analyzed by UV/Vis Spectroscopy for PAX content. The progressive loss of PAX from solution over time was taken as PAX adsorbed

onto the mineral surface. Example calculations PAX adsorption density and equivalent monolayer coverage are presented in Appendix A (Note: PAX molecule cross–sectional area was taken to be 25 $Å^2$ [82]).

From the "time series" tests the equilibrium time was determined. The next set of tests (second stage) were conducted to develop the adsorption isotherms by determining the final equilibrium PAX concentration for different initial PAX concentrations (2, 5, 10, 15, 20, 25, 30, 40, 50, and 100 mg/L). The PAX adsorption isotherms for both superstructures were plotted as adsorption density (mg PAX/m^2) vs. equilibrium PAX concentration (mg/L) at pH 7, 8.5, and 10.

3.1.1.5 Microflotation Procedure

Microflotation tests were conducted for 1 min on 1 g samples of purified pyrrhotite superstructures (–106/+38 μm; P80 ≈ 75 μm) using a modified Hallimond tube (180 mL) and nitrogen as gas source over a pH range of 7 – 11. Prior to flotation, 1.1 g purified powder was treated with an ultrasonicator probe for 1 min in 60 mL deionized water (this time was determined to be optimal) to remove surface oxidation films. The slurry was then vacuum filtered (typically losing 0.1 g in the filter paper) after which the solids were conditioned in 40 mL of 2.5 mg/L PAX collector solution (equivalent to 100 g/ton) for 5 mins during which the solution pH was maintained. Immediately after conditioning, the slurry was transferred to the modified Hallimond tube after which deionized water (pre-adjusted pH) was added to the 180 mL volume mark. The slurry was then kept in suspension either by mechanical agitation (for magnetic pyrrhotite) or with a magnetic stir bar (for non-magnetic pyrrhotite). Nitrogen gas was introduced at 35 mL/min to the cell and the flotation timer was started when the first bubble made contact with the air-water interface. The resulting powder mass reporting to the launder after 1 min was taken as final concentrate. Microflotation tests were conducted in triplicates.

3.1.2 Batch Flotation Studies (Cu-Ni Sulfide Ores)

3.1.2.1 Four Cu-Ni Sulfide Ores with Different Non-magnetic/Magnetic Pyrrhotite Ratios (5/95%, 30/70%, 50/50%, and 95/5%)

Vale Base Metals generously provided four Cu–Ni sulfide ores (valuable sulfides: chalcopyrite {$CuFeS_2$} and pentlandite {$(Ni,Fe)_9S_8$}, major sulfide gangue: pyrrhotite) which were sourced from the Sudbury Basin (Ontario, Canada). They were unique in that they contained different feed non–magnetic (Fe_9S_{10})/magnetic (Fe_7S_8) pyrrhotite ratios (5/95%, 30/70%, 50/50%, and 95/5%). The ores were received crushed (100% passing 6 Mesh; 3.36 mm), blended, and split into 1 kg representative samples after which they were stored in a freezer. Ore elemental composition (Cu, Ni, S) was determined by ICP–OES. Sulfide mineral compositions (chalcopyrite {Cp}, pentlandite {Pn}, and pyrrhotite {Po}) were calculated using their ideal stoichiometric formulas (non-sulfide gangue {Ga} was calculated by subtraction). The formulas also accounted for 0.8 wt% Ni deportment into pyrrhotite as solid solution, which is typical of Sudbury ores, and assumed that no pyrite was present (if present, it was grouped with pyrrhotite) [12]:

$$\%Cp = 2.888*(\%Cu) \quad (3.1)$$

$$\%Pn = 0.061*(\%Cu) + 2.981*(\%Ni) - 0.060*(\%S) \quad (3.2)$$

$$\%Po = -2.639*(\%Cu) - 2.540*(\%Ni) + 2.615*(\%S) \quad (3.3)$$

$$\%Ga = 100\% - \%Cp - \%Pn - \%Po \quad (3.4)$$

Total pyrrhotite content was calculated from elemental assays (Equation (3.3)) and non–magnetic/magnetic pyrrhotite ratios were determined by XRD. Ore head assays are presented in **Table 3.1**:

Table 3.1 *– Elemental and mineral compositions (wt %) for Ores A – D.*

Ore Description		Elements (wt%)			Minerals (wt%)						
		Cu	Ni	S	Cp	Pn	Po	% Non-mag Po	% Mag Po	Ga	Po/Pn
Ore A	5% Non-Mag Po	0.46	0.76	7.53	1.3	1.8	16.5	**5**	**95**	80.3	9.0
Ore B	30% Non-mag Po	1.86	3.43	15.05	5.4	9.4	25.7	**30**	**70**	59.5	2.7
Ore C	50% Non-mag Po	3.18	2.67	12.94	9.2	7.4	18.7	**50**	**50**	64.8	2.5
Ore D	95% Non-mag Po	3.04	2.57	15.97	8.8	6.9	27.2	**95**	**5**	57.1	4.0

Grind calibration (100% mild steel rod media) was performed on the ores (as received feed: 100% passing 6 Mesh; 3.36 mm) at 63% solids to yield P80 ≈ 75 μm. The ground feed was wet–screened at 38 μm; +38 μm material was oven dried (37 ^{o}C) and subsequently dry sieved and the –38 μm material was cyclosized (CS) into 7 fractions after which it was oven dried (37 ^{o}C) as well. Overall, 12 size fractions were obtained (+150, –150/+106, –106/+75, –75/+53, –53/+38, –38/+25 (CS1), –25/+18 (CS2), –18/+15 (CS3), –15/+12 (CS4), –12/+8 (CS5), –8/+3 (CS6), and –3 μm (CS7)) and assayed (ICP-OES) to confirm adequate Cu/Ni distribution. All size fractions were analyzed by XRD to determine whether the superstructure ratio was the same as the head sample at every size class. As expected, the ratios were near-identical and no preferential grind was observed. Lastly, mineralogical analysis on polished thin sections of the 12 size fractions was accomplished by MLA. Relevant XRD and MLA data is presented in Chapter 5 (Section 5.3).

The ores (1 kg; ground to P80 ≈ 75 μm) were floated at pH 9.5 (lime system) in a 2 L Denver cell equipped with an automated froth paddle (PAX collector and MIBC frother); 5 concentrates were collected over a cumulative float time of 7 mins. For the preliminary studies, flotation was conducted with 180 g/t PAX collector and added before concentrate #1 for all four ores; the float procedure is presented in **Table 3.2**. As well, all concentrates and tails were subsequently wet screened (38 μm) to obtain +38 μm/–38 μm products which were assayed and analyzed by XRD to compare coarse and fine particle flotation. The preliminary studies were quickly conducted to assess sulfide mineral flotation and whether additional in-depth tests were to be pursued (to further investigate superstructure flotation behaviour). Interesting results were obtained during the preliminary tests and as such warranted in-depth testing. The first set of experiments were baseline tests, though, to improve on the preliminary test results, staged reagent addition was employed for the in-depth study as well as PAX dosage was normalized to ore head grades (2.3 kg/t metal was chosen and was equivalent to 23g PAX/%(Cu + Ni); **Table A1**). The baseline float procedures for Ores A – D are presented in **Table 3.3**. To assess the effect of depressants on superstructure flotation, DETA/SMBS combination (100/200 g/t) was used; float procedures are presented in **Table 3.4**.

Preliminary Study

Table 3.2 – *Preliminary study float procedure for Ores A – D: All reagents added before concentrate #1.*

Concentrate	Reagent	Dosage	Cond. Time (min)	Float Time (min)	Cum. Float Time (min)
Conc. #1	PAX MIBC	180 g/t 2 drops	2 1	0.5	0.5
Conc. #2	PAX MIBC	-- --	-- --	0.5	1
Conc. #3	PAX MIBC	-- --	-- --	1	2
Conc. #4	PAX MIBC	-- --	-- --	2	4
Conc. #5	PAX MIBC	-- --	-- --	3	7

In-depth Study

Table 3.3 *– In-depth study float procedure – baseline tests with staged reagent addition. Total PAX dosage: Ore A = 28 g/t, Ore B = 122 g/t, Ore C = 135 g/t, and Ore D =129 g/t.*

Concentrate	Reagent	Dosage (g/t)				Cond. Time (min)	Float Time (min)	Cum. Float Time (min)
		Ore A	Ore B	Ore C	Ore D			
Conc. #1	PAX MIBC	5 2 drops	22 2 drops	24 2 drops	23 2 drops	2 1	0.5	0.5
Conc. #2	PAX MIBC	5 as req.	22 as req.	24 as req.	23 as req.	1 as req.	0.5	1
Conc. #3	PAX MIBC	6 as req.	26 as req.	29 as req.	28 as req.	1 as req.	1	2
Conc. #4	PAX MIBC	6 as req.	26 as req.	29 as req.	28 as req.	1 as req.	2	4
Conc. #5	PAX MIBC	6 as req.	26 as req.	29 as req.	28 as req.	1 as req.	3	7

Table 3.4 *– In-depth study flotation procedure – DETA/SMBS tests with staged reagent addition. *Note: SMBS and DETA were added together after which the slurry was conditioned for 2 mins.*

Concentrate	Reagent	Dosage (g/t)				Cond. Time (min)	Float Time (min)	Cum. Float Time (min)
		Ore A	Ore B	Ore C	Ore D			
Conc. #1	**SMBS**	**200**	**200**	**200**	**200**			
	DETA	**100**	**100**	**100**	**100**	2*		
	PAX	5	22	24	23	2	0.5	0.5
	MIBC	2 drops	2 drops	2 drops	2 drops	1		
Conc. #2	PAX	5	22	24	23	1	0.5	1
	MIBC	as req.	as req.	as req.	as req.	as req.		
Conc. #3	PAX	6	26	29	28	1	1	2
	MIBC	as req.	as req.	as req.	as req.	as req.		
Conc. #4	PAX	6	26	29	28	1	2	4
	MIBC	as req.	as req.	as req.	as req.	as req.		
Conc. #5	PAX	6	26	29	28	1	3	7
	MIBC	as req.	as req.	as req.	as req.	as req.		

3.1.2.2 Cu-Ni Sulfide Ore (Non-magnetic/Magnetic Pyrrhotite = 42/58%)

Glencore (Sudbury Integrated Nickel Operations) kindly provided a Cu–Ni sulfide test ore (valuable sulfides: chalcopyrite {$CuFeS_2$} and pentlandite {$(Ni,Fe)_9S_8$}, major sulfide gangue: pyrrhotite) from the Sudbury Basin. The ore contained a high Po/Pn ratio (~ 7.5) with a non-magnetic/magnetic Po ratio = 42/58% and was considered to be "challenging" to process industrially due to its reactive nature during stockpiling (prone to rapid weathering), high Po/Pn ratio, and high non-magnetic Po content. Furthermore, only about 86% Ni deportment was in pentlandite (typically it is ≥ 90%) where most of the remainder was in Po, making Ni recovery targets more difficult to achieve.

All test work was completed at the XPS center in Sudbury (Ontario, Canada). The ore was crushed (–10 Mesh; 2 mm), blended, split into 2 kg representative samples, vacuum sealed and stored in a freezer prior to testing. Note: due to the reactive nature of the ore (attributed to high Po content), the samples were vacuum sealed in order to provide a secondary measure (aside from freezer storage) to preserve the samples. Mineral assays were calculated based on the knowledge that this ore contained 0.9 wt% Ni in pyrrhotite (as solid solution):

$$\%Cp = 2.888*(\%Cu) \quad (3.5)$$

$$\%Pn = 0.067*(\%Cu) + 2.920*(\%Ni) – 0.066*(\%S) \quad (3.6)$$

$$\%Po = –2.690*(\%Cu) – 2.467*(\%Ni) + 2.662*(\%S) \quad (3.7)$$

$$\%Gangue = 100\% – \%Cp – \%Pn – \%Po \quad (3.8)$$

Pyrrhotite superstructure ratios (non-magnetic/magnetic) were determined by XRD. Head assay information is given in **Table 3.5**:

Table 3.5 *– Elemental and mineral compositions (wt %) for reactive ore.*

Elements (wt%)			**Minerals (wt%)**						
Cu	Ni	S	Cp	Pn	Po	% Non-mag Po	% Mag Po	Ga	Po/Pn
0.93	1.62	13.43	2.7	3.8	28.4	**42**	**58**	65.11	7.47

The ore was ground using a rod mill (70/30% mild steel/stainless steel rod blend) at 60% solids and grind time determined for target size distribution (P80 ≈ 120 µm). The ground material was wet–screened (53 µm); +53 µm portion was dry sieved and –53 µm portion was cyclosized into seven fractions and combined accordingly based on mass distribution: CS1–2 (–53/+25 µm), CS3–5 (–25/+8 µm), CS6 (–8/+3 µm), CS7 (–3 µm). Similar to the first batch flotation study, all size classes were analyzed by XRD for superstructure ratio. It was verified that the feed superstructure ratio was essentially maintained at each size class as expected and preferential grind was not observed. Feed modal mineralogy and mineral associations for each size class was determined by QEMSCAN and mineral nickel deportment was determined by electron probe micro–analysis (EPMA). Relevant XRD and QEMSCAN/EMPA data is presented in Chapter 6 (Section 6.2).

Flotation tests were conducted on 2 kg ores, ground to P80 ≈ 120 µm, in a 4 L Denver cell (equipped with automated froth paddle) with potassium isobutyl xanthate (PIBX) collector and polypropylene glycol ether (Polyfroth W31) frother. Seven concentrates were collected over 19 mins (test with concentrate regrind had 8 concentrates). The baseline test was floated as rougher–scavenger (rougher: pH 9.2, scavenger: pH 8) to assess the impact of pH on sulfide flotation; float procedure is presented in **Table 3.6**.

Table 3.6 *– Baseline float test procedure (rougher-scavenger stages).*

Stage	Concentrate	Reagent	Dosage (g/t)	Cond. Time (min)	Float Time (min)	Cum. Float Time (min)
Rougher (pH 9.2)	**Conc. #1**	PIBX Polyfroth W31	6 2 drops	5 1	1	1
	Conc. #2	PIBX Polyfroth W31	-- as req.	-- as req.	2	3
	Conc. #3	PIBX Polyfroth W31	15 as req.	1 as req.	2	5
	Conc. #4	PIBX Polyfroth W31	10 as req.	1 as req.	2	7
Reduce pH to 8.0 by adding H_2SO_4						
Scavenger (pH 8.0)	**Conc. #5**	PIBX Polyfroth W31	15 as req.	1 as req.	4	11
	Conc. #6	PIBX Polyfroth W31	12 as req.	1 as req.	4	15
	Conc. #7	PIBX Polyfroth W31	12 as req.	1 as req.	4	19

The DETA and DETA/SMBS tests were floated as rougher only (pH 9.2) due to reduced flotation kinetics with DETA (allowing for more concentrates) and the fact that significant Po depression generally occurs at pH > 9, which was the focus of study. The float procedure is presented in **Table 3.7**. For the {acid + DETA/SMBS} tests, immediately following the grind stage the slurry was conditioned for 5 mins with sulfuric acid at pH 4 to dissolve any Ni/Cu/Fe hydroxides and oxides after which it was conditioned for 5 mins with DETA/SMBS (150/300 g/t). Following this, the slurry was brought to pH 9.2 using lime and floated with 70 g/t PIBX (see 70 g/t PIBX tests in **Table 3.7** for dosage distribution). The {acid + DETA/SMBS + aeration} tests were the same except that immediately after the slurry was brought to pH 9.2 it was aerated for 5 mins and then floated (70 g/t PIBX).

Table 3.7 *– DETA and DETA/SMBS float test procedures at two PIBX dosages (70 and 100 g/t). *Note: for the DETA/SMBS tests, both reagents were added together after which the slurry was conditioned for 5 mins.*

Stage	Concentrate	Reagent	Dosage (g/t)				Cond. Time (min)	Float Time (min)	Cum. Float Time (min)
			DETA Only Test		DETA/SMBS Test				
			PIBX = 70 g/t	PIBX = 100 g/t	PIBX = 70 g/t	PIBX = 100 g/t			
Rougher (pH 9.2)	Conc. #1	SMBS DETA PIBX Polyfroth W31	-- 150 6 2 drops	-- 150 15 2 drops	300 150 6 2 drops	300 150 15 2 drops	5* 5 1	1	1
	Conc. #2	PIBX Polyfroth W31	-- as req.	13 as req.	-- as req.	13 as req.	-- as req.	2	3
	Conc. #3	PIBX Polyfroth W31	15 as req.	10 as req.	15 as req.	10 as req.	1 as req.	2	5
	Conc. #4	PIBX Polyfroth W31	10 as req.	10 as req.	10 as req.	10 as req.	1 as req.	2	7
	Conc. #5	PIBX Polyfroth W31	15 as req.	20 as req.	15 as req.	20 as req.	1 as req.	4	11
	Conc. #6	PIBX Polyfroth W31	12 as req.	16 as req.	12 as req.	16 as req.	1 as req.	4	15
	Conc. #7	PIBX Polyfroth W31	12 as req.	16 as req.	12 as req.	16 as req.	1 as req.	4	19

For the concentrate regrind test (DETA/SMBS + grind), the DETA/SMBS (100 g/t PIBX) test was floated after which concentrates #5 – 7 were combined and ground to P80 ≈ 35 µm. The reground concentrate was then transferred to a 2 L Denver cell and conditioned with DETA/SMBS (100/200 g/t) for 5 mins at pH 9.2 after which it was floated with 25 g/t PIBX (no frother) where 4 cleaner concentrates were collected at 0.5, 1, 2, 4 mins (7.5 mins cumulative time). Of the many tests conducted, two were chosen for recovery–by–size comparison due to the availability of sufficient concentrate mass needed for cyclosizing and XRD analysis: (1) baseline test; and (2) acid + DETA/SMBS + aeration test.

3.2 Instruments

3.2.1 ICP–OES

Elemental compositions of the many samples used in this study were determined by ICP–OES (Thermo Scientific iCAP 6500 ICP–OES CID Spectrometer), from which mineral compositions were calculated from their ideal stoichiometric formulas. For samples containing mainly sulfide minerals (*i.e.* purified minerals), they were easily digested in aqua

regia ($HCl:HNO_3$ molar ratio = 3:1); typically 0.1 g sample was digested in 20 mL aqua regia at 95°C over 2 hrs. For samples containing sulfides and many insoluble minerals (*e.g.* oxides and silicates, *etc.*), sodium peroxide (Na_2O_2) fusion was required to first sinter the samples at 650°C in zirconia crucibles (effectively digesting the sample into the melt) which then was digested in 5% nitric acid and subsequently analyzed by ICP–OES.

3.2.2 Powder X–Ray Diffraction

The discrimination of pyrrhotite superstructures can be accomplished by several methods (see Section 2.2.4); most of these are qualitative. A handful of quantitative methods exist of which the industry standard is X-ray diffraction for several reasons: acceptable detection limit (3 – 5 wt%), reasonable error (5 – 15%, depending on the quality of diffraction pattern and calibration curve), ease of use (sulfide ores are well characterized with minimal interference from gangue minerals), and reproducibility. For these reasons, XRD was used in the present study to discriminate between non-magnetic (Fe_9S_{10}) and magnetic (Fe_7S_8) pyrrhotite superstructures using a Bruker Discover D8 – 2D Diffractometer (Co Kα radiation source). Two separate software were used interchangeably for mineral phase identification from the XRD spectra: EVA from DIFFRAC.SUITE™ software package (Bruker) and X'Pert HighScore (PANalytical).

The *peak intensity ratio* method proposed by Graham (1969)[57] was employed, which required a calibration curve made from mechanical mixtures of purified non–magnetic and magnetic pyrrhotite powders. Non–magnetic pyrrhotite contains a singlet ($d \approx 2.066$Å) and magnetic pyrrhotite contains doublets ($d \approx 2.066/2.056$Å), the low angle peak is virtually identical for both superstructures and the high angle peak of near equal intensity for magnetic pyrrhotite is separated by about 0.30–0.35°2θ (see Section 2.2.4.2) [6, 27, 28, 57]. A ratio of the low and high angle peaks are cross–referenced against a calibration curve that gives the % non-magnetic pyrrhotite as a function of the peak ratios, magnetic pyrrhotite determined by difference [57, 59]. The calibration curve depicted in **Figure 3.2** was developed from mechanical mixtures (0/100%, 15/85%, 33/67%, 50/50%, 67/33%, 85/15% and 100/0%) of purified natural non-magnetic/magnetic superstructures. For a given base–metal sulfide ore, total pyrrhotite content is determined *via* metal/sulfur assays and the non-magnetic pyrrhotite

proportion is calculated from the calibration curve (intensity ratio = $\mathbf{I}_{51.40^o}/\mathbf{I}_{51.75^o}$, Co K$\alpha$ radiation):

$$\% \text{ Non-magnetic Po} = -7.687\left[\ln\left(\frac{\mathbf{I}_{51.4}}{\mathbf{I}_{51.75}}\right)\right]^2 + 52.16\left[\ln\left(\frac{\mathbf{I}_{51.4}}{\mathbf{I}_{51.75}}\right)\right] + 23.461 \quad (3.9)$$

$$\% \text{ Magnetic Po} = 100 - \% \text{ Non-magnetic Po} \quad (3.10)$$

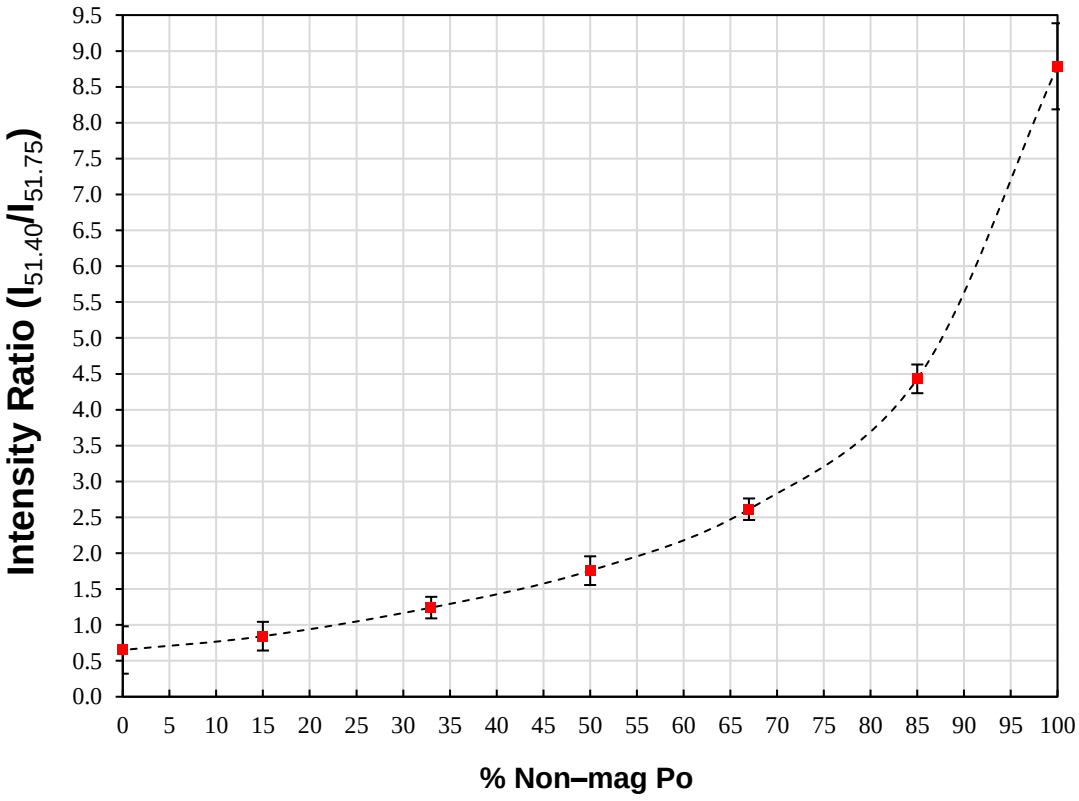

Figure 3.2 *– Proportion of non-magnetic (Fe_9S_{10}) in magnetic (Fe_7S_8)/non-magnetic (Fe_9S_{10}) pyrrhotite mixtures based on intensity ratio ($I_{51.40}/I_{51.75}$) using CoKα radiation. Magnetic pyrrhotite calculated by difference. Note: for* $I_{51.40}$ and $I_{51.75}$, d ≈ *2.066 and 2.056Å, respectively. Error bars denote a 2σ error.*

3.2.3 Automated Mineralogy

Mineralogical analysis of the ores (mineral abundance, liberation, associations and nickel deportment) was conducted on samples used in the batch flotation tests (Chapters 5 and 6). For the 4 ore samples provided by Vale Base Metals, Vale Technical Services in Sheridan Park in Mississauga (Ontario, Canada) characterized the samples by MLA. MLA analysis was completed using a JEOL 6400 SEM (operated at 20 kV). The ore provided by Glencore was characterized at the XPS center in Sudbury (Ontario, Canada) by QEMSCAN

and EPMA. QEMSCAN analysis was completed using a FEI Quanta 650 Field Emission Gun SEM (operated at 20 kV); for nickel deportment (*e.g.* in pyrrhotite as solid solution), electron probe micro–analysis (EPMA) was conducted using a Cameca SX–100 Microprobe.

Both MLA and QEMSCAN are automated scanning electron microscope techniques using Energy Dispersive X-ray Spectroscopy (EDS) and grey level contrast from Backscatter Electrons (BSE), analysis is conducted on polished sections of sized minerals. The X-ray spectra and BSE intensities are processed by a software to identify constituent elements which are cross-referenced against a mineral library to identify specific minerals based on their distinct elemental ratios. Both systems can easily distinguish most base metal sulfide minerals, however due to the extreme similarities between non–magnetic (Fe_9S_{10}) and magnetic (Fe_7S_8) pyrrhotite (having very similar Fe/S ratios) in the SEM, pyrrhotite superstructure discrimination and quantification is difficult and generally not feasible under most operating conditions. Thus, pyrrhotite quantification is accomplished *via* chemical assays (ICP-OES and/or MLA/QEMSCAN), however the data must be combined with XRD (to yield superstructure ratio) in order to quantify the superstructures.

3.2.4 Sonication Treatment

Sonication pre-treatment of the superstructure powders (before PAX adsorption and microflotation studies) was conducted using an ultrasonicator probe at 50% amplitude that was attached to a Hielscher Ultrasound Technology UP400S UltraSonic Processor (400 W / 24 kHz). As discussed in the previous sections, sulfide minerals undergo surface oxidation during processing and handling (even during prolonged storage) and require some pre-treatment in order to obtain “fresh” surfaces just prior to experimental test work. Many options were available to achieve this, however, to maintain the particular particle size distributions, sonication pre-treatment with an ultrasonicator probe was chosen. The sonication time varied depending on the study and mass of the powder, exact sonication times are given in the specific procedures.

3.2.5 Frantz Isodynamic Separator

To separate non-magnetic pyrrhotite from gangue minerals such as silicates/metal oxides for the purpose of upgrading the non-magnetic pyrrhotite content (flotation tails sample; see Section 3.1.1.2), a Frantz Isodynamic Separator was used, pictured in **Figure 3.3**. Though the name implies poor magnetic susceptibility, non-magnetic pyrrhotite is antiferromagnetic (sometimes referred to as "paramagnetic") and can be recovered with a high applied magnetic field strength. Prior to separation, the material was sized and ferromagnetic particles were removed by a hand magnetic (1000 Gauss). The mineral particles were then fed dry into a vibrating chute that is inclined at two angles (θ_1 and θ_2); the chute is situated between an electromagnetic coil [1]. The coil provides a magnetic force for particle attraction (this can be increased with an increase in current) to overcome the gravitational pull. Due to gravity and vibration, the particles flow towards the end of the chute; those with an appreciable magnetic susceptibility (*i.e.* paramagnetic particles) will be attracted to the magnet and will report to the right side, whereas for particles where the magnetic strength was insufficient will report to the left side [1]. The material reporting to the right side can then be further upgraded by reprocessing the material with higher magnetic field strengths (by increasing the current). Individual size classes of non-magnetic pyrrhotite were processed in this manner and yielded ~ 90% purity.

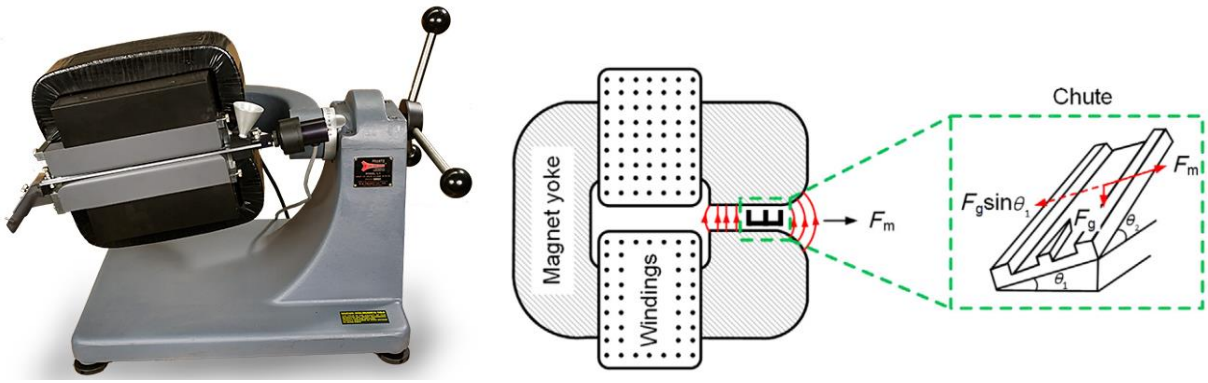

Figure 3.3 *– (left) Frantz Isodynamic Separator, reproduced from www.sgfrantz.com; (right) Frantz Isodynamic Separator presented diagrammatically, reproduced from Wills and Finch (2016)[1].*

3.2.6 Cyclosizer

For ore feed mineralogy (liberation, associations, *etc.*) and certain float concentrates/tails samples, material sizing into many fine fractions was necessary. Typically, above 38 μm, classification by sieves is adequate; however, below 38 μm sieving is not preferred due to screen blinding by fine particles (especially below 25 μm). In such cases, other equipment such as a cyclosizer (CS) becomes attractive; they are widely used for sub-sieve size classification in the 8 – 50 μm range [1]. A typical unit (M16 Cyclosizer by MARC Technologies Pty Ltd) consisting of five cyclones is presented in **Figure 3.4** which was used in the present study. The cyclones are connected in series such that the vortex outlet (overflow) from one cyclone feeds the next (the apex retaining the coarse particles). The particle sizes progressively become finer with each cyclone due to a successive decrease in cyclone inlet area and vortex outlet diameter which results in increasing centrifugal forces, permitting finer particle separation. A more in-depth explanation can be found in Wills and Finch (2016)[1].

During this study, the material was first wet-screened (either 53 or 38 μm), after which the undersize (–53 or –38 μm) was passed through a pre-cyclone unit to separate the –3 μm fraction (slime fraction labelled as CS7). The remainder mass (–53/+3 or –38/+3 μm) was introduced as the feed to the cyclosizer, separating the material into 5 fractions (CS1–5) after which the overflow of the last cyclone (–12/+3 μm) was then further separated in another independent cyclone unit to yield CS6 (–8/+3 μm).

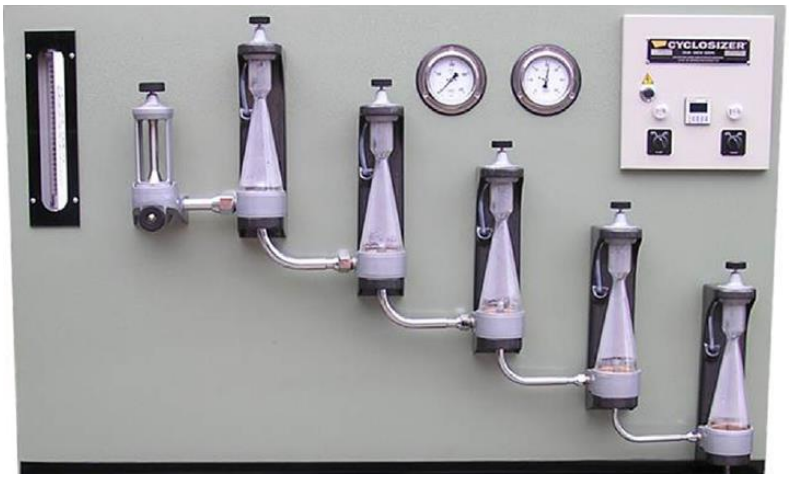

Figure 3.4 *– Cyclosizer unit from MARC Technologies Pty Ltd., reproduced from Wills and Finch (2016)[1].*

3.2.7 Brunauer–Emmett–Teller (BET) Surface Area

Mineral surface areas (–38 μm fraction) were determined with a Micromeritics Tristar surface area and porosity analyzer, using the Brunauer–Emmett–Teller (BET) model for gas adsorption. Prior to analysis, the powder samples were degassed under nitrogen at 70 ^{o}C for 24 hrs followed by 1 hr vacuum degassing, after which they were immediately placed in the analyzer. The BET surface areas for magnetic and non–magnetic pyrrhotite were 1.86 and 6.63 m^2/g, respectively. The large difference was attributed to different particle size distributions for the two samples resulting from the different grinding methods used for each superstructure (see Chapter 4). Particle size distribution was determined by a Horiba Laser Scattering Particle Size Analyzer – LA–920.

3.2.8 Zeta Potential

The Brookhaven NanoBrook 90Plus Zeta Instrument was used to determine the mineral surface potential at the shear plane (zeta potential) using the electrophoretic technique for pH 2 – 11. The method uses the movement of charged particles relative to the liquid under an applied electric field. The mobility of fine particles suspended in a background electrolyte solution (*e.g.* 0.001 mol/L KCl) is directly proportional to the applied field. Thus, if the solution dielectric constant and viscosity are known and the particle velocity can be determined using laser scattering, the zeta potential can be calculated.

3.2.9 UV–Vis Spectroscopy

Quantification of xanthate was accomplished using a Perkin Elmer Lambda 20 UV/Vis Spectrometer in the ultraviolet range. An initial sweeping scan was conducted to identify the major xanthate ion peaks (primary: 301 nm; secondary: 226 nm) and to verify that no xanthate degradation products were present [82]. Major xanthate species and their associated wavelengths are presented in **Table 3.8** and **Figure 3.5**. Calibration standards of *n*-amyl xanthate in DI water (0 ("blank"), 0.5, 5, 25 and 50 mg/L) were used for the analysis of solution samples with unknown xanthate concentration from the adsorption studies.

Table 3.8 *– Xanthate species and their wavelengths, reproduced from Rao (2004)[82].*

Sepecies	Wavelength (nm)	ε, Extinction Coefficient (L/(mol·cm))
CS_2	206.5	60,000 – 70,000
Monothiocarbonate	223	12,200 – 13,300
Xanthate Ion	226 **301**	8,750 17,500
Dixanthogen	238 283	17,800 8,600
Xanthic Acid	270	10,700

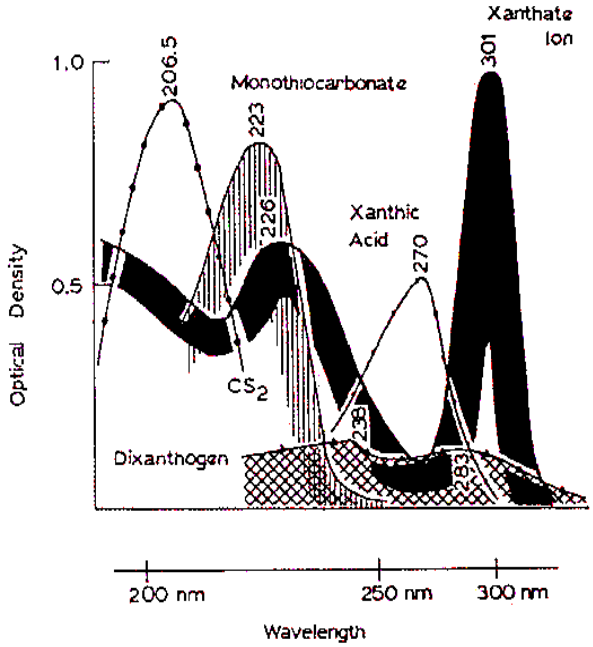

Figure 3.5 *– Major xanthate species and their wavelengths, reproduced from Rao (2004)[82].*

3.2.10 Flotation

3.2.10.1 Microflotation

Microflotation tests were conducted on 1 g samples of purified pyrrhotite superstructure powders over 1 min with nitrogen as gas source (see procedure in Section 3.1.1.5). The main advantage of conducting microflotation tests is the ability to reasonably assess the floatability of single minerals under various pH conditions when limited mineral mass is available. Two types of microflotation units were available; Partridge–Smith cell (60 mL) and modified Hallimond tube (180 mL). The latter was used for the main reason that operator error was lower over the former; preliminary studies using both cells demonstrated that the data was much more reproducible with the Hallimond tube. A schematic of the Hallimond tube is shown in **Figure 3.6**. A test powder is transferred to the tube above the glass frit, air is introduced and hydrophobic particles attach to the rising bubbles. The loaded bubbles break when they contact the air-water interface, allowing the particles to fall into the concentrate launder. The recovery is calculated based on concentrate mass divided by feed mass.

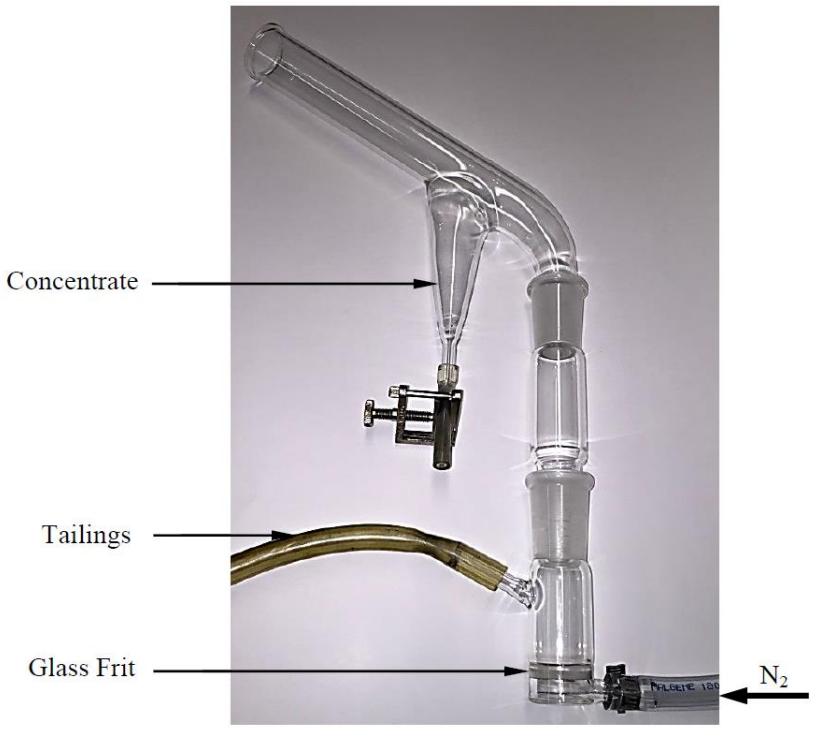

Figure 3.6 *– Microflotation cell (modified Hallimond tube), reproduced from Mohammadi-Jam (2016)[107].*

3.2.10.2 Batch Flotation

Batch flotation was conducted using a Denver D12 laboratory flotation machine (an example is shown in **Figure 3.7**) in 2 and 4 L cells on 1 – 2 kg ground ore. The cells are mechanically agitated (with variable speed control) to ensure particle suspension and air is introduced *via* the impeller shaft where it is sheared into fine bubbles by the impeller. As the bubbles rise through the pulp, hydrophobic particles attach to the bubbles and report to the froth phase, which is skimmed and collected as concentrate. To reduce variability between test repeats, the Denver cell was equipped with an automated froth paddle (**Figure 3.7**). Reagents can be added at the beginning or stage-wise, for specific procedures see Section 3.1.2.

Figure 3.7 *– (Left) Denver D12 laboratory flotation machine, reproduced from Wills and Finch (2016)[1]; (right) cell equipped with automated froth paddle.*

Chapter 4
Single Mineral Studies

4.1 Introduction

Information on pyrrhotite surface chemistry and flotation is abundant in the literature, however data on the individual superstructures is lacking with only a few studies published in the past 3 decades [11, 13-16]. As industrial concentrators transition away from the use of magnetic separators (forcing both magnetic (Fe_7S_8) and non-magnetic (Fe_9S_{10}) superstructures to report to the same flotation circuit) as well as the need to reject more pyrrhotite to meet same metal concentrate grade/recovery, interest in the superstructure behaviour has been renewed recently [16]. This largely stems from the fact that the pyrrhotite system is very complex and relevant superstructure information is scarce.

As both superstructures report to the same flotation circuit, they exhibit different flotation responses and concentrators are actively documenting the differences in order to develop better depression strategies. Recent industrial flotation data supports the many accounts in the literature that pyrrhotite superstructures float differently and that non-magnetic is more floatable over magnetic pyrrhotite [16]. It must be noted, however, that there are conflicting reports in the literature as well, where magnetic pyrrhotite is stated as being more floatable. Oxidation studies are also inconsistent with several studies supporting both superstructures as being more prone towards oxidation over the other, leaving researchers perplexed. Aside from ore related issues (*e.g.* mineral associations, *etc.*), the contradictory

findings of many researchers are likely to be the result of mischaracterization of the pyrrhotite specimens under investigation, as well as inadequate specimen handling prior to test work. Pyrrhotite is most commonly found as an intergrown mixture of magnetic (Fe_7S_8) and non-magnetic (Fe_9S_{10}) superstructures and is extremely prone to surface oxidation. Thus, a significant effort must be made to ensure the specimen is well characterized (quantifying the superstructures in the sample) and that the specimen surface is free of oxidation products just prior to test work since even freezer storage will inevitably lead to some degree oxidation.

A few in-depth studies, namely Kolahdoozan (1996)[11] and Becker (2009)[13], have investigated the superstructures under many conditions where the researchers took great care to characterize the samples prior test work. The researchers compared superstructure microflotation, potassium *n*-amyl xanthate (PAX) collector adsorption in the presence of various flotation reagents, and oxygen uptake (*i.e.* oxidation); these were summarized in Sections 2.3.2.3 and 2.4.4. Kolahdoozan (1996) demonstrated that PAX adsorption (pH 7, 8.5, and 10) on both superstructures is different (regardless if they were synthetic or naturally occurring pyrrhotites); whereas magnetic pyrrhotite had much higher PAX adsorption under most conditions. Interestingly, microflotation tests showed that both superstructures exhibited near identical flotation responses for pH 2 – 11 (non-magnetic being slightly more floatable for pH > 10). Becker (2009) showed that magnetic pyrrhotite ores exhibited higher oxygen uptake (pH 7 and 10) under the various conditions over those containing non-magnetic pyrrhotite, strengthening the argument that magnetic pyrrhotite is more prone to oxidation. Furthermore, ores containing entirely non-magnetic pyrrhotite were more floatable (pH 7 and 10) than those containing entirely magnetic pyrrhotite or mixtures of the superstructures. The researcher did note, however, that microflotation results could not be entirely credited to pyrrhotite crystallography alone, rather the overall flotation is a summation of crystallography (number of vacancies), reactivity towards oxygen, metal content (Fe^{3+} and Ni^{2+}), as well as mineral associations (with more floatable sulfides).

As there is still a significant gap in understanding the pyrrhotite superstructure behaviour and confusion due to conflicting reports, single mineral studies on purified superstructures were first pursued to examine the superstructures independently before

proceeding to batch flotation tests. The results of this study would also serve to contribute to the growing superstructure database. Primary focus was placed on mineral surface studies (zeta potential (pH 2 – 11) and *n*-amyl xanthate collector adsorption (pH 7, 8.5, and 10)) and microflotation (pH 7 – 11) with/without sonication pre-treatment to gain an understanding of the mechanisms responsible for the different flotation responses. The important findings from the studies and relevant discussions are presented.

4.2 Feed Material

Two ore samples were sourced from Canada (Sudbury (Ontario) and Voisey's Bay (Newfoundland and Labrador)) and required upgrading to obtain relatively pure magnetic and non-magnetic pyrrhotite samples for single mineral studies. The purification procedures can be found in Chapter 3 (Sections 3.1.1.1 and 3.1.1.2). **Table 4.1** displays the composition of each purified sample by size and the pyrrhotite superstructure content in each as well. **Figure 4.1** displays the XRD patterns for each purified sample by size, the patterns confirmed that the major minerals were pyrrhotite, chalcopyrite, and pentlandite (as proposed by the assay data) and that no pyrite or any secondary copper and nickel sulfide minerals were present. The –38 μm fraction was used for zeta potential and PAX adsorption tests, the –106/+38 μm range was used for microflotation tests, and +106 μm fraction was kept in reserve. The –38 μm fraction was also analyzed for its average surface area (g/m^2) by the BET method in order to calculate PAX adsorption density (mg PAX/m^2) on mineral surfaces (adsorption tests). The average magnetic and non-magnetic pyrrhotite (–38 μm) BET surface area was 1.86 and 6.63 m^2/g, respectively. The large difference was attributed to different particle size distributions for the two samples resulting from the different grinding methods employed for each superstructure during purification (**Figure 4.2**).

Table 4.1 *– Mineral assay (wt%) by size class. Note: Cp – chalcopyrite, Pn – pentlandite, Po – pyrrhotite, Mag Po – Fe_7S_8, Non-mag Po – Fe_9S_{10}, and Ga – non-sulfide gangue.*

	Magnetic Pyrrhotite (Fe_7S_8)						Non-magnetic Pyrrhotite (Fe_9S_{10})					
Size Class (µm)	Cp	Pn	Po	Mag Po	Non-Mag Po	Ga	Cp	Pn	Po	Mag Po	Non-Mag Po	Ga
+106	1.6	5.0	85.4	92	8	8.0	0.1	1.6	90.8	5	95	7.4
-106/+75	1.4	5.1	86.4	89	11	7.0	0.0	1.6	91.7	6	94	6.6
-75/+53	1.1	4.5	88.3	89	11	6.0	0.0	1.6	90.1	6	94	8.3
-53/+38	1.1	4.5	86.7	90	10	7.8	0.0	1.5	88.0	5	95	10.5
-38	3.7	6.3	81.6	89	11	8.4	0.7	3.5	80.0	6	94	15.8

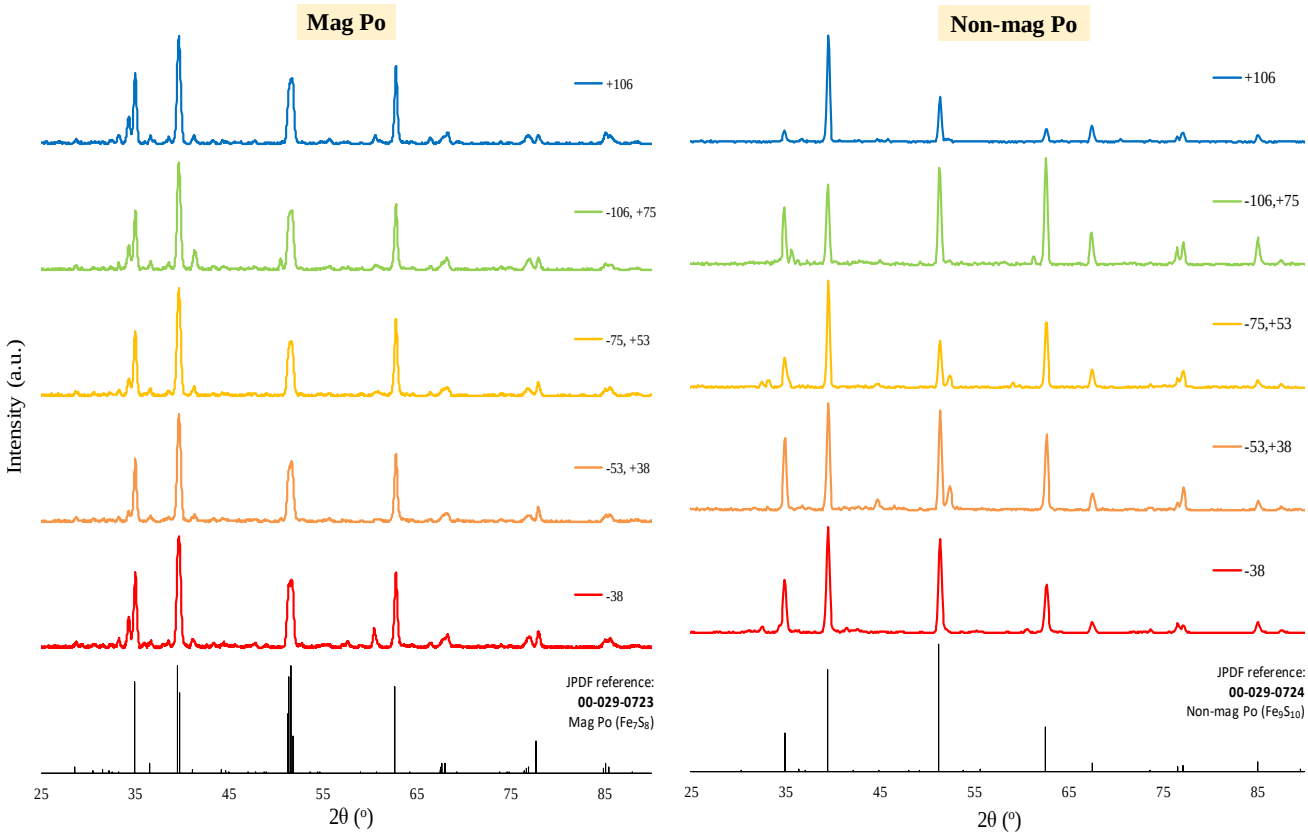

Figure 4.1 *– Size-by-size XRD patterns of purified pyrrhotite samples; (a) magnetic (Fe_7S_8); (b) non-magnetic (Fe_9S_{10}).*

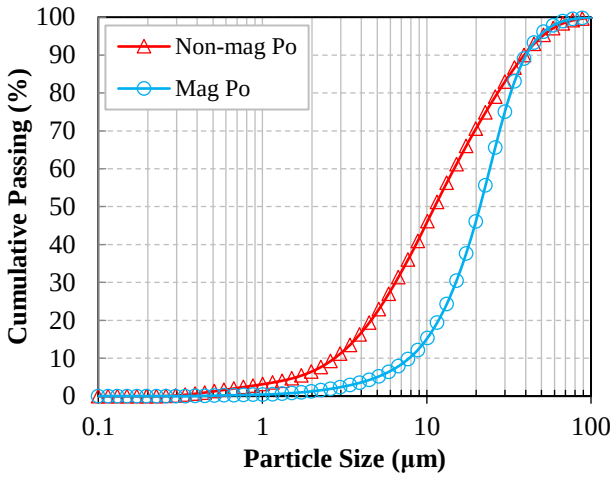

Figure 4.2 *– Particle size distribution (cumulative passing %) for the superstructures.*

4.3 Results and Discussion

4.3.1 Zeta Potential

As with most pyrrhotite superstructure data, there are conflicting reports for the zeta potential isoelectric points (IEP); the literature presents quite a large range (pH_{IEP} = 2 – 9.6) [11, 83-87]. Metal sulfides are expected to have pH_{IEP} below about 3.5 [83]. This makes it challenging to infer mineral–reagent interactions and adsorption mechanisms (*physisorption* or *chemisorption*) and comparison of results across several studies. Since sulfides are prone to oxidation (which generally shifts the IEP to much higher pH values), it was suspected that literature pH_{IEP} differences were the consequence of the level of mineral surface oxidation. During preliminary testing, baseline curves (unground minerals exposed to air) gave pH_{IEP} > 5.5 for both superstructures, resembling values of metal hydroxides/oxides (*e.g.* $Fe(OH)_3$ and Fe_2O_3). Thus the procedure was modified; evaluation of zeta potentials was completed on freshly ground powders during which a significant effort was placed into ensuring that oxygen contact was minimized.

Superstructure powders were analyzed as is (baseline), with $NiSO_4$, $CuSO_4$, and PAX collector; zeta potential results are presented in **Figure 4.3**. Baseline curves and pH_{IEP} values were identical for both superstructures (~ 3.5); IEP was in the expected range. With "fresh" surfaces, the superstructures appear to have the same surface potential over the tested

pH range (2 – 11). Although not tested, it is hypothesized that the surface potentials would diverge with exposure to air, with magnetic pyrrhotite likely oxidizing faster and expected to have a larger positive shift in pH_{IEP}. With $NiSO_4$ and $CuSO_4$ activators (separate tests), surface potentials were increased into the positive region for both superstructures; the increase was most significant where the baseline potentials were negative, indicating electrostatic adsorption of nickel and copper ions.

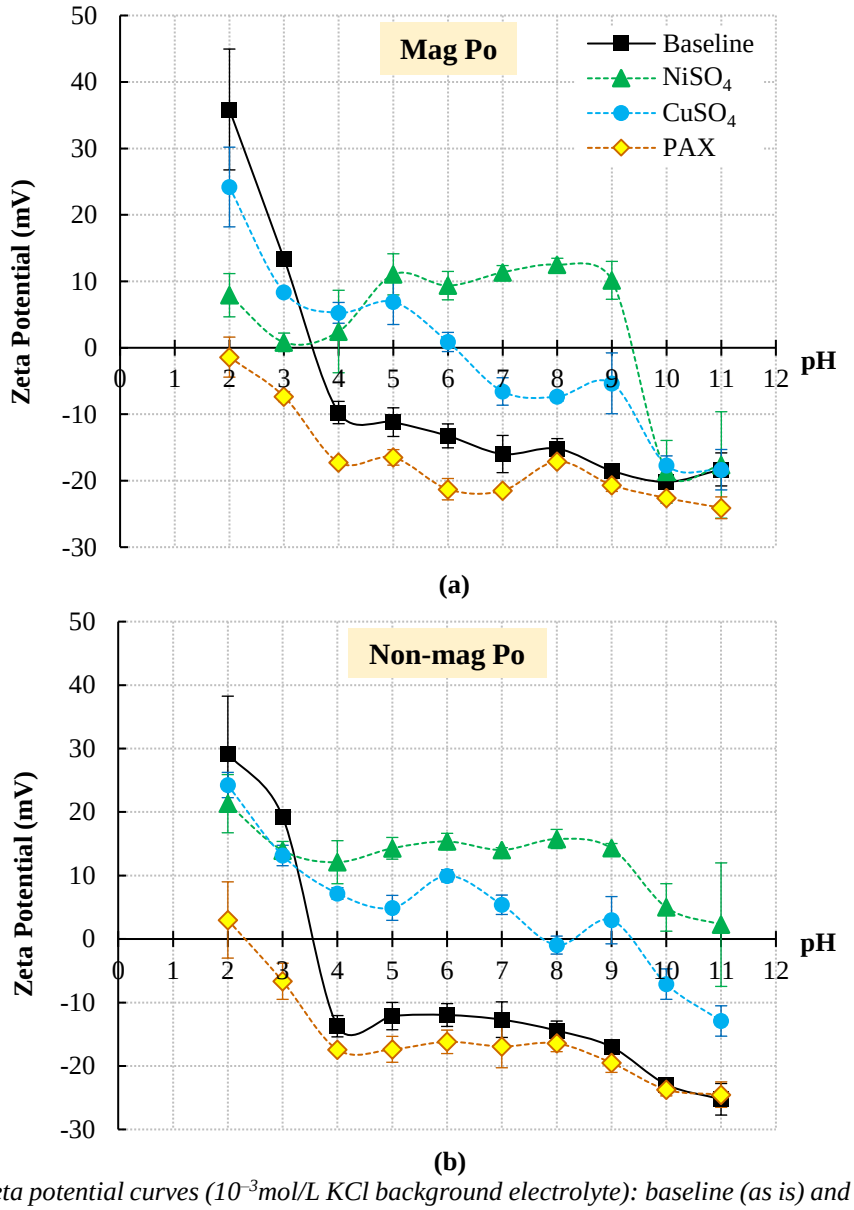

Figure 4.3 *– Zeta potential curves (10^{-3}mol/L KCl background electrolyte): baseline (as is) and with 10^{-4}mol/L $NiSO_4$, $CuSO_4$, and PAX; (a) magnetic pyrrhotite (Fe_7S_8); (b) non-magnetic pyrrhotite (Fe_9S_{10}). Error bars denote 2σ error.*

Speciation diagrams for $NiSO_4$ and $CuSO_4$ are shown in **Figure 4.4**, major adsorbing nickel and copper species were taken to be Ni^{2+}, $Ni(OH)^+$, Cu^{2+} and $Cu(OH)^+$ (the $Cu_2(OH)_2^{2+}$species may have a minor influence). A decline in surface potentials was observed at about pH 9 for $NiSO_4$ and pH 6 – 7 for $CuSO_4$ curves (both superstructures), which roughly corresponds to the onset of $Ni(OH)_2$ and CuO (initially believed to be $Cu(OH)_2$) precipitation. In the presence of nickel and copper ions, the freshly ground superstructures exhibited similar surface potential trends; slightly higher potentials were observed in neutral to alkaline pH for non-magnetic pyrrhotite. Although this was not investigated further, the slight difference was interpreted as more iron hydroxides coating magnetic pyrrhotite as a result of hydrolysis that interfered with nickel and copper uptake.

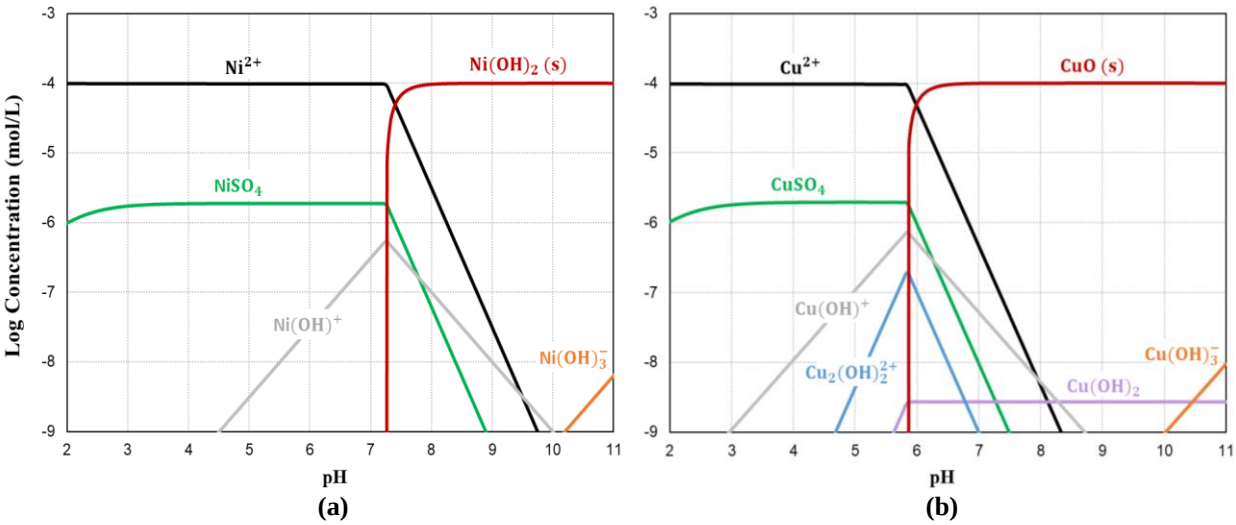

Figure 4.4 *– Speciation diagram displayed as log concentration (mol/L) vs. pH; (a) 10^{-4}mol/L $NiSO_4$; (b) 10^{-4}mol/L $CuSO_4$. Diagrams were calculated at 25 °C and 1 atm using HYDRA and MEDUSA (Puigdomenech, 2009, 2010).*

With PAX collector addition, the largest effect on surface potentials was below pH 3.5 where the superstructures were net positively charged and a portion of the xanthate was negatively charged (since amyl xanthate pKa ~ 5, primary speciation below pH 3.5 is undissociated HX with some free X^-). Thus, below pH 3.5, electrostatic adsorption of free collector (X^-) significantly lowered surface potentials, yielding similar curves for both superstructures. The commonly referenced reaction is shown in Equation (4.1); Fe(III)

surface sites (as $Fe(OH)[S]^+$) attract X^- molecules and form the Fe(OH)[S][X] surface complex[93]:

$$Fe(OH)[S]^+ + X^- \leftrightarrow Fe(OH)[S][X] \quad (4.1)$$

The initial $Fe(OH)[S]^+$ site is said to arise due to partial oxidation of pyrrhotite surfaces (*i.e.* requiring the presence of dissolved oxygen) where Fe(II) is oxidized to Fe(III). As the zeta potential test work was conducted in the virtual absence of oxygen, partial oxidation of pyrrhotite was viewed as unlikely but still possible as it is extremely reactive, however this was thought not to be the case since it would have been reflected in the pH_{IEP} (if oxidized it would be >> 3.5). It is proposed that rather than partial/superficial oxidation, the $Fe(OH)[S]^+$ site may already be present on pyrrhotite since it is now known to have both Fe^{2+} and Fe^{3+} in its superstructures.

With increasing pH, surface potentials were lowered further, though the difference compared to baseline reference curves was not as significant as that observed for pH < 3.5. Considering that for pH > 3.5 the superstructures are net negatively charged and same with free xanthate, adsorption by a chemisorption mechanism in this region would normally be proposed. However, the prominent chemisorbing xanthate species is known to be dixanthogen (X_2), which requires an initial physisorption step (Equation (4.1)) after which the adsorbed xanthate is further oxidized to dixanthogen by dissolved oxygen:

ANODIC SITE: $$Fe(OH)[S][X] + X^- \leftrightarrow Fe(OH)[S][X_2] + 2e^- \quad (4.2)$$

CATHODIC SITE: $$\frac{1}{2} O_2 + 2e^- + H_2O \leftrightarrow 2OH^- \quad (4.3)$$

It is therefore postulated that the small decrease in surface potentials occurring at pH > 3.5 still included physisorption (X^- adsorbing onto $Fe(OH)[S]^+$ sites that would still be present) as this would lower the surface potentials, and further oxidation to dixanthogen would be possible only in an oxidative environment. Rao and Finch (1991) identified surface adsorbed xanthate on pyrrhotite (speculated to be Fe(OH)[S][X]) in both nitrogen and air environments at pH > 3.5 (pH 6 and 8.4), however dixanthogen was only found in air systems [94]. The researchers also noted that the quantity of adsorbed xanthate (Fe(OH)[S][X]) at the pyrrhotite surface was about the same in both nitrogen and air environments, the major difference was

the amount of dixanthogen (only present in air systems). To investigate the effect of air on surface potentials, a few tests were conducted with aeration; after conditioning with PAX, the superstructures were aerated for 1 minute and immediately analyzed. The resulting curves (not presented) were virtually the same as the original PAX curves in **Figure 4.3**. Since the oxidation of surface adsorbed xanthate to dixanthogen is considered to be fast, it was likely that dixanthogen formed; the fact that a further shift in surface potentials was not observed was thought to be because of the lack of charge on the dixanthogen molecule. Thus, it is believed that for pH > 3.5, xanthate initially adsorbs by a physisorption mechanism and may subsequently convert to dixanthogen given that sufficient oxygen is present.

4.3.2 PAX Adsorption

Since the change in surface potentials with PAX was negligible past pH 8 when compared to baseline potentials and the fact that pyrrhotite flotation is generally conducted in the alkaline region (typically > 9 if its depression is targeted), PAX adsorption on the superstructures was studied further for pH > 7. It was expected that with increasing pH a decrease in adsorption would be observed, partly due to significant $Fe(OH)_3$ formation but also because of OH^- ions hindering adsorption in accordance to the Barsky relationship ($[X^-]/[OH^-]$ = constant) [93, 94]. Literature data for xanthate adsorption on pyrrhotite superstructures is limited, the present test work also aimed to supplement the adsorption results from Kolahdoozan (1996) by testing naturally occurring superstructures at the same pH conditions (pH 7, 8.5, and 10) [11]. The Kolahdoozan (1996) study investigated synthetic superstructures and naturally occurring magnetic pyrrhotite (Section 2.3.2.3).

The objective of this adsorption study was to develop and compare magnetic and non-magnetic pyrrhotite PAX adsorption isotherms under three pH conditions (7, 8.5, and 10) while also comparing the findings to pyrrhotite isotherms available in the literature. The first task was to determine the adsorption equilibrium time required; the highest initial PAX concentration (100 mg/L) was chosen as reference point for which the adsorption density (mg PAX/m^2) over time is displayed in **Figure 4.5**. Equilibrium was achieved after approximately 360 mins for both superstructures and as such all subsequent testing with other

PAX concentrations (< 100 mg/L) was conducted for at least 360 mins. The results demonstrated that the superstructures had significantly different amounts of xanthate uptake with magnetic pyrrhotite having much more, this will be discussed in further detail during the isotherm analysis. Both the rate of PAX adsorption and final equilibrium adsorption density decreased with increasing pH, both of which are the result of increasing OH^- concentration at higher pH which hinders PAX uptake as well as iron hydroxide formation. Among many sulfide minerals[108, 109], this adsorption trend with respect to alkaline pH has been well documented in the literature for pyrrhotite, though little information is present on the superstructures[11, 96, 97].

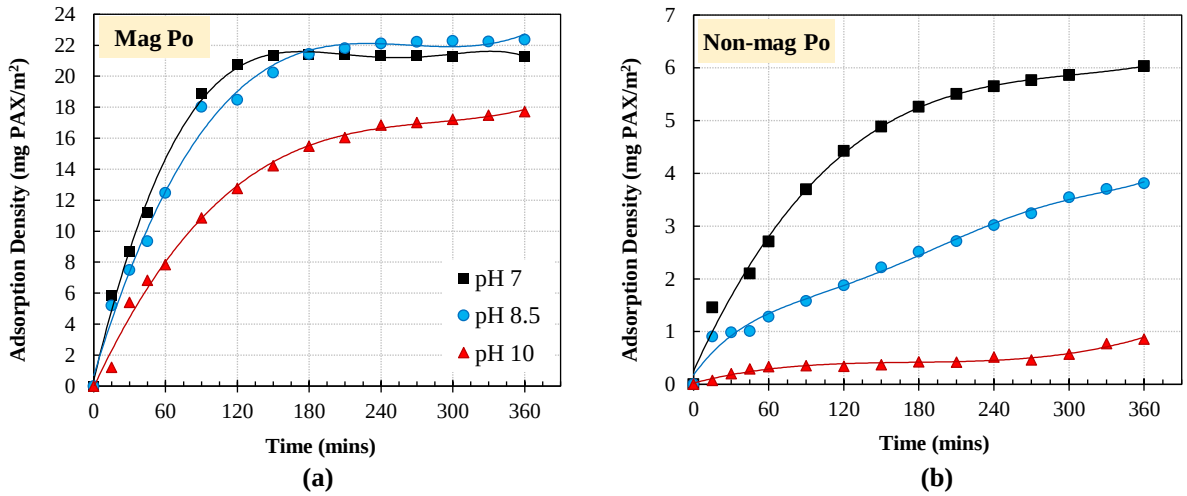

Figure 4.5 *– Mineral PAX adsorption density (mg PAX/m^2) vs. time (mins) from solution initially containing 100 mg/L PAX; (a) magnetic pyrrhotite (Fe_7S_8); (b) non-magnetic pyrrhotite (Fe_9S_{10}).*

With tests completed for several initial PAX concentrations (2, 5, 10, 15, 20, 25, 30, 40, 50, and 100 mg/L), adsorption isotherms were constructed by plotting PAX adsorption density against equilibrium PAX concentration. The results are displayed in **Figure 4.6** for pH 7, 8.5, and 10. Aside from the clear pH dependence (lower pH favouring higher PAX uptake) yielding different isotherms, the major observable difference was the superstructure interaction with PAX as exemplified by their individual isotherms. Magnetic pyrrhotite consistently adsorbed much more xanthate onto its surface compared to non-magnetic pyrrhotite, easily surpassing monolayer coverage in most cases. Furthermore, the isotherm trends were linear with respect to equilibrium PAX concentration, resembling Freundlich-

type isotherms. On the other hand, non-magnetic pyrrhotite PAX uptake was significantly less and generally below monolayer coverage. The isotherms resembled Langmuir-type behaviour that approached monolayer coverage with increasing equilibrium PAX concentration.

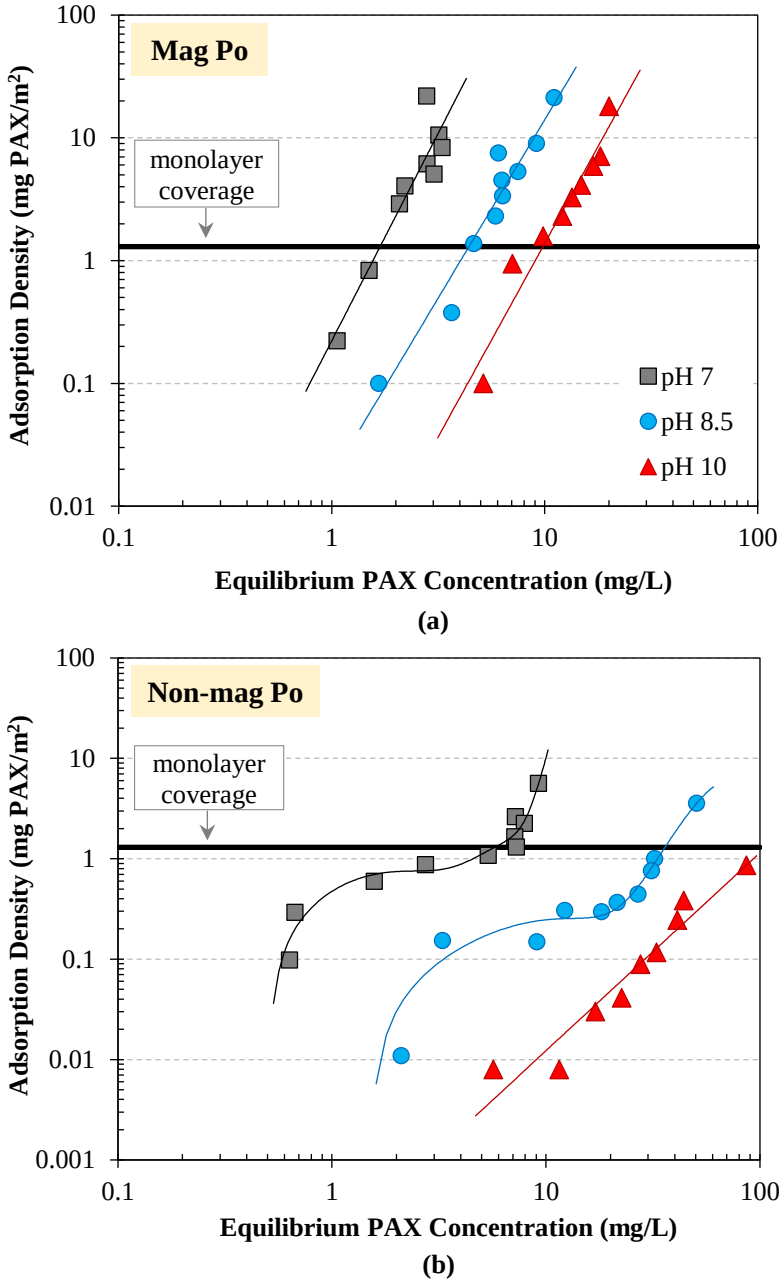

Figure 4.6 *– Adsorption isotherms (PAX adsorption density vs. equilibrium PAX concentration); (a) magnetic pyrrhotite (Fe_7S_8); (b) non-magnetic pyrrhotite (Fe_9S_{10}). Note: black line represents equivalent monolayer PAX coverage on the superstructures.*

To explain the difference in superstructure adsorption, the presence of chalcopyrite (Cp) and pentlandite (Pn) in the samples (**Table 4.1**, –38 μm fraction) was assessed first as they have higher metal–xanthate stability constants and therefore could enhance xanthate uptake. Magnetic pyrrhotite contained 3.7% Cp and 6.3% Pn (~ 10% Cu/Ni sulfides) and non-magnetic pyrrhotite contained 0.7% Cp and 3.5% Pn (~ 4.2% Cu/Ni sulfides). This variation may explain in part the differing superstructure isotherms, especially the Freundlich-type behaviour exhibited by magnetic pyrrhotite as it contained more than five times the Cp content and more than twice the Cu/Ni sulfide content. However, Kolahdoozan (1996), who investigated PAX adsorption onto naturally occurring magnetic pyrrhotite (0.2% Cp, 4.4% Pn, and 91.7% Po) as well as both synthetic superstructures, encountered similar superstructure behaviour as those presented in **Figure 4.6**. The natural magnetic pyrrhotite sample exhibited the highest adsorption densities (with some assistance from Cu/Ni sulfides); interestingly, the synthetic magnetic pyrrhotite PAX uptake was second highest and also far superior to the synthetic non-magnetic pyrrhotite. It appears that magnetic pyrrhotite, irrespective of associated Cu/Ni sulfides, uptakes significantly more PAX than the non-magnetic variety. As discussed previously, the adsorption of xanthate follows a two-step mechanism; initially by physisorption onto Fe(III) sites (*i.e.* $Fe(OH)[S]^{+}$) that produces an Fe-xanthate surface complex after which with sufficient oxygen is oxidized to dixanthogen (chemisorption). Since magnetic pyrrhotite naturally contains more Fe^{3+} in its structure over non-magnetic pyrrhotite (**Table 2.2**) as well as its higher reactivity towards oxygen that would promote Fe^{2+} oxidation to Fe^{3+}, it may be favoured to have a higher PAX adsorption density. This higher xanthate uptake for magnetic pyrrhotite raises a question as to the relative floatability of the superstructures; the expectation being that magnetic pyrrhotite would be significantly more floatable. Interestingly, the general observation in both lab-scale and industrial test work is that non-magnetic pyrrhotite is much more floatable which seems to contradict the xanthate adsorption findings. It is therefore speculated that the xanthate speciation may also be different on the superstructures in that different proportions of Fe(OH)[S][X] and $Fe(OH)[S][X_2]$ are present, the latter of which is significantly more hydrophobic and is the species responsible for enhancing pyrrhotite floatability. Thus, it may

be that non-magnetic pyrrhotite contains more Fe(OH)[S][X_2] (dixanthogen) on its surface. This hypothesis has some validity if open circuit potentials (OCP) of the superstructures are compared; reference to OCP is commonly used to show that in cases where it is higher than the X^-/X_2 redox potential, then oxidation/formation of dixanthogen will occur on the pyrrhotite surface (see Section 2.3.2.3 for more information). The X^-/X_2 redox couple (E_h; standard hydrogen electrode – SHE) may be approximated by Equation (4.4) (for pH > 5):

$$E_h = E_h^o - 0.0591\log[X^-] \quad (4.4)$$

The standard redox potential (E_h^o) for *n*-amyl xanthate is – 0.158V and at typical concentrations (*e.g.* $[X^-] = 10^{-4}$ mol/L) the calculated redox potential (E_h) is 0.078V. Above this value, xanthate oxidation to dixanthogen is favoured. Literature data on OCP of superstructure mineral electrodes has shown differences; Becker (2009) found that at pH 7 non-magnetic pyrrhotite had higher OCP (0.170 V) over magnetic pyrrhotite samples (0.117 – 0.140 V) [13]. Thus, the above data demonstrates the plausibility of more dixanthogen residing on the surface of non-magnetic over magnetic pyrrhotite.

4.3.3 Microflotation

To determine whether the higher xanthate uptake by magnetic pyrrhotite directly correlated to higher flotation recoveries over non-magnetic pyrrhotite (as would be anticipated based on the adsorption studies), microflotation tests were conducted in a modified Hallimond tube. If the results showed similar superstructure recoveries or if non-magnetic pyrrhotite recovery was higher, it would strengthen the argument that different xanthate surface speciation exists on the superstructures. Before superstructure flotation could be compared, preliminary tests were completed to determine mineral sonication pre-treatment time (to remove surface oxidation products) and the PAX dosage at which a difference in superstructure flotation responses could be observed. The results are presented in **Figure 4.7**.

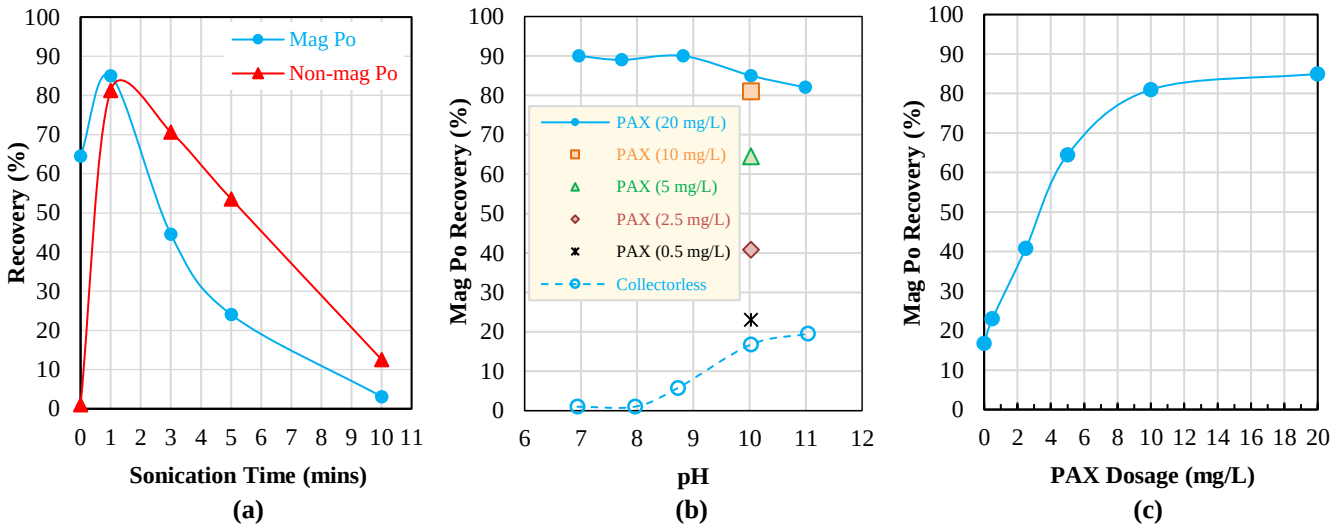

Figure 4.7 *– Preliminary tests; (a) superstructure microflotation recovery (pH 8, PAX = 5 mg/L) as a function of sonication pre-treatment time; (b) magnetic pyrrhtotie (Fe_7S_8) microflotation recovery for pH 7-11 with differerent PAX dosage; (c) magnetic pyrrhtotie (Fe_7S_8) microflotation recovery at pH 10 as a function of PAX dosage.*

The superstructures were subjected to a sonication pre-treatment study (up to 10 mins) in order to determine the minimum sonication time required to "freshen" the surfaces; immediately after sonication the minerals were floated at pH 8 and 5 mg/L PAX (**Figure 4.7**(a)). During mineral purification the powders were partially oxidized, sonication time of ~ 1 min was deemed optimal in cleaning the surfaces after which a decline in recoveries was observed. The decline was the result of re-oxidation of mineral surfaces since the atmosphere was not controlled and oxygen inevitably attacked the surfaces (also accelerated by the higher temperatures, ~ 35 ^{o}C, encountered during prolonged sonication). It is also noted that with increasing sonication time magnetic pyrrhotite exhibited lower recoveries in comparison to non-magnetic pyrrhotite, this was interpreted as the result of higher reactivity of magnetic pyrrhotite towards oxygen that lead to a higher degree of surface passivation (rendering it more hydrophilic) [14]. As ample magnetic pyrrhotite material was available, it was chosen as the test case to determine the ideal PAX dosage at which the superstructures could be compared. With very high PAX dosage (*i.e.* 20 mg/L; ~ 800 g/t), pyrrhotite recovery was virtually the same for pH 7 – 11 (80 – 90 %) as shown in **Figure 4.7**(b). Typically, if the collector dosage is not very high, a decline in pyrrhotite recovery is initiated close to pH 8 after which a significant recovery decrease is observed for pH > 8 (See **Figure 2.16**(a)). Thus,

various PAX dosages (0.5 – 20 mg/L) were trialed at pH 10 as the sensitivity to collector dosage would be highest at this pH since pyrrhotite is very floatable for pH < 8 even at low dosages. The flotation recovery–PAX dosage relationship (pH 10) is displayed in **Figure 4.7**(c). PAX dosage of 2.5 mg/L was chosen for subsequent studies (superstructure comparison) as it lay between the two recovery extremes (collectorless and 20 mg/L PAX dosage).

Microflotation results for the superstructures are presented in **Figure 4.8** with and without 1 min sonication pre-treatment. The data without sonication pre-treatment is presented because it demonstrates the depressing effect of surface oxidation products that were produced during mineral purification and handling prior to test work, leading to erroneous results. The data shows a much higher flotation recovery for magnetic pyrrhotite (both with and without collector) and virtually no flotation response for non-magnetic pyrrhotite. When tested with 1 min of sonication pre-treatment, the flotation responses changed; magnetic pyrrhotite recovery (with collector only) increased (~ 12 %) and non-magnetic pyrrhotite recovery increased drastically (both with and without collector; 20 – 80 % increase).

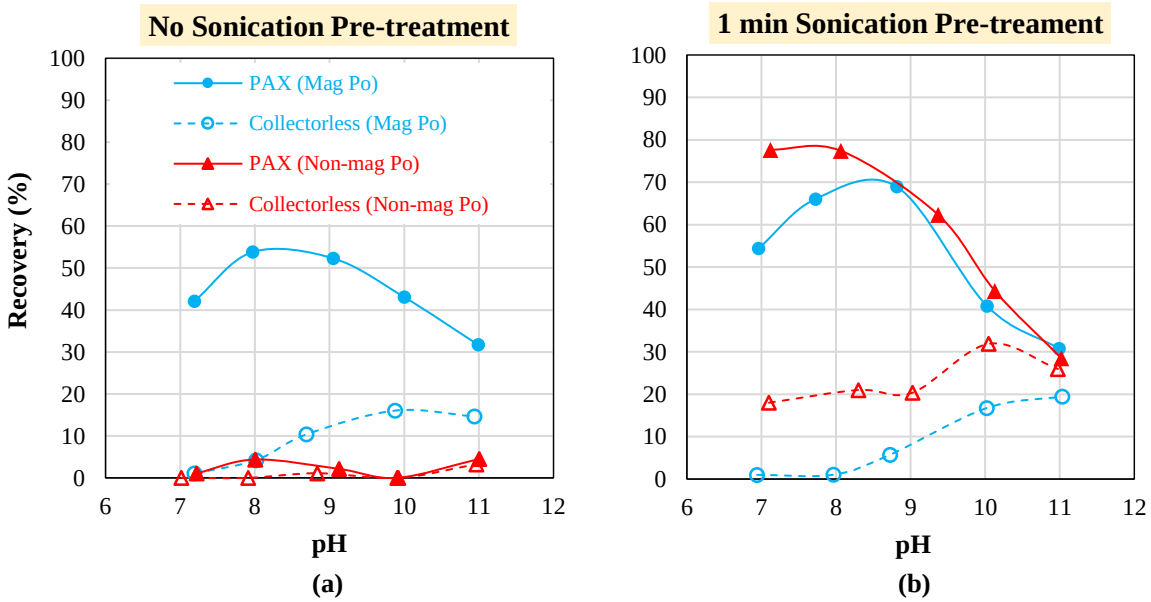

Figure 4.8 *– Pyrrhotite superstructure microflotation recovery as a function of pH (collectorless and PAX = 2.5 mg/L); (a) no sonication pre-treatment; (b) with 1 min sonication pre-treatment.*

Firstly, it is noted that for collectorless flotation, non-magnetic pyrrhotite exhibited higher floatabilities over magnetic pyrrhotite and for both superstructures their recoveries gradually increased with increasing pH. This increase in hydrophobicity may be explained by higher sulfide mineral reactivity at alkaline pH that promotes mineral dissolution and also polysulfide/elemental sulfur formation on pyrrhotite surfaces (under mildly oxidative conditions). The excess surface sulfur (whether it is $Fe(OH)S_2$ or S^o) under these conditions is the species responsible for pyrrhotite's self-induced floatability (see Sections 2.3.1.2 and 2.4.1), a commonly proposed reaction is as follows [8]:

$$Fe_{(1-x)}S + 3(1-x)H_2O \leftrightarrow (1-x)Fe(OH)_3 + S^o + 3(1-x)H^+ + 3(1-x)e^- \quad for\ \ 0 < x \leq 0.125 \qquad (4.5)$$

The above reaction is only applicable to mildly oxidative conditions. Though there is considerable debate as to the actual sulfur species responsible for collectorless floatability, most researchers agree that its formation is directly related to the flotation pulp potential [11]. The literature does not explicitly give the redox range for pyrrhotite's collectorless floatability, however a survey of a few studies gives the range: 0 – 0.300 V (SHE) [8, 20]. The measured pulp potential in the present test work for both superstructures during collectorless flotation dropped linearly from ~ 0.400 to 0.200 V (SHE) for pH 7 to 11, respectively. The potentials incidentally fell into the ideal collectorless flotation range for pH 9 – 11, which appears to coincide with higher collectorless flotation recoveries observed in **Figure 4.8**(b). Though the analysis of redox potentials supports the observation of higher collectorless flotation for pH > 9, it does not explain why non-magnetic pyrrhotite collectorless flotation was consistently higher than magnetic pyrrhotite. It is assumed here that more surface sulfur species (relative to $Fe(OH)_3$) resided on non-magnetic pyrrhotite, however, this requires further investigation.

With sonication pre-treatment and PAX collector, both superstructures exhibited very similar flotation responses. Non-magnetic pyrrhotite recovery was highest in neutral to mildly alkaline pH (7 – 8) after which a steep decline was observed with higher pH as anticipated, matching collectorless flotation at pH 11. As discussed previously, the steep

decline was due to much lower xanthate uptake at higher pH (OH^- interference) as well as increased hydrophilic $Fe(OH)_3$ formation on the mineral surface. Magnetic pyrrhotite flotation was similar, however, a recovery maximum was observed between pH 8 and 9. Leppinen (1990) also observed similar behaviour for magnetic pyrrhotite, two recovery peaks were noted; first at pH 3 and a second smaller peak at pH 8 [110]. Moreover, a much larger flotation maximum was observed between pH 7 and 9 when magnetic pyrrhotite was activated by $CuSO_4$ (reproduced in **Figure 4.9**), suggesting that the behaviour is amplified by trace ions.

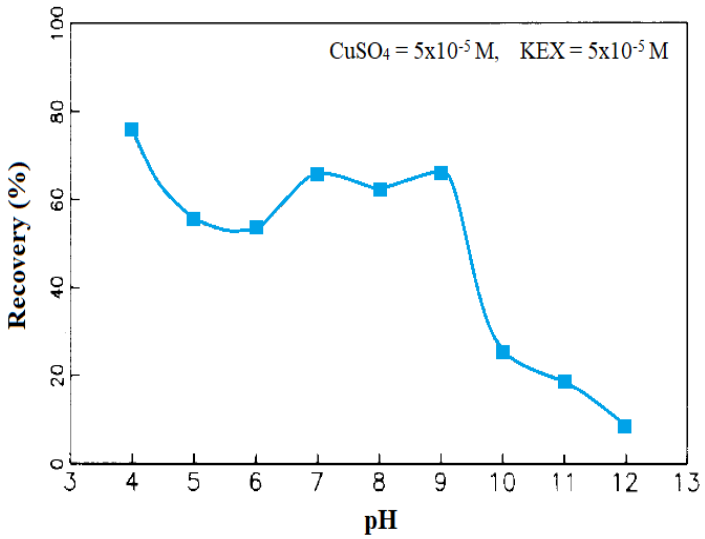

Figure 4.9 *– Magnetic pyrrhotite (Fe_7S_8) microflotation recovery after 5x10^{-5}mol/L $CuSO_4$ activation (5x10^{-5}mol/L KEX collector), modified from Leppinen (1990)[110].*

From **Table 4.1** it is noted that for the microflotation samples the magnetic pyrrhotite contained trace chalcopyrite (1.2% average) whereas non-magnetic pyrrhotite did not. Aside from the chalcopyrite influence, based on the data in **Figure 4.7**(b,c) and **Figure 4.8**(b), this flotation behaviour is also likely due to xanthate concentration (amount of dixanthogen on surface) and the amount of hydrophobic sulfur species on the surface. At neutral to mildly alkaline pH, xanthate uptake is high though little surface sulfur species is present relative to pH 9 – 11 as demonstrated by collectorless flotation. With pH increase, xanthate uptake is lowered yet surface sulfur species has increased, which may be the ideal situation for flotation since sufficient dixanthogen as well as hydrophobic sulfur species are present that render magnetic pyrrhotite more floatable over other pH conditions. With very

high pH, xanthate uptake is extremely low and even with higher surface sulfur, magnetic pyrrhotite flotation is reduced and is lowest overall. This flotation behaviour of magnetic pyrrhotite may be a special case that stems from the use of low xanthate concentration (2.5 mg/L) and interestingly not observed for non-magnetic pyrrhotite at the same concentration, again suggesting lower amounts of dixanthogen on magnetic pyrrhotite relative to non-magnetic pyrrhotite. As shown in **Figure 4.7**(b), this peculiar behaviour can be overcome with higher xanthate concentration (*e.g.* 20 mg/L) which yields a flotation response for magnetic pyrrhotite that is commonly observed for pyrrhotite under high collector dosage conditions (fairly consistent for pH 7 – 11) [11].

Overall, forgoing the peculiar behaviour of magnetic pyrrhotite between pH 7 and 9 occurring at what is interpreted as low collector dosage (also attributed to the amount of hydrophobic sulfur species and trace chalcopyrite), the two superstructures largely exhibit the same flotation responses when surface oxidation products are removed prior to flotation. Under certain circumstances (*i.e.* at low collector concentration), the superstructure flotation can differ slightly and is credited to the amount of dixanthogen present on the superstructures (non-magnetic proposed to have more dixanthogen) that leaves non-magnetic pyrrhotite somewhat more floatable. Kolahdoozan (1996) observed near-identical flotation responses for both synthetic superstructures, supporting the findings from this test work [11]. Becker (2009) found non-magnetic pyrrhotite more floatable with and without xanthate collectors, which the researcher states that the difference in floatability was credited to superstructure reactivity towards oxygen (oxidation) though many other mineralogical factors can also influence the outcome such as trace element content (Fe^{3+} and Ni^{2+}) and mineral associations [13, 14]. Taking the results of these studies into account, it appears that when surface oxidation products are removed and sufficient xanthate is present (permitting adequate dixanthogen), magnetic and non-magnetic pyrrhotite superstructures behave virtually the same, however, in real systems (*i.e.* industrial operation) where surface oxidation is inevitable their flotation will differ significantly [16].

4.4 Summary

4.4.1 Zeta Potential

Zeta potential analysis of freshly ground pyrrhotite superstructures in the virtual absence of oxygen demonstrated that their isoelectric points (IEP) were identical (pH_{IEP} ~ 3.5) and that they have the same surface potential curves over the tested pH range (2 – 11). The superstructures are expected to have different zeta potential curves in the presence of oxygen due to their different reactivities; magnetic pyrrhotite having much higher reactivity and therefore would exhibit a higher pH_{IEP}. With $NiSO_4$ and $CuSO_4$ activators, surface potentials were increased into the positive region for both superstructures; the increase was most significant where the superstructure potentials (without reagents) were negative, indicating electrostatic adsorption of nickel and copper ions. Based on speciation curves, major adsorbing species were believed to be Ni^{2+}, $Ni(OH)^{+}$, Cu^{2+} and $Cu(OH)^{+}$. With PAX collector, the largest effect on surface potentials was below pH 3.5 where the superstructures were net positively charged and free xanthate was negatively charged. Thus, below pH 3.5, electrostatic adsorption of free collector (X^{-}) significantly lowered surface potentials (forming Fe(OH)[S][X] surface complex), yielding similar curves for both superstructures. For pH > 3.5, surface potentials were lowered slightly and remained the same even when the solution was aerated (promoting dixanthogen formation). The suggested adsorption mechanism in the literature appears to be valid (xanthate initially adsorbing by physisorption and may subsequently convert to dixanthogen given that sufficient oxygen is present). To determine the extent of adsorption for pH > 7 where pyrrhotite flotation is generally conducted, PAX adsorption studies were completed at pH 7, 8.5, and 10.

4.4.2 PAX Adsorption

With increasing pH (7 to 10), the rate of PAX adsorption and final equilibrium adsorption density (mg PAX/m^2) decreased; both of which were the result of increasing OH^{-} concentration at higher pH as well as iron hydroxide formation that hindered PAX uptake. Aside from the clear pH dependence yielding different isotherms, the major observable difference in the data was the superstructure interaction with PAX. Magnetic pyrrhotite

consistently adsorbed much more xanthate onto its surface as compared to non-magnetic pyrrhotite, the former easily surpassed monolayer coverage in most cases while the latter generally remained below monolayer coverage.

The adsorption of xanthate follows a two-step mechanism; initially by physisorption onto Fe(III) sites (*i.e.* $Fe(OH)[S]^{+}$) that produces an Fe(III)-xanthate surface complex after which with sufficient oxygen is oxidized to dixanthogen (chemisorption). Since magnetic pyrrhotite naturally contains more Fe^{3+} in its structure over non-magnetic pyrrhotite as well as its higher reactivity towards oxygen that would promote Fe^{2+} oxidation to Fe^{3+}, it may be favoured to have a higher PAX adsorption density.

From a flotation standpoint, this higher PAX uptake by magnetic pyrrhotite appeared to contradict the flotation trends observed in the literature. The majority of lab-scale and industrial data in the literature shows that non-magnetic pyrrhotite is much more floatable (in some cases superstructure flotation is the same), thus it was speculated that the xanthate speciation may also be different on the superstructures. It was hypothesized that different proportions of Fe(OH)[S][X] and $Fe(OH)[S][X_2]$ are present on the superstructures, the latter of which is significantly more hydrophobic. Thus, the case may be that non-magnetic pyrrhotite contains more $Fe(OH)[S][X_2]$ (dixanthogen) on its surface. To determine whether the higher PAX uptake by magnetic pyrrhotite directly correlated to higher flotation recoveries over non-magnetic pyrrhotite, microflotation studies were conducted.

4.4.3 Sonication Pre-Treatment and Microflotation

Sonication pre-treatment of the superstructure powders was deemed necessary to remove surface oxidation products (produced during mineral purification and handling) prior to flotation, as without sonication the flotation results were clearly erroneous (non-magnetic pyrrhotite did not float at all even with collector). About 1 min of sonication was found to be optimal where higher sonication times gave declining recoveries; this was due to re-oxidation of superstructure surfaces as the oxygen would inevitably attack the fresh surfaces and form hydrophilic iron hydroxides.

Superstructure collectorless flotation was found to be different where non-magnetic pyrrhotite was more floatable in the pH range 7 – 11. For both superstructures, a gradual

increase in recovery was observed with increasing pH. This was interpreted as the result of the redox potential being in the ideal collectorless flotation range (0 – 0.300 V) for pH > 9 that promoted the formation of hydrophobic sulfur species on the superstructure surfaces.

In the presence of PAX collector, the superstructures largely exhibited the same flotation responses when surface oxidation products were removed prior to flotation. Under certain circumstances (*i.e.* at low collector concentration), their flotation differed slightly which was credited to the amount of dixanthogen present on the superstructures (with some influence from hydrophobic sulfur species and trace chalcopyrite content). Non-magnetic pyrrhotite was proposed to have more dixanthogen which rendered it somewhat more floatable over magnetic pyrrhotite. Nonetheless, under most conditions, "fresh" superstructures are predicted to float similarly and would differ when they are allowed to oxidize prior to flotation.

4.5 Key Findings

Overall, zeta potential analysis of the superstructures demonstrated their similar behaviour for pH < 9 (minerals alone and in the presence of Ni^{2+}, Cu^{2+}, and PAX collector) when their surfaces are "fresh". The results also supported xanthate adsorption by an initial physisorption mechanism. PAX adsorption studies demonstrated that xanthate uptake was much higher for magnetic over non-magnetic pyrrhotite for all pH conditions tested (7, 8.5, and 10). This lead to the hypothesis that different proportions of Fe(OH)[S][X] and Fe(OH)[S][X_2] (dixanthogen) are present on the superstructures and that non-magnetic pyrrhotite likely contains more dixanthogen as it is commonly cited to be more floatable. This area requires further investigation, perhaps by Fourier-transform Infrared Spectroscopy (FT-IR) to identify the xanthate speciation on superstructure surfaces. Microflotation investigations showed that when surface oxidation products are removed and sufficient xanthate is present (permitting adequate dixanthogen), magnetic and non-magnetic pyrrhotite superstructures behave virtually the same. It is acknowledged that in real systems (*i.e.* industrial operation) where surface oxidation is inevitable, superstructure flotation will differ significantly due to their different reactivities towards oxygen. Non-magnetic pyrrhotite is

projected to be more floatable under such conditions. To investigate this area further and mimic real systems, larger-scale (1 – 2 kg) batch flotation tests were pursued on well characterized ore samples.

Chapter 5
Batch Flotation Study #1

5.1 Introduction

The single mineral studies in the previous Chapter investigated superstructure surface-reagent interactions as well as their microflotation responses under ideal conditions (fresh mineral surfaces). The results demonstrated that the superstructures do exhibit surface chemical differences, though these differences did not directly translate to their flotation behaviour. Under the *idealized* test conditions, the superstructures exhibited very similar flotation responses. The next step was to investigate the superstructures in bench-scale flotation tests (2 separate studies) as these would be more representative of plant practices (*e.g.* freshly ground ore followed by immediate flotation) and would provide valuable information on superstructure floatability in *real systems* where mineral oxidation (as well as interactions with other minerals and grinding media) was allowed to take place.

This Chapter summarizes the results and major findings of the first batch flotation study with and without DETA/SMBS depressants, comparing 4 Cu-Ni sulfide ores having different non-magnetic/magnetic pyrrhotite ratios (5/95, 30/70, 50/50, 95/5%). The study also investigated superstructure flotation recovery-by-size in order to reproduce industrial results and assess the effects of DETA/SMBS depressant combination on both superstructures.

5.2 Objectives

Four Cu-Ni sulfide ores were sourced from the Sudbury Basin; each having a different non-magnetic/magnetic pyrrhotite ratio (5/95, 30/70, 50/50, 95/5%). The major objectives of this study were as follows:

(1) Compare ores based on feed superstructure ratio
Effect of pyrrhotite superstructure content on Cu/Ni metallurgy (also Po-Pn selectivity) and final pyrrhotite recovery

(2) Compare superstructure flotation and recovery-by-size relationship
Do they float differently? Is there a higher non-magnetic pyrrhotite recovery in coarse fraction and high magnetic pyrrhotite in the fine fraction?

(3) Effect of DETA/SMBS depressants on the superstructures
Is it possible to alter the superstructure recovery-by-size relationship using conventional depressants?

This study was completed in two parts; the first was a preliminary investigation to observe pyrrhotite superstructure behaviour and refine reagent dosages and the second part was a more in-depth analysis and incorporated DETA/SMBS depressants. For all tests, the samples were also split into coarse and fine fractions (+38 and –38μm) to understand the recovery-by-size relationship. The float procedures and characterization techniques/instrumentation can be found in Chapter 3 (Sections 3.1.2.1 and 3.2).

5.3 Feed Mineralogy

The head assay for each ore is displayed in **Table 5.1** and the modal mineralogy and nickel deportment are presented in **Table 5.2**. The data essentially confirms that the major sulfides in each ore were chalcopyrite, pentlandite, and pyrrhotite. The majority of the gangue was represented by silicate minerals. Though there were differences among all the ores, Ores B, C, and D were fairly similar, having total sulfide content between 38 – 47% (somewhat similar head assays). Ore A was quite different than the rest, being a low-grade ore, only ~ 19% was accounted by sulfides and the remainder being almost entirely silicate gangue. This stark difference was also reflected in the mineral nickel deportment data; showing similar

nickel deportment for Ores B, C, and D (92 – 95% Ni into pentlandite and 5 – 8% Ni in pyrrhotite), whereas Ore A only had ~ 81% Ni as pentlandite, the remainder being in pyrrhotite. This relationship is commonly observed for low grade ores (**Figure 5.1**) where a significant amount of the nickel is hosted in pyrrhotite (presumably as solid solution).

The ores were ground to the target grind distribution (P80 ≈ 75 μm) and cyclosized; both the size-by-size superstructure ratios (**Figure 5.2**) and modal mineralogy (**Figure 5.3** – **Figure 5.6**) were analyzed. As expected, for each ore the head assay superstructure ratio was essentially maintained at every size class (minor discrepancy observed for Ore C; the non-magnetic/magnetic pyrrhotite ratio was closer to 55/45% rather than 50/50%). This was a necessary step which verified that selective grind of magnetic over non-magnetic pyrrhotite did not occur and therefore would not be responsible for magnetic and non-magnetic pyrrhotite recovery in the fine and intermediate size classes, respectively.

Table 5.1 *– Ore description and composition (elemental and mineral assays). Mineral assays calculated assuming 0.8 wt% Ni in Po. Note: Non–mag Po =* Fe_9S_{10} *and Mag Po =* Fe_7S_8*.*

Ore Description		Elements (wt%)			Minerals (wt%)						
		Cu	Ni	S	Cp	Pn	Po	% Non-mag Po	% Mag Po	Ga	Po/Pn
Ore A	5% Non-Mag Po	0.46	0.76	7.53	1.3	1.8	16.5	**5**	**95**	80.3	9.0
Ore B	30% Non-mag Po	1.86	3.43	15.05	5.4	9.4	25.7	**30**	**70**	59.5	2.7
Ore C	50% Non-mag Po	3.18	2.67	12.94	9.2	7.4	18.7	**50**	**50**	64.8	2.5
Ore D	95% Non-mag Po	3.04	2.57	15.97	8.8	6.9	27.2	**95**	**5**	57.1	4.0

Table 5.2 *– Ores A, B, C, and D: (Left) modal mineralogy; (right) nickel deportment.*

Mineral	Ore A	Ore B	Ore C	Ore D
Chalcopyrite	1.31	5.87	10.27	9.19
Pentlandite	1.61	9.29	7.63	6.91
Pyrrhotite	15.25	24.09	19.67	30.38
Pyrite	0.13	0.00	0.00	0.01
Cubanite	0.01	0.05	0.06	0.07
Bornite	0.01	0.02	0.01	0.01
Sphalerite	0.01	0.02	0.03	0.03
Other Sulfides	0.46	1.24	0.15	0.22
Total Sulfide & PM	**18.80**	**40.58**	**37.85**	**46.82**
Olivine	0.02	0.89	0.14	0.19
Orthopyroxene	0.02	5.55	0.12	0.05
Clinopyroxene	18.64	2.78	0.18	0.64
Amphibole	22.37	15.27	3.78	17.65
Epidote	8.91	0.12	0.75	0.49
Chlorite	14.42	0.12	0.49	1.59
Biotite	0.50	4.32	7.45	8.10
Muscovite	1.03	0.04	0.25	0.13
Quartz	4.00	6.14	17.17	7.81
Plagioclase	9.39	16.70	17.76	11.60
Kspar	0.13	3.36	9.94	2.05
Other Silicates	0.49	0.29	1.14	0.75
Total Silicates	**79.92**	**55.58**	**59.18**	**51.05**
Apatite	0.09	0.25	0.23	0.29
Magnetite	0.15	2.63	1.25	0.89
Ilmenite	0.11	0.53	0.06	0.39
Calcite	0.85	0.19	1.05	0.30
Other Oxides	0.08	0.23	0.37	0.26
Total Phosphate, oxide, carb, other	**1.27**	**3.85**	**2.97**	**2.13**

Mineral	Ore A	Ore B	Ore C	Ore D
Pentlandite	81.42	94.22	95.17	91.86
Pyrrhotite	18.03	5.67	4.82	8.06
Pyrite	0.51	0.00	0.00	0.03
Millerite	0.04	0.10	0.02	0.05

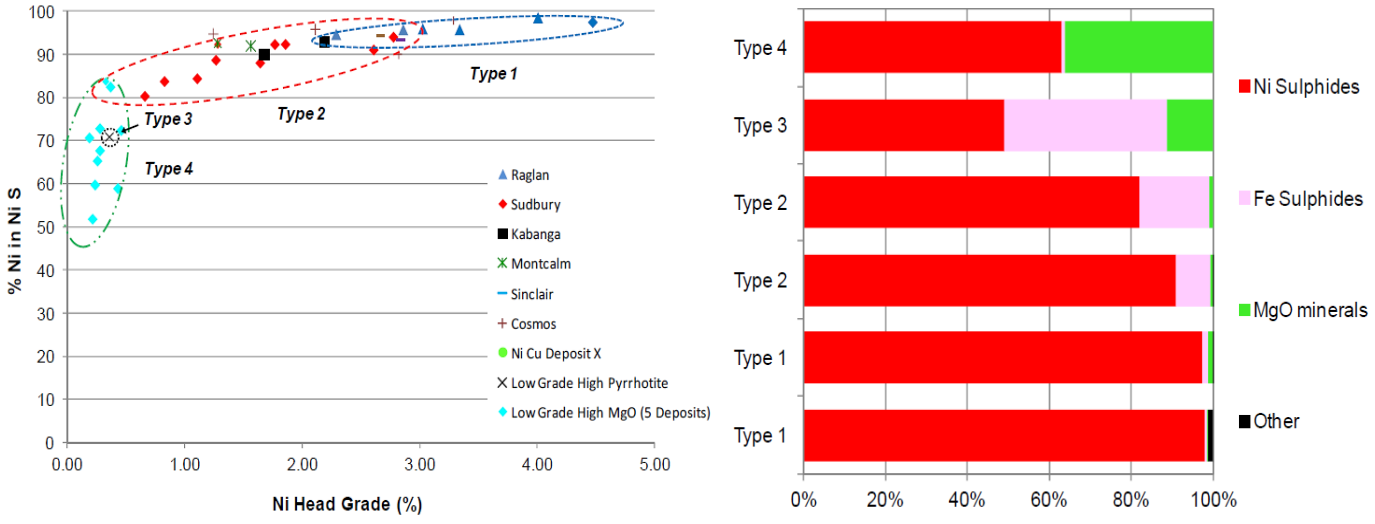

(a) **(b)**

Figure 5.1 *– (a) Nickel as nickel sulfide (i.e. pentlandite and millerite) versus nickel head grade; (b) nickel deportment for different ore types. Reproduced from Lawson et al. (2014)* [16].

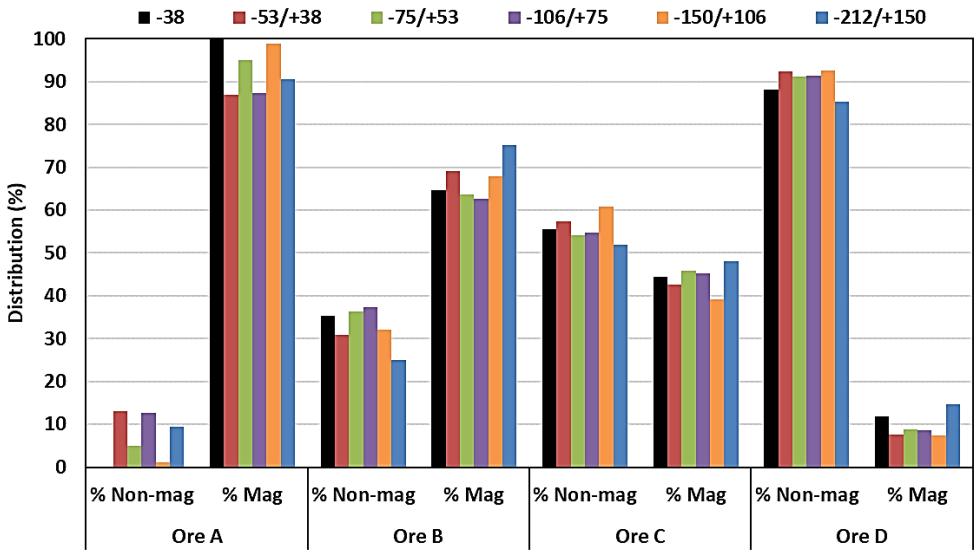

Figure 5.2 *– Ores A, B, C, and D superstructure ratio by size class.*

Size-by-size mineralogy verified that the sulfides were reporting to size classes below 106 µm – in other words, the chosen target grind was adequate and ideal for batch flotation testing. The sulfides were well distributed across all size classes below 106 µm; pyrrhotite reported to slightly higher size classes than pentlandite and chalcopyrite, which was favourable for separation. The ores were also analyzed for mineral liberation and associations to determine if any unfavourable particle locking situations were present. Sulfide mineral liberation/association data is presented for the unsized feed samples in **Table 5.3**, liberation/association data by size class was placed in Appendix B to conserve space (**Figure B1** – **Figure B12**). All ores exhibited at least 75% sulfide mineral liberation, which was suitable for flotation testing and assessing flotation trends/selectivities. Ore A had the lowest pentlandite and chalcopyrite liberation characteristics; Ores B and C had the lowest pyrrhotite liberation. Majority of pentlandite locking was with pyrrhotite (~ 18% for Ore A and < 5% for Ores B, C, and D). Chalcopyrite locking was with all minerals (1 – 2% in most cases), no particular trend was identified. Pyrrhotite locking was primarily with gangue minerals (1 – 14%), second highest association was with pentlandite (1 – 4%). For each ore, below 106 µm, liberation by size class was very similar for all sulfides, the exception being pentlandite in Ore A (liberation increased from ~ 47% to 84% when comparing –106/+75 to –3 µm; **Figure B1**). Batch flotation tests were initiated and are summarized in the next Section.

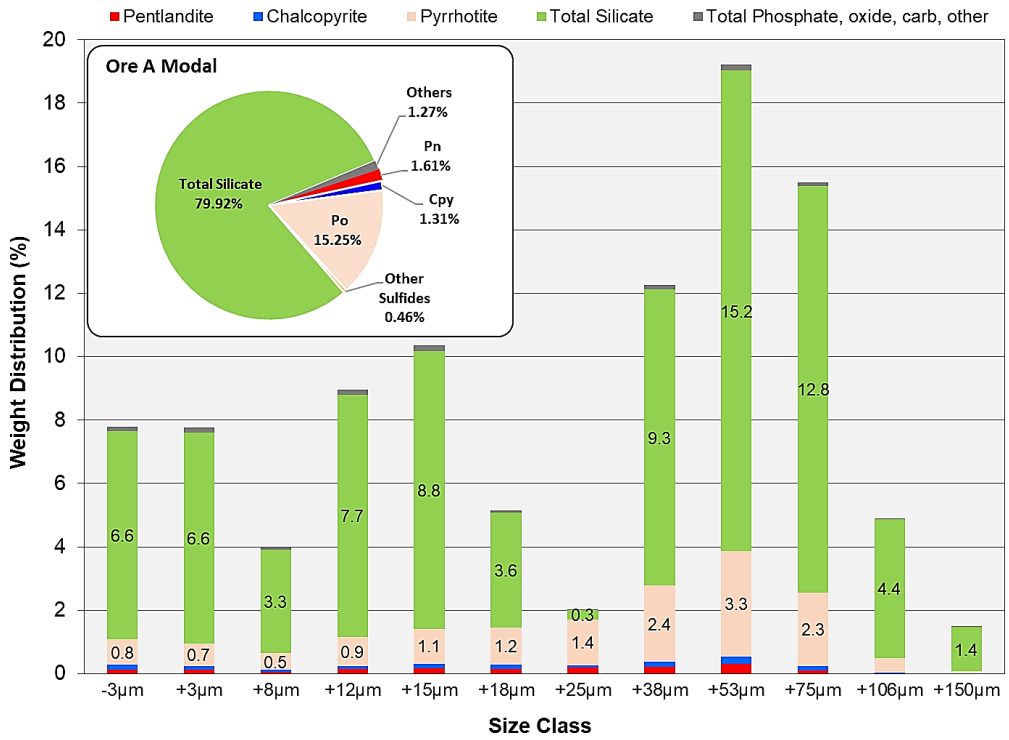

Figure 5.3 *– Ore A modal mineralogy by size class (weight % of feed). Note: figure inset displays the unsized modal mineralogy.*

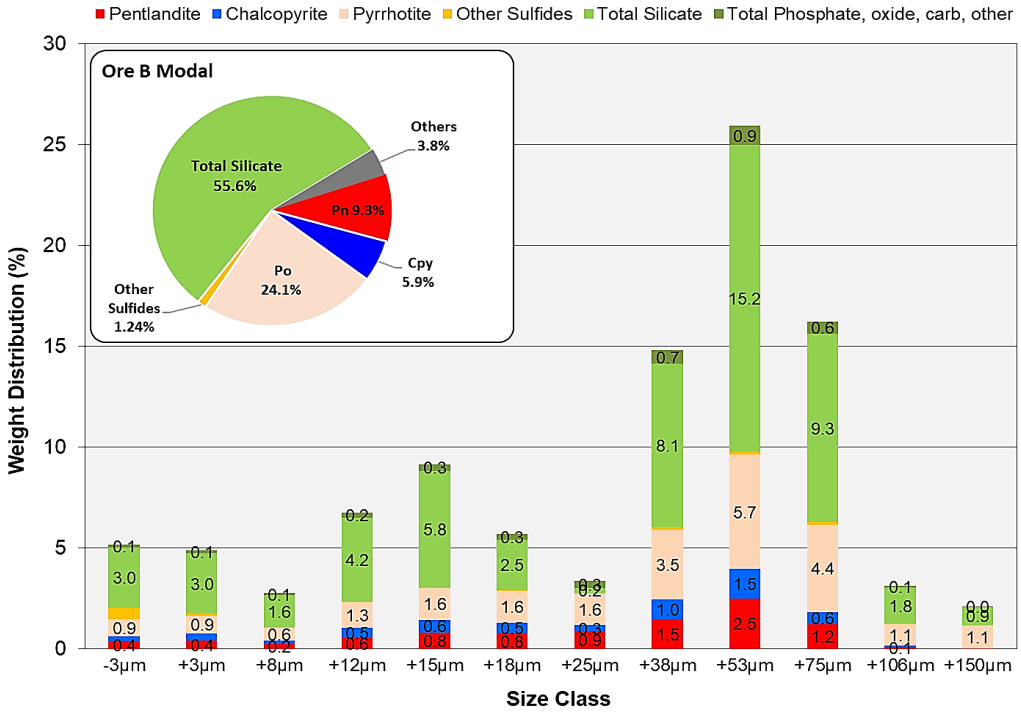

Figure 5.4 *– Ore B modal mineralogy by size class (weight % of feed). Note: figure inset displays the unsized modal mineralogy.*

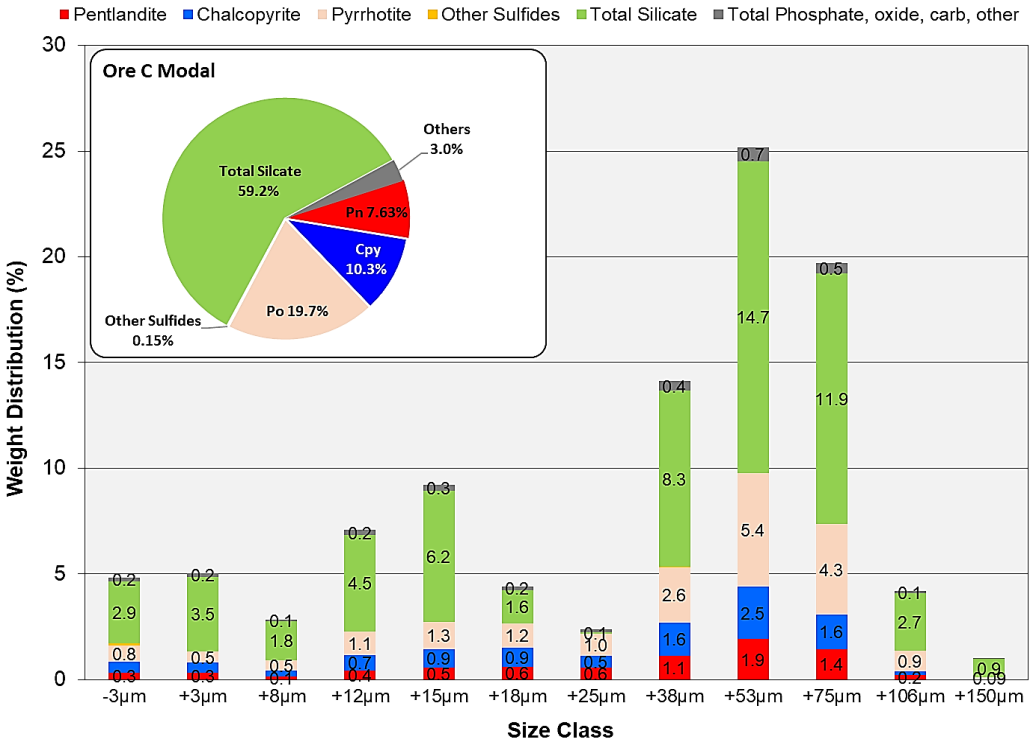

Figure 5.5 *– Ore C modal mineralogy by size class (weight % of feed). Note: figure inset displays the unsized modal mineralogy.*

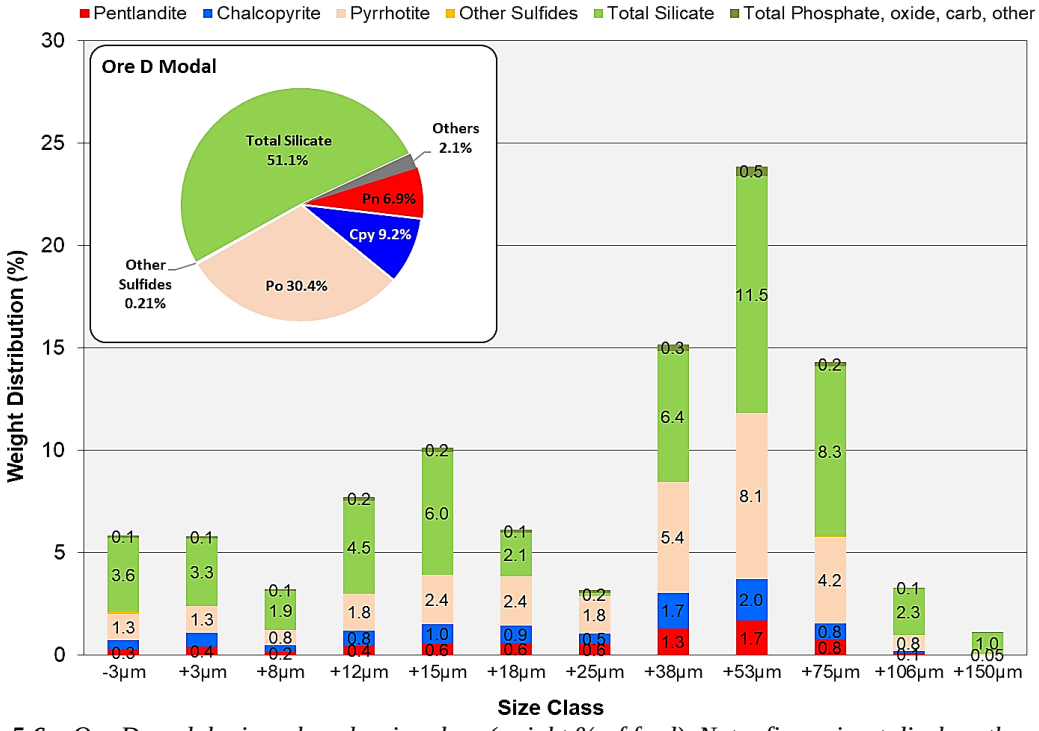

Figure 5.6 *– Ore D modal mineralogy by size class (weight % of feed). Note: figure inset displays the unsized modal mineralogy.*

Table 5.3 *– Ores A, B, C, and D pentlandite, chalcopyrite and pyrrhotite mineral liberation and associations.*

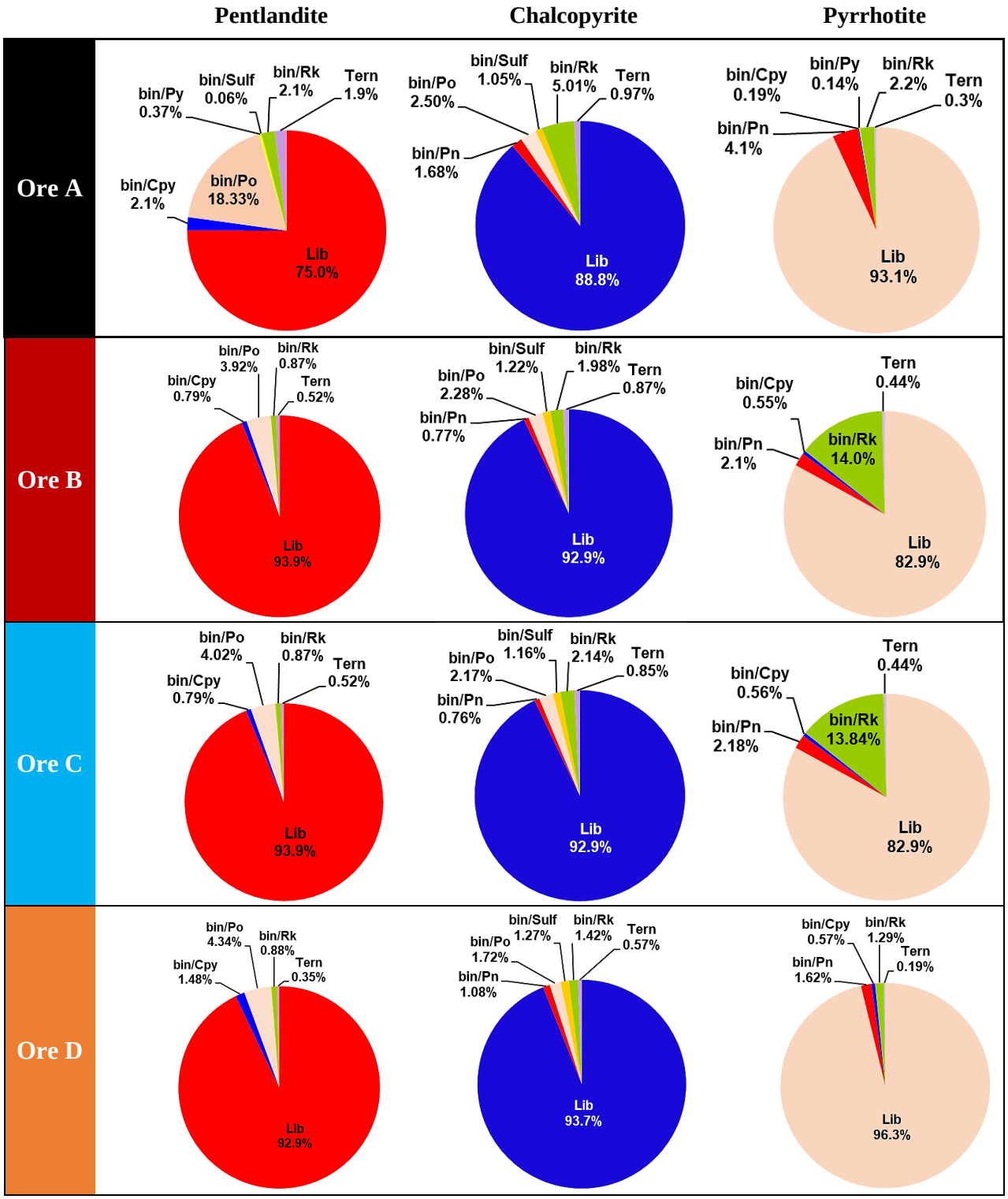

5.4 Preliminary Study (Baseline Tests)

Preliminary flotation tests were conducted to assess the pyrrhotite superstructure behaviour from the different ores and to refine the reagent scheme for a more in-depth study. All four ores were initially floated using the same amount of collector, with subsequent testing conducted with different collector dosages (calculated based on individual ore head grades). The grade-recovery curves and mineral flotation kinetics data can be found in Appendix B (**Figure B13** – **Figure B15**) and only key plots are presented in this Section. The cumulative concentrate metal grades could not be readily compared as the ores had different head grades, however concentrate upgrade ratio comparisons were taken to be an appropriate basis (**Figure B15**). The data shows that with increasing non-magnetic pyrrhotite ratio in the feed (from Ore A to D) the concentrate upgrade ratio decreased, with Ore D exhibiting the lowest upgrade ratio, the differences however were not substantial. Pyrrhotite flotation was then split into its non-magnetic and magnetic pyrrhotite curves, the kinetics data (**Figure B14**) clearly shows a difference in superstructure floatability with non-magnetic pyrrhotite being much more floatable regardless of the ore, supporting the many accounts in the literature that non-magnetic pyrrhotite is more floatable in *real systems*. Final pyrrhotite recovery was variable and it was difficult to place a trend based on ore superstructure ratio; each ore feed contained a different pyrrhotite content and therefore it was believed that residual collector on pyrrhotite (left over after chalcopyrite and pentlandite uptake) for each ore would also be different. Thus, collector dosage based on ore head grades was a better strategy and implemented for the in-depth study. Nonetheless, to compare the preliminary study pyrrhotite recovery as a function of superstructure ratio, one option was to normalize pyrrhotite behaviour by assessing the pyrrhotite (Po)-pentlandite (Pn) selectivity. Evaluation of pyrrhotite recovery from each ore at fixed pentlandite recovery was chosen to mitigate collector adsorption effects. Industrial operations generally achieve pentlandite recoveries of 80 – 85% (at final Ni concentrate grade), though a regrind circuit is commonly incorporated. For the purposes of this test work (equivalent to a primary and secondary rougher test) 85% pentlandite recovery was selected as the basis of comparison [16]. From the Po–Pn selectivity curves (**Figure 5.7**(a)) at 85% pentlandite, Ores B and C gave identical pyrrhotite recovery

(~ 20%) and Ore D gave the highest recovery (~ 30%), Note: Ore A selectivity fell between all the curves and thus not shown; excessive collector dosage, pyrrhotite binary locking and high nickel deportment were taken to be the likely causes for the poor correlation to its superstructure ratio. While pyrrhotite recovery differences among Ores B, C, and D was not substantial (at 85% pentlandite), the data suggested that for feeds containing high non-magnetic pyrrhotite ratio (> 50%) the Po–Pn selectivity becomes poorer. As "total pyrrhotite" is the weighted sum of the two superstructure curves, to assess individual superstructure behaviour, selectivity curves were re–evaluated by splitting total pyrrhotite into its pyrrhotite superstructure curves, re-plotted data is presented in **Figure 5.7**(b). The updated curves show poorer pentlandite selectivity against non-magnetic over magnetic pyrrhotite, which was consistent for all the ores. Furthermore, regardless of ore type, non-magnetic pyrrhotite curves were virtually the same, likewise, all magnetic pyrrhotite curves were the same. To show the striking consistency across the ores, all non-magnetic and magnetic pyrrhotite selectivity data was plotted (**Figure 5.8**). This data demonstrates that the observed superstructure behaviour is directly related to crystallography since their flotation performance was seen to be identical for many different ores (not to say secondary effects such as mineral locking and nickel deportment do not play a role). Since total pyrrhotite is the sum of the superstructures, the data implies that increasing non-magnetic pyrrhotite content from one ore to another would result in a proportional decrease in selectivity.

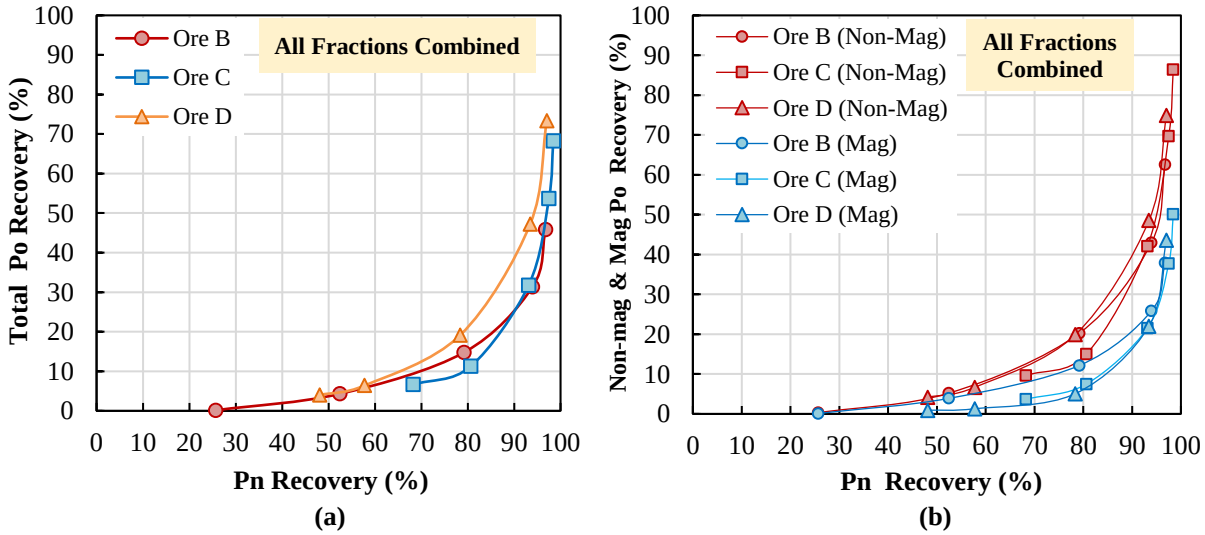

Figure 5.7 *– Preliminary study Po–Pn selectivity; (a) total Po vs. Pn; (b) Non–mag & Mag Po vs. Pn.*

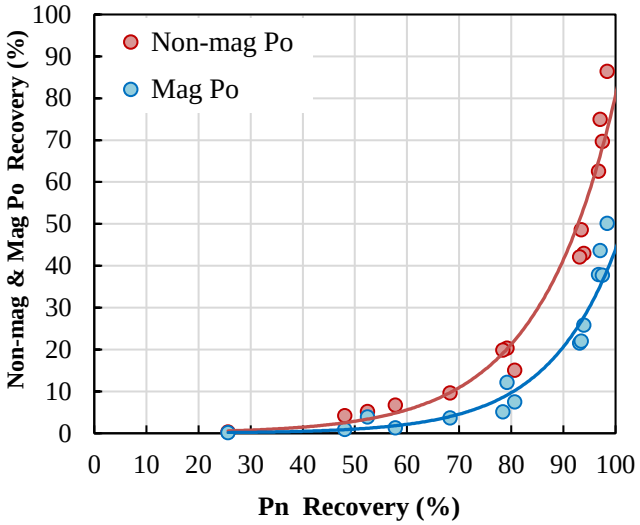

Figure 5.8 *– Preliminary study Po-Pn selectivity – Non–mag & Mag Po vs. Pn recovery.*

By examining plant data from several Cu–Ni sulfide concentrators, Lawson *et al.* (2014) identified an interesting relationship between superstructure flotation and particle size (**Figure 2.19**) [16]. The authors determined that the superstructure recovery trend was consistent across several concentrators, suggesting the behaviour was largely a crystallographic effect rather than an isolated event at a specific concentrator. Non–magnetic pyrrhotite was mainly recovered in the intermediate size range (10 – 100 µm) where it was found to have much higher flotation recovery over magnetic pyrrhotite, whereas in the fine fractions (< 10 µm) magnetic pyrrhotite recovery was superior. There are many reasons for this behaviour, the primary being superstructure reactivity towards oxygen. It has been identified by Becker (2009) and Becker *et al.* (2010), among other researchers, that magnetic pyrrhotite is much more reactive and more prone to surface oxidation, thus it is well depressed in flotation due to a larger surface density of ferric hydroxides in comparison to non-magnetic pyrrhotite [13, 14]. For the fine fraction trend (magnetic pyrrhotite being more floatable), a compelling explanation is yet to be presented, however, incomplete fine pyrrhotite oxidation (large surface areas requiring more oxygen) and thus allowing collector attachment has been proposed as a possible mechanism. Part of the present test work was to investigate this superstructure behaviour in the fine/coarse size fractions; the flotation products were split at 38 µm, where –38 and +38 µm were labelled as fine and coarse

fractions, respectively. **Figure 5.9**(a) and **Figure 5.10**(a) display the fine and coarse fraction Po–Pn selectivity (total pyrrhotite), respectively, showing much poorer selectivity in the fines over coarse sizes. This result was not surprising as it is known that fine pentlandite has poor to mediocre floatability where incidentally pyrrhotite is still sufficiently floatable. The total pyrrhotite was again separated into its superstructure curves (**Figure 5.9**(b) and **Figure 5.10**(b)). In the fines fraction, pentlandite selectivity was slightly worse against non-magnetic pyrrhotite (different result compared to Lawson *et al.* (2014)), some overlapping from magnetic pyrrhotite curves can be seen as well. Ores B – D gave similar non-magnetic pyrrhotite curves whereas magnetic pyrrhotite curves were all different, decreasing selectivity with increasing magnetic pyrrhotite content in the feed. These results showed that non-magnetic pyrrhotite was slightly more floatable in the fines, however a definitive statement could not be made due to overlapping superstructure curves. Coarse fraction superstructure selectivity resembled the results of **Figure 5.7**(b), where pentlandite selectivity against non-magnetic was poorer over magnetic pyrrhotite (similar results across Ores B – D).

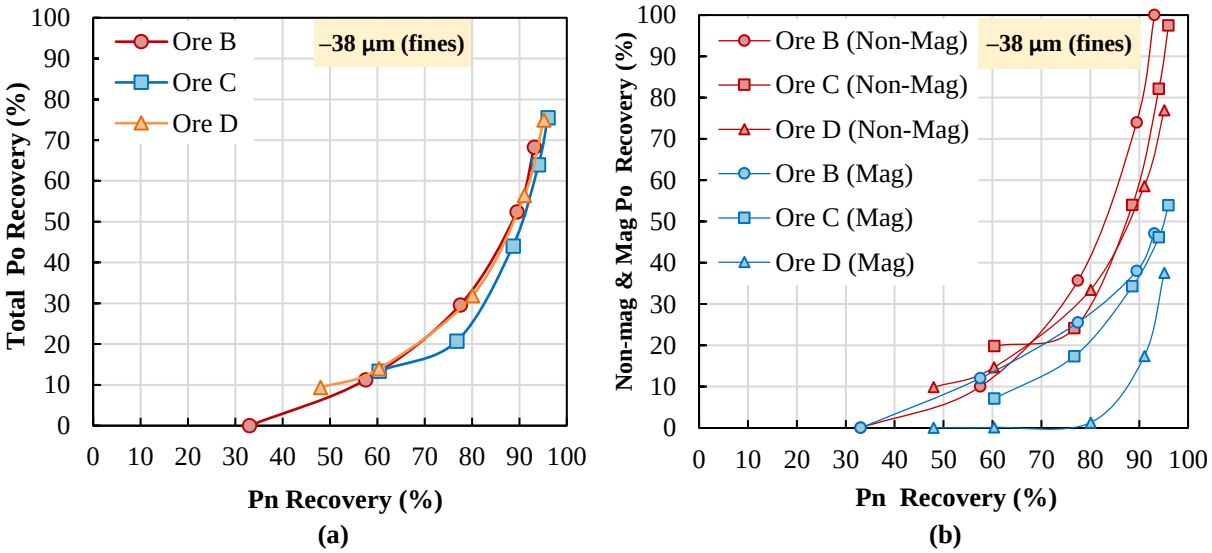

Figure 5.9 *– Preliminary study Po–Pn Selectivity: –38µm fraction (a) total Po vs. Pn; (b) Non–mag & Mag Po vs. Pn.*

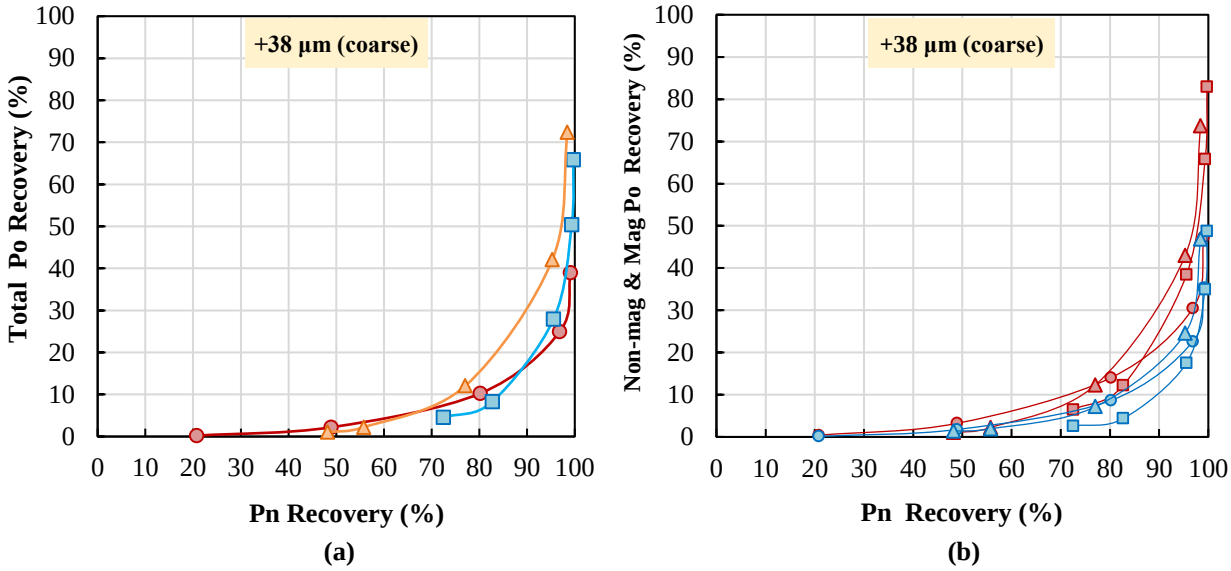

Figure 5.10 *– Preliminary study Po–Pn Selectivity: +38µm fraction (a) total Po vs. Pn; (b) Non–mag & Mag Po vs. Pn.*

Since the results of this preliminary study showed clear differences in pyrrhotite superstructure floatability for all the ores (some refinement needed for the selectivity curves), further test work was scheduled though with a more refined reagent dosage scheme to reduce the noise in the data. Two major changes were made: (i) amount of collector used for each ore was calculated based on ore head grade; and (ii) collector addition was staged rather than all dosed before concentrate #1 (**Table 3.3**); with these changes it was believed that the superstructure floatability differences could be amplified, especially in the fine and coarse size fractions. Subsequent tests incorporated the use of DETA/SMBS depressant combination (**Table 3.4**) to assess its impact on the pyrrhotite superstructures.

5.5 In-depth Study

5.5.1 Refined Baseline Tests (Staged Reagent Addition)

Baseline float test results (mineral kinetics) are presented in **Figure 5.11**, the trends being very similar to those found in the preliminary study with non-magnetic pyrrhotite consistently exhibiting much higher flotation kinetics and final recovery for all ores. Since the collector dosage was tailored to each ore and added stage-wise, it was deemed appropriate to compare total pyrrhotite kinetics and final recovery from each ore (**Figure 5.12**). As

suspected, increasing kinetics/final recovery was observed with increasing feed non-magnetic pyrrhotite ratio (Ore A to D), meaning ores containing higher relative non-magnetic pyrrhotite content would be more challenging to process (where pyrrhotite depression is concerned) over those containing more magnetic pyrrhotite. This was also reflected in the cumulative metal concentrate data (**Figure B16**), better represented by concentrate upgrade ratios (**Figure 5.13**). Upgrade ratios showed a decreasing trend with increasing feed non-magnetic pyrrhotite ratio (Ore A to D), though the effect was not substantial it does show that ores bearing higher non-magnetic pyrrhotite content would lead to lower concentrate grades.

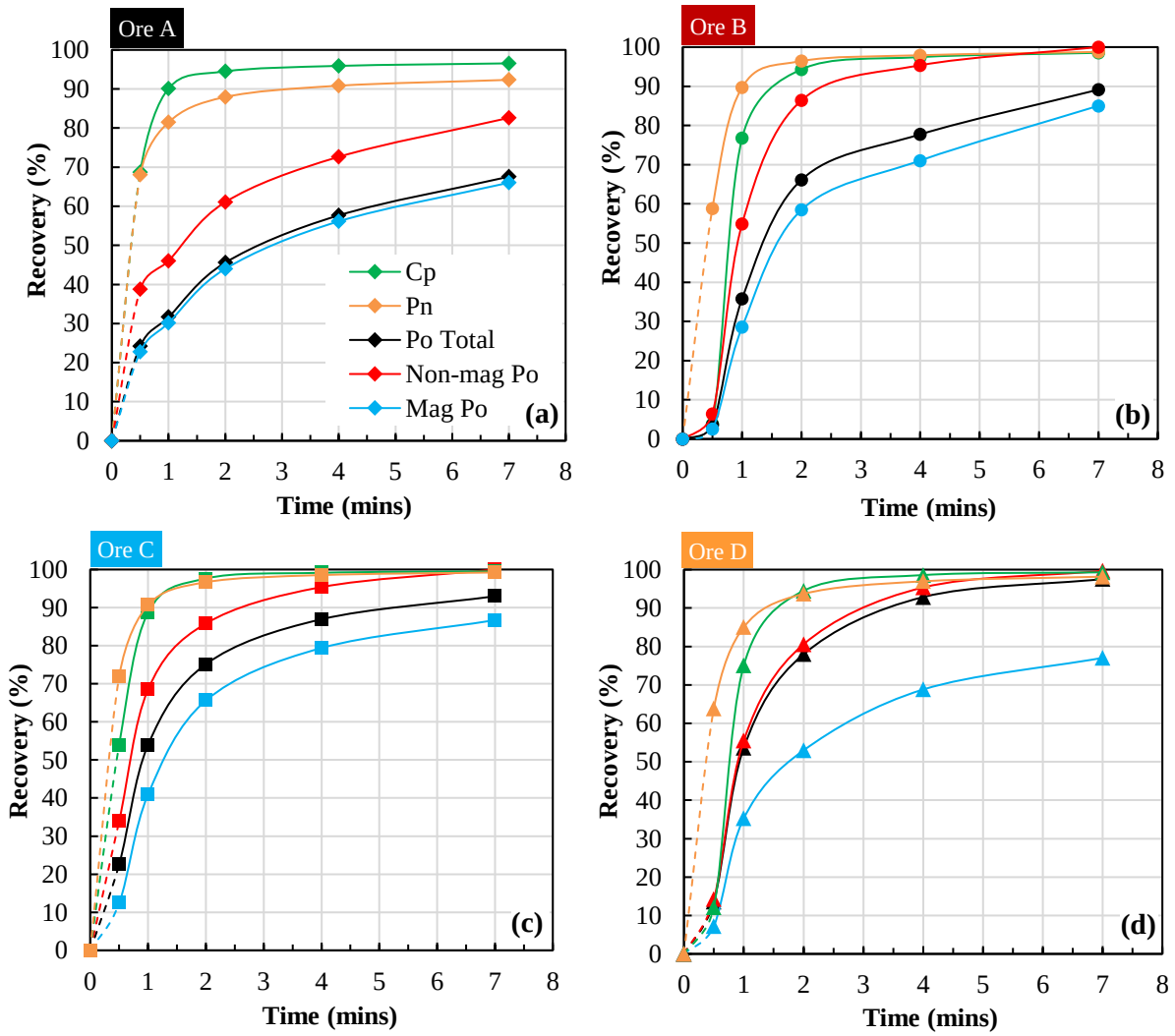

Figure 5.11 *– In-depth study (baseline) flotation kinetics; (a) Ore A; (b) Ore B; (c) Ore C; and (d) Ore D.*

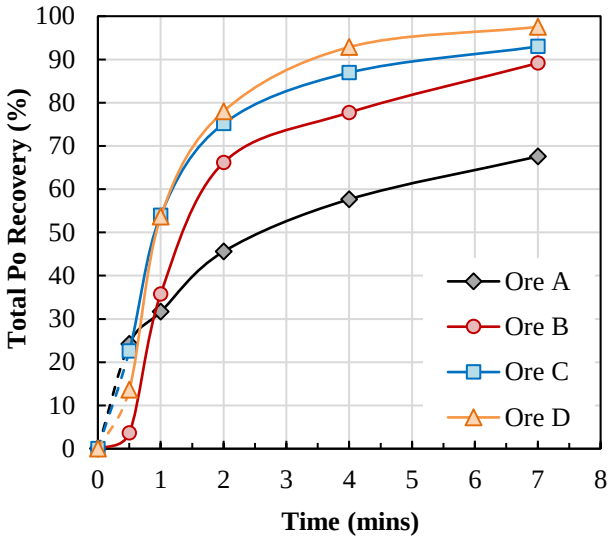

Figure 5.12 *– In-depth study (baseline) total Po flotation kinetics for all ores.*

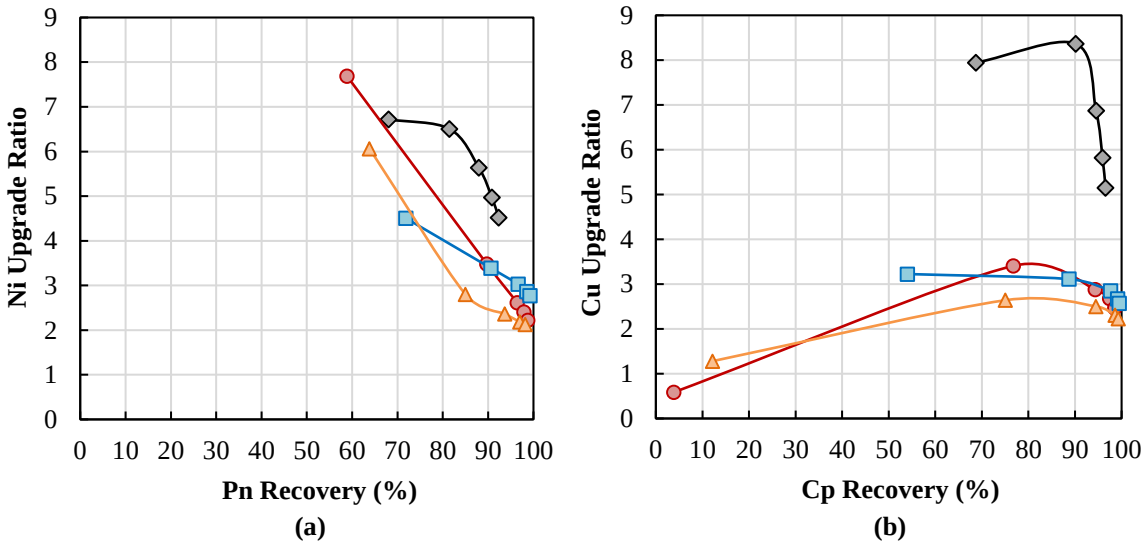

Figure 5.13 *– In-depth study (baseline) concentrate upgrade ratios for all ores; (a) nickel; and (b) copper.*

Po-Pn selectivity curves were assessed next to see whether changes had occurred with the new flotation scheme. The new baseline data is presented in **Figure 5.14** for all ores (total pyrrhotite), and **Figure 5.15** for Ores B, C, and D (Ore A was removed yet again due to severe pentlandite locking with pyrrhotite that interfered with the trends, thus it was excluded from subsequent results and placed in Appendix B – **Figure B17**). Most of the results were improved over the preliminary study trends in that the curves were more separated and a clearer relationship based on ore type was observed. For all size fractions

combined, the data indicates decreasing Po-Pn selectivity with increasing feed non-magnetic pyrrhotite ratio, as before, this trend is maintained in the coarse size fractions (+38 µm). For the fine fraction (–38 µm), the selectivities were very similar and unfortunately a trend based on ore type could not be placed (discussed below). All selectivity curves were then split into their respective non-magnetic and magnetic pyrrhotite curves. The combined fractions and +38 µm (coarse) data clearly showed much better spread between the curves due to the improved float scheme, where pentlandite selectivity against non-magnetic pyrrhotite was consistently poorer over magnetic pyrrhotite. The fine fraction (–38 µm) data seems to imply slightly worse selectivity against non-magnetic pyrrhotite, however the results were inconclusive as many overlapping curves were still observed. It was believed that this issue may be the result of dilution effects from combining very fine size fractions (< 10 µm) where perhaps magnetic pyrrhotite is more floatable with intermediate fines (10 – 38 µm) where non-magnetic pyrrhotite is more floatable, leading to noise in the data. To resolve this problem, cyclosizing the –38 µm fraction in future studies was proposed as it would allow for the separation of very fine particles from intermediate fine particles. The next step of this investigation was to assess the effect of DETA/SMBS depressant combination on the pyrrhotite superstructures from the different ores.

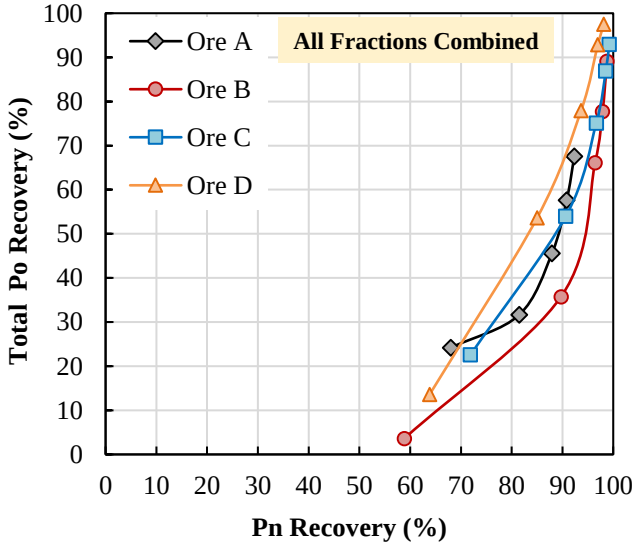

Figure 5.14 *– In-depth study (baseline) Po–Pn selectivity (total Po vs. Pn); (a) all ores; (b) all ores except Ore A; (c) –38µm fraction (fines); and (d) +38µm fraction (coarse).*

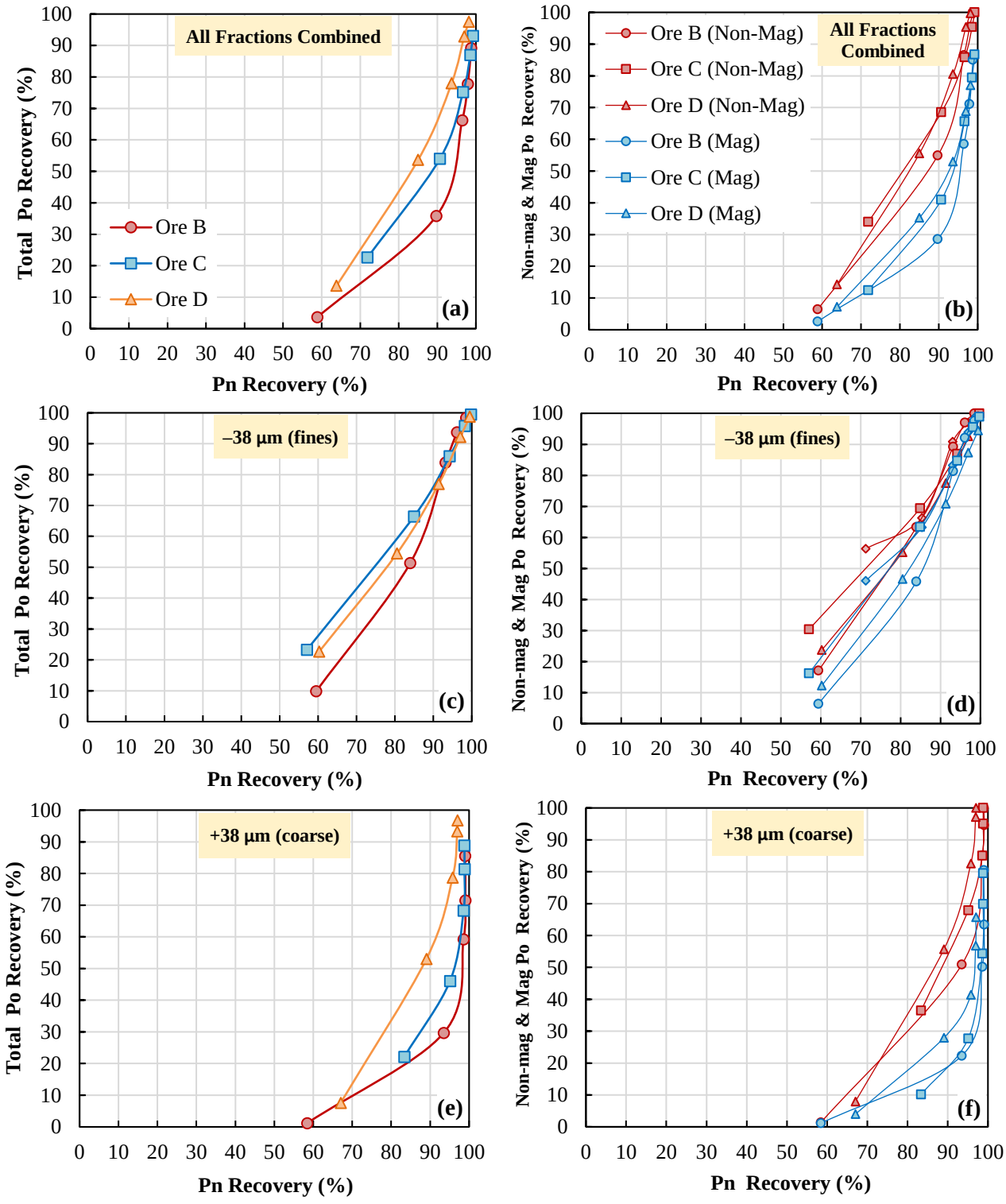

Figure 5.15 *– In-depth study (baseline) Po–Pn Selectivity: Total Po and {Non–mag & Mag Po} vs. Pn: (a,b) all fractions combined; (c,d) –38 µm fraction; (e,f) +38 µm fraction.*

5.5.2 DETA/SMBS Tests

All ores were first conditioned with DETA/SMBS and floated as per conditions outlined in **Table 3.4**. The kinetics data is presented in **Figure 5.16**. Firstly, the total pyrrhotite kinetics and final recovery mostly followed the expected trend as that observed during baseline testing (progressive increase from Ore A to D), Ore B was the outlier and found to float exceptionally well even in the presence of DETA/SMBS. A valid explanation for this anomalous behaviour could not be presented, it may have been a case of secondary ore effects being amplified (*e.g.* mineral locking, reactivity, *etc.*) or simply an overdose of collector (dosage miscalculation). Nonetheless, pyrrhotite superstructure recovery trends after DETA/SMBS treatment were more similar in comparison to those from the baseline tests. In other words, non-magnetic and magnetic pyrrhotite behaved alike after depressant conditioning. Furthermore, this change was consistent across all the ores. From the single mineral studies in Chapter 4, it was found that after mineral surface cleaning by sonication pre-treatment (removing surface oxidation products), both superstructures floated virtually the same. In the present case with DETA/SMBS, though the surfaces were not *cleaned* in the same manner as sonication pre-treatment, polysulfides and xanthate on pyrrhotite surfaces were degraded by SMBS and removal of adsorbed Ni^{2+} and Cu^{2+} ions by chelation was accomplished with DETA. Both reagents acted to remove hydrophobic and activating species on the superstructure surfaces and thus rendering them similar, leaving behind solid $Fe(OH)_3$ which is hydrophilic and detrimental to pyrrhotite's floatability.

Concentrate upgrade ratios (**Figure 5.17**) showed a slight increase for all ores with DETA/SMBS (most positive change was for Ore A), which was surprising since pyrrhotite was depressed for the all ores except for Ore B and thus higher upgrade ratios were expected. Upon further inspection of concentrate assay data, it was determined that gangue recovery had increased with DETA/SMBS and prevented an increase in the upgrade ratios. This has been reported in other test work with DETA, which can attach to gangue minerals by a physisorption mechanism and the complex is weakly floatable. In such cases, pH adjustment during concentrate cleaning stages is sufficient in removing the recovered gangue.

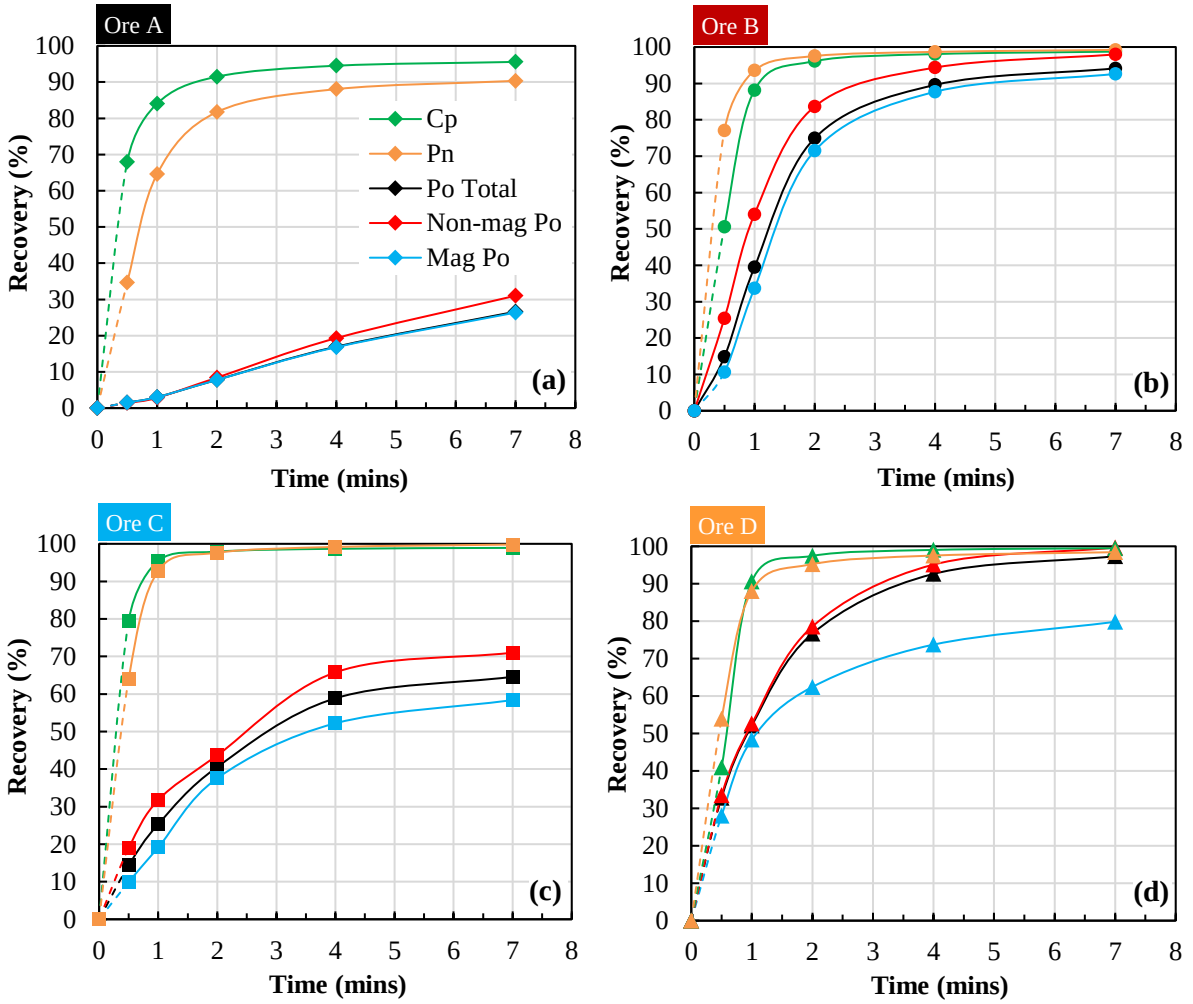

Figure 5.16 *– In-depth study (DETA/SMBS) flotation kinetics; (a) Ore A; (b) Ore B; (c) Ore C; and (d) Ore D.*

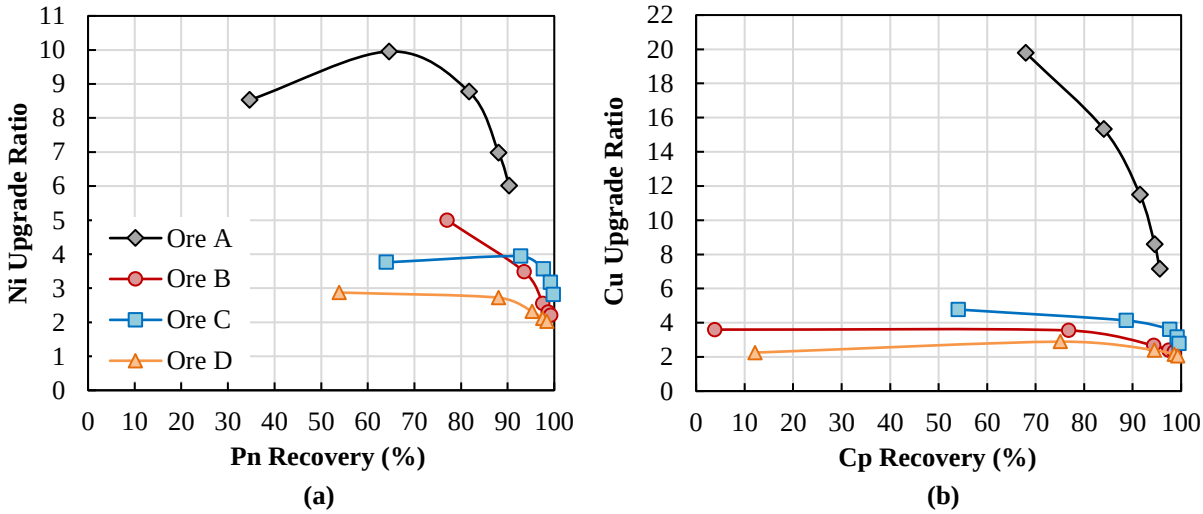

Figure 5.17 *– In-depth study (DET/SMBS) concentrate upgrade ratios; (a) nickel; and (b) copper.*

The last stage of this study was to evaluate Po-Pn selectivity curves (**Figure 5.18**) and determine whether both superstructures were depressed to the same extent with DETA/SMBS (kinetics data showed that non-magnetic pyrrhotite was still more floatable). Aside from Ore B behaviour, for all size fractions combined, the selectivity followed similar trends as seen before (progressive worsening of selectivity with increasing feed non-magnetic pyrrhotite ratio). One key distinction, however, was that the separation between the curves was much greater with DETA/SMBS than in the baseline tests. It appears that with DETA/SMBS, both superstructures were depressed, however it was more difficult to depress ores containing higher non-magnetic pyrrhotite content. The non-magnetic pyrrhotite may have been activated to a greater degree (as it is generally assumed to be) and thus requires higher DETA/SMBS dosages relative to magnetic pyrrhotite to achieve the same degree of depression. Pyrrhotite depression in the fine fraction was more challenging over the coarse fraction, the discrepancy was attributed to particle surface area differences between the two size classes; finer particles exhibit much larger specific surface areas, and thus would require more depressant for the same depressive effect as coarse particles.

The selectivity curves were then split into non-magnetic and magnetic pyrrhotite curves, and the findings support the observations made thus far; both superstructures were depressed by DETA/SMBS, however magnetic pyrrhotite was depressed to a greater degree. To clearly demonstrate this, the Ore C data is highlighted as it contained equal amounts of the superstructures; across all selectivity data (combined fractions, and fine/coarse fractions), magnetic pyrrhotite was consistently more depressed over non-magnetic pyrrhotite even though both superstructures were subjected to the same dosage of DETA/SMBS.

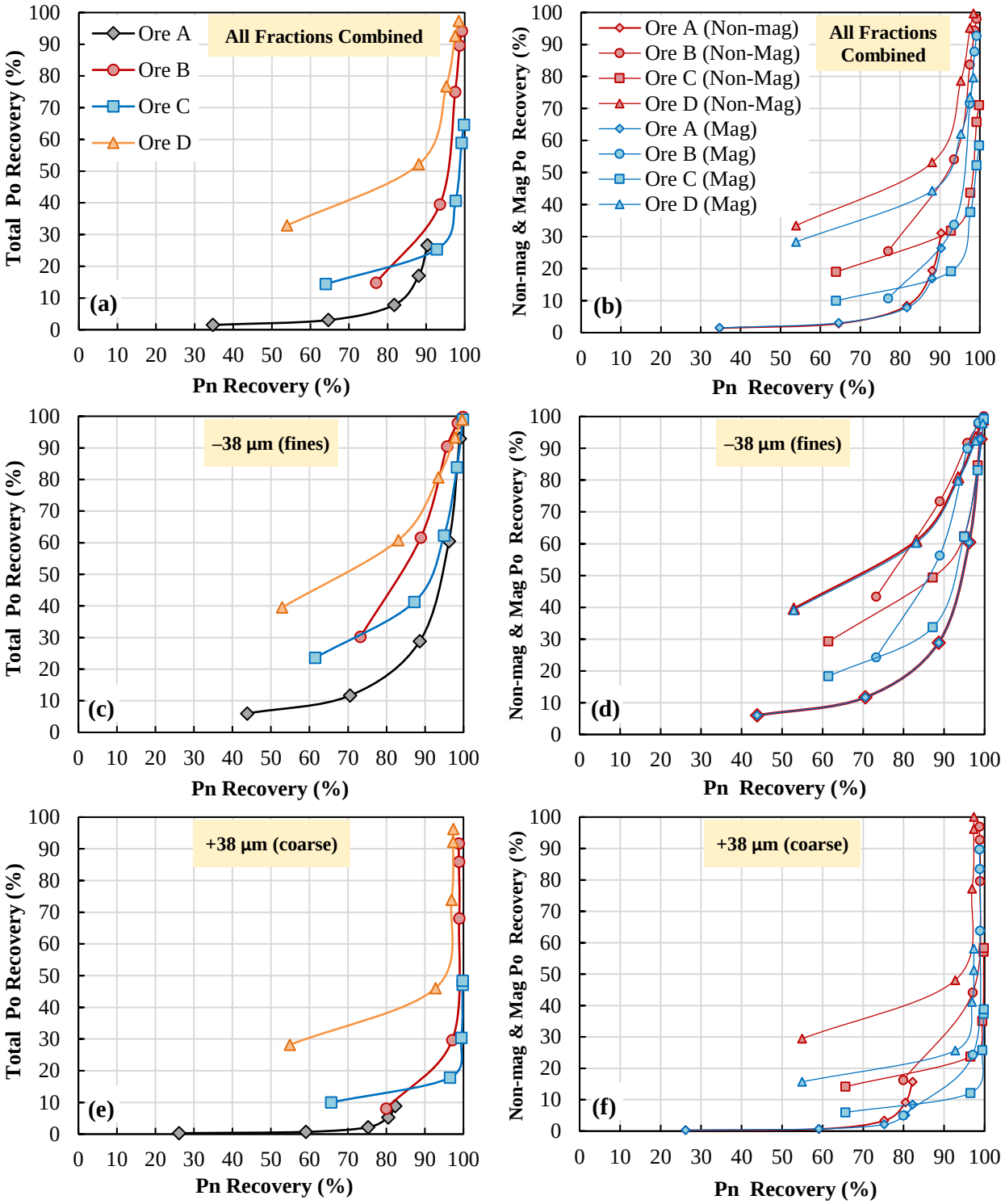

Figure 5.18 *– In-depth study (DETA/SMBS) Po–Pn Selectivity: Total Po and {Non–mag & Mag Po} vs. Pn: (a,b) all fractions combined; (c,d) –38 µm fraction; (e,f) +38 µm fraction.*

5.6 Summary and Key Findings

5.6.1 Baseline Tests

1. Staged collector addition (total dosage calculated based on ore head grades) was determined to be better for comparing pyrrhotite superstructure floatability over full collector dosage before concentrate #1;
2. Superstructure kinetics data complemented the findings of other researchers in that non-magnetic pyrrhotite was found to be significantly more floatable than magnetic pyrrhotite (consistent across all four Ores A – D). The present test work represented *real systems* where the superstructures were allowed to react with grinding media and air (oxidation was permitted), which was likely responsible for the different superstructure flotation responses;
3. Final pyrrhotite recovery increased with increasing feed non-magnetic pyrrhotite content, consequently, concentrate metal upgrade ratios decreased with increasing feed non-magnetic pyrrhotite content;
4. Pentlandite selectivity against the superstructures showed poorer selectivity against non-magnetic over magnetic pyrrhotite, which was consistent for all four ores. Furthermore, regardless of ore type, non-magnetic pyrrhotite selectivity curves were virtually the same, similarly, all magnetic pyrrhotite selectivity curves were also the same (Ore A differed from this trend due to severe pentlandite locking with pyrrhotite). This suggested that increasing non-magnetic pyrrhotite content in the float feed would result in a proportional decrease in selectivity;
5. Fine (–38 μm) and coarse (+38 μm) fraction selectivity curves showed much poorer selectivity in the fines over coarse sizes, this was attributed to poor/mediocre floatability of fine pentlandite where pyrrhotite is still sufficiently floatable;
6. For coarse fraction, selectivity against non-magnetic pyrrhotite was poorer than magnetic pyrrhotite (similar results across all four ores); and

7. In the fine fraction, selectivity against non-magnetic pyrrhotite was slightly worse, however a definitive trend based on feed non-magnetic pyrrhotite ratio could not be placed due to significant overlapping of superstructure curves. Aside from ore characteristics (*i.e.* ore mineralogy, liberation/mineral associations, grind effects, pulp potential, *etc.*), the discrepancy between the present study and the fine fraction flotation data presented by Lawson *et al.* (2014)[16] may be due to dilution effects from combining very fine particles (< 10 μm) with intermediate fine particles (10 – 38 μm). This warranted further investigation in which the fine fraction (– 38 μm) would be cyclosized to obtain a clearer picture of the superstructure behaviour in this region

5.6.2 DETA/SMBS Tests

1. DETA/SMBS combination showed depressive effects on both pyrrhotite superstructures, however, it was more effective on magnetic pyrrhotite across all four ores. This was clearly shown for Ore C (superstructure ratio = 50/50%) where magnetic pyrrhotite was more depressed over non-magnetic pyrrhotite even though both superstructures were exposed to the same amount of DETA/SMBS depressant. It was believed that non-magnetic pyrrhotite contains a higher surface density of polysulfides and activating ions (Ni^{2+} and Cu^{2+}) that requires higher DETA/SMBS dosages to achieve the same degree of depression as magnetic pyrrhotite;

2. Po-Pn selectivity curves showed that DETA/SMBS was more effective at depressing pyrrhotite in coarse size classes (+38 μm) over fine size classes (–38 μm), which was attributed to surface area effects (fine particles requiring more depressant due to much higher surface areas over coarser particles); and

3. Concentrate metal upgrade ratios with DETA/SMBS were marginally higher than baseline tests, which was surprising since pyrrhotite depression had taken place and higher upgrade ratios were expected. Upon further inspection, it was identified that higher non-sulfide gangue recovery had occurred with DETA/SMBS thereby maintaining the baseline concentrate upgrade ratios since gangue had replaced pyrrhotite (pH adjustment was proposed as a means to remove recovered gangue in subsequent cleaner stages)

Chapter 6
Batch Flotation Study #2

6.1 Introduction

This Chapter summarizes the results of the second batch flotation study on a separate ore from the Sudbury Basin, provided as a case study by Glencore (Sudbury Integrated Nickel Operations). This ore contains a high Po/Pn ratio (~ 7.5), 42% of the pyrrhotite was non-magnetic pyrrhotite, and 85.9% Ni in the feed was in pentlandite (the remaining Ni largely reported to pyrrhotite); all of which make pyrrhotite rejection industrially challenging and Ni recovery/grade targets difficult to obtain. Pyrrhotite depression from this particular ore was known to be quite challenging (based on historical plant performance) and required a comprehensive study to identify methods to target its depression (with focus on the non-magnetic pyrrhotite as it was more difficult to depress).

Part 1 (Section 6.3) of the study focused on methods to significantly depress pyrrhotite. The primary objective was to assess whether the ore could be processed "as is" or if it required blending to achieve high overall pentlandite recovery (> 85%) and low overall pyrrhotite recovery (< 20%), which typically yields acceptable final concentrate grades in industry after cleaning stages. Part 2 (Section 6.4) focused on the recovery-by-size relationship of the pyrrhotite superstructures with and without depressants (DETA/SMBS combination); main objective was to compare the superstructure relationship with that seen in industrial operations and whether it could be altered.

The ore preparation and float test procedure/conditions for Parts 1 and 2 are provided in Section 3.1.2.2).

6.2 Feed Mineralogy

The feed head assay information (*via* ICP-OES) is presented in **Table 6.1** (minerals calculated based on 0.9 wt% Ni in pyrrhotite). The feed mineralogy (*via* QEMSCAN and EPMA; completed by personnel at the XPS center) was characterized for several reasons. Firstly, it served to confirm the major Ni and Cu–bearing minerals were indeed pentlandite (Pn) and chalcopyrite (Cp), respectively, and that the major sulfide gangue was pyrrhotite (Po) rather than a mixture of Po and pyrite (Py) (both having different flotation characteristics); feed modal mineralogy (unsized) presented in **Table 6.2**.

Table 6.1 *– Feed head assay (metal and mineral wt%). Mineral assays calculated based on 0.9wt% Ni in pyrrhotite.* ***Note:*** *Pn – Pentlandite ($(Ni,Fe)_9S_8$), Cp – Chalcopyrite ($CuFeS_2$), Po – pyrrhotite ($Fe_{(1-x)}S$), Non-mag Po (Fe_9S_{10}), Mag Po (Fe_7S_8) and NSG – non–sulfide gangue.*

Elements (wt%)			Minerals (wt%)						
Cu	Ni	S	Cp	Pn	Po	% Non-mag Po	% Mag Po	Ga	Po/Pn
0.93	1.62	13.43	2.7	3.8	28.4	**42**	**58**	65.11	7.47

Table 6.2 – *Feed modal mineralogy.*

Mineral	% in Fraction
Pentlandite	3.67
Millerite	0.01
Total Ni Sulfide	***3.68***
Chalcopyrite	2.80
Bornite	0.03
Cubanite	0.09
Total Cu Sulfide	***2.92***
Pyrrhotite	25.83
Non-mag Po Split	*42*
Mag Po Split	*58*
Pyrite	0.88
Total Fe Sulfide	***26.71***

Mineral	% in Fraction
Magnetite	6.91
Quartz	5.79
Feldspars	23.98
Micas	4.74
Chlorite	6.25
Clinopyroxene	2.39
Orthopyroxene	0.38
Epidote	4.18
Amphibole	10.73
Titanite	0.62
Other	0.72
Total NSG	***66.69***

Secondly, mineral Ni deportment (**Table 6.3**) was used to quantify the amount of Ni hosted in sulfides and oxide/silicate minerals and to determine the maximum possible Ni recovery at 100% Pn recovery (it is well known that Po hosts significant amount of Ni in its matrix). About 85.9% Ni was in Pn, 0.4% in millerite, 12.4% in Po and the remainder 1.3% in non–sulfide gangue (NSG). Thirdly, modal mineralogy by size class (**Figure 6.1**(a)) relayed that the minerals (sulfides and oxides/silicates) were well distributed across all sizes and that the sulfides were reporting to the floatable size range (focus on Pn and Cp) at the target grind P80 ≈ 120 µm. From **Figure 6.1**(b), it can be observed that the head assay superstructure ratio (non-magnetic/magnetic pyrrhotite = 42/58%) is essentially maintained across all size fractions (some deviation for CS7) and, as expected, preferential superstructure grind was not observed. Lastly, mineral associations (**Figure 6.2** and **Table 6.4**) revealed that about 76.3% Pn was liberated (74 – 87% for –106 µm particles), 14% was locked (binary) to Po and 6.6% to NSG/complex particles; with majority of the locking at > 25 µm, suggesting that a regrind step may be required for improved Pn liberation from Po (similar to the scavenger concentrate regrind at Glencore's Strathcona Mill and Vale's Clarabelle Mill; **Figure 2.15**) [9, 12]. For chalcopyrite, it was 79.0% liberated (76 – 89% for –106 µm particles), 3.5% locked (binary) to Pn, 3.4% locked (binary) to Po and 14.0% to NSG/complex particles. For pyrrhotite, it was 87.2% liberated (87 – 91% for –106 µm particles), 6.9% locked (binary) to Pn, 0.6% locked (binary) to chalcopyrite/cubanite and 5.3% to NSG/complex particles.

Table 6.3 *– Feed mineral Ni deportment.*

Mineral	% Ni Deportment
Pentlandite	85.89
Millerite	0.4
Pyrrhotite	12.41
Pyrite	0.04
Micas	0.14
Chlorite	0.42
Clinopyroxene	0.06
Amphibole	0.64
Total	***100***

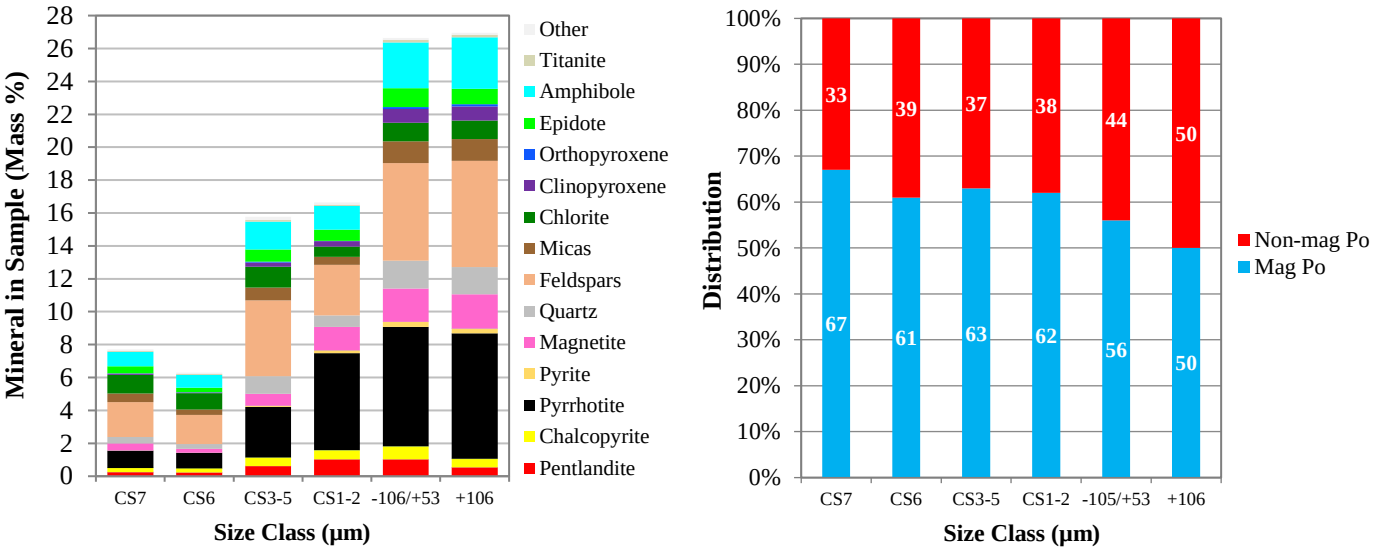

(a) (b)

Figure 6.1 *– (a) Feed modal mineralogy by size class; (b) pyrrhotite superstructure ratio (non-magnetic {Fe_9S_{10}, 5C} and magnetic {Fe_7S_8, 4C}) by size class.* ***Note:*** *cyclosize classes – CS1–2 (–53/+25µm), CS3–5 (–25/+8µm), CS6 (–8/+3µm), CS7 (–3µm).*

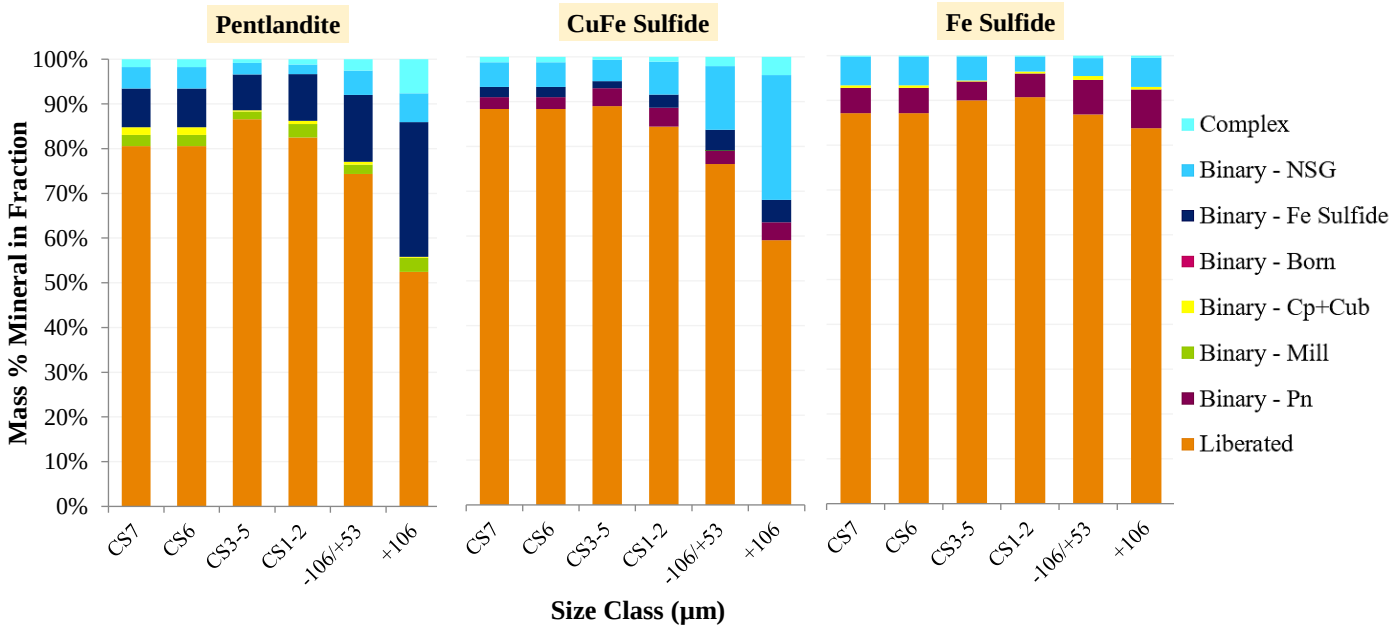

Figure 6.2 *– Mineral associations by size class of the major sulfide minerals.* ***Note:*** *cyclosize classes: CS1–2 (–53/+25 µm), CS3–5 (–25/+8 µm), CS6 (–8/+3 µm), CS7 (–3 µm). NSG: Non-Sulfide Gangue, Fe Sulfide: Pyrrhotite + Pyrite, Born: bornite, (Cp + Cub): Chalcopyrite + Cubanite, Mill: Millerite, and Pn: Pentlandite. "Liberation" refers to > 95% liberation of particle by area (for mineral of interest). "Binary" locking refers to >90% of particle area is composed of the two minerals. "Complex" locking refers to >90% of particle area composed of three ore more mineral phases.*

Table 6.4 *– Feed mineral associations by size class of pentlandite, copper iron sulfide (primarily chalcopyrite), iron sulfide (primarily pyrrhotite), and non–sulfide gangue.* ***Note:*** *cyclosize classes – CS1–2 (–53/+25µm), CS3–5 (–25/+8µm), CS6 (–8/+3µm), CS7 (–3µm).*

	Liberation Class	Combined	CS7	CS6	CS3–5	CS1–2	–106/+53	+106
Pentlandite Locking (%)	Liberated	**76.28**	80.54	80.54	86.59	82.50	74.32	52.43
	Binary – Mill	**2.48**	2.52	2.52	1.72	2.99	2.07	3.14
	Binary – Cp+Cub	**0.69**	1.74	1.74	0.26	0.71	0.66	0.27
	Binary – Fe Sulfide	**13.94**	8.67	8.67	8.05	10.48	14.98	30.12
	Binary – NSG	**4.07**	4.75	4.75	2.56	2.13	5.41	6.38
	Complex	**2.53**	1.78	1.78	0.83	1.18	2.56	7.66
	Total	***100.00***	*100.00*	*100.00*	*100.00*	*100.00*	*100.00*	*100.00*
CuFe Sulfide Locking (%)	Liberated	**79.01**	88.33	88.33	88.97	84.46	76.05	59.06
	Binary – Pn	**3.54**	2.68	2.68	4.00	4.21	2.99	4.00
	Binary – Fe Sulfide	**3.43**	2.28	2.28	1.58	2.94	4.68	4.99
	Binary – NSG	**12.17**	5.46	5.46	4.79	7.32	14.24	27.86
	Complex	**1.84**	1.25	1.25	0.65	1.07	2.04	4.09
	Total	***100.00***	*100.00*	*100.00*	*100.00*	*100.00*	*100.00*	*100.00*
Fe Sulfide Locking (%)	Liberated	**87.24**	87.14	87.14	90.02	90.77	86.87	83.81
	Binary – Pn	**6.87**	5.69	5.69	4.21	5.28	7.71	8.63
	Binary – Cp+Cub	**0.58**	0.53	0.53	0.20	0.40	0.90	0.57
	Binary – NSG	**4.90**	6.35	6.35	5.35	3.30	3.95	6.48
	Complex	**0.42**	0.29	0.29	0.22	0.25	0.57	0.51
	Total	***100.00***	*100.00*	*100.00*	*100.00*	*100.00*	*100.00*	*100.00*
NSG Locking (%)	Liberated	**91.62**	93.08	93.08	95.25	91.49	90.60	89.45
	Binary – Pn	**3.93**	2.46	2.46	2.05	4.14	5.06	4.83
	Binary – Cp+Cub	**0.93**	0.37	0.37	0.49	0.81	1.23	1.34
	Binary – Fe Sulfide	**3.29**	3.90	3.90	2.12	3.38	2.90	3.98
	Complex	**0.23**	0.19	0.19	0.10	0.18	0.21	0.38
	Total	***100.00***	*100.00*	*100.00*	*100.00*	*100.00*	*100.00*	*100.00*

6.3 Part 1 – Pyrrhotite Depression Tests

6.3.1 Baseline Test

The baseline ("blank") test was conducted with rougher (pH 9.2)/scavenger (pH 8) stages to gain an understanding of the sulfide mineral behaviour (Pn, Cp, and Po) at the two

different pH values (secondary goal was to relate the results to industrial operation), Po is generally well depressed in the pH range 9.2 – 9.5 (lime system) while Pn and Cp are still sufficiently floatable [16]. Under neutral to mildly alkaline pH's (*e.g.* pH 8), Po is also sufficiently floatable and is the basis of industrial scavenger circuits to retrieve as much Pn and Po in order to ensure a low sulfide tail (majority of which is used for mine backfill).

The grade–recovery and kinetics results are presented in **Figure 6.3** and Po–Pn selectivity presented in **Figure 6.4**. The data shows lower than expected grades and fairly high recovery of Pn, Cp, and Po in the rougher stage (with near–complete sulfide mineral recovery after scavenger stage).

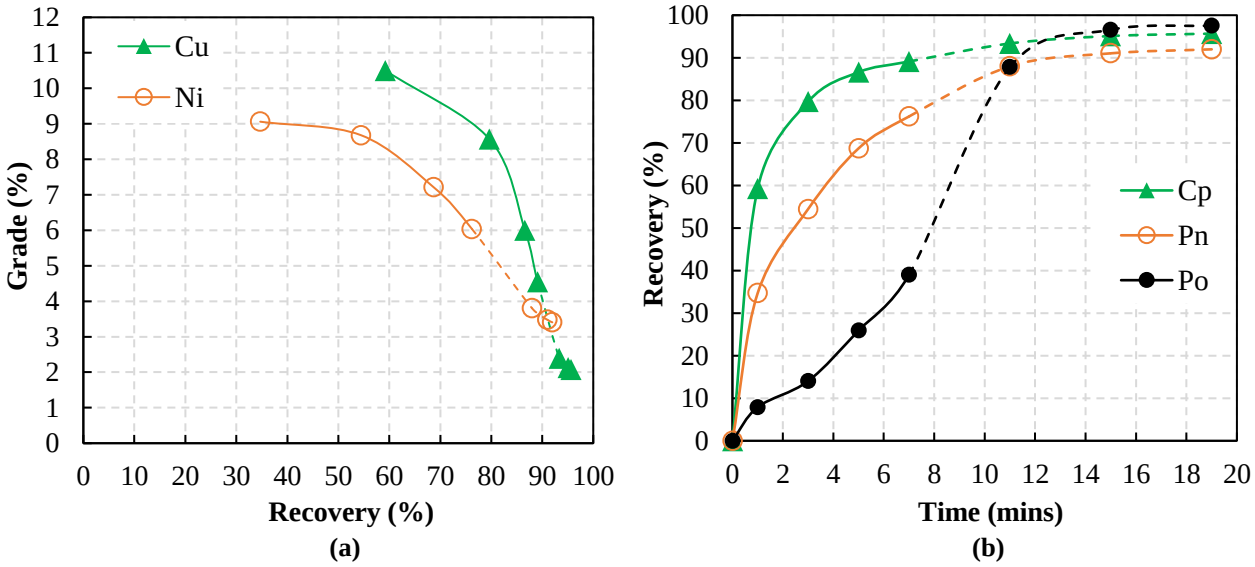

Figure 6.3 *– Baseline test (solid and dashed lines refer to rougher {pH 9.2} and scavenger {pH 8} stages, respectively), PIBX = 70 g/t; (a) Ni–Pn and Cu–Cp grade–recovery curves; (b) mineral kinetics.*

Aeration conditioning (up to 15 mins) prior to rougher flotation was also tested to selectively depress Po (data not presented), the results did show reduced Pn and Po kinetics however the Po–Pn selectivity was similar to the present baseline. Other reagent schemes were also investigated (conditioned prior to rougher flotation) including aeration with SMBS, use of 3418A promoter with/without PIBX, oxalic acid, sulfuric acid (with aeration), PIBX addition to mill, however the Po–Pn selectivity curves trended along the present baseline selectivity. Due to the reactive nature of this ore, it was speculated that perhaps the Po in the ore was already partially oxidized/pre–activated when received or it was activated during

milling by ions such as Cu^{2+} and Ni^{2+}, both scenarios would result in sufficiently floatable Po in the rougher stage (pH 9.2). From the mineral association data (**Figure 6.2** and **Table 6.4**) it was determined that pyrrhotite was well liberated (> 87%) and therefore its recovery was largely the result of its own floatability rather than due to locking with Pn or Cp. As such, this data supported the hypothesis that the Po surfaces were activated by some mechanism, most probably by heavy metal ions (historical laboratory studies and industrial data support pulp ion activation) and testing with chelating agents (*i.e.* DETA) for Po depression was pursued.

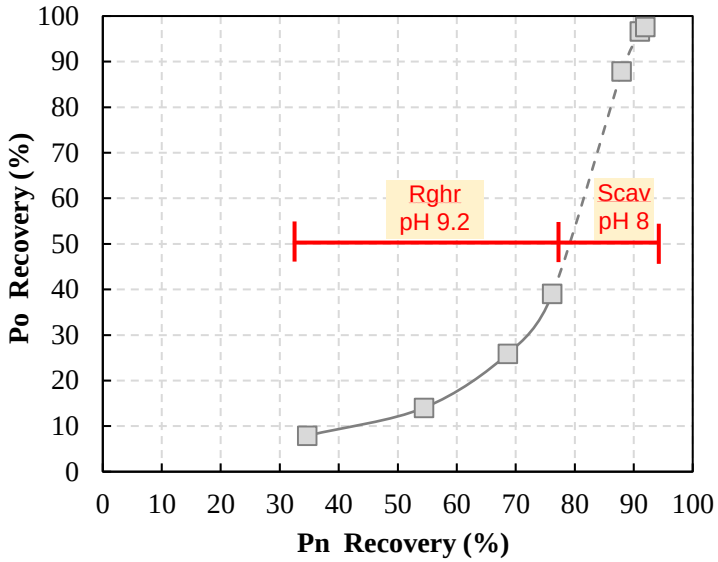

Figure 6.4 *– Baseline Po–Pn selectivity curve (solid and dashed lines refer to rougher {pH 9.2} and scavenger {pH 8} stages, respectively.*

6.3.2 Scoping Test Summary

After baseline testing, scoping tests were completed to determine reagents/depression strategies that showed promise for significant Po depression (or able to significantly alter the Po-Pn selectivity curve). Several common strategies were trialed with many reagents; selective Pn kinetics/recovery improvement, selective Po oxidation, Po surface deactivation, and additional grinding (Pn liberation from Po). The general findings are summarized in **Table 6.5**. Of these scoping tests, DETA testing was pursued further (in conjunction with SMBS and acid/aeration conditioning) as it proved to be the most effective

in depressing both Po superstructures and therefore shifting the baseline curve (**Figure 6.4**) towards Pn.

Table 6.5 *– Scoping study summary (effect on kinetics/recovery and Po-Pn selectivity).*

Description	General Summary
Kinetics & selective Pn recovery improvement	
• Sulfuric acid conditioning (pH 4)	Increases kinetics/recovery, but needs chelating agents to capture mobilized ions to prevent Po activation (use selectively)
• Oxalic acid conditioning (pH 6.5)	Some increase in kinetics/recovery, cleans all sulfides – very effective at cleaning Po (counter-productive in improving selectivity)
• Mechanical conditioning (sonication)	Not effective (no significant improvements in kinetics & selectivity), needs further development
• 3418A (low/high E_h; with/without PIBX)	Increases recovery (all sulfides) mainly at high E_h. Not effective for improving selectivity
Selective oxidation	
• Aeration (air)	Not very effective (especially on oxidized ore); no improvement in selectivity
• Aeration (air) w/ SMBS ($Na_2S_2O_5$)	Better oxidant than air alone but not great (has depressing effects on both Pn & Po)
• Flash oxidation w/ hydrogen peroxide (H_2O_2)	Extremely effective oxidant but non-selective, rapidly oxidizes all sulfides (not ideal). No improvement in selectivity
Chelation/deactivation	
• DETA	Very effective at depressing Po (improves selectivity)
• DETA w/ SMBS	More effective than DETA alone (further improvement in selectivity)
Additional grinding	Effective in improving selectivity (requires trade-off study)

6.3.3 DETA Tests

Several rougher stage float tests (pH 9.2) were conducted with DETA at 70 and 100 g/t PIBX, the results are presented in **Figure 6.5**. The role of DETA was to selectively deactivate/depress Po and the results show it was very effective (clearly demonstrated in the Po–Pn selectivity data, **Figure 6.5**(d)), also yielding higher Ni and Cu grades, **Figure 6.6**. Compared to the baseline rougher test (at 7 mins), using DETA alone and 70 g/t PIBX, 95% of the Po was depressed, 59% Pn and 25% Cp were also depressed. Due to lower flotation kinetics of all sulfides, additional rougher concentrates were added (time extended to 19 mins) to ensure plateau of Pn and Cp and to match recoveries obtained with the baseline test. It was concluded that with the use of DETA at baseline PIBX dosage (70 g/t), flotation kinetics were poor and thus the tests required more flotation time to ensure adequate recovery. The likely reason for this was DETA's affinity for the base metals (Cu^{2+}, Ni^{2+}, and Fe^{2+}), forming cation–DETA complexes both in solution and on mineral surfaces, the latter would hinder collector adsorption and therefore mineral flotation kinetics [111, 112]. To improve kinetics, DETA tests were repeated with higher PIBX dosage (100 g/t; 43% more) which was carefully chosen so as to maintain the Po–Pn selectivity obtained with DETA at 70 g/t PIBX. With higher dosage the sulfide kinetics were much improved and Po–Pn selectivity curve was essentially extended. The latter part of the curve (exponential increase in Po recovery) is commonly observed in Po–Pn systems and is generally attributed to Po–Pn locking, which is also supported by mineral liberation data in the present mineralogy test work. Though the use of DETA proved effective at depressing Po, the objectives were not all met (*i.e.* Po < 20%), thus DETA/SMBS combination was investigated.

6.3.4 DETA/SMBS Tests

As outlined by many researchers, DETA in the presence of reducing sulfite reagents (*i.e.* sodium sulfite or SMBS) is more effective as a Po depressant [64, 112, 113]. Of the many benefits, following are the primary reasons for improved Po depression with sulfites: dixanthogen formation is hindered on Po as the mineral's rest potential is lowered; degradation of hydrophobic polysulfides on Po; and $Fe(OH)[S]^{+}$ (active site on Po for

xanthate physisorption) surface species are reduced [64, 102]. The DETA/SMBS (1:2 ratio) reagent scheme was tested and the results demonstrate the positive effects of SMBS, better observed in the Po–Pn selectivity with a further improvement in the curve (shift towards Pn axis). Irrespective of PIBX dosage (70 or 100 g/t), the DETA/SMBS trends were virtually the same and improved over DETA only curves, justifying the use of SMBS.

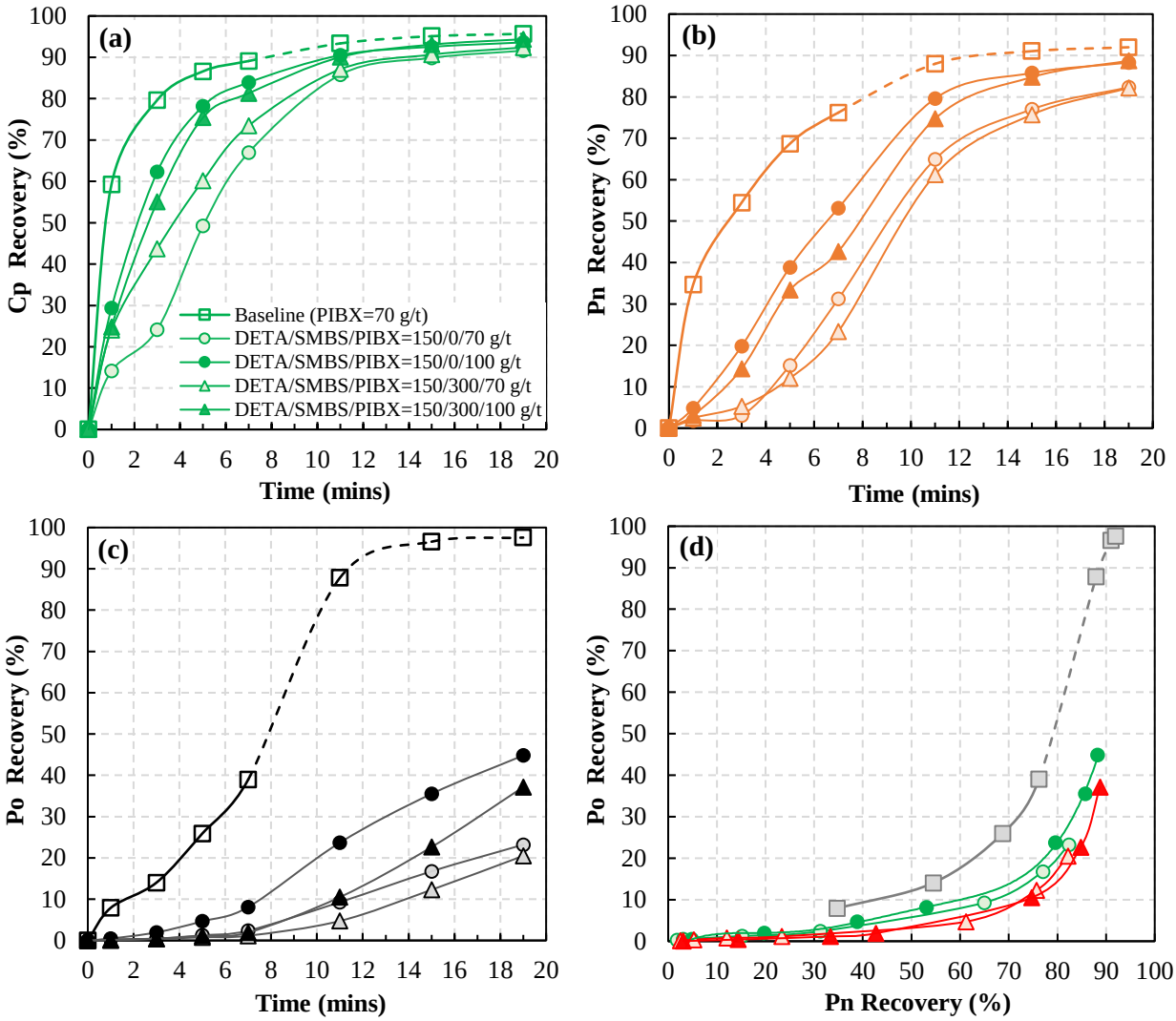

Figure 6.5 *– Flotation results at various DETA/SMBS/PIBX concentrations (solid and dashed lines refer to rougher {pH 9.2} and scavenger {pH 8} stages, respectively); (a) Cp kinetics; (b) Pn kinetics; (c) Po kinetics; (d) Po–Pn selectivity.*

Moreover, improvements in both Ni (2 – 5%) and Cu grade (1 – 8%) were observed (**Figure 6.6**) with DETA/SMBS (relative to the baseline and DETA alone tests). The results also

support the argument that SMBS assisted DETA by means of *cleaning* the Po surface and rendering it more amenable to the action of DETA since more Po was depressed after the introduction of SMBS. As with the DETA only tests, DETA/SMBS also exhibited an exponential rise in Po recovery in the latter part of the selectivity curve, though the targets were marginally met, this highlighted an area that could be improved with more testing to achieve the outlined objectives (*i.e.* < 20% Po). Before concentrate regrind tests were considered, sulfuric acid conditioning with DETA/SMBS was examined as a final measure.

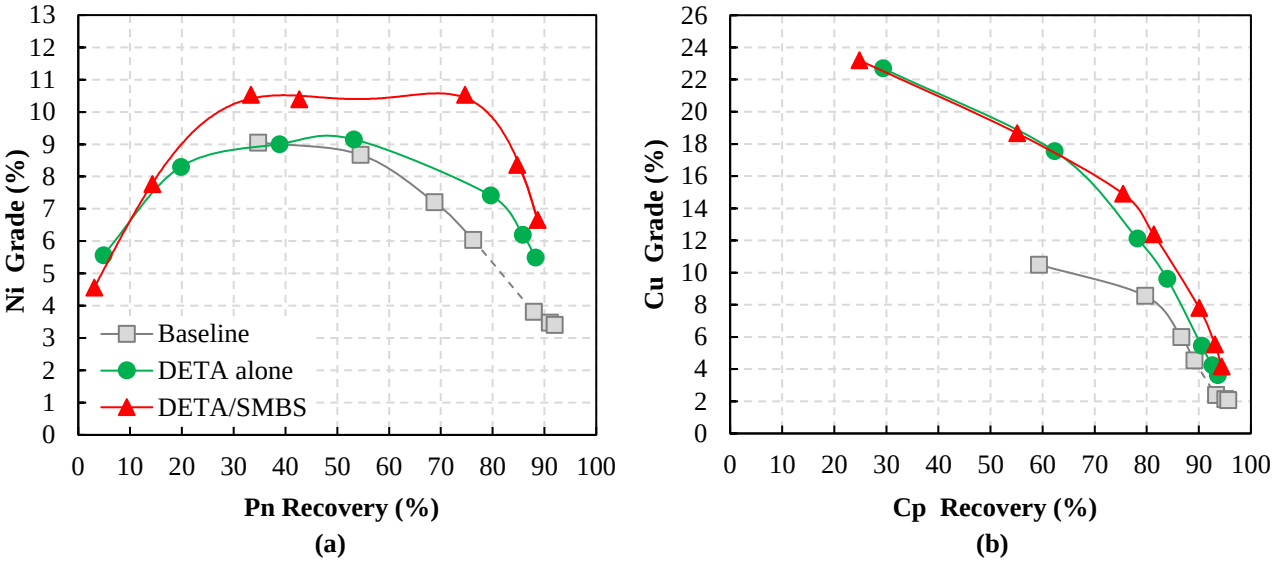

Figure 6.6 *– Grade–recovery curves with DETA and DETA/SMBS; (a) Ni–Pn grade–recovery; (b) Cu–Cp grade–recovery.*

6.3.5 Acid/Aeration Conditioning Tests (with DETA/SMBS)

Restoration of mineral surfaces using sulfuric acid with DETA/SMBS (added as rougher conditioning step) was investigated to dissolve any surface oxidation products such as metal hydroxides/oxides followed by complexation with DETA. The oxidation products may be present perhaps from stockpiling, material handling prior to test work, or resulting from the grinding step. It must be noted that during baseline scoping tests acid treatment with aeration (without DETA/SMBS) was unsuccessful in shifting the Po–Pn selectivity, it was concluded that the mobilized ions (after dissolution) had activated Po surfaces and chelating agents such as DETA may resolve this issue. Since DETA/SMBS testing showed promise,

acid conditioning with DETA/SMBS was explored primarily to increase Pn kinetics and final recovery (it was possible that Pn surfaces were also partially oxidized) while maintaining/reducing Po kinetics/recovery, allowing for a further shift in Po–Pn selectivity. It was perceived that an improvement in Po–Pn selectivity over DETA/SMBS tests after acid conditioning would support the hypothesis that the feed was partially oxidized or reactive during milling and ore pre–treatment (*i.e.* sulfuric acid cleaning) be considered prior to rougher flotation. Moreover, the outlined objectives may be attainable with acid/DETA/SMBS conditioning and concentrate regrind may not be required, as such, acid treatment tests were given priority. Sulfuric acid conditioning was conducted at pH 4 to ensure the Ni/Cu/Fe hydroxides and oxides were dissolved after which the slurry was immediately conditioned with DETA/SMBS. Following this, the slurry was brought to pH 9.2 using lime and floated. Two tests were completed: first, without aeration; and a second with 5 mins of aeration prior to PIBX addition (70 g/t). The results are presented in **Figure 6.7**. Both tests demonstrate the positive effect of acid conditioning on sulfide mineral kinetics; all were significantly improved and suggest that the ore may have indeed been partially passivated. The test without aeration shows fast Po kinetics and thus poorer Po–Pn selectivity than previous DETA/SMBS tests (though still better than baseline), acid conditioning reduced the effectiveness of DETA/SMBS since Po surfaces were also restored. The grade–recovery curves, **Figure 6.8**, were poor as well and were attributed to faster floating Po. This side–effect was anticipated and as such aeration conditioning coupled with acid/DETA/SMBS was tested to selectively oxidize Po which was shown to be effective in studies by other researchers [100]. It was believed that since Po surfaces were renewed after acid conditioning they should be amenable to aeration (surface oxidation) where previously during baseline testing they were not (the hypothesis being that the surface had already reached that state prior to flotation). The results show the benefit of aeration after acid conditioning; Po was selectively oxidized (Pn behaviour remained the same while Cp kinetics were improved). The Po–Pn selectivity clearly displays a drop in Po recovery (~ 12% absolute) compared to the test without aeration, the results were also slightly better than

previous DETA/SMBS tests. A small increase in Ni grade was observed while Cu grade declined (due to improved Pn and Po kinetics).

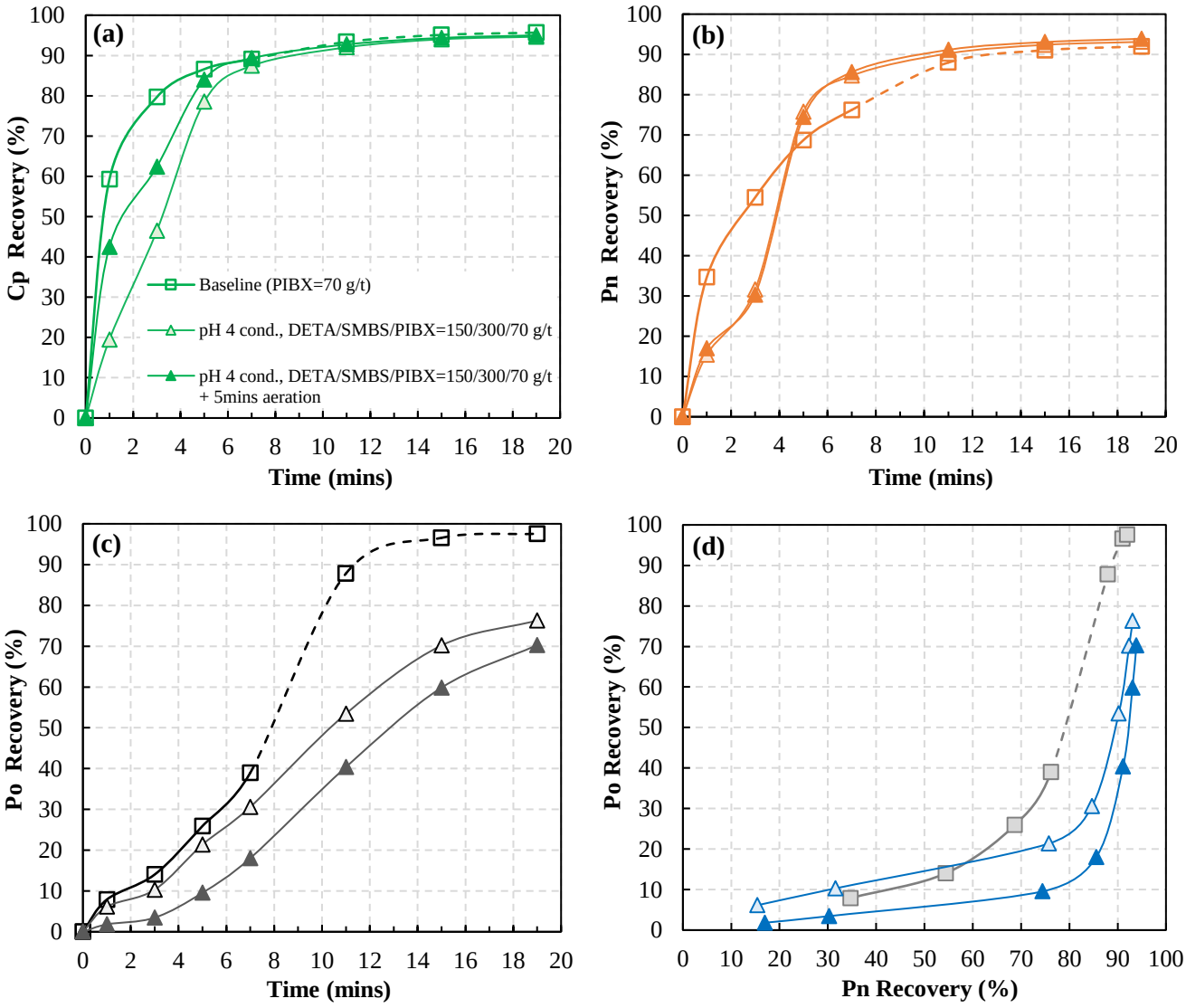

Figure 6.7 *– Flotation results of H_2SO_4/DETA/SMBS with/without aeration conditioning (solid and dashed lines refer to rougher {pH 9.2} and scavenger {pH 8} stages, respectively); (a) Cp kinetics; (b) Pn kinetics; (c) Po kinetics; (d) Po–Pn selectivity.*

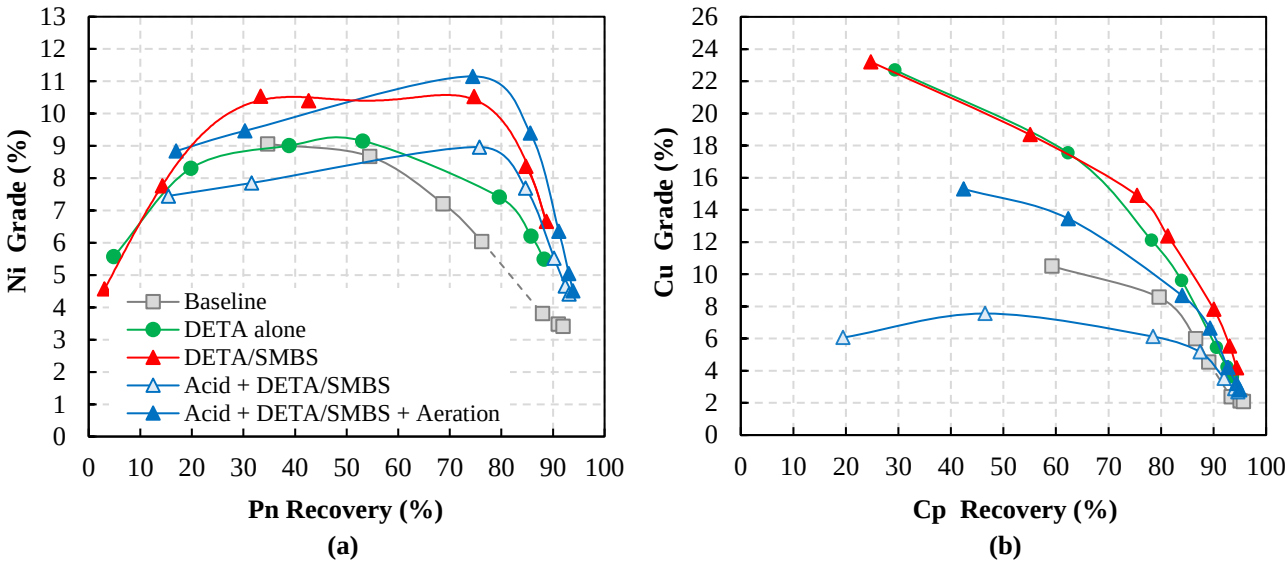

Figure 6.8 *– Grade–recovery curves with DETA and DETA/SMBS (with/without acid/aeration); (a) Ni–Pn grade–recovery; (b) Cu–Cp grade–recovery.*

Overall, the observed benefit of using acid conditioning with DETA/SMBS was increased flotation kinetics (at lower collector dosage) and was effective when combined with an aeration step; the Po–Pn selectivity results were comparable to DETA/SMBS tests with no acid conditioning. Thus, acid treatment was viewed as a technique to enhance kinetics, however, since DETA/SMBS without acid treatment/aeration could yield virtually the same results it was not investigated further. In addition, the exponential rise in Po recovery (latter portion of Po–Pn selectivity curves) was present with acid conditioning as well, which supported concentrate regrind testing.

6.3.6 Concentrate Regrind Test (with DETA/SMBS)

From the DETA/SMBS (100 g/t PIBX) Po–Pn selectivity it was determined that Po recovery significantly increased after concentrate #4. The test was repeated and concentrates #5 – 7 were combined, reground to a P80 of 35µm (chosen based on liberation data and typical plant regrind targets), and floated as rougher-cleaner stage with 4 concentrates (DETA/SMBS/PIBX = 100/200/25 g/t). The results, **Figure 6.9**, show a clear decrease in Po recovery after regrind (~ 11% Po recovery at ~ 85% Pn) with higher Ni grades (minor improvement in Cu grades), **Figure 6.10**. The data verified the assumption that exponential

rise in Po recovery was the result of binary locking with Pn and that concentrate regrind and cleaning was effective at liberating Pn particles and reducing Po recovery (~ 10% absolute). Overall, the regrind requirement was validated and gave acceptable concentrate grades which could be upgraded. Further concentrate cleaning or testing was not pursued as it was accepted that DETA/SMBS with concentrate regrind should be sufficient in achieving the outlined targets. Section 6.4 addresses pyrrhotite superstructure recovery-by-size relationships.

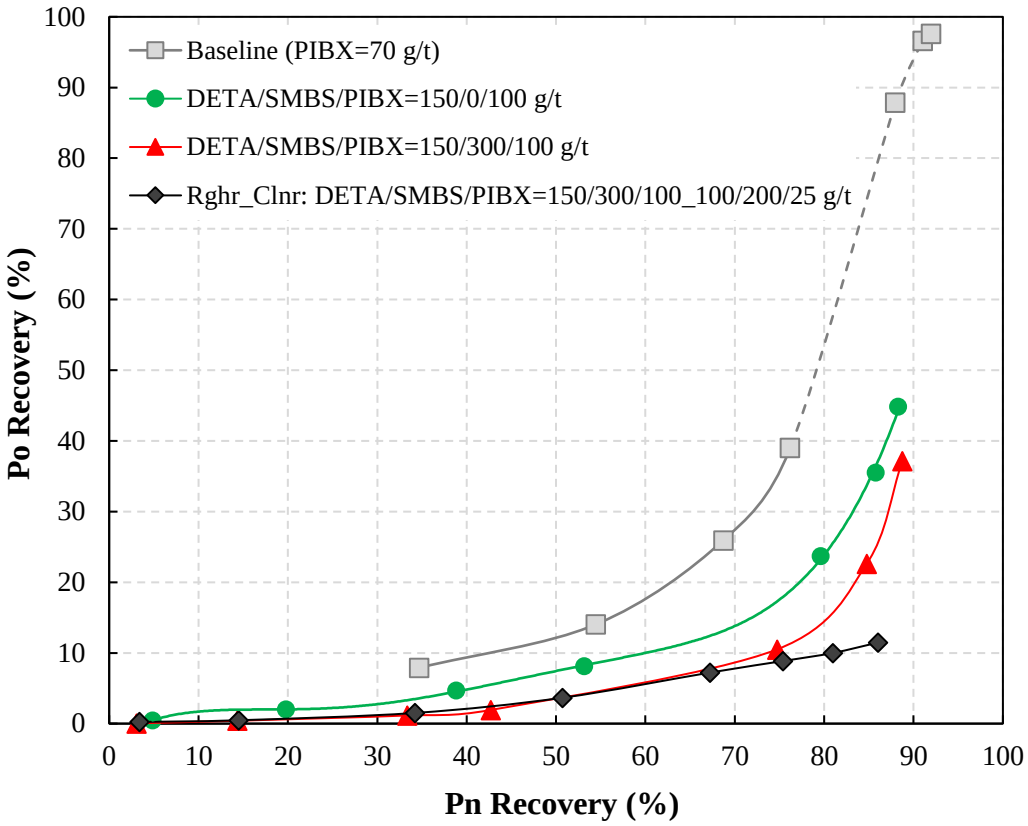

Figure 6.9 *– Po–Pn selectivity curves with DETA/SMBS/PIBX and concentrate regrind.*

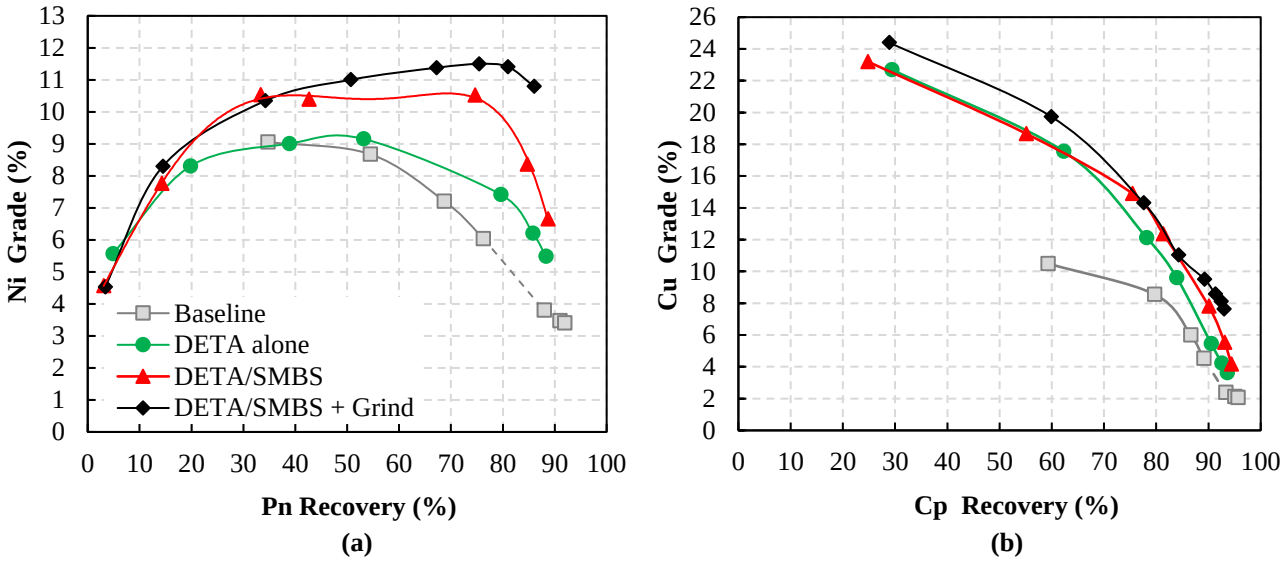

Figure 6.10 *– DETA/SMBS and concentrate regrind test; (a) Ni–Pn grade–recovery; (b) Cu–Cp grade–recovery.*

6.3.7 Summary and Key Findings

A series of scoping tests were completed on a sulfide ore (high Po/Pn: ~7.5, 42% non-magnetic Po, 85.9% Ni deportment in Pn) where pyrrhotite rejection was deemed difficult. The main objective of this test work was to assess whether the ore could be processed "as is" to achieve high Pn recovery (> 85%) while ensuring low Po recovery (< 20%). Baseline tests established that the ore was indeed challenging where Po depression by conventional means (aeration, low/high redox, high pH/lime, collector starvation) was not possible and as such depressants were required. The test work was centered around the use of DETA for its proven effectiveness for Po depression and use in some concentrators worldwide. Several strategies were tested: DETA alone, DETA/SMBS, acid/DETA/SMBS with/without aeration, and DETA/SMBS with concentrate regrind, the latter being the most effective. The important findings are summarized.

In the baseline tests, fast Po kinetics and relatively high recovery were observed for the rougher stage (pH 9.2), this gave support to the hypothesis that the Po in the ore was already partially oxidized/pre–activated when received or it was activated during milling by ions such as Cu^{2+} and Ni^{2+}, both scenarios would yield sufficiently floatable Po. The liberation data verified that Po was well liberated (> 87%) and therefore its recovery was

largely the result of its own floatability rather than due to locking with Pn or Cp. Therefore, testing with DETA for Po depression was pursued.

The role of DETA was to selectively deactivate/depress Po, and the results showed it was very effective (clear shift in the Po–Pn selectivity). Compared to the baseline rougher test, use of DETA alone resulted in significant Po depression (95%) and also depressed Pn and Cp by 59% and 25%, respectively. Furthermore, DETA also decreased the flotation kinetics of all sulfides (increasing residence times) due to its affinity for the base metals (Cu^{2+}, Ni^{2+}, and Fe^{2+}), and it was suspected to interfere with collector adsorption. Thus, additional collector (approximately 40% more) was tested, which improved the kinetics and recovery whilst not negatively impacting the newly established Po–Pn selectivity. Though the use of DETA proved effective at depressing Po, the objectives were not all met (*i.e.* Po < 20%), thus a combination of DETA and SMBS was investigated.

The DETA/SMBS (1:2 ratio) results demonstrated the positive effects of coupling SMBS with DETA, a further improvement in the Po–Pn selectivity was observed (shift towards Pn axis), justifying the use of SMBS. With increased Po rejection, improvements in both Ni and Cu grade were seen. As with the DETA only tests, DETA/SMBS also exhibited an exponential rise in Po recovery in the latter part of the selectivity curve (marginally achieving Po depression targets), highlighting the need for further testing such as sulfuric acid conditioning and concentrate regrind with DETA/SMBS to achieve the outlined objectives.

Sulfuric acid conditioning prior to DETA/SMBS addition increased flotation kinetics of all sulfides (at much lower collector dosage) and was only beneficial when combined with an aeration step (without aeration Po was sufficiently floatable). The Po–Pn selectivity results were comparable to DETA/SMBS tests with no acid conditioning. Therefore, acid treatment was viewed as a method to improve kinetics, however, since DETA/SMBS without acid treatment/aeration gave the same results it was not pursued further. Also, the exponential increase in Po recovery in latter portion of Po–Pn selectivity was still present, therefore concentrate regrind testing was assessed to further shift the selectivity towards Pn.

Concentrate regrind was very effective, yielding ~ 11% Po recovery at ~ 85% Pn recovery with acceptable concentrate grades that could be upgraded with further cleaning stages. It was accepted that DETA/SMBS with concentrate regrind should be sufficient in achieving the outlined targets. Optimization of reagent dosages (DETA/SMBS/PIBX), concentrate regrind size, and cleaner stages (*e.g.* Ni–Cu separation) to yield final concentrates were outside the scope of this test work. The next phase of this study focused on the flotation behaviour of the superstructures (non-magnetic – Fe_9S_{10} and magnetic – Fe_7S_8) by particle size and the impact of DETA/SMBS to determine its effectiveness on both superstructures. The literature is lacking information on this particular subject and since it has industrial implications the data would serve to enhance the understanding of the superstructures.

6.4 Part 2 – Flotation Recovery–by–Size Comparison of Pyrrhotite Superstructures with/without DETA & SMBS

6.4.1 Introduction

Part 1 of this study demonstrated that DETA/SMBS effectively depressed both magnetic (Fe_7S_8) and non-magnetic (Fe_9S_{10}) pyrrhotite superstructures, however, it was unclear as to whether the depression was the same for both superstructures with respect to particle size. Thus, Part 2 of the study focused on the recovery–by–size relationship with and without DETA/SMBS depressants. Additionally, superstructure flotation kinetics (cumulative recovery–by–size) was also an area of focus since this information is scarce in the literature and may aid in answering the question: *how do the different size classes of magnetic and non-magnetic pyrrhotite float with respect to time?*

A recovery–by–size relationship for the superstructures has been reported from industrial data; non-magnetic pyrrhotite follows conventional flotation recovery by particle size (highest in intermediate fractions; 10 – 100 μm) while magnetic pyrrhotite is mainly recovered in the finest fractions (< 10 μm) where entrainment effects have been mitigated [16]. This trend is observed in many concentrators worldwide, a very important point as it highlights that it is not the result of any particular plant operating strategy or orebody, rather,

it is attributed to the pyrrhotite structures (crystallography) since the relationship is maintained across several concentrators treating the same superstructures [16].

Magnetic pyrrhotite is very reactive towards oxygen as a result of its crystallography; higher structural %vacancy and number of Fe(III)–S bonds compared to non-magnetic pyrrhotite; these promote electron transfer towards oxygen [14, 46]. Thus, it is quickly passivated by hydrophilic $Fe(OH)_3$ whereas non-magnetic pyrrhotite is kinetically less reactive, and therefore permits more collector adsorption, while at the same time being more surface activated by pulp ions (Cu^{2+} and Ni^{2+}). The superstructure–oxygen reactivity supports the observed flotation differences, though the fine fraction magnetic recovery is rather peculiar. It may be associated with higher surface areas exhibited by fine particles, requiring more oxygen to reach the same degree of oxidation as intermediate/coarse particles (this would perhaps present a kinetic window that allows finer particles to have better attachment to collector and cations). Regardless, the lack of information in this area emphasized the need for further investigation into the superstructure behaviour with regards to particle size, comparing the observed industrial superstructure relationship with those from lab–scale tests.

6.4.2 Results and Discussion

6.4.2.1 Baseline and DETA/SMBS Tests (All Size Classes Combined)

It is well known that Po flotation kinetics are poor for pH > 9 (lime system) while Pn and Cp are sufficiently floatable, permitting effective separation between valuable sulfides and sulfide gangue, as such many Cu–Ni plants operate at pH > 9 to depress Po [16]. On the other hand, under neutral to mildly alkaline pH (*i.e.* 7 – 8), Po is sufficiently floatable, this pH is commonly used in scavenger operation in Cu–Ni plants and therefore was also used for laboratory scavenger testing in order to compare sulfide mineral behaviour (Pn, Cp, and Po). The baseline test was completed with both rougher (pH 9.2)/scavenger (pH 8) stages, which was originally done to evaluate sulfide kinetics and Po floatability at the two pH conditions. As ample material was available from baseline testing this was seen as an opportunity to study superstructure flotation at both pH 9.2 (rougher) and 8 (scavenger). Baseline Po–Pn selectivity and kinetics results of the combined size classes are presented in

Figure 6.11. The second test, acid/DETA/SMBS coupled with aeration (**Figure 6.11**) was successful in significantly depressing Po while maintaining Pn and Cp recoveries, matching the DETA/SMBS tests. Since much of the material was also available from this test, it was used to compare against the baseline. The grade–recovery curves are presented in **Figure 6.12** and show improvements both in Ni and Cu grades (especially Ni) as a result of significant Po depression.

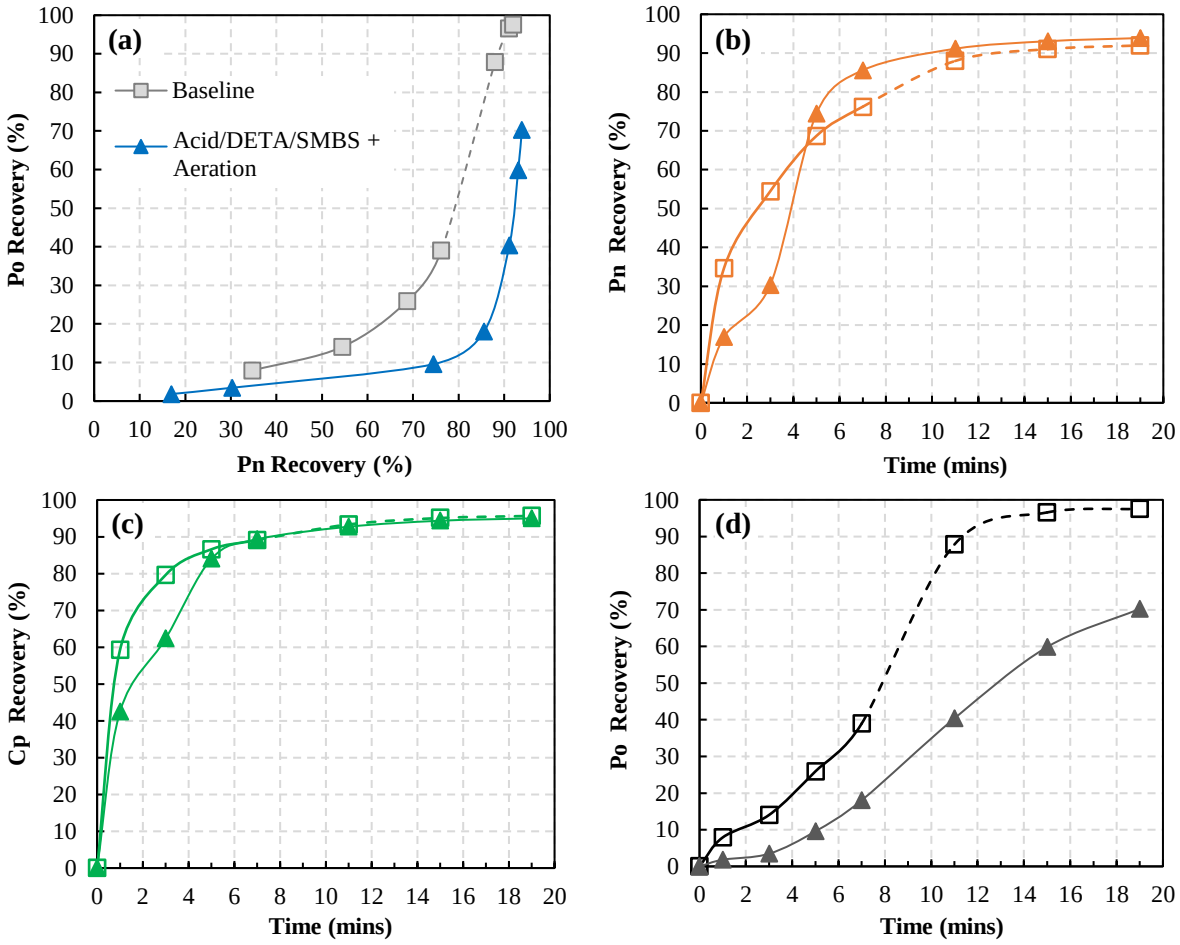

Figure 6.11 *– Flotation results of Baseline (solid and dashed lines refer to rougher {pH 9.2} and scavenger {pH 8} stages, respectively) and H_2SO_4/DETA/SMBS with aeration tests (all size classes combined); (a) Po–Pn selectivity; (b) Pn kinetics; (c) Cp kinetics; (d) Po kinetics.*

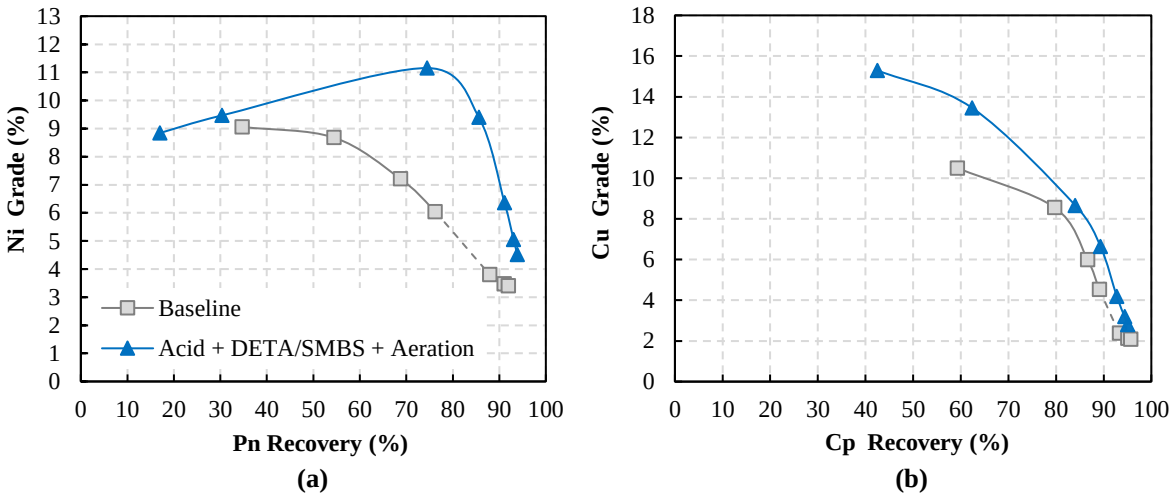

Figure 6.12 *– Flotation results of Baseline (solid and dashed lines refer to rougher {pH 9.2} and scavenger {pH 8} stages, respectively) and H_2SO_4/DETA/SMBS with aeration tests (all size classes combined); (a) Ni–Pn grade–recovery; (b) Cu–Cp grade–recovery.*

6.4.2.2 Baseline and DETA/SMBS Tests (Cumulative Recovery–by–Size)

The baseline and DETA/SMBS tests were re–evaluated based on cumulative recovery–by–size (with focus on the superstructures). Before this analysis was conducted, some concentrates were viewed as being redundant due to either low mass or close proximity to other points on the Po–Pn selectivity curve, therefore these samples were combined. For the baseline test, concentrates #5 – 7 were combined and for the DETA/SMBS test concentrates #1 – 2 and 6 – 7 were combined, overall, both tests had 5 final concentrates, labelled in **Figure 6.13**.

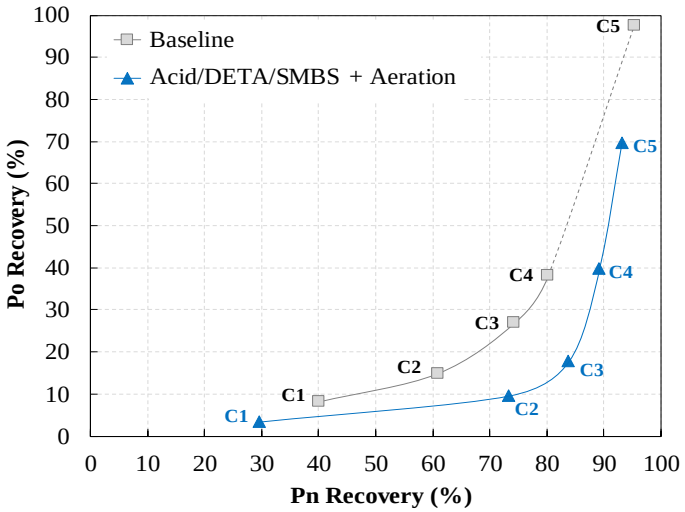

Figure 6.13 *– Comparison of Baseline and {Acid/DETA/SMBS + aeration} test Po–Pn selectivity.*

The mineral flotation kinetics for both tests (all size fractions combined) are presented in **Figure 6.14**; the data shows reduced kinetics with DETA/SMBS for all minerals, though largest effect was on pyrrhotite as discussed previously. A minor change was observed in the magnetic and non-magnetic pyrrhotite flotation; with all size fractions combined, both superstructures appeared to behave the same with and without DETA/SMBS. Nonetheless, it was speculated that perhaps the behaviour may be different with respect to particle size, each concentrate was then analyzed by size class; **Figure 6.15** displays the coarse particle (+25 µm) flotation kinetics and **Figure 6.16** presents the fine particle (–25 µm) flotation kinetics. For coarse particles, Pn and Cp exhibited highest kinetics in the middlings fraction (–106/+25 µm) whereas pyrrhotite recovery increased with decreasing particle sizes. In the middlings, non-magnetic pyrrhotite exhibited higher kinetics/recovery over magnetic pyrrhotite without DETA/SMBS, interestingly, with DETA/SMBS both superstructures behaved almost the same.

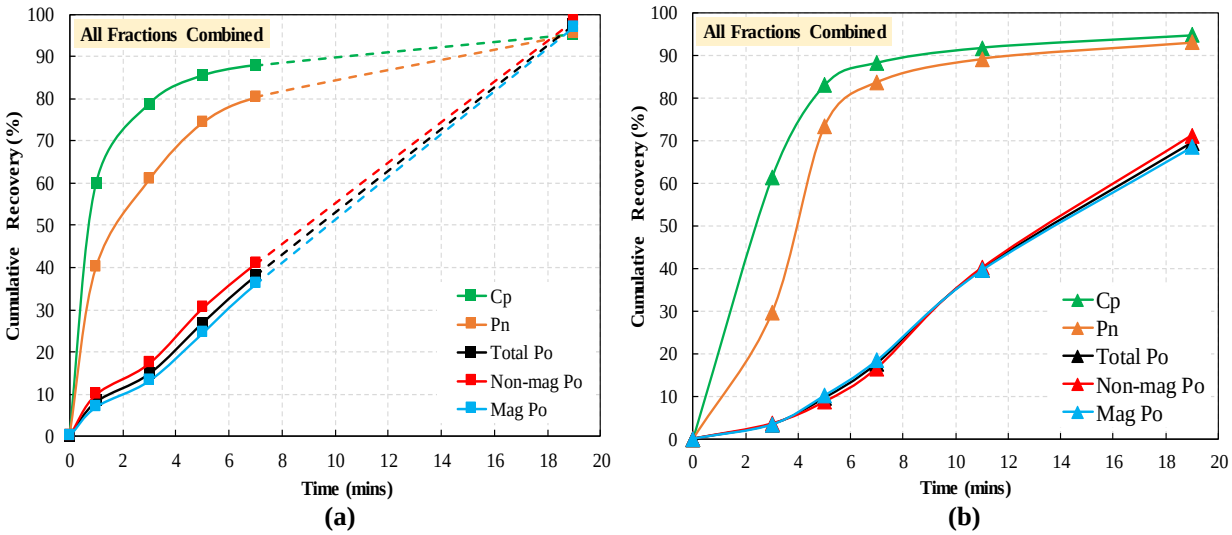

Figure 6.14 *– Comparison of mineral kinetics; (a) baseline test; (b) Acid/DETA/SMBS + aeration test.*

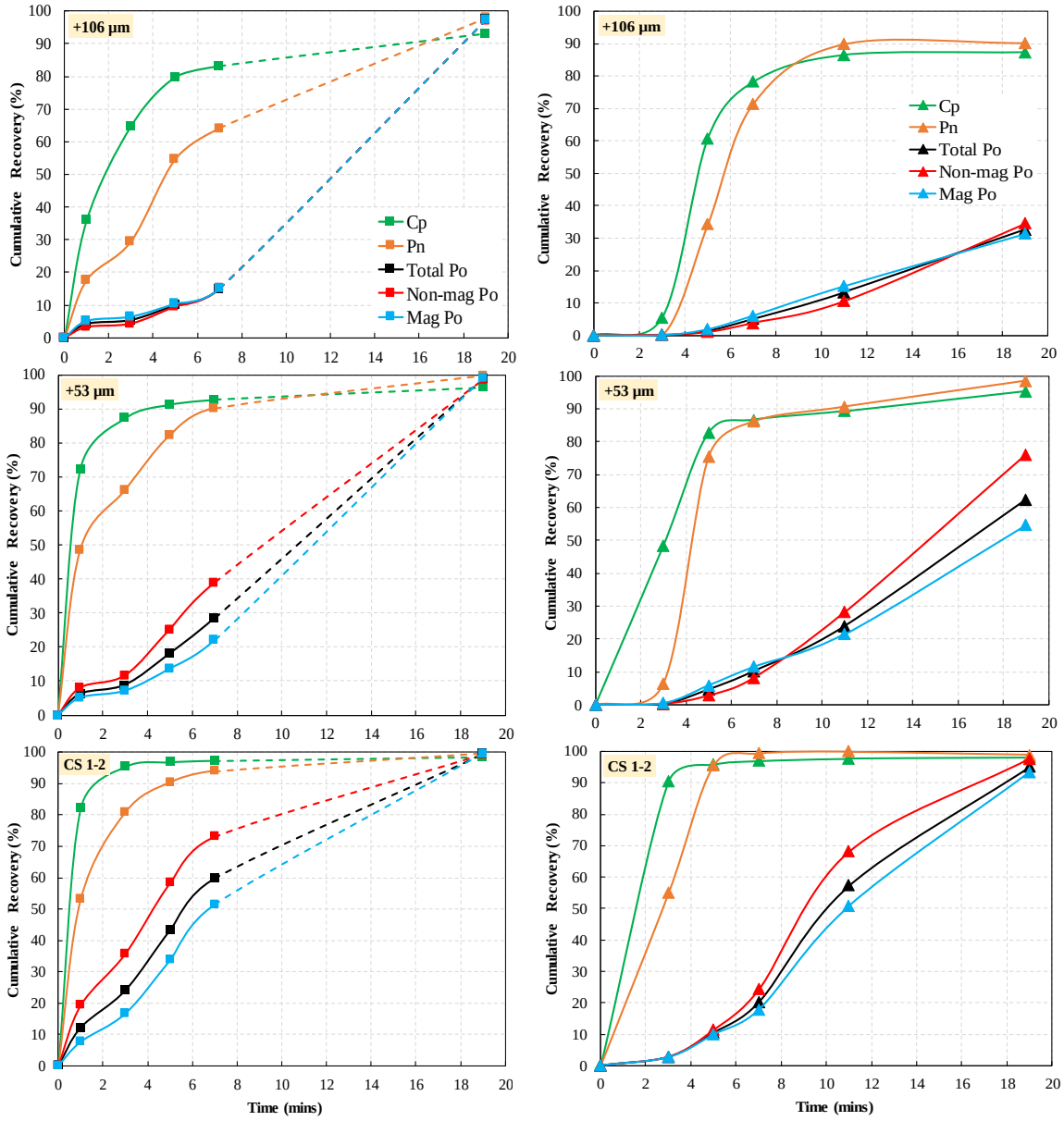

Figure 6.15 *– Comparison of mineral kinetics (coarse particle sizes); (a) baseline test; (b) Acid/DETA/SMBS + aeration test. Note: CS1-2: –53/+25µm.*

Comparing fine particle flotation, Pn and Cp recovery was as expected (highest in middlings and reduced with decreasing particle sizes) and with DETA/SMBS an improvement in both was observed (higher for Cp). Pyrrhotite flotation was the same across all fine sizes with magnetic pyrrhotite exhibiting much higher floatability, with DETA/SMBS their floatability was reduced and similar, demonstrating the surface cleaning effects of

acid/DETA/SMBS/aeration treatment. To better understand the changes taking place, it was deemed appropriate to further evaluate the results as cumulative mineral recovery versus particle size, this data is presented in **Figures 6.17** to **6.21**.

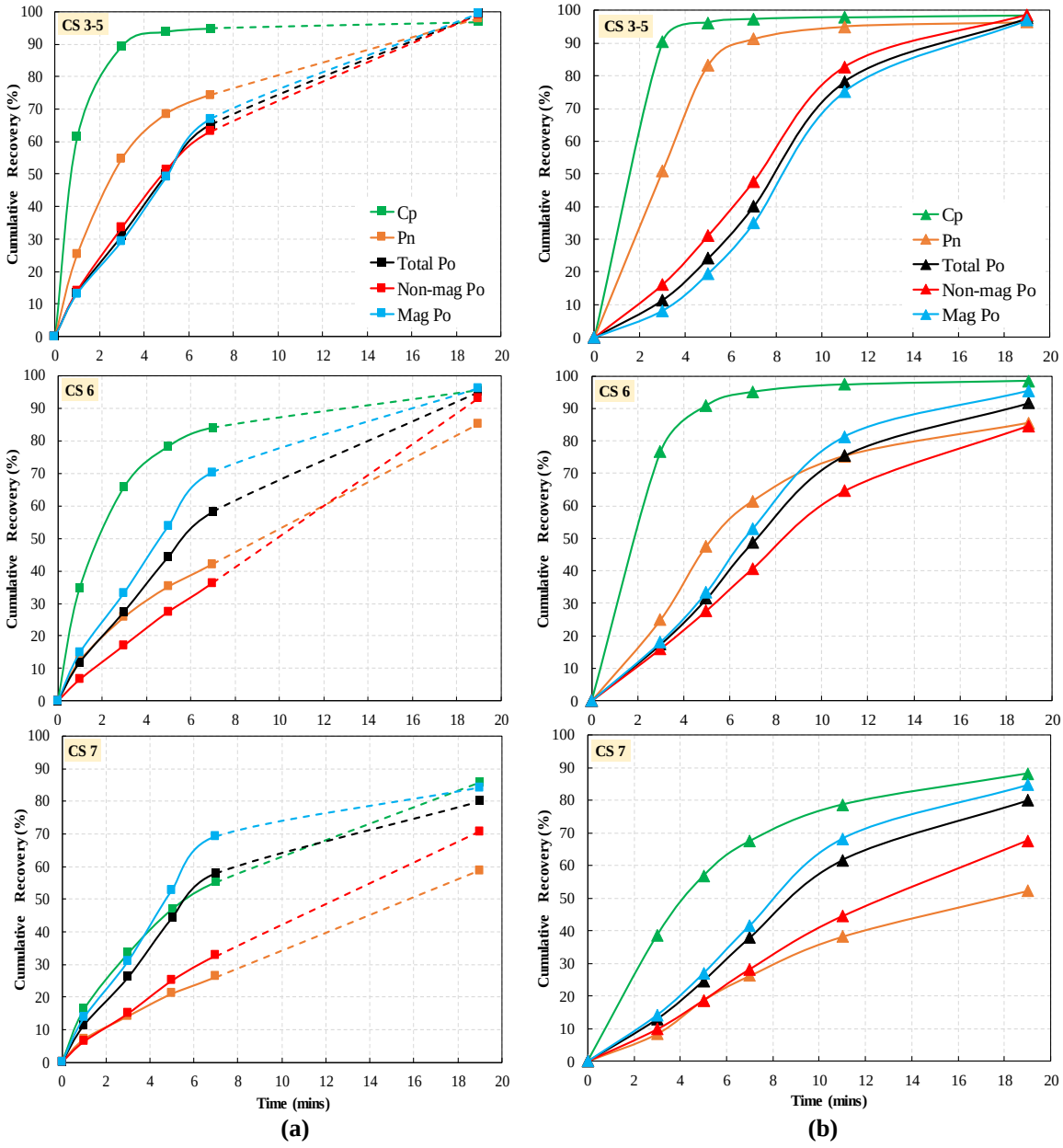

Figure 6.16 *– Comparison of mineral kinetics (fine particle sizes); (a) baseline test; (b) Acid/DETA/SMBS + aeration test. Note: CS3–5 (–25/+8 µm), CS6 (–8/+3 µm), and CS7 (–3 µm).*

Overall, for the baseline rougher stage (pH 9.2; solid lines in Figures) without DETA/SMBS, as discussed, typical cumulative recovery–by–size relationships can be seen in **Figure 6.17**(a) and **Figure 6.18**(a) for Cp and Pn, respectively; largest recovery in the intermediate sizes with progressive increase over time. Fine Pn recovery was notably low (commonly observed) and may be the result of oxidation [20]. Total pyrrhotite (**Figure 6.19**(a)) was the weighted average of magnetic and non-magnetic pyrrhotite recoveries (**Figure 6.20**(a) and **Figure 6.21**(a)) and was largely recovered in the fine and intermediate sizes (low recoveries in the coarse fraction). Interestingly, the superstructure trend of fine magnetic pyrrhotite and intermediate non-magnetic pyrrhotite recovery was observed in the rougher stage and supports the industrial superstructure relationship recently presented by Lawson *et al.* (2014) and data from XPS (courtesy of Lori Kormos), **Figure 2.19** [16]

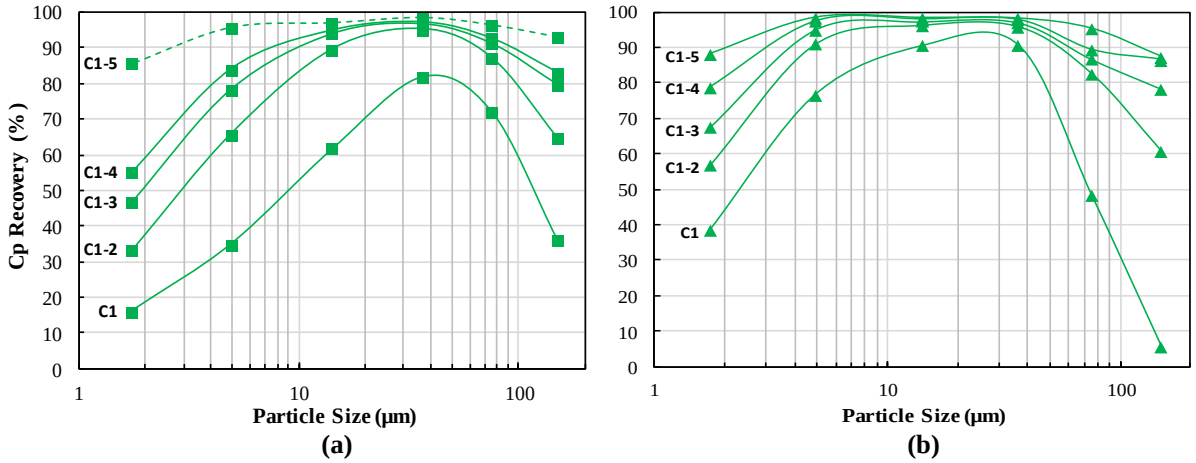

Figure 6.17 *– Chalcopyrite cumulative size-by-size recovery (a) Baseline test; (b) Acid/DETA/SMBS + aeration test.*

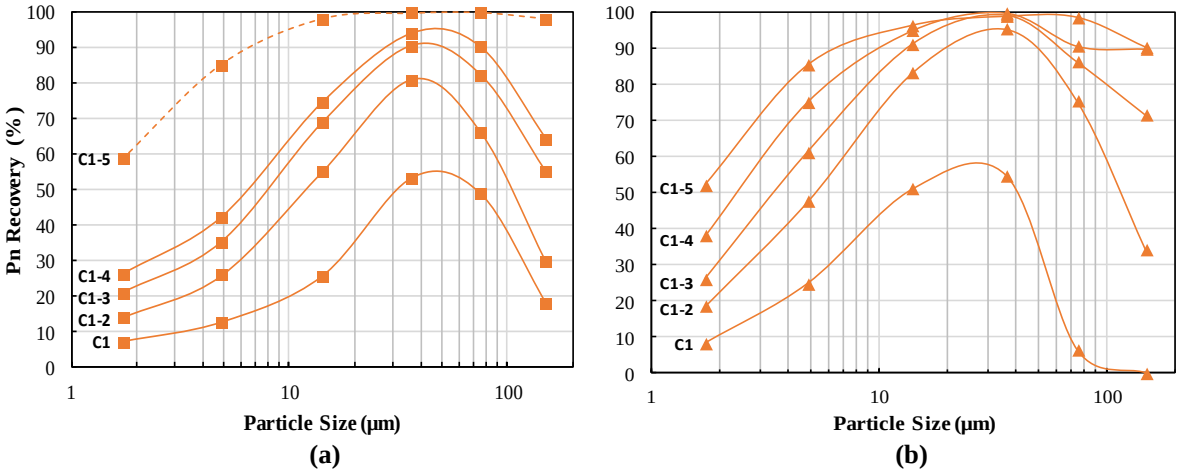

Figure 6.18 *– Pentlandite cumulative size-by-size recovery (a) Baseline test; (b) Acid/DETA/SMBS + aeration test.*

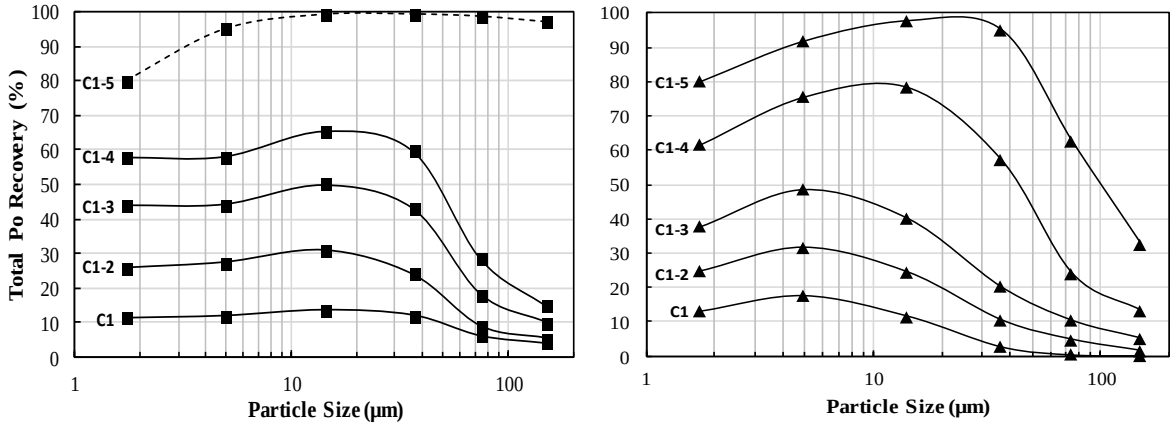

Figure 6.19 *– Pyrrhotite cumulative size-by-size recovery (a) Baseline test; (b) Acid/DETA/SMBS + aeration test.*

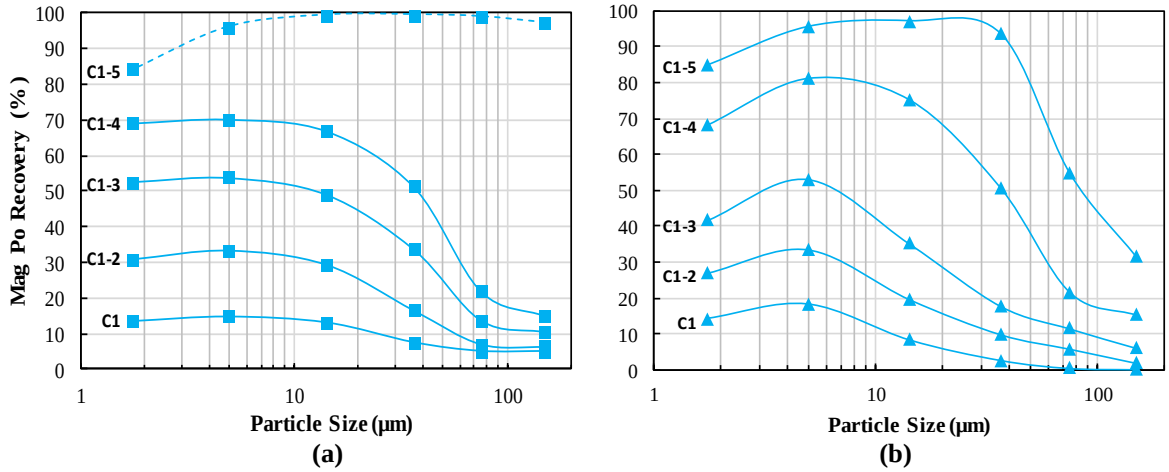

Figure 6.20 *– Magnetic pyrrhotite cumulative size-by-size recovery (a) Baseline test; (b) Acid/DETA/SMBS + aeration test.*

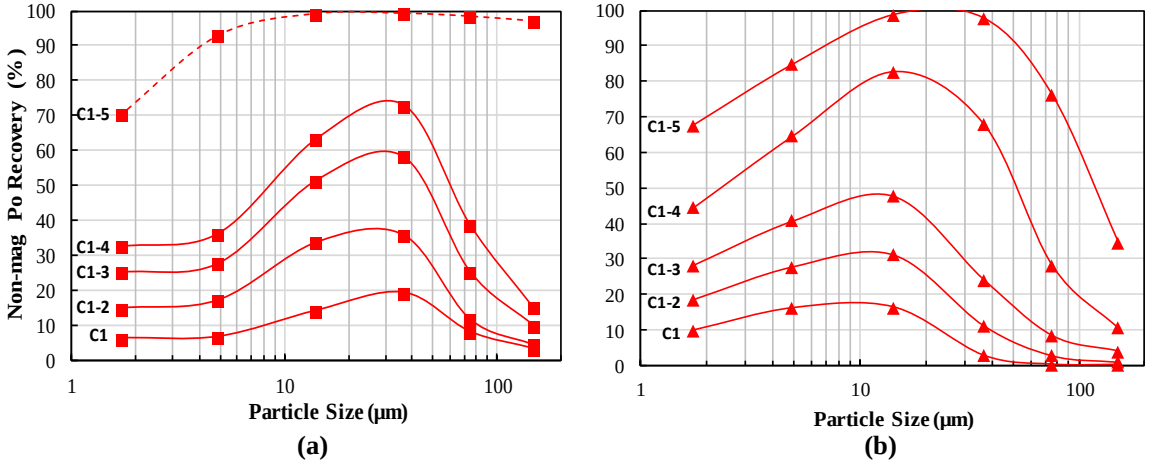

Figure 6.21 *– Non-magnetic pyrrhotite cumulative size-by-size recovery (a) Baseline test; (b) Acid/DETA/SMBS + aeration test.*

This study is the first to confirm this superstructure recovery–by–size relationship in a controlled lab setting. The reasons for this behaviour were discussed in Section 2.4.4 with superstructure reactivity towards oxygen being primary (especially under alkaline conditions). Another key finding was that magnetic and non-magnetic pyrrhotite floated in the same manner with respect to time, in other words, magnetic pyrrhotite continued to float in the fine fractions and non-magnetic pyrrhotite proceeded to float well in the intermediate sizes with no apparent change in behaviour over time. Thus, it was believed that surface oxidation (the factor responsible for the difference) was rapid on magnetic pyrrhotite and most probably occurred during the milling stage.

Evaluation of the scavenger stage (pH 8; dashed lines in Figures) shows all sulfide mineral recovery to be complete at all size classes except for < 10μm (due to poor bubble–particle attachment and perhaps surface oxidation). This lower pH was effective at promoting sulfide recovery though at the expense of selectivity against sulfide gangue, nonetheless, the results show that the differences in superstructure recovery–by–size were minimized at pH 8 as both magnetic and non-magnetic pyrrhotite trends were virtually identical. From these results, it was interpreted that pH 8 and perhaps lower were ideal for Po flotation regardless of superstructure due to slower oxidation rates that permit not only non-magnetic pyrrhotite but also significant magnetic pyrrhotite recovery. At higher pH (*i.e.* > 9), surface oxidation is accelerated especially for magnetic pyrrhotite and is most probably the driving factor that causes the differences in superstructure flotation. Moreover, under alkaline conditions magnetic pyrrhotite displays a higher degree of surface passivation whereas non-magnetic pyrrhotite exhibits a kinetic window where it is not only naturally floatable ("cleaner surface") but also amenable to surface activation by Cu^{2+} and Ni^{2+} ions, both of these would render non-magnetic pyrrhotite much more floatable.

DETA/SMBS combination was very effective in depressing pyrrhotite while maintaining high Cp and Pn recoveries and shifted the Po–Pn selectivity towards Pn. The cumulative recovery (**Figure 6.17**(b) and **Figure 6.18**(b)) showed improved Cp and Pn recoveries at pH 9.2 (especially in the fines) with DETA/SMBS over the baseline rougher. The pyrrhotite recoveries (**Figure 6.19**(b), **Figure 6.20**(b) and **Figure 6.21**(b)), though

appearing high due to the exponential rise in pyrrhotite in the last 2 concentrates, are better compared with baseline data at the same pentlandite recovery. From the selectivity curve (**Figure 6.13**), baseline concentrates #1 – 3 and DETA/SMBS concentrates #1 – 2 were chosen as the basis of comparison since the pentlandite recovery was identical (~ 75%). Total pyrrhotite and superstructure data is shown in **Figure 6.22** and **Figure 6.23**, respectively.

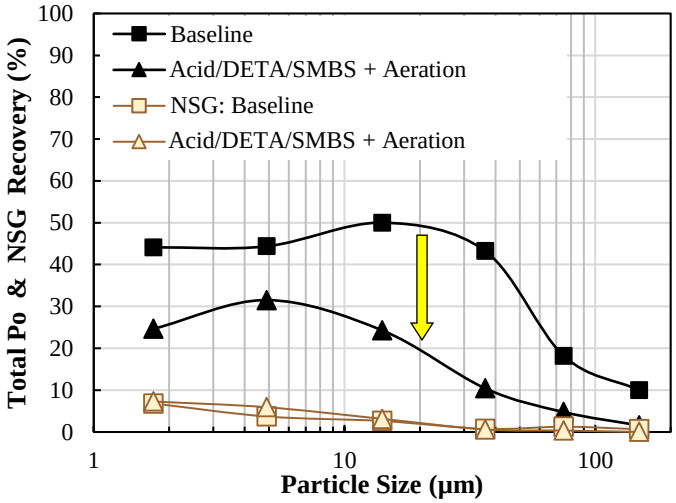

Figure 6.22 *– Pyrrhotite size-by-size recovery comparison at same pentlandite recovery (~ 75%) between Baseline and {Acid/DETA/SMBS + aeration} tests.*

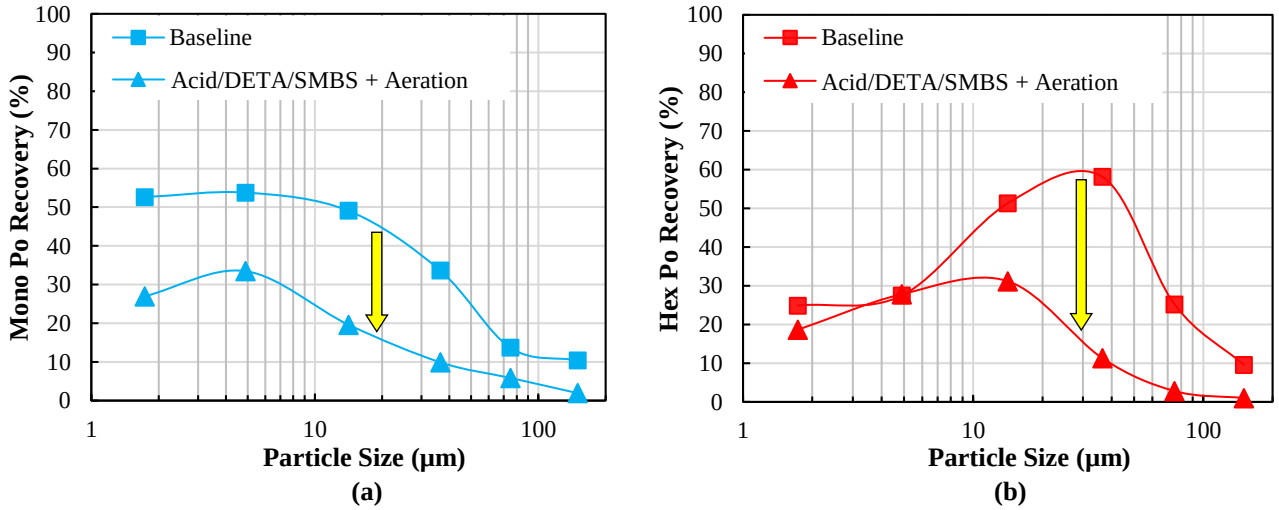

Figure 6.23 *– Size-by-size recovery comparison at same pentlandite recovery (~ 75%) between Baseline and {Acid/DETA/SMBS + aeration} tests; (a) Magnetic pyrrhotite; (b) Non-magnetic pyrrhotite.*

As explained previously, total pyrrhotite recovery (10 – 50% across fine/intermediate sizes) was significantly reduced with DETA/SMBS after which only fine particle pyrrhotite recovery was observed (5 – 30%); this was classified as weakly floatable pyrrhotite. These results are also presented as Po–Pn selectivity by size class (**Figure 6.24** (total pyrrhotite), **Figure 6.25** (magnetic pyrrhotite) and **Figure 6.26** (non-magnetic pyrrhotite)). Entrainment was considered for fine Po flotation, however when comparing non-sulfide (NSG) recoveries (< 10%; this relayed the degree of entrainment) with pyrrhotite recoveries it was evident that pyrrhotite was indeed floating (Note: NSG recovery was unchanged between the baseline and DETA/SMBS tests). Evaluation of the superstructures after DETA/SMBS conditioning shows that both fine magnetic pyrrhotite and intermediate non-magnetic pyrrhotite recoveries were largely reduced (5 – 30%). They were both effectively depressed by DETA/SMBS and remarkably their flotation responses after deactivation were nearly identical (thus essentially having the same Po–Pn selectivity; **Figure 6.25**(b) and **Figure 6.26**(b)). This analysis provides more support as to the likely mechanisms at play that permit magnetic and non-magnetic pyrrhotite to float differently. Since DETA acts to remove adsorbed Cu^{2+}/Ni^{2+} ions (with assistance from acid dissolution) and SMBS degrades polysulfide films, it was clear that in the absence of these activating ions/polysulfides the superstructures floated similarly [100, 111]. With these ions present, magnetic pyrrhotite flotation was enhanced only in the fine fractions (intermediate/coarse sizes oxidized due to high reactivity towards oxygen) and non-magnetic pyrrhotite enhanced mostly in the intermediate sizes (and likely preserved by Cu^{2+}/Ni^{2+} ions from oxidation as well). In other words, their preferential floatabilities in their respective size classes were essentially amplified by activating ions. Thus, it is believed that *superstructure reactivity towards oxygen* and the *presence of activating ions* (*e.g.* Cu^{2+} and Ni^{2+}) in an *alkaline environment* (*i.e.* pH > 9) are the major contributing factors causing superstructure flotation to be different.

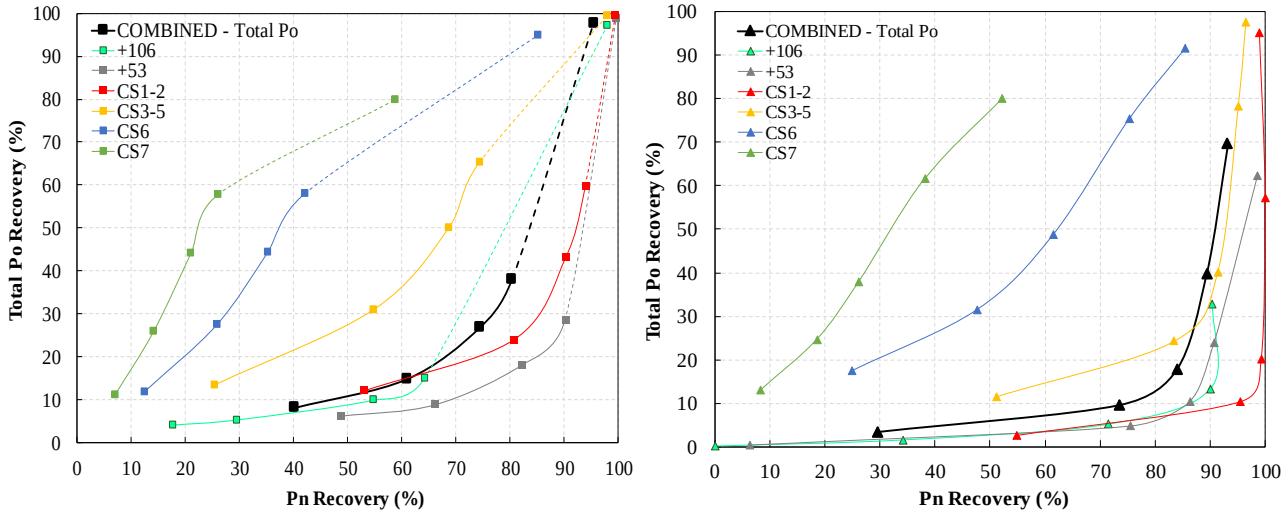

Figure 6.24 *– Po–Pn selectivity by size class for Total pyrrhotite (black line is the calculated selectivity when all size classes are combined);* ***(a)*** *Baseline test;* ***(b)*** *DETA/SMBS test.*

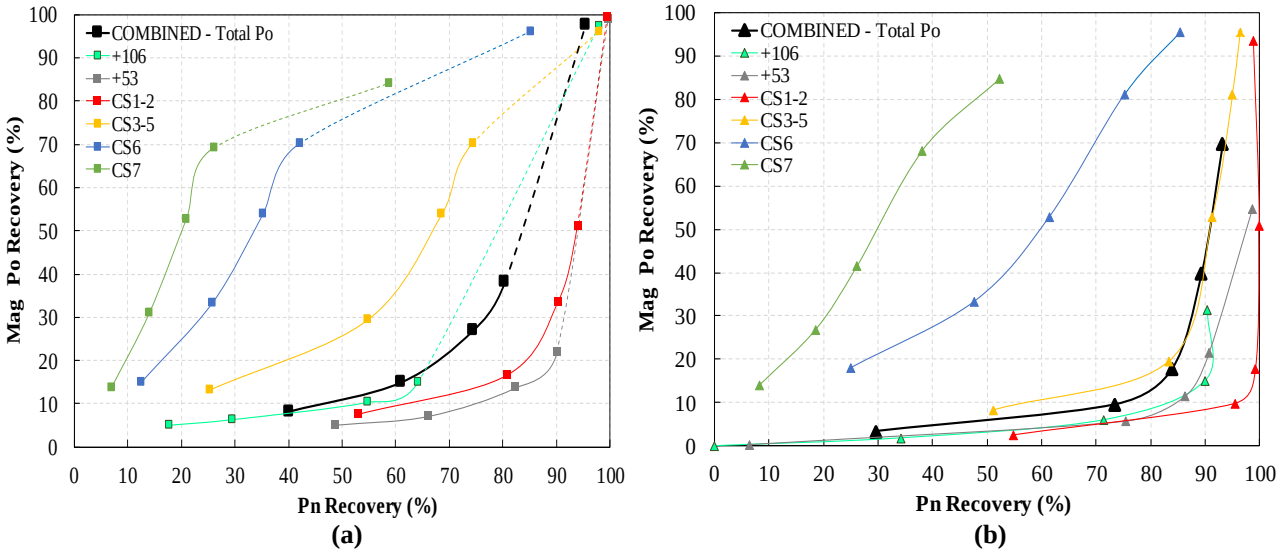

Figure 6.25 *– Po–Pn selectivity by size class for Magnetic pyrrhotite (black line is the calculated selectivity when all size classes are combined);* ***(a)*** *Baseline test;* ***(b)*** *DETA/SMBS test.*

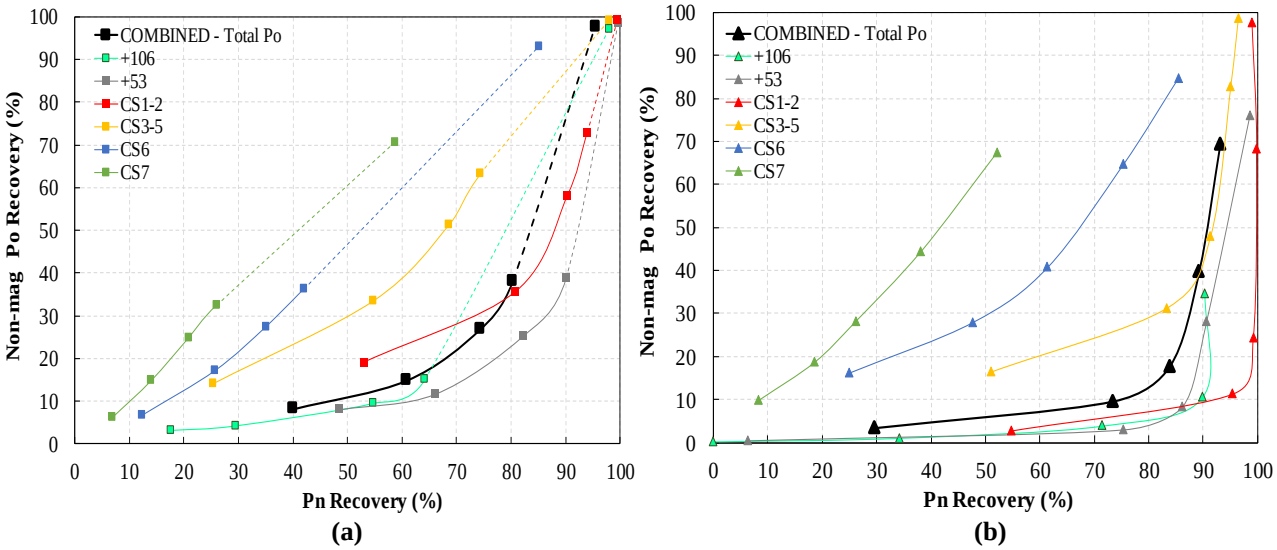

Figure 6.26 *– Po–Pn selectivity by size class for Non-magnetic pyrrhotite (black line is the calculated selectivity when all size classes are combined);* ***(a)*** *Baseline test;* ***(b)*** *DETA/SMBS test.*

6.4.3 Summary and Key Findings

Based on the observed trends, as well as the prominent theories presented in the literature, several conclusions are drawn and a few mechanisms are proposed that are responsible for the different superstructure flotation responses by particle size:

1. From the baseline rougher test (pH 9.2) – no depressants, superstructure flotation recovery–by–size was very similar to the recent industrial data presented by Lawson *et al.* (2014) and provided by XPS (courtesy of Lori Kormos) – **Figure 2.19** [16]; non-magnetic pyrrhotite having conventional flotation recovery by particle size (highest in intermediate fractions: 10 – 100 µm) while magnetic pyrrhotite being primarily recovered in the finest fractions (< 10 µm). This test work was the first to reproduce this relationship at the lab-scale level. The likely contributing factors for this flotation difference were substantial surface passivation incurred by magnetic over non-magnetic pyrrhotite which also permitted a larger degree of surface activation for non-magnetic pyrrhotite by Cu^{2+} and Ni^{2+} ions;

2. Baseline scavenger test (pH 8) – no depressants showed similar superstructure flotation across all size classes, suggesting that mildly alkaline conditions (and likely acidic–neutral) did not cause significant surface passivation on magnetic pyrrhotite due to slower

oxidation rates and therefore did not hinder collector uptake by either superstructure, yielding similar floatabilities;

3. Superstructure flotation behaviour by size class was essentially the same with respect to time; fine magnetic pyrrhotite and intermediate non-magnetic pyrrhotite recoveries increased in their respective size classes with flotation time. In other words, surface oxidation was rapid on magnetic pyrrhotite and likely occurred during the milling stage;
4. DETA/SMBS (150/300 g/t) was found to be very effective at depressing both pyrrhotite superstructures, especially in the intermediate and coarse size classes (> 30 μm);
5. After DETA/SMBS conditioning, both magnetic and non-magnetic pyrrhotite recovery–by–size was identical (complemented by superstructure Po–Pn selectivity by size), flotation was largely observed in the fine fraction (< 10 μm) – regarded as weakly floatable Po; and
6. The major factors causing measurable differences in the superstructure flotation responses: superstructure reactivity towards oxygen (differences amplified in oxidative environments), alkaline conditions (pH > 9), and presence of activating ions (*e.g.* Cu^{2+} and Ni^{2+})

Chapter 7
Conclusions, Contributions, and Future Work

7.1 Conclusions

This Chapter summarizes the major conclusions drawn from the studies presented in Chapters 4 – 6 on non-magnetic (Fe_9S_{10}) and magnetic (Fe_7S_8) pyrrhotite superstructures, contributions to original knowledge, and recommendations for future work.

7.1.1 Single Mineral Tests

Chapter 4 detailed the results of single mineral studies (mineral surface potentials with and without reagents for pH 2 – 11; PAX collector adsorption at pH 7, 8.5, and 10; and microflotation with and without sonication pre-treatment for pH 7 – 11). The tests were conducted in *ideal conditions* where mineral oxidation was minimized, the following were the major findings:

1. Zeta potential analysis showed that the superstructures had near-identical surface potentials under the various test conditions (minerals alone and in the presence of Ni^{2+}, Cu^{2+}, and *n*-amyl xanthate collector) when their surfaces were *fresh* (*i.e.* minimal contact with oxygen). In a low oxygen environment, superstructure isoelectric points were found to be identical ($pH_{IEP} \approx 3.5$ without reagents), with reagents their pH_{IEP} was shifted to ~ 9 with Ni^{2+} (added as $NiSO_4$) and 6 – 7 with Cu^{2+} (added as $CuSO_4$). The results also supported the theory of xanthate adsorption by an initial physisorption mechanism;

2. Xanthate collector adsorption studies demonstrated that xanthate uptake was much higher for magnetic over non-magnetic pyrrhotite for all pH conditions tested (7, 8.5, and 10), likely because of more Fe^{3+} sites (as $Fe(OH)[S]^{+}$) on magnetic pyrrhotite. From this, it was proposed that different proportions of xanthate surface complexes (Fe(OH)[S][X] and $Fe(OH)[S][X_2]$ (dixanthogen)) are present on the superstructures and that non-magnetic pyrrhotite likely contains more dixanthogen; and
3. Microflotation investigations showed that when surface oxidation products have been removed (*via* sonication pre-treatment) and sufficient xanthate is present (permitting adequate dixanthogen), non-magnetic and magnetic pyrrhotite superstructures behaved virtually the same

The main takeaway from these studies was that when mineral surface oxidation has been minimized (surfaces being preserved just before testing), the superstructures behave very similarly. In *real systems* (*e.g.* industrial operations), this is rarely the case since the minerals are continuously reacting and exposed to various reagents and oxygen, thus oxidation is inevitable. It was expected that in such conditions the superstructures would behave differently, to investigate this, the next phase of test work examined superstructure behaviour in reactive environments (in the presence of oxygen, grinding media, pulp ions, and other sulfide minerals).

7.1.2 Batch Ore Flotation Tests

Chapters 5 and 6 presented the results of two separate batch flotation studies with and without DETA/SMBS depressants with focus on superstructure recovery-by-size relationships. DETA/SMBS was used for two reasons; (1) the combination imparts a surface cleaning effect on pyrrhotite and therefore would aid in determining why the superstructures behave differently in *real systems* (DETA removes adsorbed Cu^{2+} and Ni^{2+} activating ions that enhance pyrrhotite floatability and SMBS degrades polysulfides and xanthate collector); and (2) it is a common pyrrhotite depressant used in industrial operations, thus the findings would be directly impactful to current operations. The first study compared 4 Cu-Ni sulfide ores having different non-magnetic/magnetic pyrrhotite ratios (5/95, 30/70, 50/50, 95/5%);

and the second assessed an industrially challenging Cu-Ni sulfide ore (non-magnetic/magnetic pyrrhotite ratio = 42/58%) as a case study to understand superstructure flotation especially in the fine size classes. Both flotation studies represented *real systems* where the superstructures were allowed to react with grinding media and oxygen (oxidation was permitted). The key points from the studies are as follows:

7.1.2.1 Baseline Tests (No Depressants)

1. Majority of the baseline rougher tests were conducted between pH 9.2 – 9.5 to keep in-line with industrial operations. Superstructure flotation data (pH 9.2 – 9.5) complemented the findings of other researchers in that non-magnetic pyrrhotite was indeed significantly more floatable than magnetic pyrrhotite (kinetics and final recovery) for all ores tested, regardless of the feed superstructure ratio. The difference in their flotation behaviour was attributed to their different reactivities at pH > 9, especially towards oxygen (magnetic pyrrhotite being more reactive). Interestingly, tests conducted at pH 8 (scavenger stages) showed similar superstructure flotation (across all size classes), suggesting that mildly alkaline conditions did not cause significant surface passivation on magnetic pyrrhotite and thus did not hinder xanthate collector uptake by either superstructure, yielding similar floatabilities. The following statements all pertain to pH 9.2 – 9.5 tests as these exhibited different superstructure flotation behaviour;
2. Final pyrrhotite recovery increased with increasing feed non-magnetic pyrrhotite content, demonstrating that ores containing higher non-magnetic pyrrhotite content would be more challenging to process under alkaline pH conditions;
3. Pentlandite selectivity was poorer against non-magnetic over magnetic pyrrhotite, which was consistent for most ores. Furthermore, regardless of ore type, non-magnetic pyrrhotite selectivity curves were virtually the same when superimposed, similarly, all magnetic pyrrhotite selectivity curves were the same. Thus, their flotation behaviour was not ore-related, rather, credited to their crystallography. This suggested that increasing feed non-magnetic pyrrhotite content would result in a proportional decrease in Po-Pn selectivity;

4. Po-Pn selectivity (only comparing total pyrrhotite) in the fine (< 38 μm) and coarse (> 38 μm) size fractions showed worse selectivity in the fines over coarse sizes, this was due to poor/mediocre floatability of fine pentlandite where pyrrhotite is still sufficiently floatable;

5. Initial attempts at assessing superstructure Po-Pn selectivity curves in the fine fraction gave inconclusive results due to significant overlapping of superstructure curves. To resolve this issue, subsequent testing implemented cyclosizing of every float product which gave many individual size classes (rather than just two) particularly below 38 μm, this change was sufficient in overcoming the barriers in assessing fine particle superstructure behaviour; and

6. After cyclosizing, the data confirmed the findings of Lawson *et al.* (2014) in that non-magnetic pyrrhotite floated primarily in intermediate size classes (10 – 100 μm) while magnetic pyrrhotite floated largely in the finest sizes (< 10 μm) [16]. The likely reason for this difference was substantial surface passivation sustained by magnetic over non-magnetic pyrrhotite which also permitted a larger degree of surface activation for non-magnetic pyrrhotite by Cu^{2+} and Ni^{2+} ions

7.1.2.2 DETA/SMBS Depression Tests

1. DETA/SMBS (100/200 g/t) combination showed depressive effects on both pyrrhotite superstructures, however, at this dosage it was more effective on magnetic pyrrhotite across most of the ores tested. This was clearly shown for an ore containing 50/50% superstructure mixture where magnetic pyrrhotite was more depressed even though both superstructures were exposed to the same amount of DETA/SMBS depressant. It was believed that non-magnetic pyrrhotite contains a higher surface density of polysulfides and activating ions (Cu^{2+} and Ni^{2+}) and therefore requires higher DETA/SMBS dosages to achieve the same degree of depression as magnetic pyrrhotite. With higher depressant dosages (*e.g.* DETA/SMBS = 150/300 g/t), both superstructures were effectively depressed and to the same degree, both superstructures behaved identically in the presence of sufficient DETA/SMBS;

2. Data for concentrate metal upgrade ratios with DETA/SMBS gave mixed results; at times it was only marginally higher over baseline tests and other times it was much higher as expected since pyrrhotite depression had taken place. It was identified that higher non-sulfide gangue recovery had occurred with DETA/SMBS thereby maintaining baseline concentrate upgrade ratios since non-sulfide gangue had replaced pyrrhotite in the concentrate; and
3. DETA/SMBS was effective at depressing both superstructures especially in the intermediate and coarse size classes (> 30 μm), after which, flotation for both superstructures was largely observed in the fine fraction (< 10 μm) – regarded as weakly floatable pyrrhotite. This was attributed to surface area effects (fine particles requiring more depressant due to much higher surface areas over coarser particles)

7.1.3 Summary

From the many studies presented in this thesis, it is clear that the superstructure flotation behaviour is governed by their different surface reactivities which becomes apparent in *real systems*. This reactivity difference stems from their crystallography; magnetic/monoclinic pyrrhotite contains more structural vacancies and Fe^{3+} compared to non-magnetic/hexagonal pyrrhotite. This difference is sufficient in causing magnetic pyrrhotite to be more reactive, especially towards oxygen. In *ideal systems*, both superstructures have virtually the same flotation response, in *real systems* where their surfaces are allowed to interact with oxygen and equipment/slurry, their flotation behaviour changes significantly. The major factors that cause measurable differences in superstructure flotation responses are: presence of oxygen (oxidative conditions), alkaline conditions (pH > 9), and presence of activating ions (Cu^{2+} and Ni^{2+}). Fortunately, both superstructures can be treated to behave similarly and depressed to the same degree in real systems with the use of surface acting agents such as DETA/SMBS depressants. It should be noted that sufficient DETA/SMBS dosage is required since non-magnetic pyrrhotite contains more adsorbed ions/polysulfides than magnetic pyrrhotite.

7.2 Contributions to Original Knowledge

In the literature, there is generally a poor understanding of the pyrrhotite superstructures and their different flotation responses, with a limited number of articles having been published in the past 3 decades on their floatability. Unfortunately, much of the flotation data is contradictory with only two in-depth studies (Ph.D. theses; Kolahdoozan (1996) and Becker (2009)) providing much of the relevant and accurate information. These studies, though very informative, investigated synthetic and purified superstructure powders from ore samples and consisted of relatively small-scale flotation tests (0.25 – 2 g) where other variables could not be tested. This thesis continued from where these researchers concluded and builds on their work.

This thesis was organized into two main sections: small scale studies representing *ideal systems* and larger batch flotation studies representing *real systems*; this comparison has not been presented on the superstructures in the literature prior to this thesis and was vital in determining the major factors responsible for their differing flotation behaviour. The conclusions of this thesis have enhanced the knowledge base of the pyrrhotite superstructures and will certainly be valuable to the mineral processing industry where their rejection is targeted. The originality of this thesis is as follows:

1. Zeta potential analysis of both superstructures (minerals alone and in the presence of Cu^{2+}, Ni^{2+} and *n*-amyl xanthate) was presented for the first time in low oxygen environments, the results showed that they have the same surface charges and isoelectric points under various conditions;
2. *N*-amyl xanthate adsorption studies confirmed different amounts of xanthate uptake for the superstructures purified from natural ore samples, indicating different dixanthogen concentration on the superstructures; non-magnetic pyrrhotite data was reported for the first time;
3. It was shown that both superstructures have similar “grindability” since preferential grind of either superstructure did not occur. The feed superstructure ratio was maintained across all size classes after grinding (shown to be consistent for every ore), this was

previously questioned as the underlying cause for magnetic pyrrhotite reporting to the fine fraction and non-magnetic pyrrhotite reporting to the coarse size fractions in the concentrate;

4. Microflotation studies on the superstructures were presented with and without sonication pre-treatment to demonstrate the effects of mineral surface oxidation; a sonication study was conducted and established that an optimal sonication time existed, this has not been reported by previous researchers;

5. This thesis is the first to report the findings of large batch flotation tests conducted on 1 – 2 kg ore samples with known superstructure ratios (5/95, 30/70, 42/58, 50/50, and 95/5%), these tests represented *real systems*. All float products were balanced for superstructure content which allowed for the assessment of magnetic and non-magnetic pyrrhotite flotation kinetics, which also has not been reported for large batch flotation tests. These tests are the standard for mineral processing and have not been presented in the literature until now, previous flotation studies opted to use microflotation on 0.25 – 2 g purified samples as the method of comparison;

6. The superstructure recovery-by-size relationship observed in industrial operations was reproduced at the lab-scale for the first time. These results showed that superstructure floatability was not ore-related but due to their different crystal structures; and

7. DETA/SMBS effect on the superstructure recovery-by-size relationship was reported for the first time; it was concluded that with sufficient dosage both superstructures' recovery-by-size becomes the same, in other words, the surface products that caused them to be different in the first place were removed by DETA/SMBS

7.3 Suggestions for Future Work

Throughout the course of this thesis, several superstructure characterization techniques were used: XRD, magnetic force microscopy (MFM), SEM-EBSD, and Raman Spectroscopy, with XRD (peak-intensity ratio) being the most robust and reproducible, thus it was chosen as the main method of quantification (in conjunction with ICP-OES assay data).

The MFM, SEM-EBSD, and Raman techniques showed promise, however, required further study to make them routine methods. These would be particularly useful for characterizing samples containing less than 5 wt% pyrrhotite as well as for mineral locking between the superstructures (from MFM/SEM-EBSD), therefore it is recommended that these techniques be developed.

The xanthate collector adsorption study showed different uptake for the superstructures and since the higher uptake for magnetic pyrrhotite did not translate to higher floatability, it was concluded that likely different amounts of dixanthogen existed on the superstructures. This would be an interesting piece of information and can be retrieved from spectroscopic studies such as FT-IR.

Lastly, although DETA/SMBS depressant combination proved beneficial for depressing pyrrhotite and forced both superstructures to behave the same at adequate dosage, DETA is not a particularly environmentally friendly reagent. In addition, it results in very stable soluble Cu^{2+} and Ni^{2+} complexes in industrial tailings, which in some instances leads to high concentrations of Cu^{2+} and Ni^{2+} ions that can surpass regulatory effluent limits. Therefore, other environmentally friendly reagents that impart a similar depressive effect on the pyrrhotite superstructures and have minimal impact on downstream tailings should be investigated to mitigate the issues surrounding DETA.

References

1. Wills, B.A. and J.A. Finch, *Wills' Mineral Processing Technology*. 8th ed. 2016, Massachusetts, USA: Butterworth-Heinemann.

2. Belzile, N., Y.W. Chen, M.F. Cai, and Y. Li, *A review on pyrrhotite oxidation.* Journal of Geochemical Exploration, 2004. **84**: p. 65-76.

3. Posfai, M., T.G. Sharp, and A. Kontny, *Pyrrhotite varieties from the 9.1 km deep borehole of the KTB project.* American Mineralogist, 2000. **85**: p. 1406-1415.

4. Becker, M., J. DeVilliers, and D. Bradshaw, *The mineralogy and crystallography of pyrrhotite from selected nickel and PGE ore deposits.* Economic Geology, 2010. **105**: p. 1025-1037.

5. Li, F. and H.F. Franzen, *Phase transitions in near stoichiometric iron sulfide.* Journal of Alloys and Compounds, 1996. **238**(1-2): p. 73-80.

6. Arnold, R.G., *Range in composition and structure of 82 natural terrestrial pyrrhotites.* The Canadian Mineralogist, 1967. **9**(1): p. 31-50.

7. Manouchehri, H.R., *Pyrrhotite flotation and its selectivity against pentlandite in the beneficiation of nickeliferous ores: An electrochemistry perspective.* Minerals & Metallurgical Processing, 2014. **31**: p. 115-126.

8. Miller, J.D., J. Li, J.C. Davidtz, and F. Vos, *A review of pyrrhotite flotation chemistry in the processing of PGM ores.* Minerals Engineering, 2005. **18**: p. 855-865.

9. Peek, E., A. Barnes, and A. Tuzun, *Nickeliferous pyrrhotite - "waste or resource?"*. Minerals Engineering, 2011. **24**: p. 625-637.

10. Agar, G.E., *Flotation of chalcopyrite, pentlandite, pyrrhotite ores.* International Journal of Mineral Processing, 1991. **33**: p. 1-19.

11. Kolahdoozan, M., *Adsorption and flotation characteristics of hexagonal and monoclinic pyrrhotite*, in *Department of Mining Engineering*. 1996, Queen's University: Kingston, Canada. Ph.D. Thesis.

12. Lawson, V., A.N. Kerr, Y. Shields, P.F. Wells, M. Xu, and Z. Dai. *Improving Pentlandite Pyrrhotite Separation at INCO' s Clarabelle*. in *Centenary of Flotation Symposium*. 2005. Brisbane, Australia: AusIMM.

13. Becker, M., *The mineralogy and crystallography of pyrrhotite from selected nickel and PGE ore deposits and its effect on flotation performance*. 2009, University of Pretoria: Pretoria, South Africa. Ph.D. Thesis.

14. Becker, M., J. DeVilliers, and D. Bradshaw, *The flotation of magnetic and non-magnetic pyrrhotite from selected nickel ore deposits.* Minerals Engineering, 2010. **23**: p. 1045-1052.

15. He, M.-F., W.-Q. Qin, W.-Z. Li, and F. Jiao, *Flotation performances of polymorphic pyrrhotite.* Journal of Central South University, 2012. **19**: p. 238-243.

16. Lawson, V., G. Hill, L. Kormos, and G. Marrs. *The Separation of Pentlandite from Chalcopyrite, Pyrrhotite and Gangue in Nickel Projects Throughout the World*. in *12th AusIMM Mill Operators' Conference 2014*. 2014. Townsville, Australia: AusIMM.

17. Zhao, C.-h., B.-z. Wu, and J.-h. Chen, *Electronic structure and flotation behavior of monoclinic and hexagonal pyrrhotite.* Journal of Central South University, 2015. **22**: p. 466-471.

18. Trahar, W.J. and L.J. Warren, *The flotability of very fine particles — A review.* International Journal of Mineral Processing, 1976. **3**: p. 103-131.

19. Trahar, W.J., *A rational interpretation of the role of particle size in flotation.* International Journal of Mineral Processing, 1984. **8**: p. 289-327.

20. Senior, G.D., L.K. Shannon, and W.J. Trahar, *The flotation of pentlandite from pyrrhotite with particular reference to the effects of particle size.* International Journal of Mineral Processing, 1994. **42**: p. 169-190.

21. Alsen, N., *Roentgenographische Untersuchungen der Kristallstrukturen von Magnetkies, Breithauptite, Pentlandite, Millerite und verwandten Verbindungen.* Geologiska Foreningens i Stockholm Forhandlingar, 1925. **47**: p. 19-73.

22. Hagg, G. and I. Sucksdorff, *The crystal structure of troilite and pyrrhotite.* Zeitschrift Fur Physikalische Chemie-Abteilung B-Chemie Der Elementarprozesse Aufbau Der Materie, 1933. **22**(5/6): p. 444-452.

23. Bertaut, P.E.F., *Contribution a l'Etude des Structures Lacunaires: La pyrrhotine.* Acta Crystallographica, 1953. **6**: p. 557-561.

24. Kissin, S.A. and S.D. Scott, *Phase Relations Involving Pyrrhotite Below 350°C.* Economic Geology, 1982. **77**: p. 1739-1754.

25. Wang, H. and I. Salveson, *A review on the mineral chemistry of the non-stoichiometric iron sulphide, $Fe_{1-x}S$ ($0 \leq x \leq 0.125$): polymorphs, phase relations and transitions, electronic and magnetic structures.* Phase Transitions, 2005. **78**: p. 547-567.

26. Kullerud, G. and H.L. Barnes, *Experimental Techniques in Dry Sulfide Research*, in *Research Techniques for High Pressure and High Temperature*, G.C. Ulmer, Editor. 1971, Springer-Verlag: New York. p. 289-315.

27. Kissin, S.A., *Phase Relations in a Portion of the Fe-S System*. 1974, University of Toronto: Toronto, Canada. Ph.D. Thesis.

28. Arnold, R.G., *Pyrrhotite Phase Relation Below 304 +/- 6°C at <1 Atm Total Pressure.* Economic Geology, 1969. **64**: p. 405-419.

29. Yund, R.A. and H.T. Hall, *Hexagonal and monoclinic pyrrhotites.* Economic Geology, 1969. **64**: p. 420-423.

30. Morimoto, N., A. Gyobu, H. Mukaiyama, and E. Izawa, *Crystallography and stability of pyrrhotites.* Economic Geology, 1975. **70**: p. 824-833.

31. Nakazawa, H. and N. Morimoto, *Pyrrhotite Phase Relations Below 320°C.* Proc. Japan Acad., 1970. **46**: p. 678-683.

32. Nakazawa, H. and N. Morimoto, *Phase Relations and Superstructures of Pyrrhotite, $Fe_{1-x}S$.* Materials Research Bulletin, 1971. **6**: p. 345-357.

33. Barnes, H.L., *Investigations in Hydrothermal Sulfide Systems*, in *Research Techniques for High Pressure and High Temperature*, G.C. Ulmer, Editor. 1971, Springer-Verlag: New York. p. 317-355.

34. Scott, S.D. and H.L. Barnes, *Hydrothermal growth of single crystals of cinnabar (red HgS).* Materials Research Bulletin, 1969. **4**: p. 897-904.

35. Scott, S.D. and H.L. Barnes, *Sphalerite geothermometry and geobarometry.* Economic Geology, 1971. **66**: p. 653-669.

36. Gordon, S.C. and A.M. McDonald, *A study of the composition, distribution, and genesis of pyrrhotite in the copper cliff offset, sudbury, Ontario, Canada.* Canadian Mineralogist, 2016. **53**: p. 859-878.

37. Becker, M., J. DeVilliers, and D. Bradshaw. *Evaluation of Pyrrhotite from Selected Ni and Platinum Group Element (PGE) Ore Deposits and the Influence of its Mineralogy on Flotation Performance*. in *Ninth International Congress for Applied Mineralogy*. 2008. Brisbane, Australia: AusIMM.

38. Fleet, M.E., *Phase equilibria at high temperatures*, in *Sulfide Mineralogy and Geochemistry*, D.J. Vaughan, Editor. 2006, Mineralogical Society of America: Washington DC, USA. p. 365-419.

39. Powell, A.V., P. Vaqueiro, K.S. Knight, L.C. Chapon, and R.D. Sánchez, *Structure and magnetism in synthetic pyrrhotite Fe_7S_8: A powder neutron-diffraction study.* Physical Review B - Condensed Matter and Materials Physics, 2004. **70**: p. 1-12.

40. Izaola, Z., S. González, L. Elcoro, J.M. Perez-Mato, G. Madariaga, and A. García, *Revision of pyrrhotite structures within a common superspace model.* Acta Crystallographica Section B: Structural Science, 2007. **63**(5): p. 693-702.

41. DeVilliers, J., D. Liles, and M. Becker, *The crystal structure of a naturally occurring 5C pyrrhotite from sudbury, its chemistry, and vacancy distribution.* American Mineralogist, 2009. **94**: p. 1405-1410.

42. DeVilliers, J. and D. Liles, *The crystal-structure and vacancy distribution in 6C pyrrhotite.* American Mineralogist, 2010. **95**: p. 148-152.

43. Elliot, A.D., *Structure of pyrrhotite 5C (Fe_9S_{10}).* Acta Crystallographica Section B: Structural Science, 2010. **66**: p. 271-279.

44. Liles, D. and J. DeVilliers, *Redetermination of the structure of 5C pyrrhotite at low temperature and at room temperature.* American Mineralogist, 2012. **97**: p. 257-261.

45. Vaughan, D.J., E.J. Schwarz, and D.R. Owens, *Pyrrhotites from the Strathcona mine, Sudbury, Canada: A thermomagnetic and mineralogical study.* Economic Geology, 1971. **66**: p. 1131-1144.

46. Pratt, A.R., I.J. Muir, and H.W. Nesbitt, *X-ray photoelectron and Auger electron spectroscopic studies of pyrrhotite and mechanism of air oxidation.* Geochimica et Cosmochimica Acta, 1994. **58**: p. 827-841.

47. Theodossiou, A., *Measurements of the Hall effect and resistivity in pyrrhotite.* Physical Review, 1965. **137**: p. 1321-1326.

48. Menyeh, A. and W. O'Reilly, *The Magnetization Process In Monoclinic Pyrrhotite (Fe_7S_8) Particles Containing Few Domains.* Geophysical Journal International, 1991. **104**: p. 387-399.

49. Worm, H.-U., D. Clark, and M.J. Dekkers, *Magnetic Susceptibility of Pyrrhotite: Grain Size, Field and Frequency Dependence.* Geophysical Journal International, 1993. **114**: p. 127-137.

50. Li, F. and H.F. Franzen, *Ordering, incommensuration, and phase transitions in pyrrhotite. II. A high-temperature x-ray powder diffraction and thermomagnetic study.* J. Solid State Chem., 1996. **126**: p. 108-120.

51. O'Reilly, W., V. Hoffmann, A.C. Chouker, H.C. Soffel, and A. Menyeh, *Magnetic properties of synthetic analogues of pyrrhotite ore in the grain size range 1-24 um.* Geophysical Journal International, 2000. **142**: p. 669-683.

52. Gilder, S.A., R. Egli, R. Hochleitner, S.C. Roud, M.W.R. Volk, M. Le Goff, and M. De Wit, *Anatomy of a pressure-induced, ferromagnetic-to-paramagnetic transition in pyrrhotite: Implications for the formation pressure of diamonds.* Journal of Geophysical Research: Solid Earth, 2011. **116**: p. 1-16.

53. Dorogina, G.A., R.I. Gulyaeva, E.N. Selivanov, and V.F. Balakirev, *Thermal and thermomagnetic properties of pyrrhotites.* Russian Journal of Inorganic Chemistry, 2015. **60**: p. 301-306.

54. Koulialias, D., J. Kind, M. Charilaou, P.G. Weidler, J.F. Löffler, and A.U. Gehring, *Variable defect structures cause the magnetic low-temperature transition in natural monoclinic pyrrhotite.* Geophysical Journal International, 2016. **204**: p. 961-967.

55. Arnold, R.G., *Equilibrium relations between pyrrhotite and pyrite from 325^o to 743^{o}C.* Economic Geology, 1962. **57**: p. 72-90.

56. Arnold, R.G. and L.E. Reichen, *Measurement of the metal content of naturally occurring, metal-deficient, hexagonal pyrrhotite by an x-ray spacing method.* The American Mineralogist, 1962. **47**: p. 105-111.

57. Graham, A.R., *Quantitative Determination of Hexagonal and Monoclinic Pyrrhotites by X-Ray Diffraction.* The Canadian Mineralogist, 1969. **10**: p. 4-24.

58. Skála, R., I. Císařová, and M. Drábek, *Inversion twinning in troilite.* American Mineralogist, 2006. **91**: p. 917-921.

59. Arnold, R.G., *Mixtures of hexagonal and monoclinic pyrrhotite and the measurement of the metal content of pyrrhotite by x-ray diffraction.* The American Mineralogist, 1966. **51**: p. 1221-1227.

60. Carpenter, R.H. and G.A. Desborough, *Range in solid solution and structure of naturally occurring troilite and pyrrhotite.* American Mineralogist, 1964. **49**: p. 1350-1365.

61. Janzen, M.P., R.V. Nicholson, and J.M. Scharer, *Pyrrhotite reaction kinetics: Reaction rates for oxidation by oxygen, ferric iron, and for nonoxidative dissolution.* Geochimica et Cosmochimica Acta, 2000. **64**: p. 1511-1522.

62. Puigdomenech, I., *HYDRA: Hydrochemical Equilibrium-Constant Database*. 2009, Royal Institute of Technology: Stockholm, Sweden.

63. Puigdomenech, I., *MEDUSA: Make Equilibrium Diagrams Using Sophisticated Algorithms*. 2010, Royal Institute of Technology: Stockholm, Sweden.

64. Wang, H., *A Review on Process-Related Characteristics of Pyrrhotite.* Mineral Processing and Extractive Metallurgy Review, 2007. **29**: p. 1-41.

65. Mycroft, J.R., H.W. Nesbitt, and A.R. Pratt, *X-ray photoelectron and Auger electron spectroscopy of air-oxidized pyrrhotite: Distribution of oxidized species with depth.* Geochimica et Cosmochimica Acta, 1995. **59**: p. 721-733.

66. Payant, R., F. Rosenblum, J.E. Nesset, and J.A. Finch, *The self-heating of sulfides: Galvanic effects.* Minerals Engineering, 2012. **26**: p. 57-63.

67. Janzen, M.P., *Role of ferric iron, trace metal content, and crystal structure on pyrrhotite oxidation*. 1996, University of Waterloo: Waterloo, Canada. M.Sc. Thesis.

68. Gauvreau, B., *Sudbury Sulphide Ore Oxidation: A Geological and Mineralogical Investigation*. 2002, Laurentian University: Sudbury, Canada. B.Sc. Thesis.

69. Ekmekci, Z., M. Becker, E.B. Tekes, and D. Bradshaw, *An impedance study of the adsorption of $CuSO_4$ and SIBX on pyrrhotite samples of different provenances.* Minerals Engineering, 2010. **23**: p. 903-907.

70. Ekmekci, Z., M. Becker, E.B. Tekes, and D. Bradshaw, *The relationship between the electrochemical, mineralogical and flotation characteristics of pyrrhotite samples from different Ni Ores.* Journal of Electroanalytical Chemistry, 2010. **647**: p. 133-143.

71. Spira, P. and F. Rosenblum. *The oxygen demand of flotation pulps*. in *6th Annual Meeting of the Canadian Mineral Processors*. 1974. Ottawa, Canada: Canadian Mineral Processors.

72. Vanyukov, A.V. and N.N. Razumovskaya, *Hydrothermal oxidation of pyrrhotites.* Izv Vyssh Uchelon Zaved, Tsvetn, Metall., 1979. **6**: p. 605-610.

73. Yakhontova, L.K., L.G. Nesterovich, and A.P. Grudev, *New data on natural oxidation of pyrrhotite.* Vestnik Moskovskogo Universiteta Geologiya, 1983. **38**: p. 41-44.

74. Orlova, T.A., V.M. Stupnikov, and A.L. Kresan, *Mechanism of oxidative dissolution of sulphides.* Zhurnal Prikladnoi Khimii, 1988. **61**: p. 2172-2177.

75. Kwong, Y.T.J., *Prediction and prevention of acid rock drainage from a geological and mineralogical perspective*. 1993, National Hydrology Research Institute: Saskatoon, Saskatchewan (Canada). p. 1-66.

76. Lehmann, M.N., P. Kaur, R.M. Pennifold, and J.G. Dunn, *Comparative study of the dissolution of hexagonal and monoclinic pyrrhotites in cyanide solution.* Hydrometallurgy, 2000. **55**: p. 255-273.

77. Cheng, X. and I. Iwasaki, *Pulp Potential and Its Implications to Sulfide Flotation.* Mineral Processing and Extractive Metallurgy Review, 1992. **11**: p. 187-210.

78. Greet, C.J., J. Kinal, and P. Steinier. *Grinding Media — Its Effect on Pulp Chemistry and Flotation Behaviour — Fact or Fiction?* in *Centenary of Flotation Symposium*. 2005. Brisbane, Australia: AusIMM.

79. Hamilton, I.C. and R. Woods, *An investigation of surface oxidation of pyrite and pyrrhotite by linear potential sweep voltammetry.* Journal of Electroanalytical Chemistry and Interfacial Electrochemistry, 1981. **118**: p. 327-343.

80. Buckley, A.N. and R. Woods, *X-ray photoelectron spectroscopy of oxidized pyrrhotite surfaces I. Exposure to air.* Applications of Surface Science, 1985. **22-23**: p. 280-287.

81. Davis, J.A. and D.B. Kent, *Surface complexation modeling in aqueous geochemistry.* Mineral-Water Interface Geochemistry, 1990. **23**(1): p. 177-260.

82. Rao, S.R. and J. Leja, *Surface Chemistry of Froth Flotation*. Vol. 1&2. 2004, New York, USA: Kluwer Academic/Plenum Publishers.

83. Bebie, J., M.A.A. Schoonen, M. Fuhrmann, and D.R. Strongin, *Surface Charge Development on Transition Metal Sulfides: An Electrokinetic Study.* Geochimica et Cosmochimica Acta, 1998. **62**: p. 633-642.

84. Kosmulski, M., *Surface Charging and Points of Zero Charge*. 2009, Florida, USA: CRC Press.

85. Ney, P., *Zeta-Potentiale und Flotierbarkeit von Mineralen*. 1973, Wien and New York: Springer-Verlag.

86. J. Dekkers, M. and M. A.A. Schoonen, *An electrokinetic study of synthetic greigite and pyrrhotite.* Geochimica et Cosmochimica Acta, 1994. **58**: p. 4147-4153.

87. Xu, Z.R., S.R.; Finch, J.A.; Kelebek, S.; Wells, P., *Role of diethylene triamine (DETA) in pentlandite-pyrrhotite separtion - Part 1: complexation of metals with DETA.* Transactions of the Institution of Mining and Metallurgy Section C-Mineral Processing and Extractive Metallurgy, 1997. **106**: p. C15-C20.

88. Acar, S. and P. Somasundaran, *Effect of dissolved mineral species on the electrokinetic behaviour of sulfides.* Minerals Engineering, 1992. **5**: p. 27-40.

89. Somasundaran, P. and D. Wang, *Solution Chemistry: Minerals and Reagents*. 2006, Amsterdam, Netherlands: Elsevier Science.

90. Winter, G. and R. Woods, *The Relation of Collector Redox Potential to Flotation Efficiency: Monothiocarbonates.* Separation Science, 1973. **8**: p. 261-267.

91. Allison, S.A., L.A. Goold, and A. Granville, *A Determination of the Products of Reaction Between Various Sulfide Minerals and Aqueous Xanthate Solution , and a Correlation of the Products with Electrode Rest Potentials.* Metallurgical Transactions, 1972. **3**: p. 2613-2618.

92. Moslemi, H., P. Shamsi, and F. Habashi, *Pyrite and pyrrhotite open circuit potentials study: Effects on flotation.* Minerals Engineering, 2011. **24**: p. 1038-1045.

93. Hodgson, M. and G.E. Agar, *Electrochemical Investigations into the Flotation Chemistry of Pentlandite and Pyrrhotite: Process Water and Xanthate Interactions.* Canadian Metallurgical Quarterly, 1989. **28**: p. 189-198.

94. Rao, S.R. and J.A. Finch, *Adsorption of Amyl Xanthate at Pyrrhotite in the Presence of Nitrogen and Implications in Flotation.* Canadian Metallurgical Quarterly, 1991. **30**: p. 1-6.

95. Bozkurt, V., Z. Xu, and J.A. Finch, *Pentlandite/pyrrhotite interaction and xanthate adsorption.* International Journal of Mineral Processing, 1998. **52**: p. 203-214.

96. Allison, S.A.C., C. T., *An investigation into the flotation behaviour of pyrrhotite.* International Journal of Mineral Processing, 2011. **98**: p. 202-207.

97. Kolahdoozan, M. and W.T. Yen. *Pyrrhotite - An Important Gangue and a Source for Environmental Pollution*. in *Green Processing 2002*. 2002. Cairns, Australia: AusIMM.

98. Kelebek, S. *The effect of oxidation on the flotation behaviour of nickel-copper ores*. in *XVIII International Mineral Processing Congress*. 1993. Sydney, Australia: AusIMM.

99. Khan, A. and S. Kelebek, *Electrochemical aspects of pyrrhotite and pentlandite in relation to their flotation with xanthate. Part-I: Cyclic voltammetry and rest potential measurements.* Journal of Applied Electrochemistry, 2004. **34**: p. 849-856.

100. Yoon, R.-H., C.I. Basilio, M.A. Marticorena, A.N. Kerr, and R. Stratton-Crawley, *A Study of the Pyrrhotite Depression Mechanism by Diethylenetriamine.* Minerals Engineering, 1995. **8**: p. 807-816.

101. Mendiratta, N.K., *Kinetic Studies of Sulfide Mineral Oxidation and Xanthate Adsorption*. 2000, Virginia Polytechnic Institute and State University: Virginia, USA. Ph.D. Thesis.

102. Tukel, C. and S. Kelebek, *Modulation of xanthate action by sulphite ions in pyrrhotite deactivation/depression.* International Journal of Mineral Processing, 2010. **95**: p. 47-52.

103. Guo, B., Y. Peng, and R. Espinosa-Gomez, *Cyanide chemistry and its effect on mineral flotation.* Minerals Engineering, 2014. **66-68**: p. 25-32.

104. Wercholaz, C.R., *Non-magnetic pyrrhotite and its effect on ore processing*. 2009, University of Toronto: Toronto, Canada. B.Sc. Thesis.

105. He, S.H., S. Grano, H.M. Manoucheri, A. Taylor, and V. Lawson. *The critical influence of pulp oxygen content on the separation of pentlandite from pyrrhotite in two process streams of the Clarabelle Mill of VALE INCO, Sudbury, Canada*. in *24th International Mineral Processing Congress*. 2008. Beijing, China: IMPC.

106. Rao, S.R., *Xanthates and related compounds*. 1971: M. Dekker, New York.

107. Mohammadi-Jam, S., *An Investigation into the Applicability of Inverse Gas Chromatography to Mineral Flotation*. 2016, McGill University: Montreal, Canada. Ph.D. Thesis.

108. Fuerstenau, M.C., M. Misra, and B.R. Palmer, *Xanthate adsorption on selected sulfides in the virtual absence and presence of oxygen, Part 1.* International Journal of Mineral Processing, 1990. **29**: p. 111-119.

109. Fuerstenau, M.C., M. Misra, and B.R. Palmer, *Xanthate adsorption on selected sulfides in the virtual absence and presence of oxygen, Part 2.* International Journal of Mineral Processing, 1990. **29**: p. 111-119.

110. Leppinen, J.O., *FTIR and flotation investigation of the adsorption of ethyl xanthate on activated and non-activated sulfide minerals.* International Journal of Mineral Processing, 1990. **30**: p. 245-263.

111. Xu, Z.H., S.R. Rao, J.A. Finch, S. Kelebek, and P. Wells, *Role of diethylene triamine (DETA) in pentlandite-pyrrhotite separation .1. complexation of metals with DETA.* Transactions of the Institution of Mining and Metallurgy Section C-Mineral Processing and Extractive Metallurgy, 1997. **106**: p. C15-C20.

112. Kelebek, S. and C. Tukel, *The effect of sodium metabisulfite and triethylenetetramine system on pentlandite-pyrrhotite separation.* International Journal of Mineral Processing, 1999. **57**(2): p. 135-152.

113. Chimbganda, T., M. Becker, J.L. Broadhurst, S.T.L. Harrison, and J.P. Franzidis, *A comparison of pyrrhotite rejection and passivation in two nickel ores.* Minerals Engineering, 2013. **46-47**: p. 38-44.

Organization of the Appendix

The Appendix was separated into two Sections (A and B). Appendix A presents extra information for Chapter 3; (1) example calculations for the PAX adsorption tests (pertaining to Section 3.1.1.4); and (2) example of collector dosage used in industrial operations for various base metal sulfide ores (based on feed metal tons) which was used as a starting point for the batch ore flotation tests (pertaining to Section 3.1.2.1). Appendix B provides the supplementary information for Chapter 5 (pertaining to Sections 5.3 – 5.5), which includes Ores A – D mineral liberation/associations by size class, preliminary and in-depth study grade-recovery, mineral kinetics, concentrate Ni/Cu upgrade ratios, and Po-Pn selectivity.

Appendix A

Example Calculation for PAX Adsorption Tests

PAX adsorption density and PAX equivalent monolayer coverage for the non-magnetic pyrrhotite superstructure powder (same calculations for magnetic pyrrhotite):

(1) PAX adsorption density on non-magnetic pyrrhotite powder (100 mg/L initial PAX concentration, 2.75 mg/L equilibrium PAX concentration (after 360 mins))

$$\text{PAX Adsorption Density} = \frac{([\text{PAX}]_{initial} - [\text{PAX}]_{equilibrium}) * \text{Volume}}{\text{mineral surface area}}$$

$$= \frac{\left(100\,\frac{\text{mg}}{\text{L}} - 2.75\,\frac{\text{mg}}{\text{L}}\right) * 0.100\ \text{L}}{0.2500\ \text{g} * 6.626\ \frac{\text{m}^2}{\text{g}}}$$

$$= 5.871\ \frac{\text{mg (PAX)}}{\text{m}^2\ \text{(mineral)}}$$

(2) PAX equivalent monolayer coverage for non-magnetic pyrrhotite

(i) PAX cross-sectional area per mg $= \frac{(\text{PAX molecule cross} - \text{sectional area}) * \text{Avogadro's number}}{\text{MW}_{\text{PAX}}}$

$$= \frac{\left(25\,\frac{\text{Å}^2}{\text{molecule}} * \frac{(1\text{x}10^{-10})^2\text{m}^2}{\text{Å}^2} * \frac{6.022 * 10^{23}\ \text{molecules}}{\text{mole}}\right)}{202{,}000\ \frac{\text{mg}}{\text{mole}}}$$

$$= 0.745\ \frac{\text{m}^2\ \text{(PAX)}}{\text{mg (PAX)}}$$

(ii) Equivalent monolayer coverage $= \frac{\left(\frac{\text{PAX cross} - \text{sectional area}}{\text{mg PAX}}\right) * \text{mg PAX adsorbed}}{\text{mineral surface area}}$

$$= \left(\frac{\text{PAX cross} - \text{sectional area}}{\text{mg PAX}}\right) * \text{PAX adsorption density}$$

$$= 0.745\ \frac{\text{m}^2\ \text{(PAX)}}{\text{mg (PAX)}} * 5.871\ \frac{\text{mg (PAX)}}{\text{m}^2\ \text{(mineral)}}$$

$$= 4.37$$

Table A1 *– Example of collector types and dosage based on metal tons; reproduced from Wills and Finch (2016)[1].*

Operation	Metals	Collector	Dosage (kg t^{-1} metal)
Strathcona Mill	Ni–Cu	PIBX	2.8 (Ni + Cu)
Clarabelle Mill	Ni–Cu	SAX	2.1 (Ni + Cu)
Thomson	Ni–Cu	SAX	1.3 (Ni + Cu)
Louvicourt Mine	Cu–Zn–Au–Ag	Aerophine 3418A	1.6 (Cu)
		PAX 51	0.5 (Cu)
		Flex 41	0.5 (Zn)
Les Mine Selbaie	Cu–Zn–Au–Ag	SIPX	1.1 (Cu)
		SP129	0.6 (Zn)
Myra Falls	Cu–Zn–Au–Ag	PAX: Aerofloat 208	0.7 (Cu + Zn)
		(73:27 blend added to both circuits)	1.5 (Cu + Zn)
Mine Bouchard-Hebert	Cu–Zn–Au–Ag	3418A (to Cu circuit)	3.5 (Cu)
		3148A (to Zn circuit)	0.7 (Zn)
		Aerofloat 208	2.1 (Cu)
Mine Langlois	Cu–Zn–Au–Ag	208 (to Cu circuit)	3.3 (Cu)
		3418 (to Cu circuit)	5.4 (Cu)
		3418 (to Zn circuit)	0.6 (Zn)
Matagami Mine	Cu–Zn–Au–Ag	Aero 3477 (to Cu circuit)	4.6 (Cu)
		Aero 3418A (to Cu circuit)	0.4 (Cu)
		Aero 3418A (to Zn circuit)	0.5 (Zn)
Brunswick Mine	Pb–Zn–Cu (Ag)	80:20 SIPX:PAX	1.8 (Pb + Zn + Cu)
		Aero 241	0.1 (Pb + Cu)
		Aerophine 5100	0.1 (Cu)
Heath Steele	Pb–Zn–Cu (Ag)	SIPX	1.0 (Pb + Zn + Cu)
		Aero 241	0.3(Pb + Zn + Cu)
		Aerophine 5100	0.2 (Pb + Zn + Cu)

Key (family type for trade name reagents): PIBX, potassium isobutyl xanthate; SAX, sodium amyl xanthate; SP129, blend of dithiophosphate and mercaptobenzothiazole plus diamine modifier; Aerophine 3418A, dithiophosphinate; PAX, potassium amyl xanthate; Flex 41, xanthate; SIBX, sodium isobutyl xanthate; Aerofloat 208, dithiophosphate; Aero 3477, dithiophosphate; Aero 241, dithiophosphate; Aerophine 5100, allyl isobutyl thionocarbamate.

Appendix B

Supplementary Information for Chapter 5 (Sections 5.3 – 5.5)

Note: Ore A = 5% Non-mag Po, Ore B = 30% Non–mag Po, Ore C = 50% Non–mag Po, and Ore D = 95% Non–mag Po.

Ore A

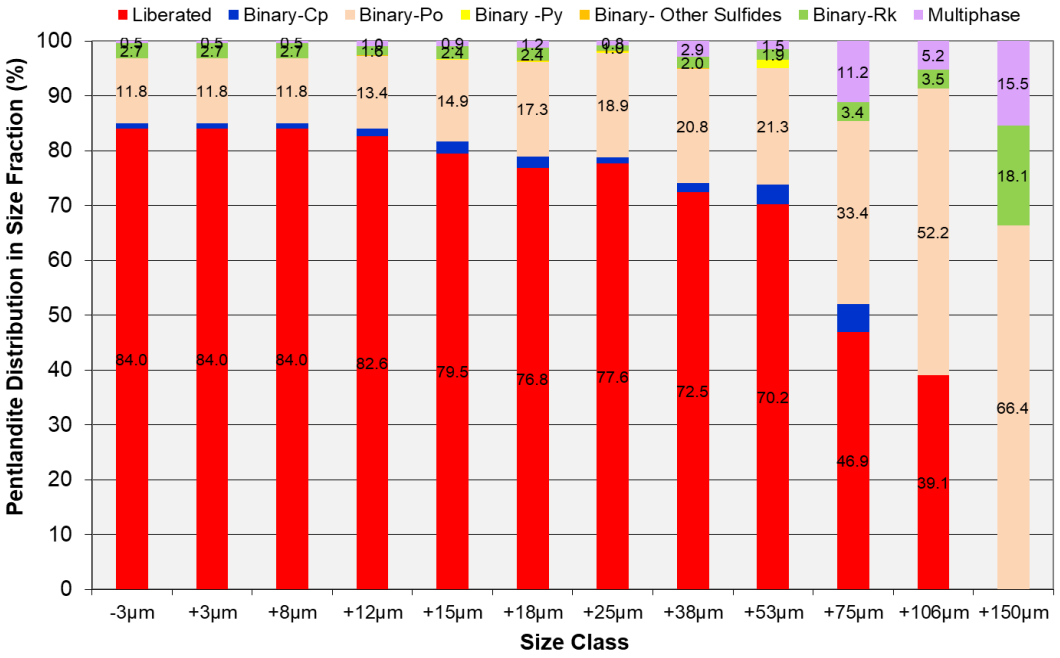

Figure B1 *– Ore A: pentlandite liberation/mineral associations by size class.*

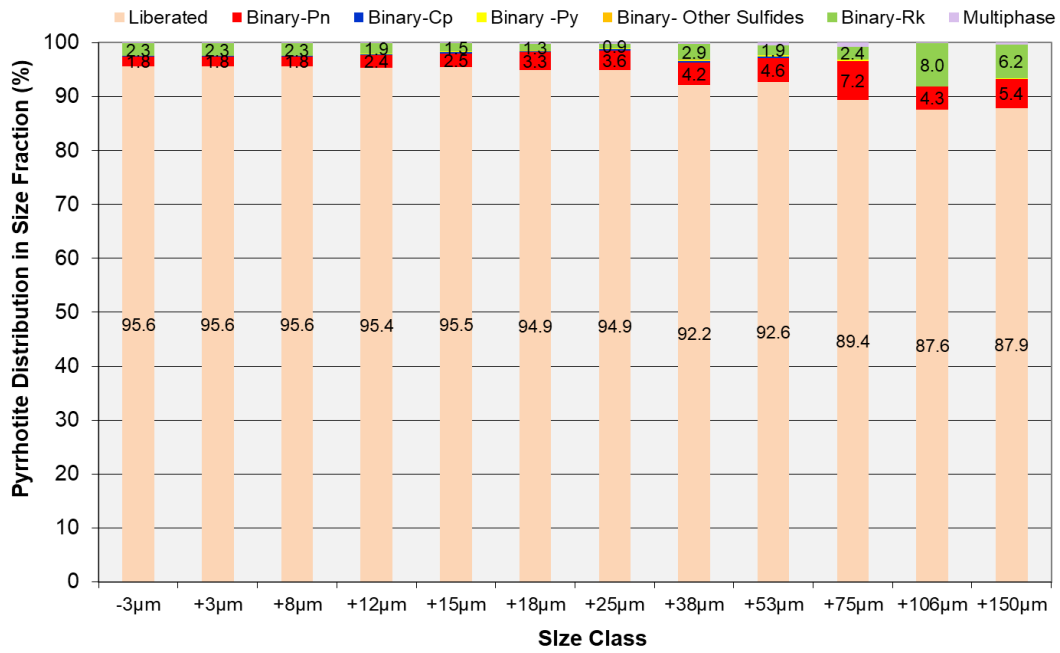

Figure B2 *– Ore A: pyrrhotite liberation/mineral associations by size class.*

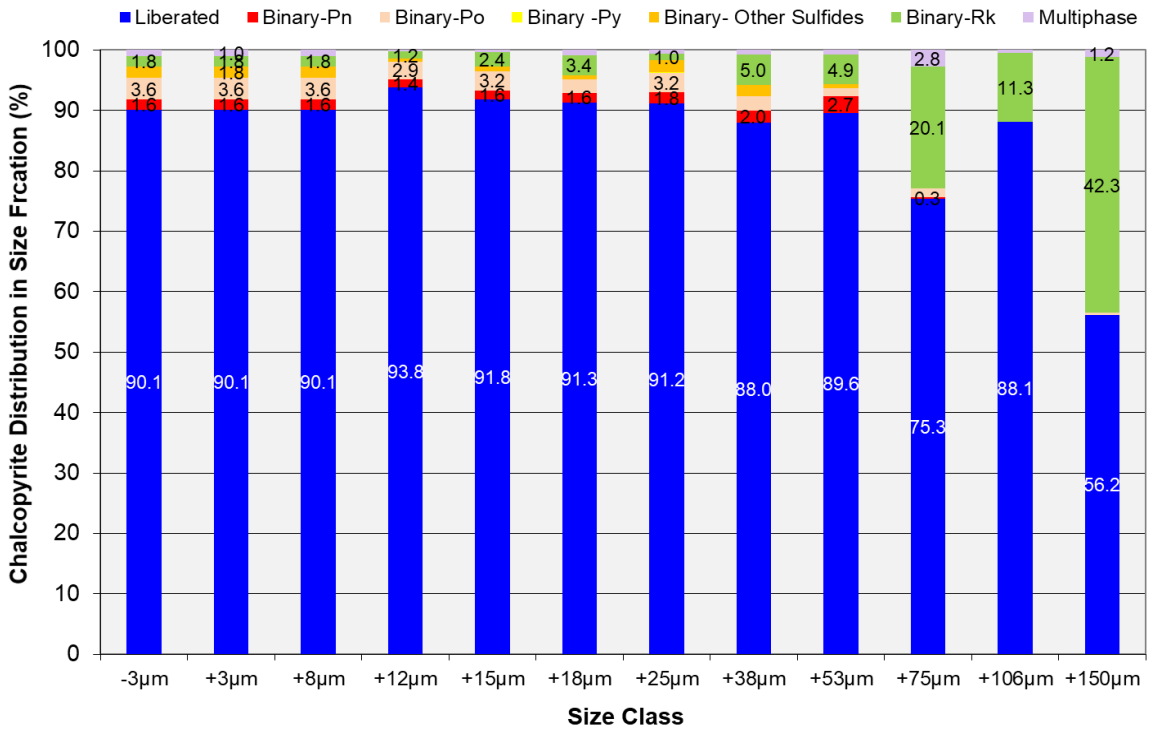

Figure B3 *– Ore A: chalcopyrite liberation/mineral associations by size class.*

Ore B

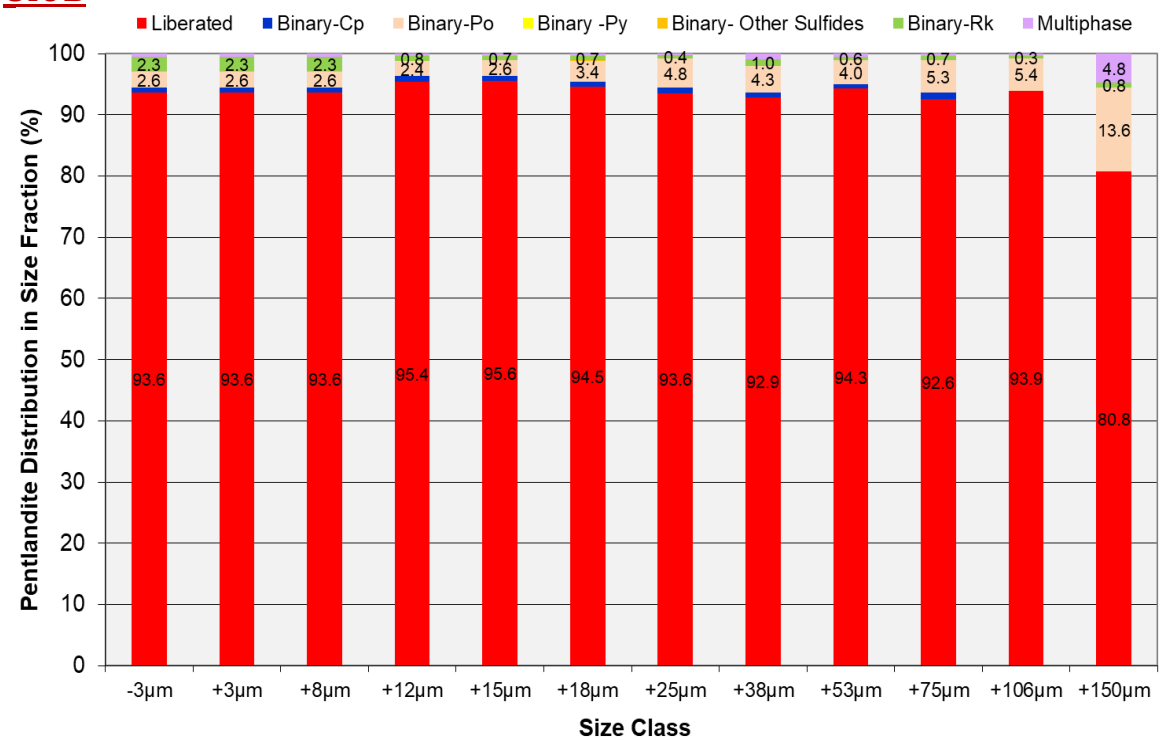

Figure B4 *– Ore B: pentlandite liberation/mineral associations by size class.*

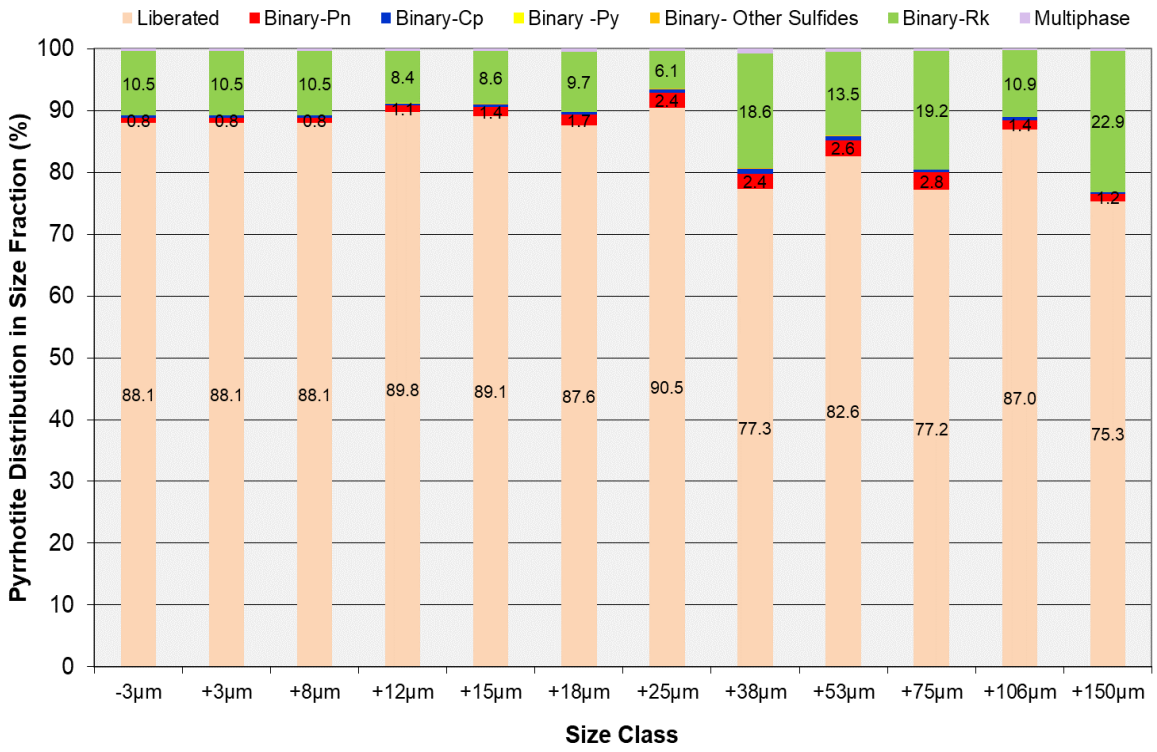

Figure B5 *– Ore B: pyrrhotite liberation/mineral associations by size class.*

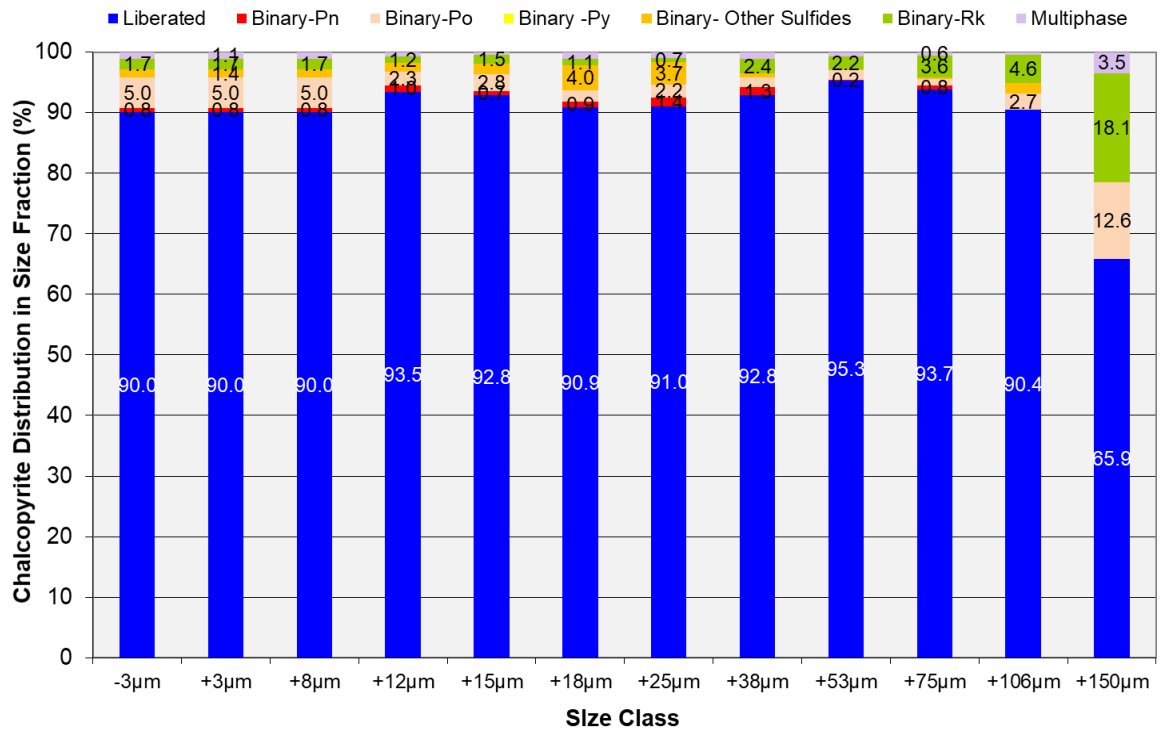

Figure B6 *– Ore B: chalcopyrite liberation/mineral associations by size class.*

Ore C

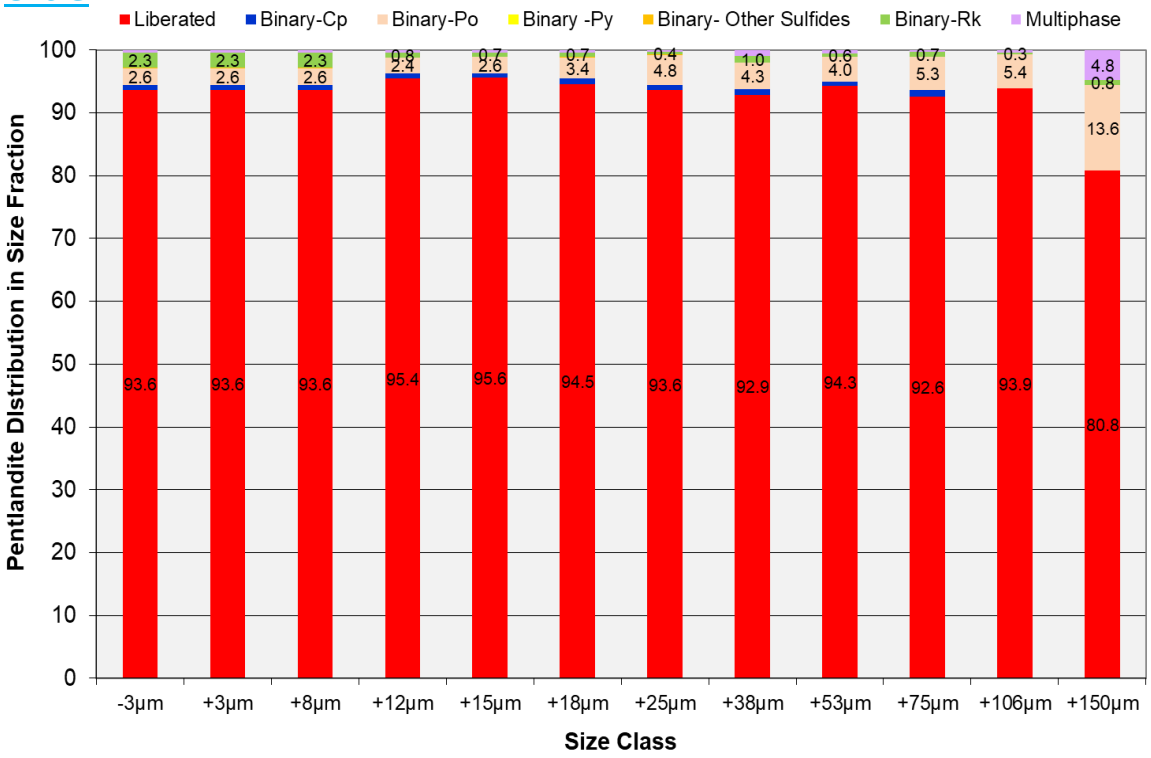

Figure B7 *– Ore C: pentlandite liberation/mineral associations by size class.*

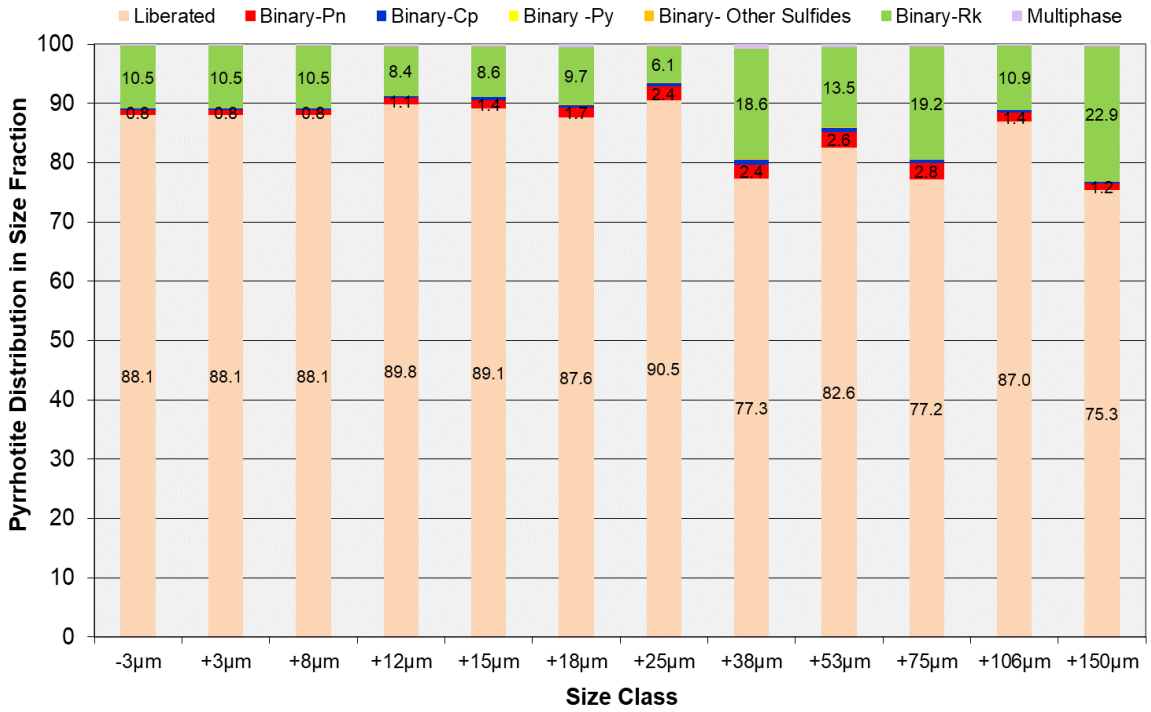

Figure B8 *– Ore C: pyrrhotite liberation/mineral associations by size class.*

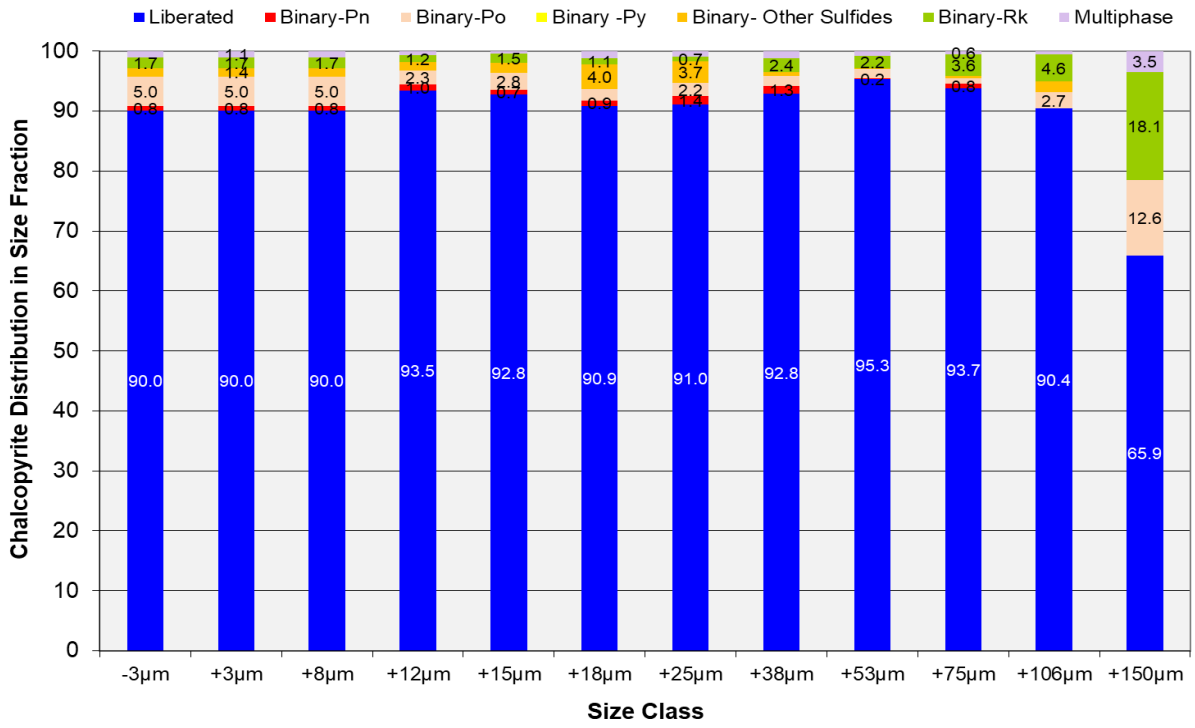

Figure B9 – *Ore C: chalcopyrite liberation/mineral associations by size class.*

Ore D

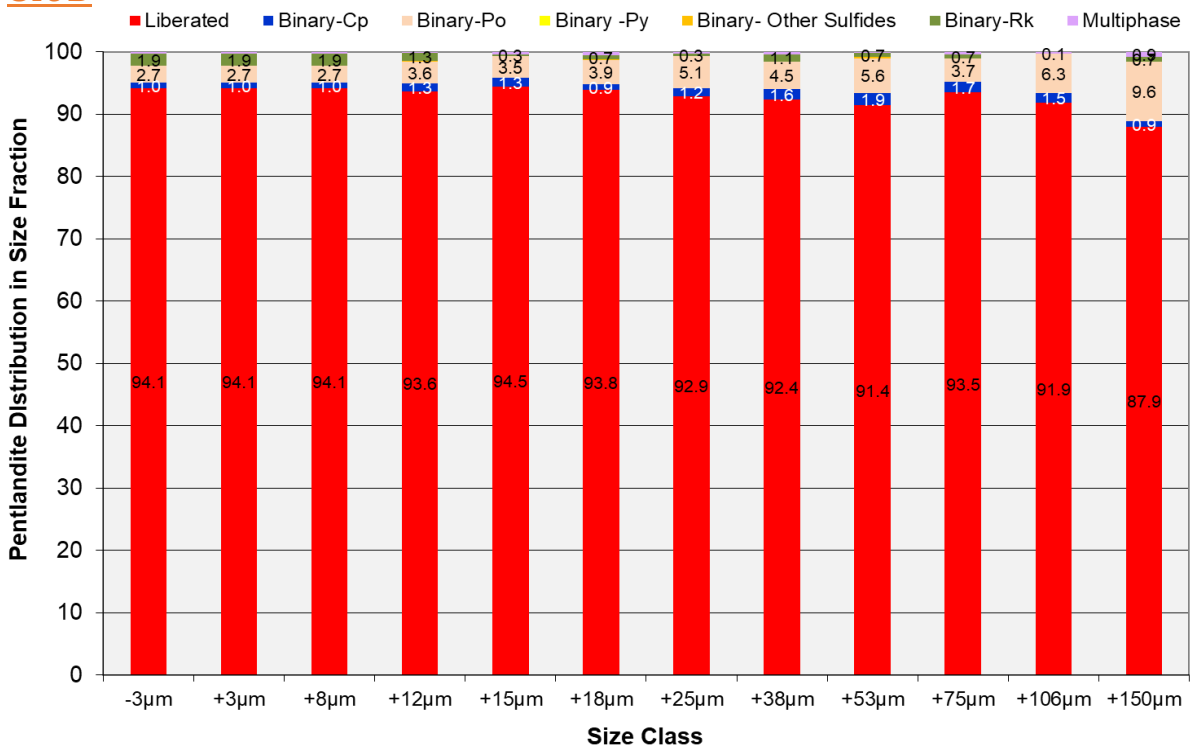

Figure B10 – *Ore D: pentlandite liberation/mineral associations by size class.*

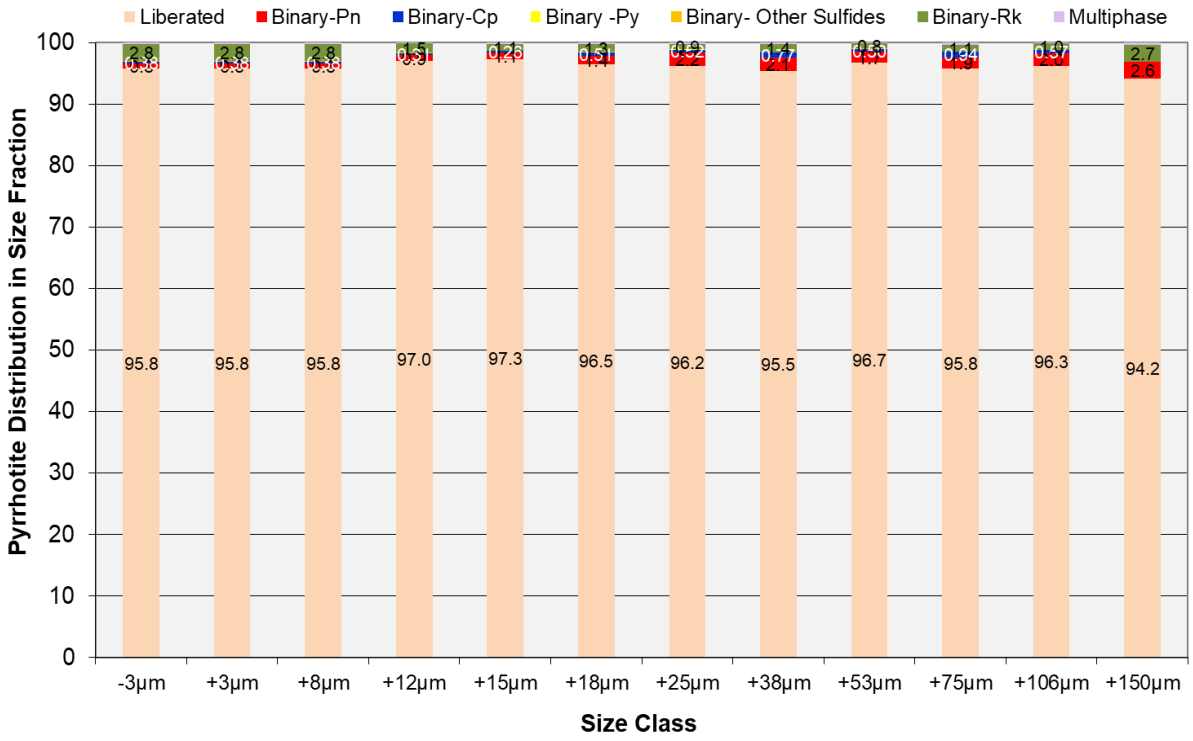

Figure B11 – *Ore D: pyrrhotite liberation/mineral associations by size class.*

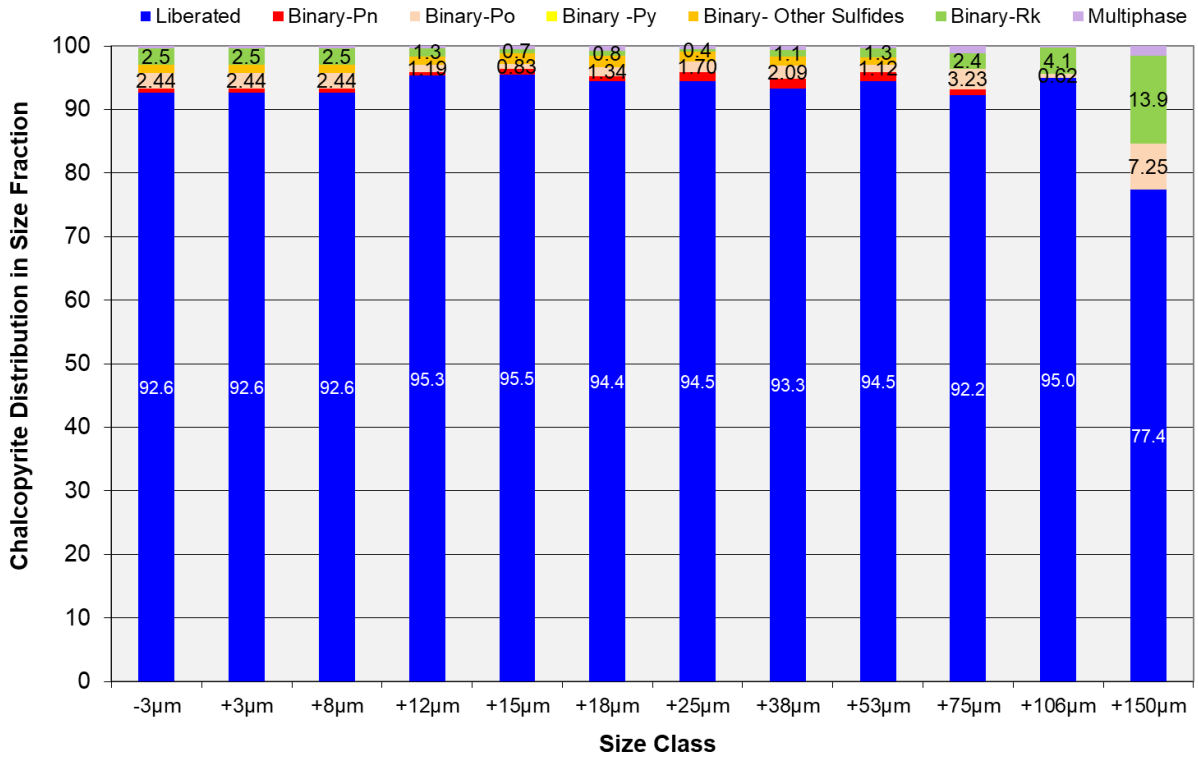

Figure B12 – *Ore D: chalcopyrite liberation/mineral associations by size class.*

Preliminary Study

Grade-Recovery, Mineral Kinetics, and Concentrate Ni & Cu Upgrade Ratios

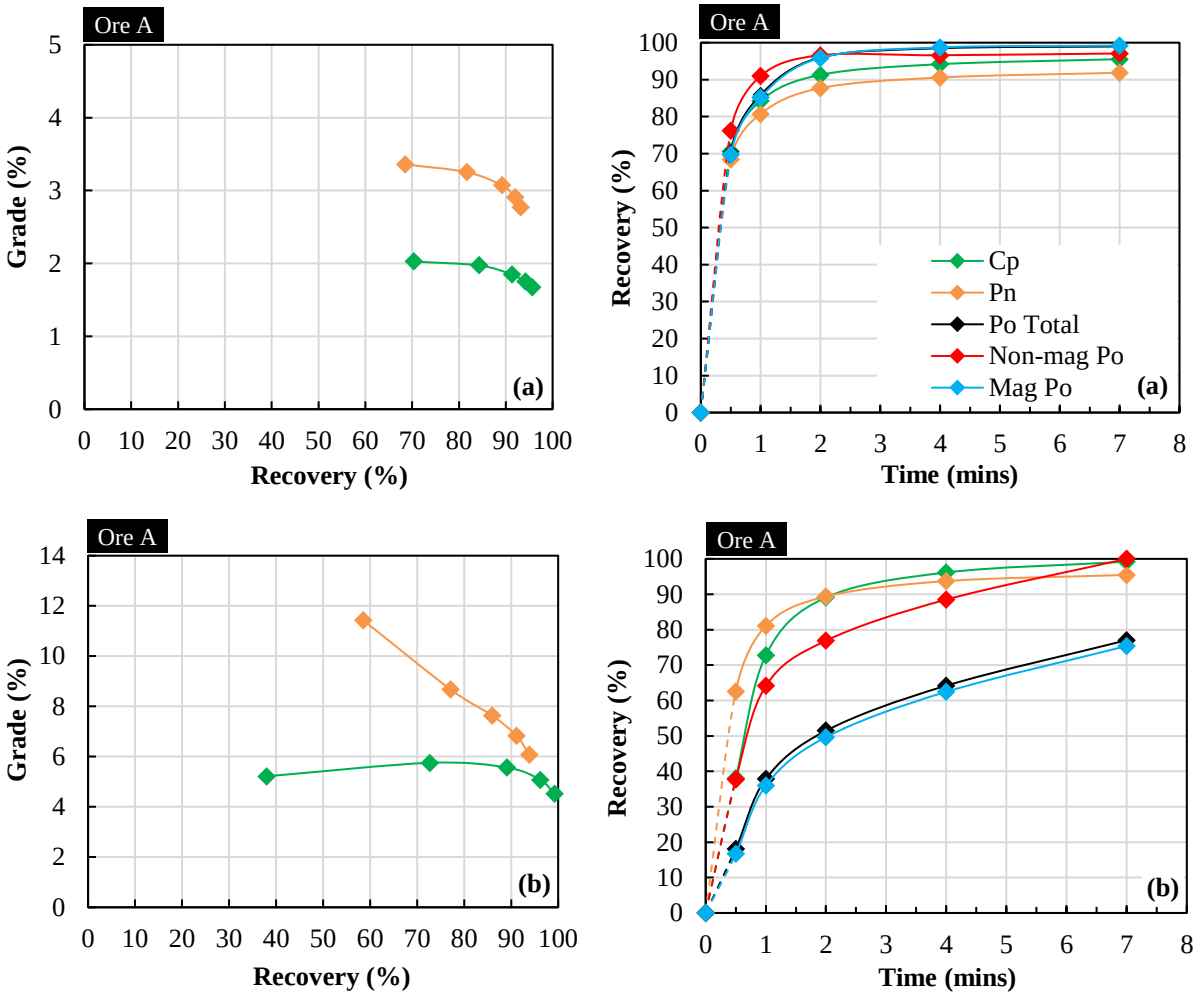

Figure B13 *– Preliminary study Ore A cumulative grade–recovery and mineral kinetics curves; (a) PAX dosage = 180 g/t; (b) PAX dosage = 28 g/t.*

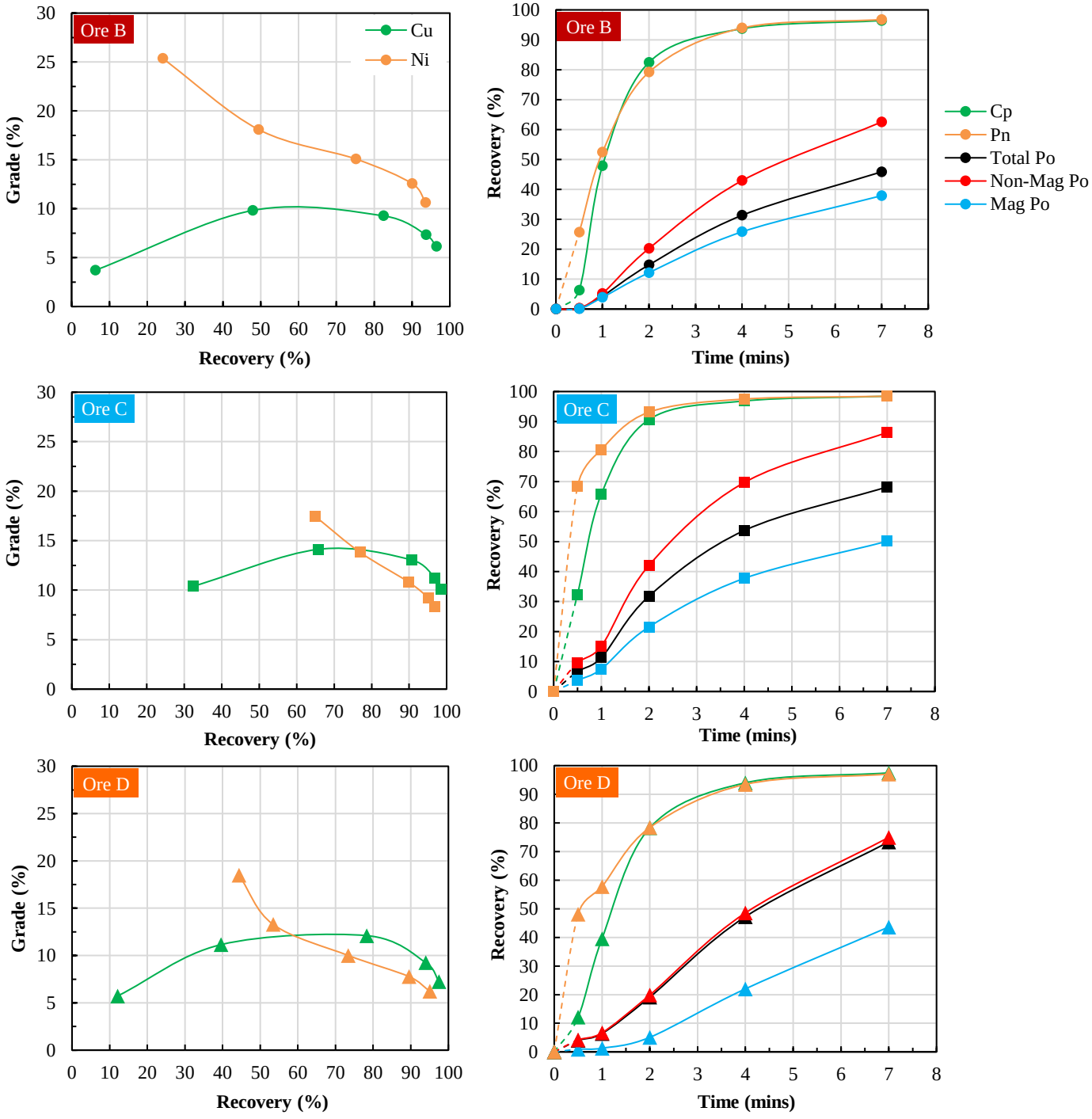

Figure B14 *– Preliminary study cumulative grade–recovery and mineral kinetics curves.*

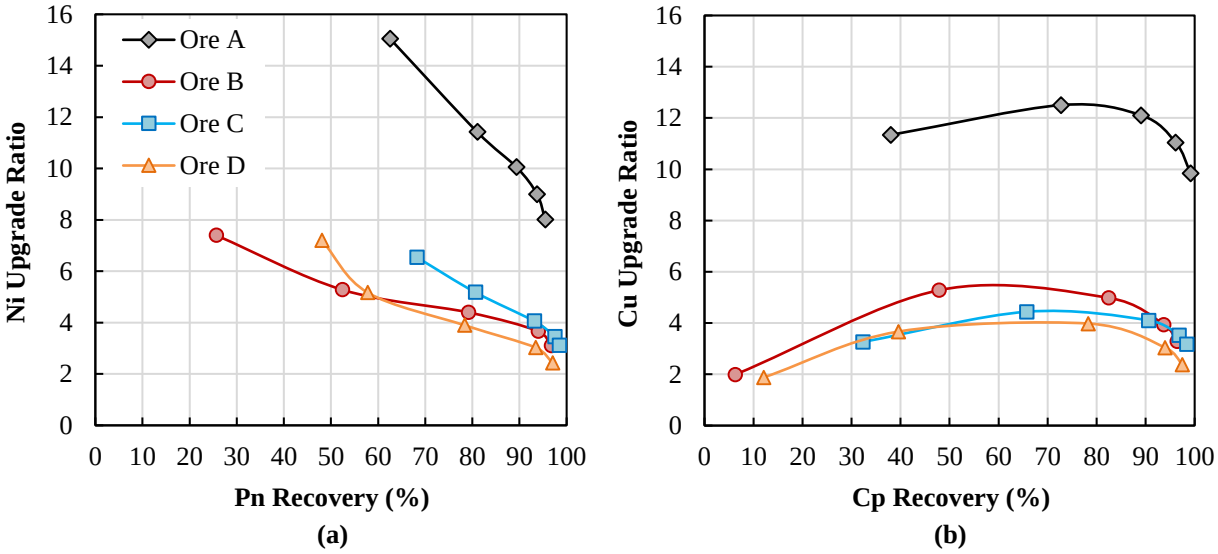

Figure B15 *– Preliminary study upgrade ratio for each ore; (a) nickel; (b) copper.*

In-depth Study

Baseline Tests (Staged Reagent Addition) – Grade-Recovery and Po-Pn Selectivity Curves

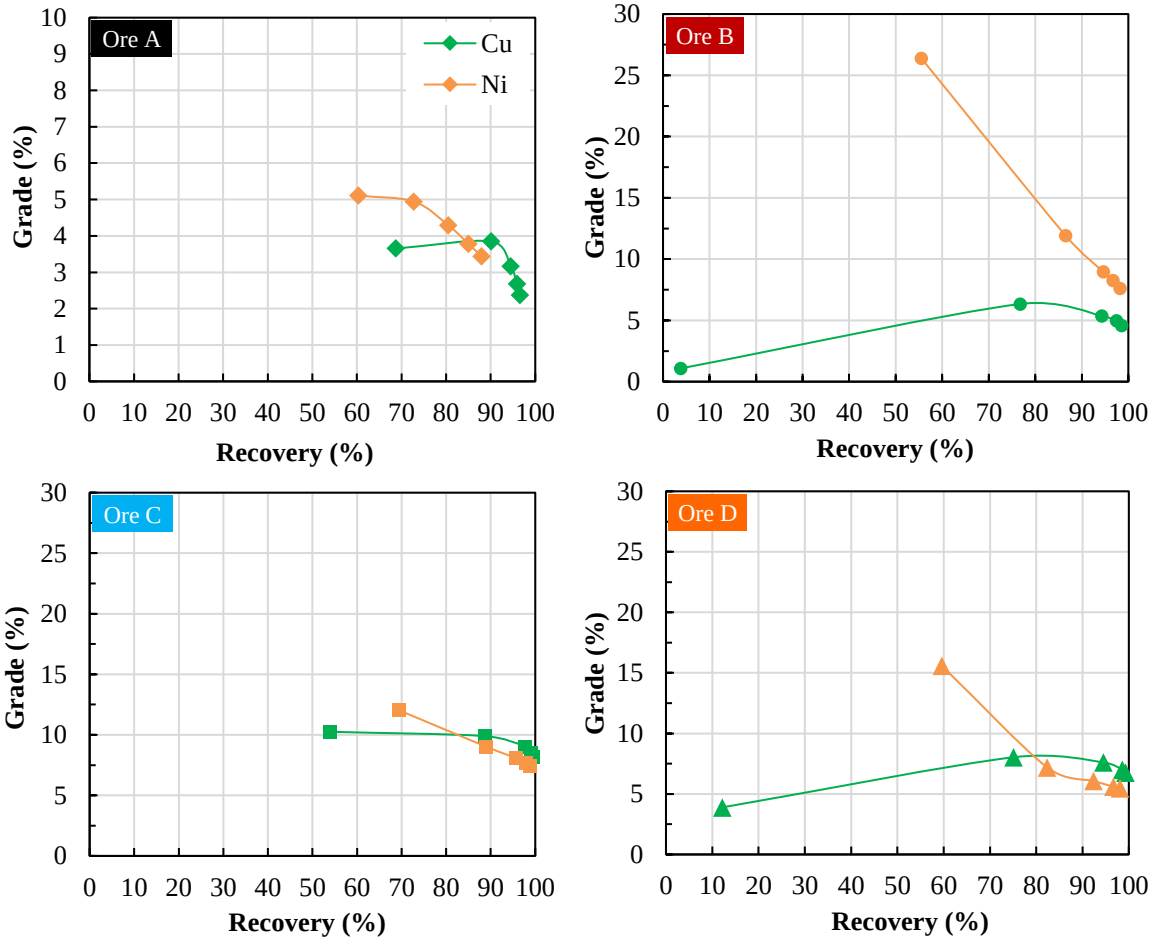

Figure B16 *– In-depth study (baseline) cumulative grade–recovery and mineral kinetics curves.*

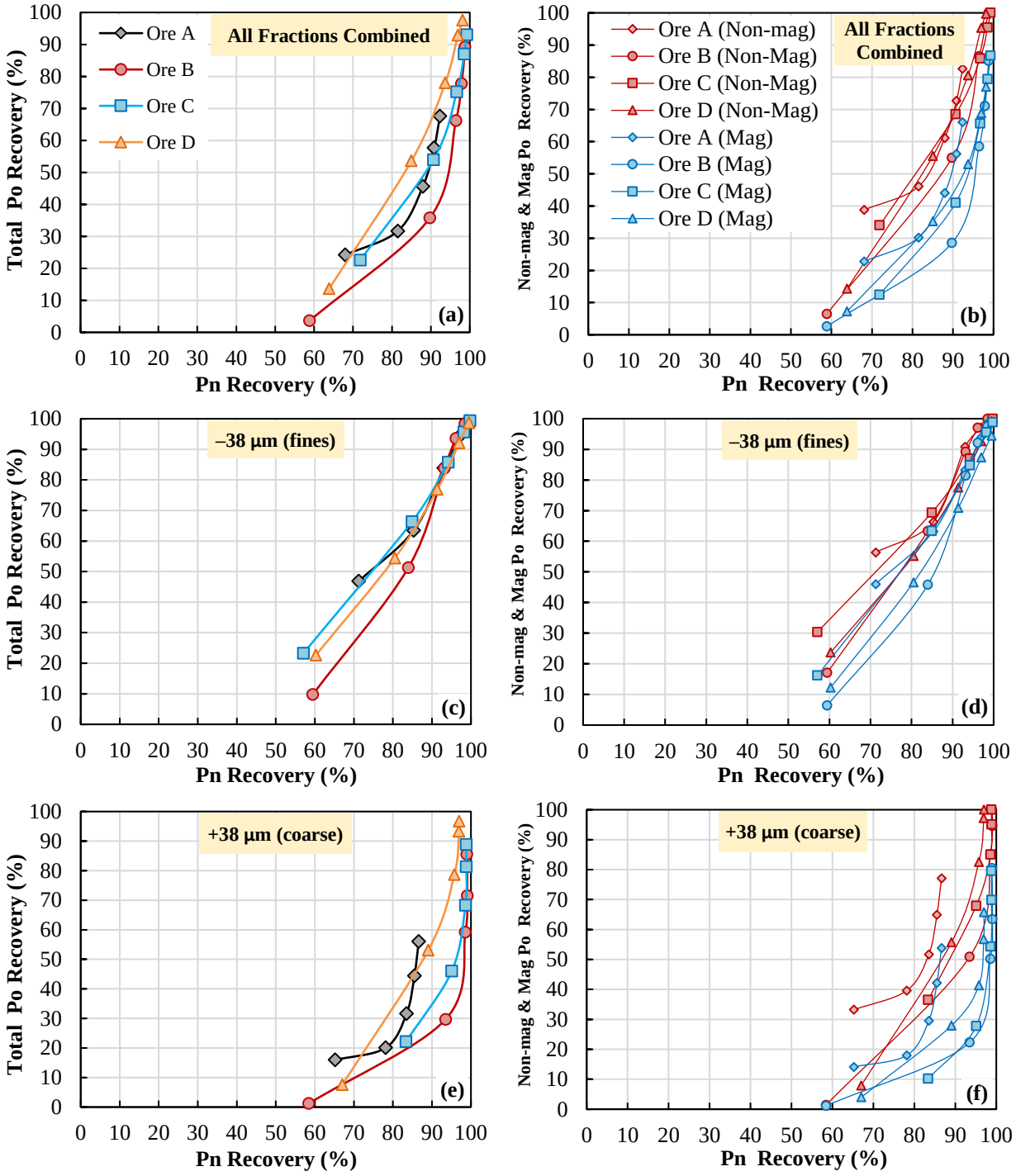

Figure B17 *– In-depth study (baseline) Po–Pn Selectivity: Total Po and {Non–mag & Mag Po} vs. Pn: (a,b) all fractions combined; (c,d) –38 µm fraction; (e,f) +38 µm fraction.*

DETA/SMBS Tests – Grade Recovery Curves

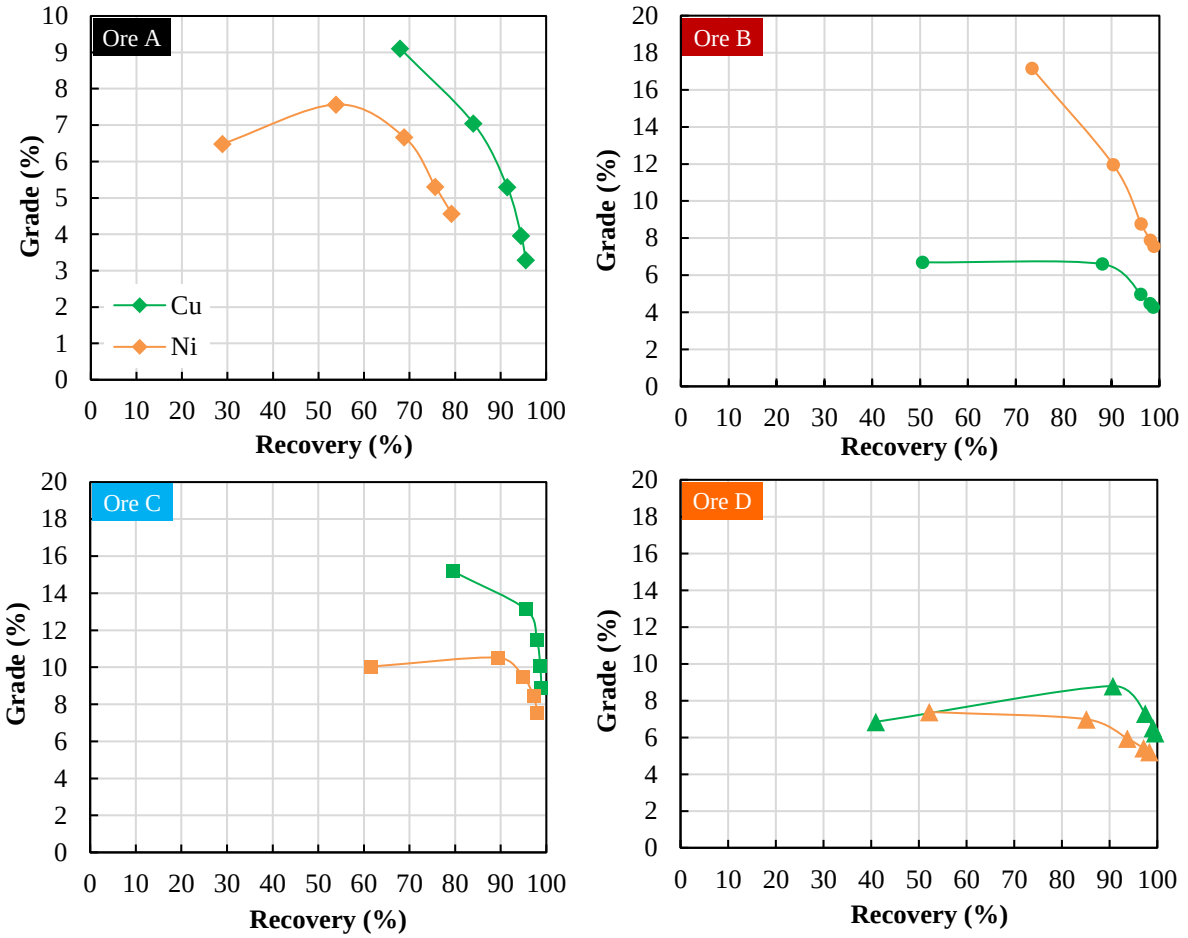

Figure B18 *– In-depth study (DETA/SMBS) cumulative grade–recovery and mineral kinetics curves: (a) Ore B; (b) Ore C; and (c) Ore D.*